Thèse de l'Université Sorbonne Paris Cité
Préparée à l'Université Paris Diderot
Et à l'IPGP - Équipe de Planétologie et Sciences Spatiales

**École Doctorale STEP'UP (ED560)**

# Effect of the north/south dichotomy on the thermal evolution and structure of Mars

par


## Mélanie THIRIET


présentée et soutenue publiquement le
22 octobre 2018

**Thèse de doctorat de Sciences de la Terre et de l'Environnement**
**Spécialité de doctorat : géophysique**

Dirigée par :

| | |
|---|---|
| **Chloé MICHAUT**<br>Professeur (École Normale Supérieure de Lyon) | Directrice de thèse |
| **Doris BREUER**<br>Professeur (German Aerospace Center - DLR) | Co-directrice de thèse |

Devant un jury composé de :

| | |
|---|---|
| **Philippe LOGNONNÉ**<br>Professeur (Institut de Physique du Globe de Paris) | Président du jury |
| **Gaël CHOBLET**<br>Chargé de Recherche CNRS (Laboratoire de Planétologie et Géodynamique) | Rapporteur |
| **Ulrich R. CHRISTENSEN**<br>Professeur (Max Planck Institute for Solar System Research) | Rapporteur |
| **Antoine MOCQUET**<br>Professeur (Laboratoire de Planétologie et Géodynamique) | Examinateur |
| **Chloé MICHAUT**<br>Professeur (École Normale Supérieure de Lyon) | Directrice de thèse |
| **Doris BREUER**<br>Professeur (German Aerospace Center - DLR) | Co-directrice de thèse |

# CONTENTS

# REMERCIEMENTS

Je tiens en tout premier lieu à remercier mes directrices de thèse Chloé Michaut et Doris Breuer sans qui ce travail n'aurait pas vu le jour. Merci à vous de m'avoir fait confiance en me laissant travailler dans la plus grande autonomie tout en sachant me faire profiter de votre expérience et de vos conseils avisés dans les moments cruciaux. Cette thèse doit également beaucoup à Ina Plesa qui m'a appris les subtilités du code Gaia, toujours avec un sourire et une patience à toute épreuve ! Je remercie également Mélanie Drilleau qui a su faire preuve d'une pédagogie remarquable pour partager ses connaissances en sismologie avec une néophyte en la matière comme moi, et ce dans l'atmosphère angoissante des toutes dernières semaines de thèse. Enfin un immense merci à Philippe Lognonné ainsi qu'à toute l'équipe InSight pour le temps et l'énergie incroyables qu'ils ont consacrés à cette mission, une belle aventure tant humaine que scientifique qui fut le coeur de ce travail.

Au rang de ce qui contribuèrent grandement à l'émulation scientifique autour de cette thèse je n'oublierai pas les conseils avisés de Cinzia Farnetani, Laure Ménadier et Alexandre Fournier. J'ai également une pensée chaleureuse envers ce dernier, Éric Gayer, mes co-encadrants de TD ainsi que mes élèves pour le plaisir que j'ai eu à partager avec eux ma première expérience d'enseignement : des moments d'évasion durant des périodes parfois difficiles que comporte toute thèse. Des instants salvateurs qui trouvèrent également leur source auprès de la troupe de Caprice(s), de mon EOS 500 - fidèle compagnon de mes froides vadrouilles dans le tout Paris -, des rudes entraînements marathon mais également en chacune des rencontres de hasard dans les AJ berlinoises qui firent de mon séjour au pays de Goethe une aventure de chaque jour.

Au moment où j'écris ces quelques lignes je m'apprête non sans émotion à quitter l'équipe de Lamarck qui m'accompagna ces trois dernières années, à la fois si longues et si courtes. Merci à vous tous ainsi qu'à toute l'équipe du DLR pour votre accueil, et en particulier Claudine pour sa patience à m'expliquer inlassablement les mystères de l'administratif - ma bête noire -, Virgile pour les longues poses thé à refaire le monde, Balthasar pour avoir transformé ma semaine d'astreinte au CDD en un de mes meilleurs souvenirs (merci pour ton sourire !), Aurélien pour son humeur "buccolique" et Foivos pour son humour si particulier qui réchauffa notre bureau. Enfin toute ma gratitude envers Henri, Guillaume et Taichi pour m'avoir accompagnée dans le sprint final de la soutenance et pour leur bonne humeur sans faille !

Mais s'il est vraiment un pan relationnel qui me fut vital c'est celui de ma famille. Je ne serai jamais assez reconnaissante du soutien sans faille de ma mère ni de l'entérêt indéfectible de mon père et de mes frères envers mon sujet qui souvent ranima mon amour pour la recherche

dans les moments de doute. Aujourd'hui toutes mes pensées s'envolent vers mon rayon vert, mon edelweiss des montagnes et mon doc, sources immuables d'inspiration et de tendresse.

Flo : parfois les mots semblent bien pâles donc je me contenterai de te dire merci pour tout !

# ABSTRACT

**Keywords :** Mars, north/south dichotomy, thermal evolution, scalings laws of convection, elastic lithosphere thickness, crustal properties, surface wave propagation, InSight mission.

Mars's crustal dichotomy in altitude and aspect between the southern highlands and the northern lowlands is one of the most stricking feature of the planet that probably dates back from the early stages of the planet. This surface crustal dichotomy probably extends in depth implying, in particular, north/south differences in crustal thickness and perhaps in composition. In this thesis, we focus on the consequences of such a potential dichotomy in crustal properties on Mars thermal evolution and structure.

The use of 1-D parametrized thermal models is required to explore large ranges of crustal properties. By comparing 1-D and 3-D thermal models in Monte Carlo simulations, we first search for appropriate scaling parameters ($a_{rh}$ and $\beta^u$ here) to describe the heat flux through the mantle's upper layers for a cooling planet in stagnant lid convection. Although those scaling parameters are sensitive to the model set-up and, in particular, to the heating mode that evolves with time, we show that one pair of $a_{rh}$ and $\beta^u$ can suitably describe the entire thermal evolution of Mars. We also test the effect of varying parameters such as the mantle aspect ratio, rheological parameters, surface and internal temperatures, and find that a unique parameter combination $a_{rh} = 2.16$ and $\beta^u = 0.345$ can be used for all those models.

Using these scaling laws in 1-D thermal models, we then search the northern and southern crustal properties that could explain the observations of recent volcanism and the elastic lithosphere thickness estimates : $\sim 25$ km during the Noachian in the south, and a large present-day difference below the two polar caps ($> 300$ km in the north and $> 110$ km in the south). We find that $55-65$ % of the bulk radioelement content are in the crust, and most of it ($43-51$ %) in the southern one. The southern crust could be less dense than the northern one (up to 480 kg/m$^3$) and might contain a non-negligible proportion of felsic rocks. Our models predict present-day north/south surface heat flux of $17.1-19.5$ mW/m$^2$ and $24.8-26.5$ mW/m$^2$, respectively, and a large difference in lithospheric temperatures between the two hemispheres ($170-304$ K in the shallow mantle).

In the context of the InSight mission, we finally investigate the effect of our thermal models on surface wave propagation. We find that surface wave velocities mostly depend on the crustal thickness and, to a lesser extent, on the crustal composition and lithospheric temperatures. Along great circles the dispersion curves are influenced by the properties of the two hemispheres but probably mostly by those of the southern one that covers a wider area. If the

northern hemisphere is not enough sampled or if the north/south contrast in crustal thickness is small ($\sim$ 20 km), constraining the northern crust's properties might be hard with only surface wave analysis.

# RÉSUMÉ

**Mots-clés :** Mars, dichotomie nord/sud, évolution thermique, lois d'échelle de convection, épaisseur élastique de la lithosphère, propriétés de la croûte, propagation des ondes de surface, mission InSight.

La dichotomie d'aspect et d'altitude entre les hémisphères nord et sud de Mars est l'une des plus anciennes et des plus impressionnantes structures qui marquent la surface de la planète. Cette dichotomie de surface s'étend probablement en profondeur, impliquant des différences en terme d'épaisseur, et potentiellement de composition, entre les croûtes des deux hémisphères. Dans ce manuscrit nous étudions les conséquences d'une éventuelle dichotomie entre les propriétés crustales nord et sud sur l'évolution thermique et la structure interne de Mars.

Afin d'explorer de vastes gammes de paramètres, l'utilisation de modèles thermiques 1-D paramétrés est nécessaire. En comparant des modèles 1-D et 3-D dans des simulations Monte Carlo, nous déterminons des paramètres d'échelle appropriés ($a_{rh}$ et $\beta^u$ dans cette étude) pour décrire le flux de chaleur observé à travers les couches supérieures du manteau lors du refroidissement d'une planète présentant une couche stagnante à sa surface. Bien que ces paramètres d'échelle soient sensibles, en particulier, au mode de chauffage du manteau qui évolue dans le temps, une unique paire de $a_{rh}$ et $\beta^u$ peut décrire de manière satisfaisante l'évolution thermique de Mars. Nous testons par ailleurs l'effet de différents paramètres (rayon du noyau, températures interne et de surface...) et montrons qu'une paire identique de paramètres $a_{rh} = 2.54$ et $\beta^u = 0.335$ peut être utilisée pour tous ces cas de figure.

En utilisant ces lois d'échelle dans des modèles thermiques 1-D, nous recherchons les propriétés des croûtes nord et sud pouvant expliquer l'existence d'un volcanisme récent sur Mars ainsi que les estimations des épaisseurs de la lithosphère élastique : $\sim 25$ km durant le Noachien et une grande différence actuelle sous les deux calottes polaires ($> 300$ km au nord et $> 110$ km au sud). Nos résultats indiquent que $55-65$ % de la totalité des éléments radioactifs de la planète doivent être concentrés dans la croûte, principalement dans celle du sud ($43-51$ %) qui peut être moins dense que la croûte nord et contenir une proportion non négligeable de roches felsiques. Nous prédisons des flux de chaleur de surface actuels de $17.1-19.5$ mW/m$^2$ dans le nord et $24.8-26.5$ mW/m$^2$ dans le sud, ainsi qu'une grande différence entre les températures lithosphériques des deux hémisphères ($170-304$ K dans le manteau peu profond).

Dans le contexte de la mission InSight, nous étudions également l'effet de nos modèles thermiques sur la propagation des ondes de surface. Nous trouvons que les vitesses des ondes de surface dépendent principalement de l'épaisseur de la croûte ainsi que, dans une moindre

mesure, de la composition de la croûte et des températures lithosphériques. Le long d'un grand cercle, elles sont influencées par les propriétés des deux hémisphères mais probablement surtout par celles de l'hémisphère sud qui est plus vaste. Si l'hémisphère nord n'est pas assez représenté sur ce trajet, ou si le contraste entre les épaisseurs crustales nord/sud est faible ($\sim$ 20 km), les propriétés de la croûte nord devraient difficilement être contraintes par la seule analyse des ondes de surface.

# PRÉAMBULE

Depuis aussi longtemps que l'humanité a les yeux tournés vers l'immensité des cieux, Mars la rouge la fascine. Bien que dix fois plus petite que la Terre, la proximité de cette planète, la quatrième du système solaire, a rendu possible son observation à l'oeil nu dès l'Antiquité. Mais ce n'est cependant qu'avec l'avènement de l'exploration spatiale que toutes les richesses de sa surface et de son activité géologique passée ont commencé à être pleinement dévoilées. Si les premières missions n'avaient levé le voile que sur une infime portion de sa surface et laissé entrevoir un monde très cratérisé assez similaire à la Lune, la netteté et la résolution des images de Mariner 9 au début des années 70 ont permis d'obtenir une topographie détaillée ainsi que de mettre en évidence des structures de surface étonnament variées (volcans, mesas, rifts, vallées, dunes, calottes) et qui, bien que différentes, étaient étonnament similaires à celles observées sur notre propre planète (Figures 1 et 2).

Un des plus grands étonnements provint certainement de la découverte d'une dichotomie d'altitude et d'aspect très marquée entre les deux hémisphères de la planète se traduisant par une surface sud beaucoup plus rugueuse et cratérisée en comparaison des vastes plaines du nord plus lisses et moins élevées. Aujourd'hui encore, l'origine de cette dichotomie crustale ainsi que ses conséquences sur la dynamique interne de la planète demeurent très énigmatiques et représentent un des enjeux majeurs de la recherche martienne. Une seconde observation, et de taille, fût la découverte des plus grands volcans boucliers connus dans le système solaire, vestiges d'une activité géologique intense par le passé et jusqu'alors insoupçonnée pour une planète de la taille de Mars. Ces volcans se répartissent en deux zones géographiques principales au niveau de la ceinture équatoriale : Elysium Mons ainsi que d'autres édifices plus mineurs à l'est, tandis que le panorama de l'ouest est largement dominé par le bouclier de Tharsis. Ce dernier consiste en un immense renflement crustal de 5500 km de diamètre regroupant de multiples stratovolcans, caldeiras ou patera, et est profondément marqué par la présence de cinq volcans boucliers majeurs : Ascraeus Mons, Arsia Mons et Pavonis Mons à l'est, Olympus Mons à l'ouest (le plus haut volcan du système solaire avec plus de 22 km de hauteur pour 650 km de diamètre, Figure 1e) et Alba Patera au nord (le plus large des volcans boucliers connus avec 1600 km de diamètre) (*Plescia*, 2004). À l'est du renflement de Tharsis, comme un clin d'oeil au dieu de la guerre de la Rome Antique qui valut son nom à la planète, l'impressionnante cicatrice de Valles Marineris (Figure 1g) entaille profondément le relief et illustre une fois de plus la démesure des structures martiennes avec une profondeur pouvant atteindre 10 km, plusieurs centaines de kilomètres de large et 3500 km de long (soit environ 10 fois plus imposant que le Grand Canyon du Colorado à titre illustratif). Il s'agit en effet du plus vaste système de canyons connu dont la formation résulterait probablement de la fracture

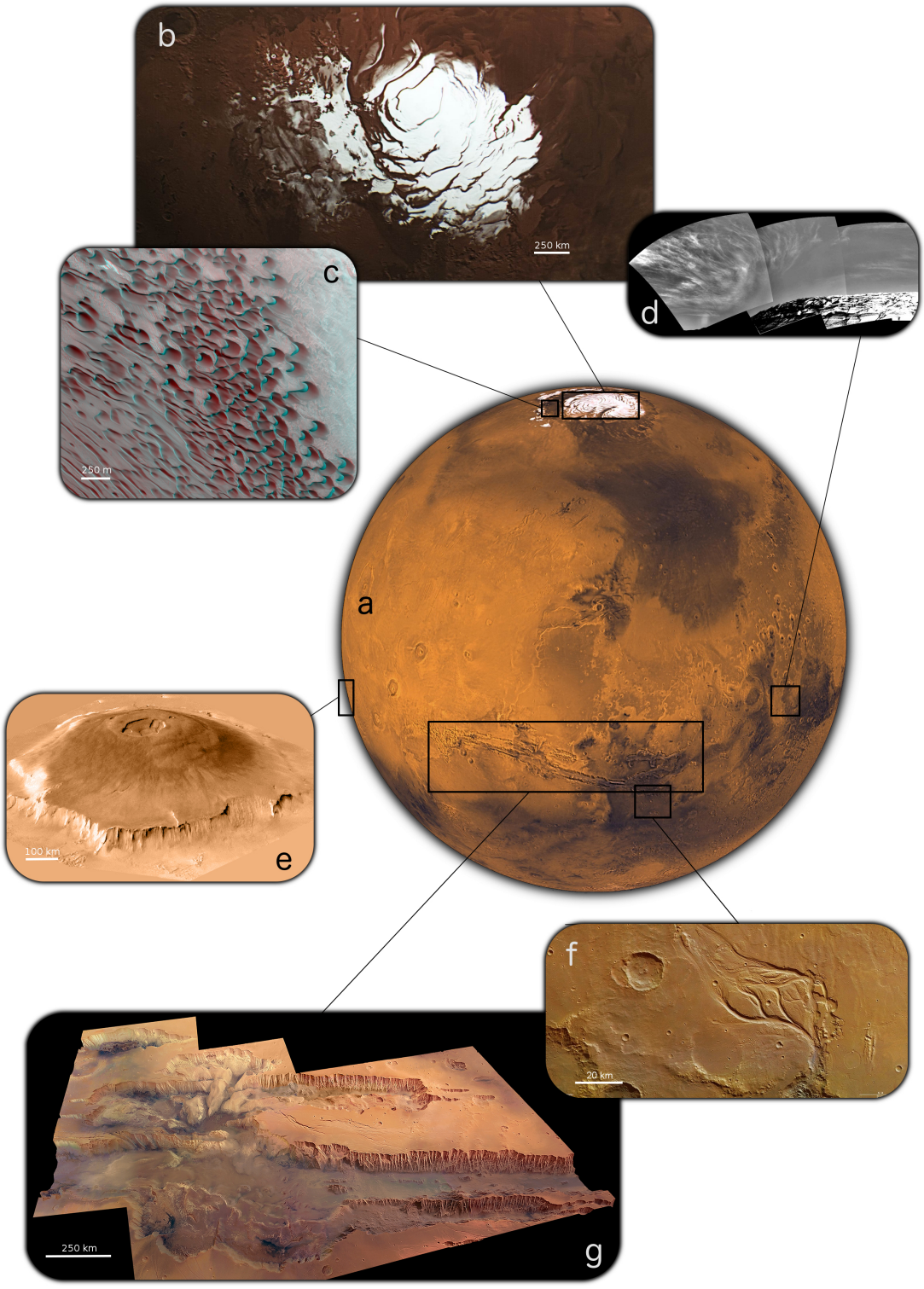
b
250 km
c
250 m
d
a
100 km
e
f
20 km
250 km
g

**FIGURE 1** – Structures martiennes de surface. (a) Image en mosaïque de Mars reconstituée à partir des images prises par l'orbiteur Viking 1 (crédits NASA). (b) Image de la calotte polaire nord prise par l'instrument High Resolution Stereo Camera (HRSC) de la mission Mars Express (crédits ESA/DLR/FU Berlin) (c) Champ de dunes barkhanes localisé dans le bassin boréal imagé par l'instrument High Resolution Imaging Science Experiment (HiRISE) de la sonde Mars reconnaissance Orbiter (crédits : NASA/JPL/University of Arizona). (d) Image prise par le rover Opportunity montrant la présence de cirrus très similaires à ceux observés sur Terre (crédits NASA Opportunity, jour Sol 290). (e) Reconstruction 3-D du volcan Olympus Mons situé sur le plateau de Tharsis (crédits : Viking/NASA/JPL). (f) Ancien réseau hydrologique de la vallée d'Osuga, situé près de Valles Marineris (image prise par l'instrument HRSC. crédits : ESA/DLR/FU Berlin). (g) Vue 3D de Valles Marineris réalisée à partir des photos et des données altimétriques MOLA (Mars Orbiter Laser Altimeter) prises par la sonde spatiale Mars Express (crédits : ESA/DLR/FU Berlin).

de la croûte fragilisée par la mise en place du bouclier de Tharsis (*Montgomery et al.*, 2009). D'autres vastes dépressions de forme circulaire sont également visibles à la surface de Mars, vestiges et témoins de la violence du bombardement intense qui sévissait durant les premiers stades d'évolution du système solaire. Parmi les plus spectaculaires de ces bassins d'impact on citera notamment le bassin d'Hellas dans le sud qui correspond au point le moins élevé de la planète (soit 31 km plus bas que le point culminant d'Olympus Mons), ou encore le bassin d'Utopia dans le nord (Figure 2). Par la suite, faute d'une atmosphère suffisamment dense pour consumer les impacteurs, comme c'est le cas sur Terre, le bombardement, bien que déclinant, a continué de marquer la surface de la planète, expliquant le taux de cratérisation important de la surface, notamment au sud.

Décrite depuis l'Antiquité comme la planète du sang à cause de sa couleur, et de ce fait associée à un monde de violence et de mort, la vision de Mars a peu à peu évolué vers celle

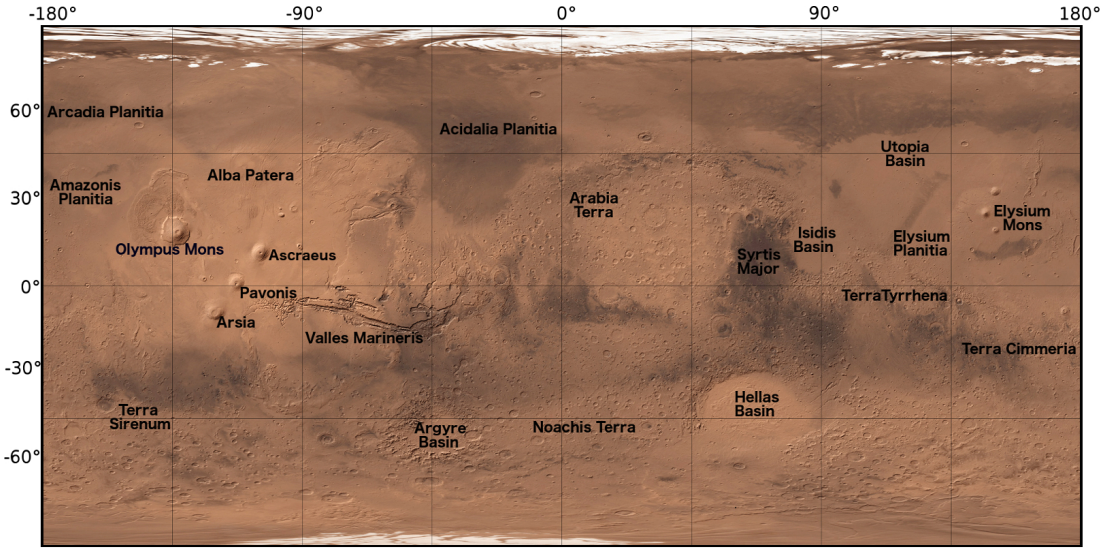


**FIGURE 2** – Localisation des structures et régions principales de Mars (crédits : NASA/JPL/USGS).

d'un habitat potentiel pour la vie. En effet, des preuves d'interactions passées entre de l'eau sous forme liquide et la surface sont encore visibles aujourd'hui dans les Terres hautes du sud où l'on observe des réseaux fluviatiles à présent asséchés, majoritairement formés sur des terrains anciens datant d'il y a environ 4 à 3.5 milliards d'années (*Carr*, 1995; *Hynek and Phillips*, 2003) (Figure 1f). La découverte de minéraux altérés par hydrothermalisme (*Christensen et al.*, 2000; *Mustard et al.*, 2008) ainsi que des traces d'érosion fluviatile datant de la même époque (*Golombek and Bridges*, 2000; *Squyres et al.*, 2004) renforcent l'idée que les conditions climatiques étaient alors favorables à la présence d'eau liquide, tout du moins durant de courtes périodes. Certaines études suggèrent même l'existence concomitante d'un vaste océan recouvert de glace au niveau de l'hémisphère nord (*Clifford and Parker*, 2001), hypothèse cependant dure à vérifier du fait des importantes modifications qui ont subséquemment remodelé la surface (*Carr and Head*, 2003). Bien que durant son évolution Mars ait perdu une grande proportion de son atmosphère et probablement de son eau, des traces de cette dernière sont encore visibles aujourd'hui. Cependant, à la différence de la Terre, les conditions de pression (610 Pa en moyenne) et de température (210 K en moyenne avec de fortes variations tant journalières que géographiques) ne permettent plus la persistance d'eau sous forme liquide à la surface de Mars. Celle-ci est donc principalement présente sous forme de glace dans le régolite peu profond (portion superficielle de la croûte fragilisée par les impacts) (*Boynton et al.*, 2002; *Feldman et al.*, 2002) ainsi qu'au niveau des calottes polaires (Figure 1b) où on la retrouve en association avec de la glace de CO2, l'élément largement majoritaire de l'atmosphère martienne (*Titus et al.*, 2003; *Bibring et al.*, 2004). Ces calottes sont le siège de processus saisonniers importants de condensation et de sublimation donnant naissance à des cirrus très similaires à ceux observés sur Terre (Figure 1d) - principalement constitués de CO2 mais également d'eau - et jouent un rôle clé dans les déplacements des masses d'air par la création de vents pouvant former des dunes actives (Figure 1c) voir même, en de rares occasions, des tempêtes de sable à l'échelle planétaire pouvant durer plusieurs mois.

L'histoire de cette planète associée à l'eau liquide et donc potentiellement à la vie, ainsi que la richesse de ses structures géologiques similaires en bien des aspects à celles que l'on connaît sur Terre, font que Mars cristallise aujourd'hui les efforts de la recherche et les espoirs d'une meilleure compréhension de l'évolution de notre propre planète. En effet, l'intense activité géologique, la tectonique des plaques ainsi que les forts taux d'érosion qui ont remodelé la surface de la Terre des milliards d'années durant, font que les traces de son passé primitif ont été éradiquées, remaniées ou enfouies, ne nous laissant que très peu d'indices sur les premiers stades évolutifs de notre planète. De grandes problématiques demeurent donc. Quels sont en particulier les mécanismes qui ont conduit au système solaire tel que nous le connaissons aujourd'hui ? Dans ce scénario, comment l'eau a-t'elle pu devenir aussi abondante sur Terre et sur Mars alors que les modèles de formation du système solaire prédisent à contrario un grand assèchement de la nébuleuse proto-planétaire à de telles distances du soleil ? Quels sont les mécanismes de différenciation qui sont rentrés en jeu lors de la formation des planètes ? Quelles étaient les conditions de la Terre primitive et comment des molécules complexes ont-elles pu se former à partir des conditions prébiotiques de l'époque ? Ou encore, comment la tectonique

des plaques s'est-elle initiée ?... Du fait de sa taille "intermédiaire" Mars a contenu suffisamment de chaleur interne pour avoir une activité géologique intense dans le passé et produire des structures comme les grands complexes volcaniques, mais trop peu d'énergie et d'érosion pour en éradiquer la présence par la suite, ce qui lui a permis de conserver des traces de l'essentiel des étapes qui ont jalonné son histoire précoce. Cette double particularité en fait donc la planète idéale pour nous offrir une fenêtre d'observation sur l'histoire de la Terre primitive et ainsi extraire des processus communs par une évolution comparative avec notre planète.

Dans ce large éventail que représentent les enjeux de la recherche actuelle sur Mars, l'objectif de cette thèse est d'étudier si la dichotomie crustale de surface entre les hémisphères nord et sud a influencé la structure interne et l'évolution thermique de la planète, et le cas échéant dans quelle mesure.

# CHAPTER 1

# THE NORTH/SOUTH CRUSTAL DICHOTOMY OF MARS

**Sommaire**

# 1 Summary

The dichotomy is recognized as being one of the oldest features of the planet and probably dates back from the very early stages of Mars's evolution. The northern lowlands are covered by extensive lava plains and are lower in altitude than the older, more craterized and higher southern highlands. Several hypothesis have been proposed to explain the formation of the dichotomy, such as a large impact either in the northern hemisphere (e.g. *Marinova et al.*, 2008) or in the southern one (*Reese et al.*, 2010), the overturn of a gravitationally unstable mantle (*Elkins-Tanton et al.*, 2003), a degree-one mantle convection (e.g. *Wise et al.*, 1979; *McGill and Dimitriou*, 1990; *Roberts and Zhong*, 2006), plate tectonics (*Sleep*, 1994; *Lenardic et al.*, 2004), or a combination of some of those processes (e.g. *Citron et al.*, 2018).

Although there is today no consensus on the dichotomy-forming event, all the proposed processes may have deeply shaped Mars's interior. In particular, the north/south difference of altitudes being isostatically compensated, a dichotomy in crustal thickness is predicted, the southern crust being thicker than the northern one. Alternatively, a difference in crustal density between the two hemispheres could explain the bimodal distribution of altitudes (*Baratoux et al.*, 2014). Indeed, felsic rocks have recently been detected throughout the highlands both by remote-sensing techniques (*Carter and Poulet*, 2013; *Wray et al.*, 2013) and in situ measurements (*Sautter et al.*, 2015; *Sautter et al.*, 2016), which might be evidences of a buried felsic component in the southern crust (*Sautter et al.*, 2015; *Sautter et al.*, 2016). A difference in composition in between the northern and southern crusts might imply a difference in radioactive element content. Furthermore, relatively old surfaces in the south are consistent with an explosive volcanism origin with fine-particulate materials, while younger surfaces in the north reflect effusive lava flows with more consolidated materials (*Bandfield et al.*, 2013). Consequently the surface thermal conductivity in the south could be significantly lower than that in the north.

The thermal evolution of a planet being especially sensitive to the crustal properties (thickness, thermal conductivity, enrichment in radioelements), it is essential to investigate the effects of the potential north/south dichotomy in crustal structure and composition on the thermal evolution and structure of the planet, which is the aim of this thesis.

# 2 La dichotomie crustale nord/sud : présent et passé

## 2.1 La dichotomie aujourd'hui

### 2.1.a Une dichotomie d'altitude et d'aspect

La dichotomie crustale est le trait le plus marquant de la surface martienne et représente un des enjeux majeurs de la recherche martienne actuelle, tant par son origine et ses implications sur la formation de la planète, que par ses répercussions sur la dynamique interne de Mars. Si elle a été mise en évidence par les images en mosaïque fournies par Mariner 9 (*Mutch et al.*, 1976) ainsi que par les orbiteurs vikings, ce n'est que récemment que l'extension réelle de cette dichotomie a commencé à être pleinement appréhendée. L'essor de l'imagerie orbitale ainsi que la multiplication des explorations in-situ ont en effet révélé que la dichotomie n'était pas seulement une structure de surface mais avait également des implications tant géophysiques (structure de la croûte, champ magnétique, processus tectoniques) que géochimiques (composition de la croûte) (*Watters et al.*, 2007).

Un des aspects les plus frappants de la dichotomie crustale est la différence d'altitude que l'on observe entre les deux hémisphères de la planète (Figure 1.1). Cette dichotomie d'élévation se traduit par une distribution quasi-bimodale des altitudes caractérisée par une différence

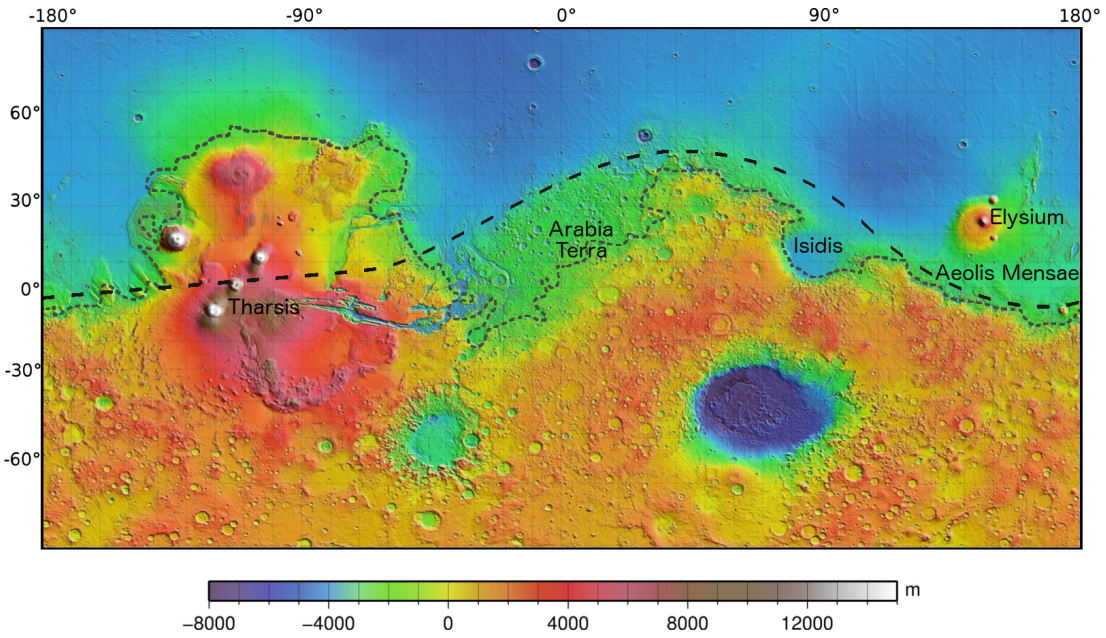


**FIGURE 1.1** – Carte dont le code couleur correspond aux données altimétriques fournies par l'instrument Mars Orbiter Laser Altimeter (MOLA) de la mission Mars Global Surveyor (MGS). Les pointillés fins représentent la limite de la dichotomie si celle-ci est définie à partir des épaisseurs de croûte estimées par *Neumann et al.* (2004) (ici épaisseur de 40 km). Les pointillés plus larges illustrent la limite définie par *Andrews-Hanna et al.* (2008) où la partie nord de Tharsis ainsi qu'Arabia Terra sont localisées dans les hautes terres (voir texte principal, section 2.1.b, pour les détails).

d'environ 5.5 km entre les pics nord et sud (*Watters et al.*, 2007) avec des pentes le plus souvent orientées vers le nord mais pas exclusivement (*Frey et al.*, 1998). Au niveau de la limite entre les deux hémisphères proprement dite, l'expression de cette différence d'altitude est très variable avec un dénivelé pouvant être relativement faible (2.5 km) au niveau de la partie ouest d'Arabia Terra (*Watters*, 2003a,b) ou beaucoup plus abrupte dans l'hémisphère est (6 km) (*Watters et al.*, 2007), ce qui semble indiquer des passés évolutifs distincts pour ces deux régions. Certaines portions de la limite sont également très pentues, probablement du fait de la redistribution ballistique des ejectas lors de grands impacts tels que celui ayant formé le bassin d'Isidis dans l'est, à la limite entre les deux hémisphères.

La dichotomie de surface est également caractérisée par une différence d'aspect et de rugosité très marquée entre les deux hémisphères qui a conduit, en partie, à l'élaboration de l'échelle des temps géologiques de *Hartmann and Neukum* (2001) (voir Figure 1.2). Les hautes terres du sud comprennent majoritairement des terrains d'âge Noachien parmi les plus anciens de la surface (*Scott and Carr*, 1978; *Scott and Tanaka*, 1986) et sont ainsi très cratérisées, incisées par de nombreuses vallées et canaux d'écoulement, préférentiellement présents autour du renflement de Tharsis et orientés vers l'hémisphère nord (*Phillips et al.*, 2001). À l'inverse, les basses terres du nord sont recouvertes de vastes plaines très lisses et beaucoup moins cratérisées, révélatrices d'âges de surface beaucoup plus récents datant le plus souvent de l'Hespérien et de l'Amazonien (Figure 1.2) (*Tanaka et al.*, 2003, 2005). Ces plaines correspondent à de vastes dépôts sédimentaires recouvrant des coulées de lave de plusieurs kilomètres d'épaisseur (*Head et al.*, 2002) et résultant de l'érosion intensive des hautes terres de l'hémisphère sud (*Tanaka et al.*, 2005) avec des remaniements de nature volcanique à proximité des grandes provinces d'Elisium et de Tharsis (*Fuller and Head*, 2002).

### 2.1.b Délimitation de la dichotomie

Si la dichotomie d'altitudes apparaît clairement après un premier examen rapide de la carte des élévations MOLA, avec des fortes altitudes dans le sud (Figure 1.1, zones en rouge) et des plus faibles dans le nord (Figure 1.1, zones en bleu), il n'en est pas de même pour la délimitation précise entre les deux hémisphères qui est moins directe. En effet, entre ces deux cas d'élévations extrêmes, généralement rencontrés au niveau des hautes latitudes, apparaissent des régions relativement étendues ayant des altitudes intermédiaires (Figure 1.1, zones en vert) et dont l'appartenance à un hémisphère ou à un autre ne semble pas claire. Comme en témoigne la complexité de la carte géologique de Mars (Figure 1.2) (*Skinner Jr et al.*, 2004; *Tanaka et al.*, 2003, 2005), ceci est en grande partie dû aux nombreux remaniements subis par la zone de transition de la dichotomie depuis sa formation, tant par des processus érosifs d'origine glaciaire, aéolienne ou fluviatile, que par l'activité des grandes provinces volcaniques qui la jouxtent, ou encore par des modifications tardives de nature tectonique dans l'hémisphère est (*Watters et al.*, 2007). La zone de transition observable aujourd'hui résultant d'une évolution longue et complexe d'une ancienne limite nord/sud mal comprise, comment faire le lien entre la dichotomie ancienne et sa relique à présent remaniée ? De même, les fortes altitudes observées

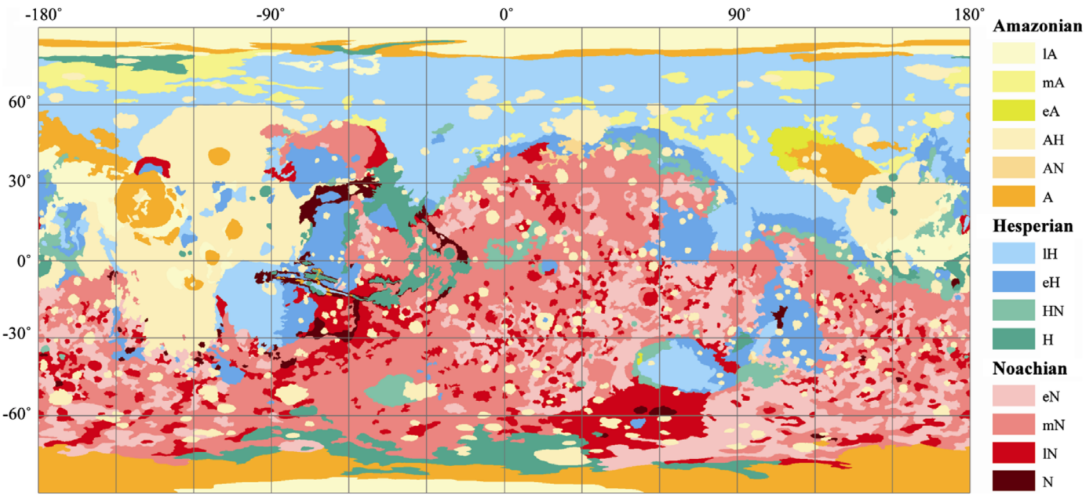


**FIGURE 1.2** – Carte chronostratigraphique de Mars, *Tanaka et al.* (2014). L'échelle des temps géologiques martiens de *Hartmann and Neukum* (2001) a été établie à partir de données stratigraphiques et de la densité des cratères d'impact (*Scott and Tanaka*, 1986; *Greeley and Guest*, 1987; *Tanaka and Scott*, 1987). Cette densité ainsi que la taille des structures d'impact sont directement corrélées à l'importance du bombardement météoritique et cométaire qui est allé décroissant durant l'évolution du système solaire : plus un terrain est impacté et avec de larges cratères plus il est ancien et inversement. Le Noachien est la période la plus ancienne (entre $-4.5$ et $\sim -3.7$ milliards d'années) et correspond à une époque de bombardement intense avec des terrains fortement cratérisés principalement localisés dans l'hémisphère sud et représentant $\sim$ 40% de la surface (*Tanaka et al.*, 1988). L'atmosphère était alors probablement épaisse, permettant la présence d'eau liquide à la surface de Mars. L'Hespérien est quant à lui caractérisé par une période d'activité volcanique intense et couvre une période allant de $\sim -3.7$ à $\sim -3$ milliards d'années, qui peut cependant différer selon l'échelle considérée. La dernière époque, l'Amazonien, correspond aux terrains les plus récents et peu cratérisés principalement situés dans l'hémisphère nord (de $\sim -3$ milliards d'années à aujourd'hui, mais là encore les âges varient fortement selon l'échelle). Malgré quelques épisodes éruptifs majeurs, l'activité volcanique a alors peu à peu diminué mais est restée présente jusqu'à très récemment (*Neukum et al.*, 2004; *Jaeger et al.*, 2007; *Vaucher et al.*, 2009; *Hauber et al.*, 2011). Abréviations : A = Amazonien, H = Hespérien, N = Noachien, l = fin ("late"), m = moyen ("middle"), e = initial ("early"). À noter : certaines unités couvrent différentes périodes (HN, AN, AH).

au niveau du renflement de Tharsis ont-elles un lien avec la dichotomie ou ne reflètent-elles qu'un impressionnant épaississement crustal lié à la mise en place de l'édifice ?

Du fait de son altitude moyenne très élevée, la région correspondant au bouclier de Tharsis a longtemps été considérée comme appartenant à l'hémisphère sud (*Wilhelms and Squyres*, 1984). Cependant, il est aujourd'hui globalement admis que la dichotomie est une des plus anciennes structures de la surface martienne (voir section 2.2), pré-datant donc la mise en place du bouclier de Tharsis, estimée quant à elle à la fin du Noachien (*Werner*, 2009). L'activité volcanique intense qui a eu lieu par la suite a donc très vraisemblablement éradiqué toute trace de l'ancienne zone de transition nord/sud dans cette région, à présent enfouie sous des kilomètres de lave et difficile à délimiter (*Neumann et al.*, 2004; *Zuber et al.*, 2000). Cependant,

les fortes anomalies gravimétriques présentes dans la région indiqueraient une compensation par flexure lithosphérique de la surcharge liée à Tharsis (*Phillips et al.*, 2001), à l'inverse de la dichotomie nord/sud qui est, quant à elle, compensée isostatiquement par des racines crustales (*Neumann et al.*, 2004; *Frey et al.*, 2002). En modélisant ces dernières, *Andrews-Hanna et al.* (2008) ont ainsi pu retracer la limite de la dichotomie sous le renflement de Tharsis (Figure 1.1, pointillés larges) et montré que celle-ci serait bien plus au sud dans cette région que ce que le laissent supposer les modèles d'épaisseur crustale (voir les pointillés fins sur la Figure 1.1 qui représentent la limite nord/sud correspondant à 40 km d'épaisseur crustale, *Neumann et al.*, 2004).

Comme évoqué précédemment, il peut également être difficile de déterminer la limite de la dichotomie dans les zones ayant une topographie intermédiaire et une transition nord/sud très lissée, tout particulièrement dans la région située au nord et à l'est d'Arabia Terra ($30-50^{\circ}$N de latitude, $0-90^{\circ}$E de longitude) ainsi qu'au niveau d'Aeolis Mensae au sud d'Elysium ($10^{\circ}$S $-10^{\circ}$N de latitude, $120-150^{\circ}$E de longitude) (*Sharp*, 1973). Ces régions présentent des structures très découpées, caractérisées par la présence d'un mélange complexe de falaises, plateaux et canyons sinueux dont l'origine reste débattue : s'agit-il d'anciennes terres élevées du sud par la suite profondément érodées, ou à l'inverse de dépôts d'érosion mis en place sur des terrains appartenant à l'hémisphère nord ? Au niveau d'Arabia Terra, l'existence d'un profond réseau de drainage (*Tanaka et al.*, 2003, 2005; *Rodriguez et al.*, 2006) ainsi que la preuve de la présence d'importants glaciers par le passé (*Head et al.*, 2003, 2006), indiquent que ces terrains ont été profondément restructurés par des processus tant fluviatiles que glaciaires. Selon *Head et al.* (2006), ces glaciers aurait même pu engendrer une retraite significative de plusieurs centaines de kilomètres en direction du sud de la limite entre les deux hémisphères de jadis durant l'Amazonien. Le fait que les anomalies magnétiques de cette région soient similaires à celles observées dans le reste de l'hémisphère austral (voir section 2.3.d), tendrait à confirmer que ces terrains correspondent à des anciennes hautes terres du sud par la suite érodées (*Andrews-Hanna et al.*, 2008). À l'inverse, des processus aeoliens seraient à l'origine de vastes dépôts de matériaux au niveau d'Aeolis Mensae qui proviendraient de l'érosion des terres du sud entre la fin du Noachien et le début de l'Hespérien (*Irwin et al.*, 2004; *Watters and McGovern*, 2006), ce qui indiquerait donc plutôt une appartenance de cette région à l'hémisphère nord. En incluant dans l'hémisphère austral la moitié sud de Tharsis ainsi que la totalité d'Arabia Terra, la portion nord originelle recouvrerait alors 42 % de la surface de Mars (*Andrews-Hanna et al.*, 2008; *Zuber*, 2001) et la limite de dichotomie aurait une forme elliptique de $10600 \times 8500$ km centrée en $67^{\circ}$N et $208^{\circ}$E (*Andrews-Hanna et al.*, 2008) (Figure 1.1, pointillés larges). Deux questions fondamentales se posent alors : quand et comment une telle structure a-t-elle pu se former ?

## 2.2 De quand date la formation de la dichotomie ?

La datation de la formation de la dichotomie martienne est directement reliée à l'âge des croûtes nord et sud de la planète. Les datations de surface indiquent des âges généralement

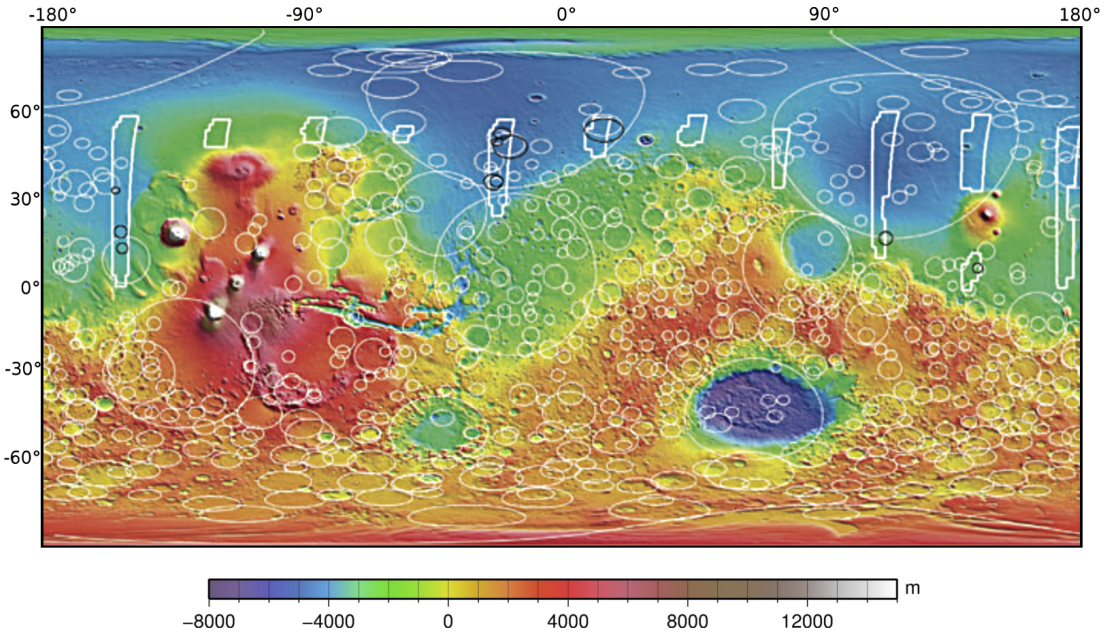


**FIGURE 1.3** – Localisation des bassins d'impact enfouis sur une carte dont le code couleur correspond aux données altimétriques MOLA (Figure issue de *Watters et al.*, 2007). Les bassins d'impact mis en évidence par *Frey* (2006a) sont représentés en blanc, ceux détectés par MARSIS en noir.

Noachien dans le sud et Hespérien-Amazonien dans le nord (Figure 1.2) ce qui suggèrerait que la dichotomie s'est formée à une époque comparable à celle de la surface nord et impliquerait une différence d'âge significative entre les croûtes des deux hémisphères. Cependant, la présence d'ilôts crustaux datant du Noachien dans les basses terres semblent indiquer une répartition des âges plus complexes qu'une bimodalité simplifiée d'âges jeunes dans le nord et anciens dans le sud. Ainsi les datations de surface peuvent largement résulter de remaniements ultérieurs de la croûte et ne reflètent probablement pas l'âge réel de la dichotomie .

Les données topographiques hautement résolues fournies par MOLA abondent en effet dans ce sens en ayant mis à jour des dépressions quasi-circulaires qui correspondent vraisemblablement à des bassins ou cratères d'impact enfouis sous la croûte nord superficielle (*Frey et al.*, 2002) (Figure 1.3). Les données de MOLA ont notamment montré qu'Utopia correspondait en réalité à un immense bassin d'impact dont la formation nécessiterait un impacteur datant du début du Noachien (*Zuber*, 2001). L'instrument Mars Advanced Radar for Subsurface and Ionospheric Sounding (MARSIS) à bord de Mars Express a confirmé d'une manière indépendante la présence d'arcs à courbure constante au niveau du sol non-exposé de Mars (*Picardi et al.*, 2005) pouvant correspondre à la bordure de bassins d'impact enfouis sous la croûte superficielle. Au vu de leur taille ($100 - 500$ km), ceux-ci seraient également en faveur d'une croûte nord datant du début du Noachien (*Watters et al.*, 2007). La croûte enfouie dans le nord pré-daterait donc notamment la formation du bassin d'Utopia, ce qui indiquerait qu'elle ait un âge similaire à celui de la croûte superficielle sud (*Watters et al.*, 2006). Cependant des dépressions quasi-circulaires ont également été découvertes dans les hautes terres (Figure 1.3)

impliquant un âge plus ancien que celui indiqué par les structures de surface pour la croûte enfouie dans le sud (*Frey*, 2006a,b). Par conséquent, la densité des structures d'impact ainsi que les données MOLA suggèreraient que la croûte sud se serait formée $\sim$ 100 millions d'années avant celle du nord (*Frey et al.*, 2002; *Frey*, 2006b) et que la dichotomie daterait probablement des premiers stades du Noachien du fait des âges très similaires des deux croûtes (*Solomon et al.*, 2005; *Nimmo and Tanaka*, 2005).

Bien que la communauté scientifique s'accorde aujourd'hui sur le fait que la dichotomie soit une des plus anciennes stuctures de la surface de Mars, de nombreuses incertitudes demeurent quant à la chronologie exacte de sa formation, en grande partie du fait des remaniements importants subis par une croûte si ancienne. En effet, des dépressions enfouies non-détectées subsistent certainement et, de ce fait, l'étude de la densité des cratères d'impact fournit une limite inférieure à l'âge réel des structures mais ne peut pas être considérée comme une datation absolue. Ainsi, la dichotomie pourrait même s'être produite il y a 4.5 Ga lors de la formation de la croûte primitive (*Solomon et al.*, 2005), bien que l'étude des failles et des structures tectoniques suggère, à l'inverse, une formation de la dichotomie bien plus tardive datant du début de l'Hespérien ($\sim$ 3.7 Ga) (*McGill and Dimitriou*, 1990).

## 2.3 Comment s'est-elle formée ?

Bien que la formation de la dichotomie soit très vraisemblablement liée à un évènement majeur de l'histoire de Mars, son origine demeure à ce jour largement débattue. Différents scénarios ont été proposés impliquant des processus soit exogéniques de type impact(s) (*Wilhelms and Squyres*, 1984; *Frey and Schultz*, 1988), soit de nature endogénique tels qu'une structure convective de degré un (*Wise et al.*, 1979; *McGill and Dimitriou*, 1990; *Zhong and Zuber*, 2001; *Roberts and Zhong*, 2006), le retournement d'un manteau gravitationnellement instable (*Elkins-Tanton et al.*, 2003; *Elkins-Tanton et al.*, 2005; *Elkins-Tanton*, 2008; *Debaille et al.*, 2009) ou encore l'existence transitoire d'une tectonique des plaques durant les premiers stades évolutifs de la planète (*Sleep*, 1994; *Lenardic et al.*, 2004). Afin de pouvoir discriminer ces modèles potentiels, d'importantes contraintes sont à prendre en considération comme l'âge de formation de la dichotomie et des croûtes nord/sud, la forme de la limite entre les deux hémisphères, ou encore l'absence de relaxation crustale à grande longueur d'onde de la différence quasi-bimodale des altitudes (*Solomon et al.*, 2005).

### 2.3.a Théorie de l'impact

Une des hypothèses les plus populaires est celle de la formation de la dichotomie par impact. Dans cette théorie, un ou plusieurs évènements seraient à l'origine d'un refaçonnement profond de l'hémisphère boréal par l'éradiquation de la croûte nord pré-existente (*Marinova et al.*, 2008). L'absence d'individualisation nette de plusieurs bassins d'impact dans les basses terres (*Zuber et al.*, 2000; *McGill and Squyres*, 1991), ainsi que la faible probabilité pour que ceux-ci se soient concentrés uniquement dans l'hémisphère nord (*McGill and Squyres*, 1991),

rendent toutefois l'hypothèse des impacts multiples (*Frey and Schultz*, 1988) peu vraisemblable. À contrario, l'hypothèse d'un impact de très grande envergure, voir géant, a été largement étudiée (*Wilhelms and Squyres*, 1984; *Frey and Schultz*, 1988; *Marinova et al.*, 2008; *Andrews-Hanna et al.*, 2008). L'envergure d'un tel impact aurait conduit à la formation d'un océan de magma à l'échelle hémisphérique qui, lors de son refroidissement, aurait formé la croûte nord secondaire (*Marinova et al.*, 2008). La création d'un disque d'accrétion autour de la planète par les éjectas de cet impact géant pourraient même expliquer la formation des deux petits satellites de Mars, Phobos et Deimos, par un processus similaire à celui avancé pour la formation de la Lune (*Rosenblatt et al.*, 2016). Cependant, la localisation de l'impact reste débattue, un évènement situé dans l'hémisphère austral ayant pu conduire, à l'inverse, à un épaississement de la croûte sud (*Reese et al.*, 2010; *Golabek et al.*, 2011).

Plusieurs arguments ont été opposés à la théorie de l'impact. En effet, l'énergie cinétique apportée par l'impacteur produirait une augmentation de chaleur très importante dans les couches tant superficielles que profondes de la planète (*Arkani-Hamed and Olson*, 2010; *Roberts and Arkani-Hamed*, 2014), entraînant une fusion tellement intense que les preuves de l'existence même du bassin d'impact - c'est-à-dire de la dichotomie - auraient alors été éradiquées (*Tonks and Melosh*, 1993). Certaines études prédisent même la destruction partielle de la planète lors d'un évènement aussi cataclysmique (*Wilhelms and Squyres*, 1984; *Nimmo and Tanaka*, 2005). Par ailleurs, peu de traces de l'impact en lui-même sont présentes au niveau de la limite entre les deux hémisphères. Ainsi, celle-ci est à première vue caractérisée par une forme compliquée (*McGill and Squyres*, 1991; *Hart et al.*, 2007), à priori peu compatible avec celle beaucoup plus régulière observée pour les plus petits cratères d'impact qui ont un pourtour le plus souvent circulaire, excepté pour des collisions se produisant à des incidences très obliques (*Gault and Wedekind*, 1978). De même, l'épaississement en anneau typiquement observé autour des cratères d'impact n'est pas retrouvé dans la topographie de la dichotomie, hormis dans les régions influencées par d'autres bassins comme Isidis (*Marinova et al.*, 2008). Cependant, outre le fait que la bordure de la dichotomie ait été fortement modifiée depuis sa formation (voir section 2.1.b), peu d'études ont été réalisées pour des structures d'impact ayant une envergure comparable à celle du bassin boréal martien. Le rapport d'aspect existant entre la structure impactée et l'impacteur étant alors largement supérieur à celui observé lors des petites collisions, on peut en effet s'attendre à ce que la géométrie du cratère soit différente comme semble le suggérer la forme elliptique des autres grands bassins d'impact connus dans le système solaire, tels que Hellas dans l'hémisphère sud de Mars (voir Figure 2) ou Aitken au pôle sud de la face cachée de la Lune. D'autre part, si la taille des petits cratères ainsi que la quantité de croûte fondue qui leur est associée sont directement reliées à l'énergie de l'impact, *Marinova et al.* (2008) ont montré que dans le cas des grandes collisions, les limites de l'excavation, l'ellipticité du bassin ainsi que la quantité de matériaux fondus étaient également corrélées à l'angle d'incidence et à la vitesse de l'impacteur. Un impact géant se produisant à des incidences relativement obliques serait alors suffisamment peu énergétique pour que les traces de cet évènement restent préservées à la surface de la planète. *Marinova et al.* (2008) ont également montré qu'un impacteur ayant un angle d'incidence de $30-60^{\circ}$, un diamètre

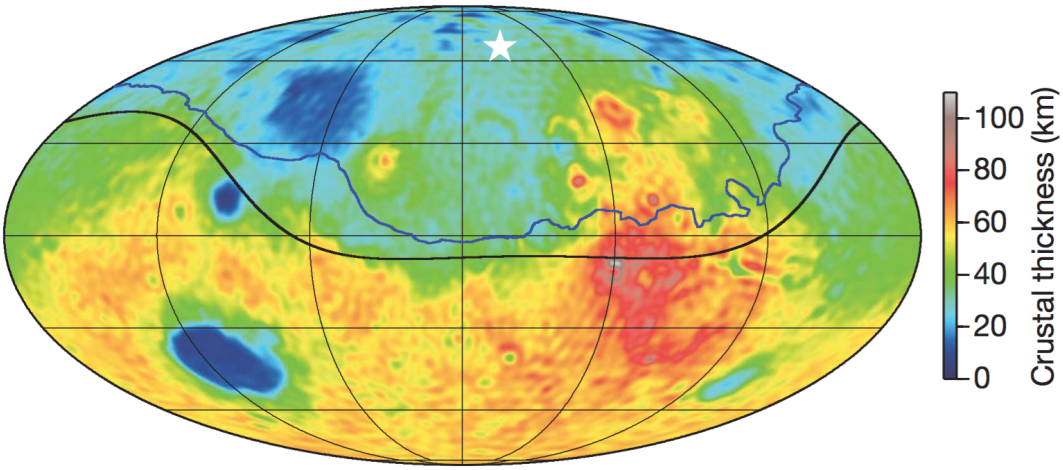


**FIGURE 1.4** – Limite de la dichotomie : comparaison entre la délimitation de *Andrews-Hanna et al.* (2008) (en noir) et les limites d'excavation crustale modélisées par *Marinova et al.* (2008) (en bleu) dans le cas où la dichotomie serait formée suite à un grand impact dans l'hémisphère nord (localisation représentée par l'étoile blanche) (Figure issue de *Marinova et al.*, 2008).

de $1600 - 2700$ km et une vitesse relative de $6 - 10$ km/s produirait alors une excavation de la croûte nord fortement similaire en taille et en ellipticité à la limite de la dichotomie définie par *Andrews-Hanna et al.* (2008) (voir section 2.1.b et Figure 1.4). Si cette hypothèse s'avérait confirmée, le bassin boréal correspondrait alors au plus grand cratère d'impact jamais observé par un facteur quatre, ce qui le positionnerait entre les collisions de type Hellas/Aitken et les impacts géants comme par exemple celui évoqué pour la formation du sytème Terre-Lune avec un impacteur de la taille de Mars. Cela impliquerait également la présence d'un impacteur de très grandes dimensions et donc un âge très ancien pour la dichotomie, cohérent avec les estimations récentes en faveur d'une croûte nord enfouie datant du début du Noachien (voir section 2.2). L'évènement se serait donc produit bien avant la fin du grand bombardement qui eût lieu durant les premières centaines de millions d'années du système solaire (*Watters et al.*, 2007).

À la lumière des connaissances que nous avons de la dichotomie martienne, si la théorie du grand impact semble aujourd'hui très prometteuse, certains problèmes restent cependant à élucider avant qu'elle ne soit pleinement convaincante. En effet, une incertitude manifeste demeure quant à la localisation précise de l'impact : *Andrews-Hanna et al.* (2008) le situent à $208^{\circ}$E$-67^{\circ}$N, *Nimmo et al.* (2008) à $170^{\circ}$E$-50^{\circ}$N, tandis que *Reese et al.* (2010) ou *Golabek et al.* (2011) le positionnent carrément au niveau de l'hémisphère opposé. Par ailleurs, la croûte jeune ayant reçu de fortes quantités de chaleur suite à l'impact, la différence d'altitude entre les deux hémisphères devrait avoir tendance à se rééquilibrer avec un flux de la croûte inférieure sud vers le nord, ce qui ne permettrait peut-être pas le maintien du relief dans le temps (*Solomon et al.*, 2005).

### 2.3.b Convection mantellique de degré 1

Alternativement la dichotomie martienne pourrait résulter de processus endogènes et être l'expression de surface de la structure interne de la planète par le passé (*Wise et al.*, 1979; *McGill and Dimitriou*, 1990; *Zhong and Zuber*, 2001; *Roberts and Zhong*, 2006). En effet, certains modèles de dynamique interne (*Zhong and Zuber*, 2001; *Roberts and Zhong*, 2006) prédisent la formation d'une structure convective de degré un dans laquelle un hémisphère est dominé par la présence d'un panache chaud tandis qu'un écoulement mantellique froid descendant est observé du côté opposé. Dans cette configuration, l'hémisphère situé au-dessus du panache est préférentiellement chauffé ce qui peut entraîner un épaississement crustal par augmentation de la fusion mantellique de ce côté-ci de la planète ou, alternativement, un amincissement si les processus magmatiques ne parviennent pas à compenser l'érosion crustale provoquée par le panache (*Zhong and Zuber*, 2001). Dans le cas de la Terre, *Zhang and Yuen* (1995) ainsi que *Bunge et al.* (1996) ont montré que la formation d'une structure convective de degré un nécessitait l'association d'une lithosphère peu résistante et d'une viscosité mantellique stratifiée, cette dernière favorisant le passage des structures à grande longeur d'onde et limitant à l'inverse l'action des plus petites. Pour Mars, une lithosphère faible d'environ 500 km (*Zhong and Zuber*, 2001) ainsi qu'un contraste de viscosité de l'ordre de 100 entre les manteaux inférieur et supérieur semblent nécessaires à la formation d'une stucture convective de degré un (*Zhong and Zuber*, 2001; *Roberts and Zhong*, 2006). Alternativement, l'existence d'une transition de phase endothermique spinelle-pérovskite dans le manteau agirait comme une barrière pour les plus petites longeurs d'onde, en étant préférentiellement pénétrable par les structures à large échelle (*Tackley et al.*, 1993). Néanmoins, du fait de la faible gravité de Mars (3.7 $m.s^{-2}$ à la surface), il n'est pas certain que les conditions de pression et de température permettent l'existence de cette zone de transition et, le cas échéant, celle-ci serait localisée près de la limite noyau-manteau (core-mantle boundary, CMB) (*Harder and Christensen*, 1996; *Breuer et al.*, 1997; *Harder*, 2000).

Cependant, à l'instar de la théorie de l'impact, certaines problématiques posées par la théorie de la convection mantellique de degré un demeurent à ce jour irrésolues. Un contre-argument majeur concerne l'incompatibilité apparente entre la formation très précoce de la dichotomie et les délais nécessaires avant la mise en place d'une structure convective de degré un (*Solomon et al.*, 2005), c'est-à-dire typiquement quelques centaines de millions d'années bien que cela dépende toutefois fortement de la viscosité mantellique, à ce jour très peu contrainte (*Roberts and Zhong*, 2006). La théorie endogénique de convection de degré un ne peut donc pas être exclue sur la base de ce seul argument, d'autant que d'importantes incertitudes demeurent quant à la datation exacte de la dichotomie (*McGill and Dimitriou*, 1990; *Roberts and Zhong*, 2006). Néanmoins, un autre challenge pour cette théorie est de parvenir à expliquer la répartition quasi-bimodale des altitudes et des épaisseurs de croûte que l'on observe entre les deux hémisphères, si l'on exclut les zones où la structure primaire de la dichotomie a été altérée (*Andrews-Hanna et al.*, 2008), c'est-à-dire les provinces volcaniques de Tharsis et Elysium, Arabia Terra et les grands bassins d'impact (voir section 2.1.b). En effet, dans le cas où l'épaississement de la croûte australe serait dû à l'existence d'une structure convective

à grande longueur d'onde, les altitudes ont tendance à être maximales au niveau de la tête du panache mais à s'étaler à distance de celle-ci, ce qui n'est à priori pas compatible avec une distribution quasi-bimodale des épaisseurs crustales (*Andrews-Hanna et al.*, 2008). Cette distibution étant à l'inverse très similaire à celles observées à plus petite échelle pour les bassins d'impact d'Hellas et Argyre, cette contrainte favoriserait plutôt une origine collisionnelle de la dichotomie.

### 2.3.c Retournement d'un manteau gravitationnellement instable

Si elle résulte de la différenciation même de la planète, la dichotomie de Mars pourrait également être encore plus primordiale que dans les deux scénarios précédemment présentés. En effet, sur la Lune on observe également deux types de terrains : les terres hautes à fort albédo principalement situées sur la face cachée, et les terres très sombres qui correspondent aux mers basaltiques de la face visible. Les terres hautes représentent les restes d'une croûte de flottaison primordiale très légère et fortement enrichie en plagioclases qui serait issue de la cristallisation fractionnée du grand océan de magma qui recouvrait la Lune après l'impact géant qui créa notre planète et son satellite. Par la suite, cette croûte fût refaçonnée par de grands impacts qui permirent la remontée de magmas et la formation des mers basaltiques lunaires. On pense aujourd'hui que l'existence de tels océans primordiaux de magma à l'échelle planétaire, ou tout du moins hémisphérique, étaient la règle plus que l'exception pour les planètes telluriques, les sources de chaleur étant à l'époque nombreuses : énergie cinétique lors de l'accrétion des planétésimaux (*Safronov*, 1972; *Wetherill*, 1980; *Tonks and Melosh*, 1993; *Halliday et al.*, 2001), impacts géants, éléments radioactifs à courte période (en particulier $^{26}Al$) et énergie gravitationnelle potentielle lors de la formation du noyau des planètes par différenciation métal/silicate (*Canup*, 2008). Ces océans de magma sont donc sûrement à l'origine des processus initiaux de différenciation compositionnelle et structurelle des planètes. Dans le cas de Mars, de dimensions plus modestes que le système Terre-Lune, l'énergie d'accrétion fut probablement moins importante et, de surcroît, potentiellement non-associée à un impact géant : la profondeur de l'océan de magma reste donc peu contrainte (*Elkins-Tanton*, 2012) et a pu, de plus, varier latéralement (*Solomatov*, 2000). Cependant, du fait de l'effet isolant de l'atmosphère primitive martienne (*Abe*, 1997), ainsi que de l'accrétion certainement très rapide de Mars en quelques millions d'années seulement (*Abe and Matsui*, 1985), l'océan de magma a pu couvrir la totalité du manteau (*Elkins-Tanton et al.*, 2003). L'existence d'un océan de magma précoce sur Mars est par ailleurs supportée par les anomalies de $^{182}W$ et $^{142}Nd$ qui indiquent une différenciation noyau/manteau très rapide, dès $13 \pm 3$ Ma (*Kleine et al.*, 2002; *Blichert-Toft et al.*, 1999; *Lee and Halliday*, 1995), nécessitant donc un état fluide des silicates et des métaux, tout du moins dans la partie supérieure du manteau (*Stevenson*, 1988).

Sur Mars le refroidissement de l'océan magmatique primordial se fit vraisemblablement de bas en haut, le gradient adiabatique étant supposé être plus pentu que la courbe du solidus (e.g. *Solomatov*, 2000). Deux scénarios extrêmes de refroidissement ont cependant pu se produire selon la taille des minéraux et de leur vitesse de cristallisation (*Solomatov*, 2000; *Plesa et al.*,

2014). Dans le premier cas un refroidissement rapide a entraîné la formation de petits cristaux dans un manteau quasiment homogène, à l'exception d'une couche supérieure appauvrie par l'extraction de la croûte (*Schott et al.*, 2001; *Ogawa and Yanagisawa*, 2011). Dans le second scénario la cristallisation lente et fractionnée du magma a abouti à la formation de minéraux légers contenant du magnésium dans les couches profondes proches de la CMB, tandis que les magmas évolués enrichis en fer ont engendré des cumulats denses vers la surface. Cette stratification en densité étant gravitationnellement instable, elle aurait pu conduire à un retournement du manteau engendrant potentiellement une structure crustale de degré un (*Elkins-Tanton et al.*, 2003), c'est-à-dire avec un épaississement de la croûte au niveau du panache convectif et un amincissement du côté opposé (*Elkins-Tanton et al.*, 2003; *Elkins-Tanton et al.*, 2005; *Debaille et al.*, 2009). Cependant, à l'inverse de la théorie de la convection de degré un, ce panache ne se maintiendrait pas dans le temps, ce qui, sur une croûte aussi jeune et chaude que celle évoquée dans la théorie du retournement de manteau, provoquerait un relâchement rapide de la différence de topographie en $\sim 100$ Ma si aucun processus additionnel ne vient la maintenir (*Nimmo and Stevenson*, 2001; *Roberts and Zhong*, 2006; *Solomon et al.*, 2005). De plus, les conditions elles-même du retournement prêtent à débât étant donné que les mécanismes impliqués dans la mobilisation des couches supérieures (censées être les plus froides et les plus visqueuses du manteau) ne sont pas claires, les modèles proposés par *Elkins-Tanton et al.* (2003, 2005) considérant un manteau isovisqueux peu réaliste. Par ailleurs, en aboutissant à une stratification stable en densité ce scénario arrête la convection en moins d'1 Ga (*Plesa et al.*, 2014), ce qui est peu cohérent avec les observations de surface qui indiquent à l'inverse un volcanisme actif, et donc une activité interne, jusqu'à récemment (*Hartmann et al.*, 1999; *Hauber et al.*, 2011; *Neukum et al.*, 2004; *Werner*, 2009) (voir chapitre 2, section 3.3).

Alternativement, un océan de magma moins profond, ou une séquence de cristallisation engendrant un gradient de densité plus faible ont été évoqués (*Plesa et al.*, 2014). De même, une cristallisation fractionnée hétérogène entre les deux hémisphères aurait pu créer la dichotomie crustale que l'on observe aujourd'hui et serait typiquement retrouvée dans le cas d'un océan hémisphérique et non global, résultant par exemple d'un impact (*Golabek et al.*, 2011; *Andrews-Hanna et al.*, 2008; *Nimmo et al.*, 2008; *Marinova et al.*, 2008; *Reese and Solomatov*, 2006).

### 2.3.d Tectonique des plaques

Un des grands mystères qui entoure la dynamique interne de notre planète concerne l'existence ainsi que l'initiation de la tectonique des plaques, phénomène unique dans le système solaire à l'heure actuelle. Cependant, des indices laissent penser que de la tectonique des plaques a également pu exister sur d'autres planètes par le passé et, en particulier, sur Mars. En effet, l'existence d'une tectonique des plaques ancienne a été évoquée du fait de la similitude de Tharsis et des basses terres du nord avec l'arc volcanique et le plancher océanique retrouvés sur Terre au niveau des zones de subduction (*Sleep*, 1994; *Lenardic et al.*, 2004). Les données magnétiques obtenues par Mars Global Surveyor sont venues corroborer cette hypothèse en ré-

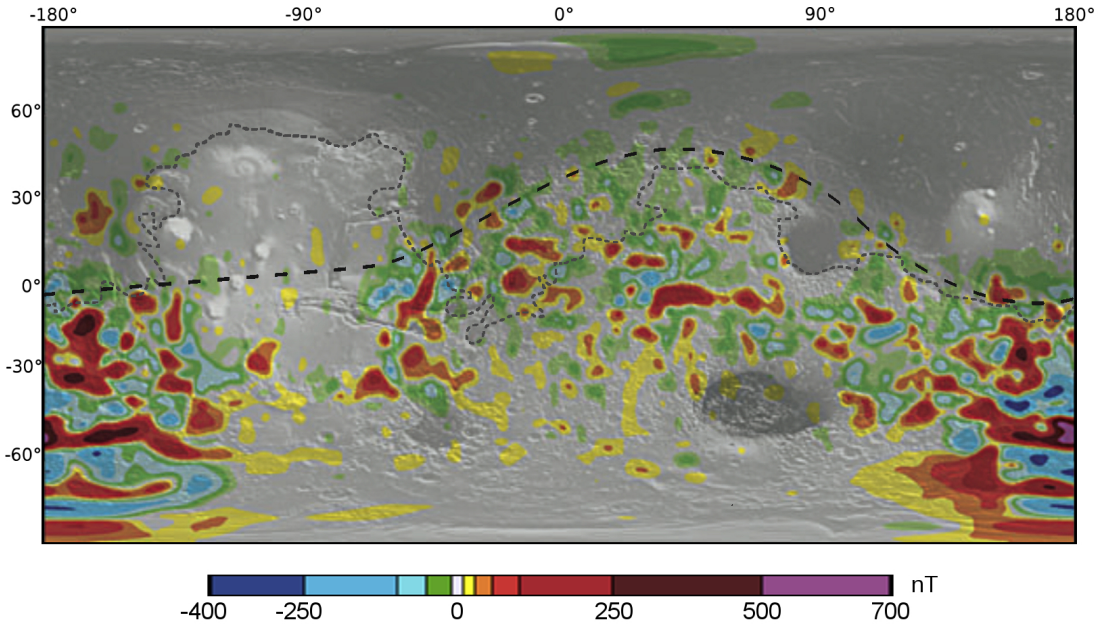


**FIGURE 1.5** – Composante radiale du champ magnétique pour une altitude normalisée à 200 km (*Purucker et al.*, 2000) (Figure d'après *Watters et al.*, 2007). Une répartition linéaire nord/sud des anomalies magnétiques est visible entre 120˚E et 240˚E, entre les provinces volcaniques de Tharsis et d'Elysium. Les pointillés fins indiquent la limite nord/sud correspondant à une épaisseur crustale de 40 km selon les estimations de *Neumann et al.* (2004). Les pointillés larges représentent la limite de la dichotomie définie par *Andrews-Hanna et al.* (2008).

vélant par endroits une répartition linéaire des anomalies magnétiques rémanentes (*Connerney et al.*, 1999) (voir Figure 1.5). Bien qu'à une échelle beaucoup plus large ($\sim$ 100 km d'espacement), cette linéation serait très similaire à celle observée au niveau du plancher océanique terrestre ($\sim$ 10 km d'espacement) où elle est due à la combinaison de la divergence des plaques et des inversions du champ magnétique. Dans la théorie où la dichotomie reflèterait une activité tectonique passée, les hautes terres du sud s'apparenteraient alors à un continent tandis que les basses régions plus jeunes du nord correspondraient à de la croûte océanique recyclée (*Sleep*, 1994).

Cependant, l'existence d'une tectonique des plaques dans le passé est loin de faire l'unanimité car il n'existe pas de preuves géologiques ou topographiques en faveur de la présence d'une ancienne zone de subduction le long de la limite de la dichotomie (*McGill*, 2000). De plus, ce scénario n'expliquant pas en réalité la formation de la dichotomie mais plutôt ses conséquences, comment la tectonique des plaques se serait-elle initiée dans un seul hémisphère ? Par ailleurs, comment le recyclage de la croûte des basses terres peut-il être compatible avec les observations récentes pointant vers un âge quasiment similaire entre les croûtes nord et sud (*Pruis and Tanaka*, 1995) (voir section 2.2) ? Enfin, tout comme pour le scénario de convection de degré un, le délai de mise en place d'une dynamique interne liée à de la tecto-

nique des plaques semble trop long pour permettre la formation très précoce de la dichotomie (*Solomon et al.*, 2005).

### 2.4 Conclusion : vers un scénario de formation hybride ?

S'il est aujourd'hui largement admis que la dichotomie est une des structures les plus anciennes de Mars, remontant peut-être même aux tout premiers stades de la planète, sa formation en elle-même est toujours très énigmatique. En effet, comme nous venons de le voir, aucun des scénarios jusqu'à présent envisagés, qu'il soit de nature endogénique ou exogénique, n'est compatible avec toutes les contraintes dont nous disposons (âge de la dichotomie et des croûtes nord/sud, forme elliptique de la dichotomie, absence de relaxation visqueuse des différences d'altitude, répartition bimodale des épaisseurs de croûte). Alternativement, des scénarios alliant certaines des théories précédemment évoquées peuvent également être envisagés. Ainsi, par exemple, *Citron et al.* (2018) proposent une théorie où un impact de grande envergure excaverait la croûte primordiale dans l'hémisphère nord, créant ainsi non seulement une différence d'épaisseur entre les deux hémisphères, mais peut-être également de composition. Cet impact favoriserait par la suite la formation d'une structure de convection mantellique de degré un avec un panache qui migrerait préférentiellement en moins de 100 Ma sous la croûte épaissie et donc isolante de l'hémisphère sud aux antipodes de l'impact. La fusion partielle entraînée par le panache mantellique permettrait ainsi d'épaissir encore plus la croûte sud et d'assurer la pérennité de la différence de relief entre les deux hémisphères tout en n'éradiquant pas la forme elliptique du bassin d'impact boréal initial retrouvée par *Andrews-Hanna et al.* (2008). Ce scénario permettrait donc de résoudre deux problématiques inhérentes à chacune des théories prises isolément, c'est-à-dire le manque de conservation du relief dans le temps pour la théorie de l'impact, et les délais de mise en place de la dichotomie pour la convection mantellique de degré un.

## 3 The dichotomy : implications for north/south crustal properties

Although there is today no consensus on the dichotomy-forming event, all of the potential processes mentioned in section 2.3 act on a global scale and may thus have influenced the entire planet structure. During this thesis, we investigated, more particularly, the potential implications of the dichotomy for Mars's thermal structure and evolution. Indeed, since the crustal properties (thickness, enrichment in radioelements, thermal conductivity) have a large impact on the thermal evolution of a planet (*Grott and Breuer*, 2009; *Grott et al.*, 2013; *Laneuville et al.*, 2013; *Sekhar and King*, 2014), it is crucial to understand how those properties are affected by the Martian dichotomy. Especially, to which extent does the surface dichotomy continue in depth and does it reflect a north/south difference in crustal thickness ? Moreover, if the northern and southern crusts have been formed by distinct processes, do they have the same composition and thermal properties ?

## 3.1 A dichotomy in crustal structure ?

### 3.1.a Crustal thickness

One of the best ways to constrain the subsurface structure of a planet is the analysis of seismic waves, a method that have been successfully applied for the Earth and the Moon. Unfortunately, so far, and before the landing of the InSight spacecraft that is expected in November 2018, there has been no seismometer on Mars's surface that have successfully recorded seismic events. However, alternative means can be used to probe Mars's internal structure from orbit, such as the analysis of the gravity field and rotational parameters - that provides, in particular, estimates of the moment of inertia factor - or the combined analysis of gravitational (from Mars Global Surveyor, MGS, and Mars Odyssey missions) and MOLA topographic data (*Zuber et al.*, 2000; *Neumann et al.*, 2004; *Wieczorek and Zuber*, 2004; *Wieczorek*, 2007). With this latter method, if assuming a simplified uniform crustal density, subsurface mass variations can be obtained by subtracting the theoretical gravitational anomaly due to surface topography (Figure 1.6a) from the free-air gravity (Figure 1.6b). The resulting Bouguer gravity is then inverted to retrieve depth variations of the crust-mantle interface and thus crustal thicknesses (Figure 1.6c).

In the case of a uniform crustal density, the Martian gravity field is well explained by an isostatic compensation of the north/south dichotomy with lateral variations in crustal thickness (*Zuber et al.*, 2000; *Neumann et al.*, 2004) that might explain the 3.3 km mass-center figure offset of Mars directed towards the Tharsis province (*Wieczorek*, 2007). The Bouguer inversion of gravity and topography data suggests an average crustal thickess of $57 \pm 24$ km when considering all studies (*Zuber et al.*, 2000; *Neumann et al.*, 2004; *Wieczorek and Zuber*, 2004; *Wieczorek*, 2007). However, this average value, as well as the total range of thicknesses, strongly depend on the density contrast between the crust and the mantle that is assumed for the inversion. For instance, given an average crustal thickness of 45 km (*Zuber et al.*, 2000) and a crust-mantle density difference of 600 kg m$^{-3}$ (i.e. a crustal density of 2900 kg m$^{-3}$), *Neumann et al.* (2004) estimate average values of 32 km and 58 km for the northern lowlands and the southern highlands, respectively. An additional constraint arises from the absence of viscous relaxation of the topography at the dichotomy boundary, which puts an upper bound of 100 km for the maximum crustal thickness (*Nimmo and Stevenson*, 2001). Crustal flow of lower crustal materials would indeed be observed in the case of a strong change in crustal thickness because of the presence of lateral pressure gradients, even in the case of an isostatic compensation of the dichotomy (*Zuber et al.*, 2000; *Nimmo and Stevenson*, 2001; *Nimmo*, 2005). However, given the aqueous past of Mars, the cooling rate of the crust might have been influenced by the presence of an hydrothermal circulation that could lengthen by many orders of magnitude the time scale for the relaxation of crustal thickness variations (*Parmentier and Zuber*, 2007).

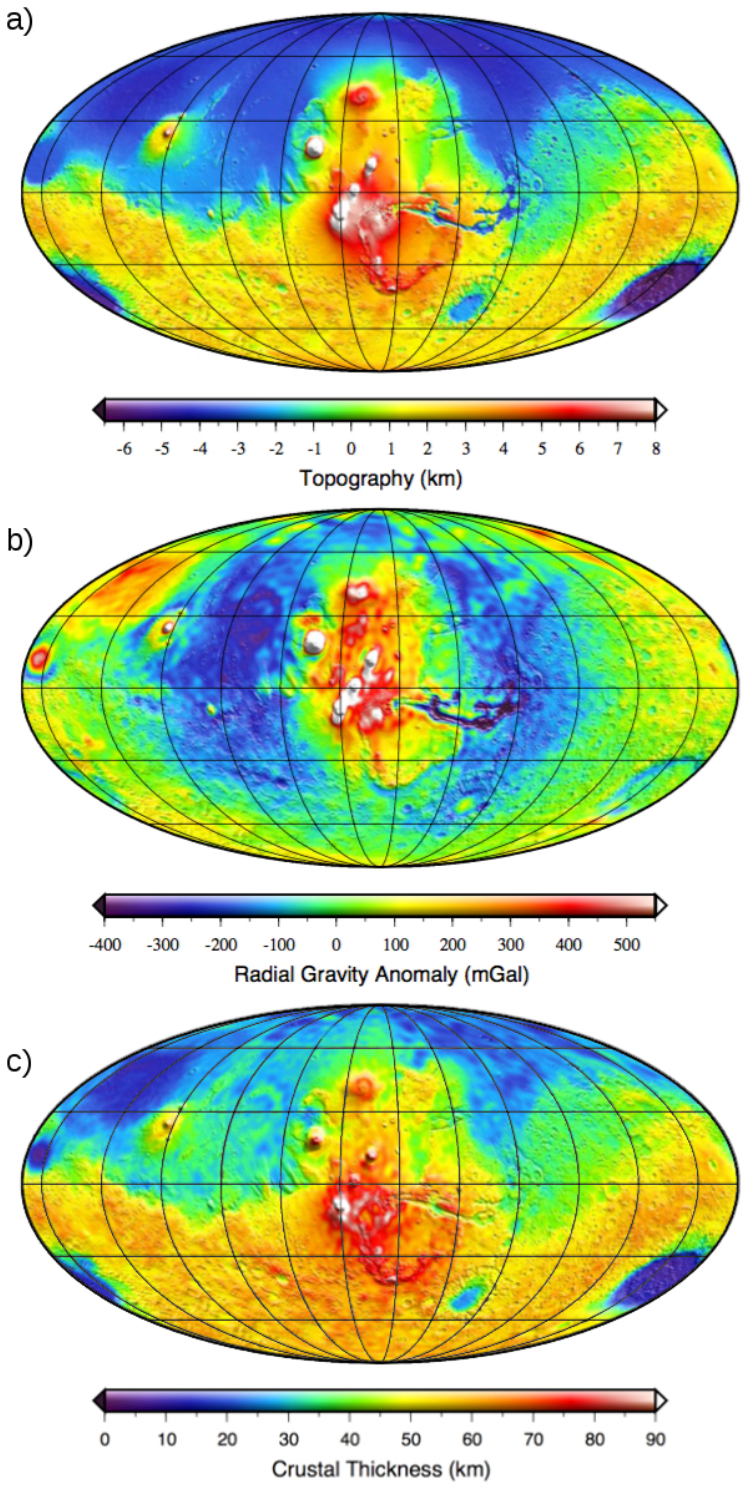


**FIGURE 1.6** – Crustal thickness estimates given gravity and topography data (Figure from *Wieczorek*, 2007). (a) Global MOLA topography of Mars derived from the 719 degree spherical harmonic model *MarsTopo*719 (*Smith et al.*, 2001). (b) Radial free-air gravity evaluated at a radius of 3396 km with a truncation of the harmonic coefficients of *JGM*95*J*01 beyond degree 75 and setting the $J_2$ term to zero (MGS gravity field measurements). (c) Crustal thickness model of *Wieczorek* (2007) derived from gravity and topography data.

### 3.1.b Crustal density

As highlighted in the previous section 3.1.a, knowledge of the average crustal density is very essential as it determines the interior structure of a planet, especially when using the inversion method of geophysical data (gravity field and topography) to retrieve lateral crustal thickness variations. However, most of crustal thickness estimates were made before strong petrological constraints were available (*Zuber et al.*, 2000; *Zuber*, 2001; *Neumann et al.*, 2004; *McGovern et al.*, 2004; *Wieczorek*, 2007). Therefore, a range of crustal density limited to $2700 - 3100$ kg m$^{-3}$ was used, i.e. values that are usely representative for terrestrial planets. Since then, the knowledge that we have of the surface chemistry and mineralogy has been improved both by orbital spectroscopy measurements (Mars reconnaissance orbiter, Mars express) and in situ analyses (Spirit, Opportunity and Curiosity rovers, Phoenix probe). By realizing a combined analysis of Shergottite-Nakhlite-Chassignites (SNC) meteorite composition, surface concentration of Fe, Al, Ca, SI and K (measured by the Gamma-Ray Spectrometer, or GRS, of the Mars Odyssey mission), as well as the reconstruction of mineral assemblages resulting from low-pressure crystallization of primitive mantle melts, *Baratoux et al.* (2014) point to high grain density values $>$ 3100 kg m$^{-3}$ (up to $>$ 3600 kg m$^{-3}$), at least for the materials that are close to the surface. Moreover, as expected, lateral variations of density are observed (Figure 1.7) : the highest density areas generally correspond to the Hesperian and Amazonian volcanic units of Elysium and Tharsis, whereas the low density regions are found in the Noachian crust. Such large crustal density values between 3200 and 3500 kg m$^{-3}$ would imply a lower crust-mantle density contrast and, thus, higher average crustal thicknesses ($\sim$ 100 km) than previously thought, that can, however, be compatible with the observed moment of inertia factor if a larger or denser core is assumed (*Baratoux et al.*, 2014). Nevertheless, due to material compaction with depth and the largely unknown porosity, it remains unclear if surface estimates of the density can be extrapolated to the entire crust. Moreover, variations of rock composition with depth are possible and, in the case of a light component buried in the thick southern crust, could explain the absence of the topographic relaxation of the dichotomy for crustal thicknesses $>$ 100 km, as predicted by *Nimmo and Stevenson* (2001) (*Baratoux et al.*, 2014).

There is, however, no consensus for the large crustal densities given by *Baratoux et al.* (2014). On the contrary, by using the admittance between topography and gravity calculated from satellite tracking data, *Goossens et al.* (2017) have estimated a very low average value of $2582 \pm 209$ kg m$^{-3}$ - close to the density of the Moon's primary anorthositic crust - and higher values of 2900 kg m$^{-3}$ over the large volcanic complexes of Elysium and Tharsis. This lower average density might result, for instance, from the effects of porosity and potentially implies a large crust-mantle density contrast. This new crustal density estimate would thus not only lead to a lower average crustal thickness (42 km), but also to smaller lateral variations and therefore a smoother map than that obtained by *Wieczorek* (2007) (Figure 1.6c), except in the large volcanic complexes. However, such a low average crustal density is hardly reconciliable with the analysis of meteorite major element chemistry and GRS surface concentrations of Fe, Al, Ca, SI and K.

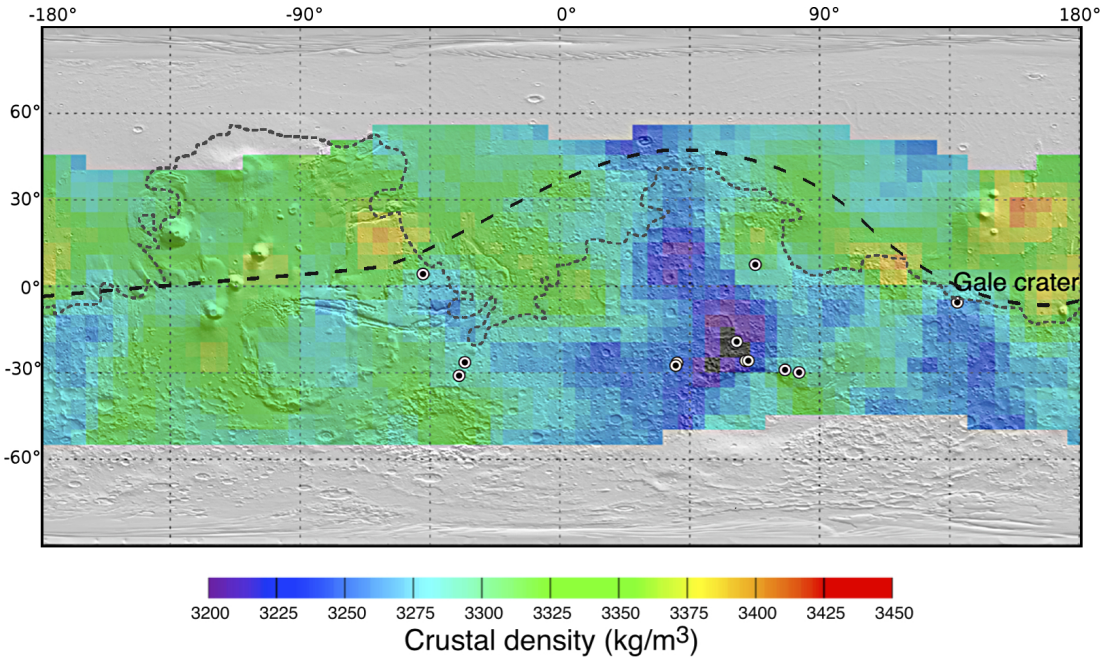


**FIGURE 1.7** – Density map of surface rocks using GRS geochemical maps of FeO, $Al_2O_3$, CaO, $SiO_2$, $K_2O$ (Figure from *Baratoux et al.*, 2014). Black and white circles show locations where felsic rocks have been potentially identified (*Carter and Poulet*, 2013; *Wray et al.*, 2013; *Sautter et al.*, 2015) (see section 3.2.c) that generally lie on low density areas. The dotted black line represents the dichotomy boundary delimitation of *Watters et al.* (2007) that corresponds to the 40 km contour of the crustal thickness given the estimates of *Neumann et al.* (2004). The larger dashed black line indicates the dichotomy boundary defined by *Andrews-Hanna et al.* (2008).

## 3.2 A dichotomy in crustal composition and thermal properties ?

### 3.2.a Crust formation and volcanic evolution : two stories closely linked

The knowledge of crustal rock thermal properties, and especially their radioelement content and thermal conductivity, is essential to model the thermal evolution of a planet. These properties depend on the composition, the compaction state and the petrology of the crust that largely result from magmatic processes.

Geochemical analysis of the Martian meteorite isotopes such as $U-Th-Pb$ (*Chen and Wasserburg*, 1986), $Rb-Sr$ (*Borg et al.*, 1997) and $Sm-Nd$ (*Borg et al.*, 2003; *Foley et al.*, 2005) suggests the early formation of a primary crust at $\sim 4.5$ Gyr, within $\sim 30-50$ Myr of the first solar system solid formation. This primary crust might have been $\sim 20-30$ km thick (*Norman*, 2002; *Wieczorek and Zuber*, 2004) but it remains unclear, however, to which extent it has been reshaped, buried or even eradicated since then by the dichotomy formation and subsequent magmatic processes. Indeed, an intense volcanic activity probably occurred during the early Noachian period with global distributed central volcanoes and plain volcanism (*Xiao et al.*, 2012) leading to abundant crustal formation (*McEwen et al.*, 1999; *Head et al.*, 2001; *Zuber*, 2001) and reshaping a large part of the surface. Thereafter, crustal production was cer-

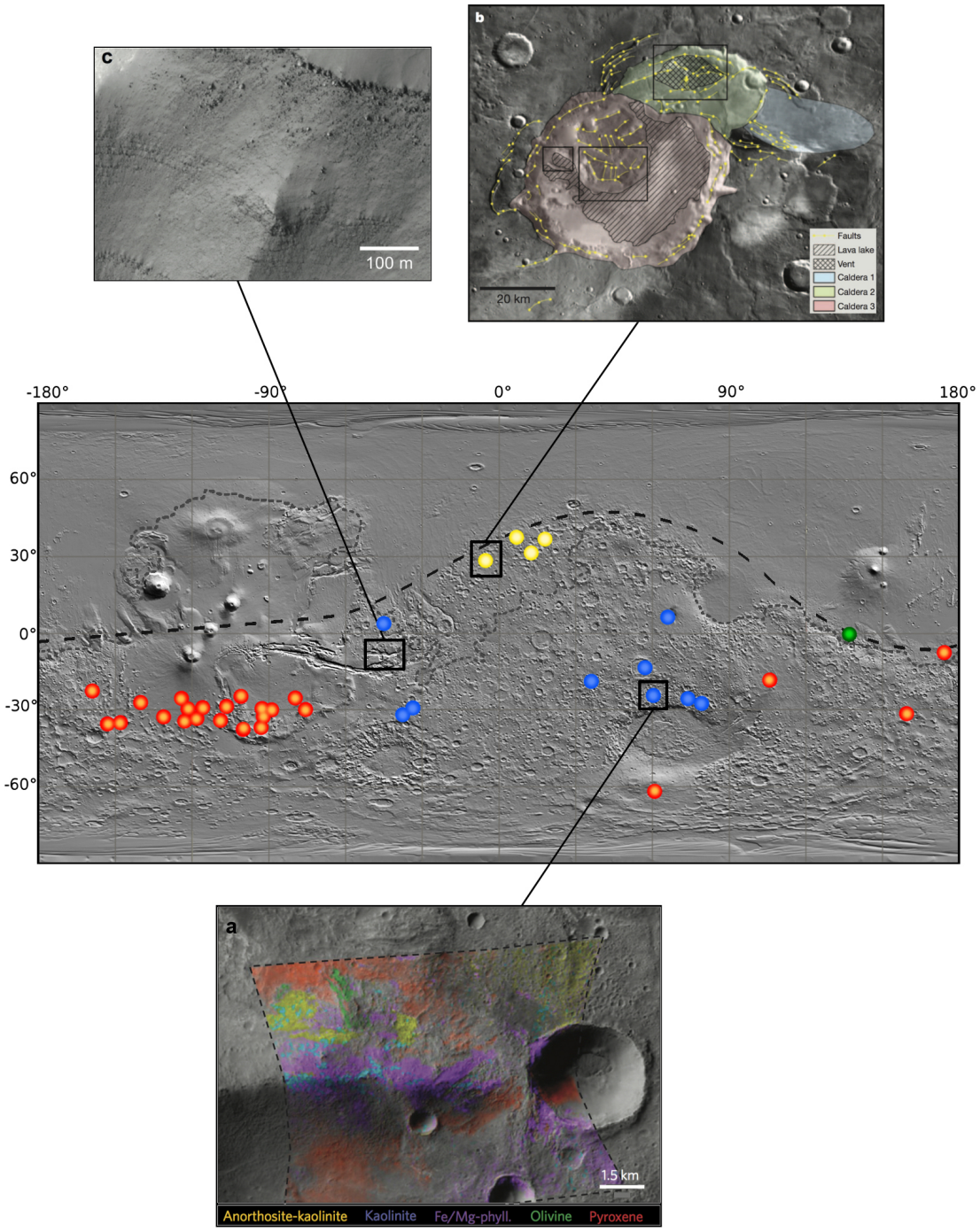
c
100 m
b
20 km
Faults
Lava lake
Vent
Caldera 1
Caldera 2
Caldera 3
-180°
-90°
0°
90°
180°
60°
30°
0°
-30°
-60°
a
1.5 km
Anorthosite-kaolinite
Kaolinite
Fe/Mg-phyll.
Olivine
Pyroxene

FIGURE 1.8

**FIGURE 1.8** – New insights on crustal properties. Over a MOLA-shaded relief topographic map, red points correspond to the ancient volcanoes detected by *Xiao et al.* (2012) and the yellow ones to the supervolcanoes of *Michalski and Bleacher* (2013). The potential locations of anorthosites found by *Carter and Poulet* (2013) and *Wray et al.* (2013) are indicated by the blue points, whereas the green one corresponds to the detection by *Sautter et al.* (2015) of felsic rocks very similar to those of the early terrestrial crust. The black dotted line represents the 40 km contour of the crustal thickness estimates of *Neumann et al.* (2004), whereas the larger dashed line indicates the dichotomy boundary defined by *Andrews-Hanna et al.* (2008). A potential anorthosite-bearing exposure in the northern Hellas region detected by *Carter and Poulet* (2013) is shown in (a) with a Thermal Emission Spectrometer image (centred at 66.5°E, −25.2°N) overlapped with CRISM mineral maps, that indicates the presence of anorthosites mixed with olivine (green), pyroxene (red) and kaolins (yellow). Alteration products are represented in blue (kaolins) and in purple (Fe/Mg-rich clays) (image from *Carter and Poulet*, 2013). (b) The geological mapping of Eden patera in Arabia Terra over THEMIS data reveals the presence of three distinct caldera (indicated by color shading) very similar to those observed for terrestrial supervolcanoes (image from *Michalski and Bleacher*, 2013). (c) MRO High Resolution Imaging Science Experiment image showing layered exposures within Coprates Chasma in Valles Marineris. The absence of boulders below the top part of the wall indicates that the lower layers are poorly consolidated and easily disaggregated (image from *Bandfield et al.*, 2013).

tainly still significant until the early Hesperian (*Head et al.*, 2002), though the bulk of the crust was probably mostly formed before 4 Gyr (*Nimmo and Tanaka*, 2005). Indications by Martian meteorite isotopic analysis of the early formation of long-lived chemical reservoirs that did not remix since then (*Jagoutz*, 1991; *Papike et al.*, 2009) suggest only few or no crustal recycling into the mantle (see chapter 2, section 4 for details). From the end of the Noachian, this global volcanism was then focused in the large volcanic provinces through large shield volcanoes, essentially at Elysium and Tharsis, probably because of the presence of stable mantle plumes located below those regions (e.g. *Solomon et al.*, 2005; *Li and Kiefer*, 2007; *Grott and Breuer*, 2009). However, $1-2$ km of Hesperian deposits were emplaced in the northern plains during this period, which likely implied associated magmatic intrusions at depth that might have contributed to $10-20$ km of crustal thickness in some areas (*Greeley and Schneid*, 1991). During the Amazonian, the volcanism steadily decreased and produced very localized lava flows having properties very similar to those of terrestrial basaltic ones. However, though being declining, this activity persisted until very recent periods, the younger lava flows identified on Elysium and Olympus Mons slopes being less than 100 Myr old (*Hartmann et al.*, 1999).

### 3.2.b The duality between old clastic materials and younger lavas

For a long time, effusive volcanism has been thought to be the most prevalent volcanic style throughout the Martian history (e.g. *McEwen et al.*, 1999). Nevertheless, if the Amazonian and Hesperian type of volcanism is largely representated by Elysium and Tharsis provinces (*Werner*, 2009), a significant fraction of the surface shows the trace of ancient basaltic processes of unknown origin (*Greeley and Spudis*, 1981). Recent studies have given new insights into Noachian volcanic processes. For instance, *Xiao et al.* (2012) have revealed the presence of

a large number of $50-100$ km diameter central volcanoes preserved in the highly impacted highlands that correspond to ancient Noachian structures predating Tharsis and Elysium formation (see Figure 1.8 for locations). Moreover, *Michalski and Bleacher* (2013) have detected in Arabia Terra the presence of irregularly shaped craters that represent a new type of martian volcanic edifices, very similar to terrestrial supervolcanoes (Figure 1.8b). Interestingly, all those ancient eruptive structures are associated with widespread unconsolidated fine-grained materials that can correspond to pyroclastic deposits, an alternative origin to the prevalent vision of a mega-regolith formed by impact events (*Pike*, 1980; *Schultz*, 2002). By associating the Thermal Emission Imaging System (THEMIS) dataset with highly resolved images of the surface in ancient preserved outcrops, *Bandfield et al.* (2013) have confirmed this hypothesis by showing a duality in the nature of the Martian crust. Indeed, young lava flows are characterized by high strength materials, whereas fine-particulate volcanic products constituting the old exposures are on the contrary poorly consolidated. Evidence for those unconsolidated terrains being widespread, explosive volcanism was probably the dominant eruptive style during the Noachian with a subsequent transition to Hesperian effusive volcanism (*Robbins et al.*, 2011; *Bandfield et al.*, 2013). The thickness of this poorly consolidated layer is estimated to $2-10$ km according to the available insights into old exposures constituted by outcrops within the $7-10$ km vertical relief on Valles Marineris walls (Figure 1.8c) and materials excavated by impact events. In terms of crustal thermal properties, this could imply a lower thermal conductivity for the poorly consolidated upper crustal layer of the highlands.

### 3.2.c A large felsic component buried in the southern crust ?

The primary Martian crust was probably formed within several tens of million years and then buried or reshaped by secondary volcanism (see section 3.2.a). Moreover the Noachian ancient crust of Mars might have resulted from explosive volcanism, whereas the younger crustal portions were rather created by effusive lava flows probably originating from a more depleted mantle. In this context, does this ancient crust have the same composition than the secondary one ?

Both orbital spectroscopy (*Christensen et al.*, 2005; *Mustard et al.*, 2005; *Baratoux et al.*, 2011), in situ analysis and study of SNC meteorites (*Aoudjehane et al.*, 2012; *Humayun et al.*, 2013; *Agee et al.*, 2013) all pointed to a Martian surface largely basaltic in composition with a low silica content (e.g. *McSween et al.*, 2003; *Christensen et al.*, 2005; *Mustard et al.*, 2005; *McSween et al.*, 2006; *Poulet et al.*, 2009). The only well-accepted detection of intermediate-to-felsic igneous rocks was a unit in the Nili Patera caldera of Syrtis Major, recognized to have a dacitic composition (*Christensen et al.*, 2005). On Earth, in contrast, many types of rocks are observed and associated with distinct chemical properties. Indeed, beyond basaltic volcanism, the magmatic processes associated to plate tectonics can produce siliceous melts through partial melting of evolved rocks or fractional crystallization, implying the common presence in subduction zones of intrusive igneous plutons containing felsic rocks and its volcanic equivalent, rhyolite (*Ashwal*, 2010). Felsic rocks are also observed on the remnants of the lunar

primary crust (*Ohtake et al.*, 2009), where plagioclases were concentrated near the surface by crystallization and differentiation of the lunar magma ocean (*Wood et al.*, 1870; *Warren*, 1985). On Mars, such process of felsic rocks formation is unlikely because plagioclase is stable at pressure $< 1$ GPa, hence at a much shallower depth on Mars ($\lesssim 80-100$ km) than on the Moon ($\lesssim 200$ km) (*Elkins-Tanton et al.*, 2005). Furthermore, given the lack of evidence for plate tectonics in the past (*McGill*, 2000; *Breuer and Spohn*, 2003; *Solomon et al.*, 2005; *Roberts and Zhong*, 2006) (see section 2.3.d), the large spectrum of rock composition observed on Earth in subduction zones might be absent on Mars.

However, by using the infrared and visible spectra provided by the Compact Reconnaissance Imaging Spectrometer for Mars (CRISM), *Carter and Poulet* (2013) and *Wray et al.* (2013) have recently detected iron-bearing plagioclase-rich rocks that have spectral signatures consistent with ferroan anorthosites. Altogether, eight sites have been reported (Figure 1.8, blue points), all located in the highlands, in the rims of the Holden crater and of large craters ($> 50$ km) located in the northern region of Hellas (Figure 1.8a), in the wall of a small valley in Xanthe Terra north of Valles Marineris, and on crater floors and intercrater plains in northeast Noachis Terra. For the majority of those locations, the co-occurence of kaolins (the preferential degradation product of anorthosites) (Figure 1.8a) may suggest in situ hydrous alteration, which constrains the formation time of felsic rocks to the end of the Noachian (*Carter and Poulet*, 2013).

In situ measurements have shown that such felsic rock occurences, that seemed very sparse from orbit, may in reality be much more common than previously thought. Indeed, felsic rocks have first been identified on the Mars Pathfinder landing site (*Brückner et al.*, 2003), and have then been detected by the rover Curiosity at the Gale crater, which has revealed an unexpected magmatic diversity and the widespread presence of silica-rich materials (*Sautter et al.*, 2015; *Sautter et al.*, 2016) (Figure 1.8, green point). Some of these rocks are even petrologically very similar to Archaean trondhjemites, tonalites and granodiorites, that constitute oldest remnants of the early terrestrial continental crust (*Sautter et al.*, 2015; *Sautter et al.*, 2016).

Taken together, in situ measurements and orbital analysis converge towards early magmatic processes similar to that observed on Earth (*Gunnarsson et al.*, 1998), implying a much more complex crustal composition than a purely basaltic one for Mars. Although our knowledge of the surface composition has been improved in recent years, the clues that we have on the buried part of the crust remain very sparse. Noachian terrains are of small size and have been buried under alteration or volcanic products, and covered by mantling dust (*Mustard et al.*, 2005) : it is thus challenging to constrain the chemical nature of the primary crust from orbit or even from the analysis of SNC meteorites that are all, except for one, Amazonian in age (*Nyquist et al.*, 2001). Therefore, does the scarcity of felsic rock detections indicate a plutonic origin of anorthosites through differentiation processes, like on Earth, or does it only reflect the difficulty to clearly identify the anorthosite spectral signature from orbit (*Carter and Poulet*, 2013; *Wray et al.*, 2013; *Sautter et al.*, 2015) ? One has to note that all felsic exposures have been detected either in ancient Noachian terrains (*Leonard and Tanaka*, 2001; *Deit et al.*, 2013;

*Farley et al.*, 2014) or in the rim and floor of impact craters, implying an excavation from depths larger than 5 km (*Quantin et al.*, 2012). Some of the exposures are also close, as, for instance, at Noachis Terra (*Wray et al.*, 2013), suggesting a common buried source in the highlands (*Carter and Poulet*, 2013). The existence of such a light buried felsic component would lower the thickness of the southern crust that is required to compensate the north/south difference in relief and, therefore, reconcile the large surface densities estimated by *Baratoux et al.* (2014) with the absence of crustal flow at the dichotomy boundary, supposed to occur for large crustal thicknesses (*Nimmo and Stevenson*, 2001).

### 3.2.d Crustal radiolement content

The thermal evolution of a planet is largely influenced by the bulk radioelement content (e.g. *Grott and Breuer*, 2008a, 2009), as well as its vertical distribution between the mantle and the crust (e.g. *Sekhar and King*, 2014).

For Mars, different compositional models for the bulk radioelement abundance have been derived from the chemical analysis of SNC meteorites that gives K and Th concentrations of $200-2600$ ppm and $0.1-0.7$ ppm, respectively (*Meyer*, 2003). Large discrepancies are thus observed among the potential compositional models and the predicted heating rate could vary by a factor of $2-3$ (Table 1.1). *Grott and Breuer* (2008a) have shown that the high initial amounts of internal heat production predicted for the radioelement concentrations of *Lodders and Fegley* (1997) are incompatible with the absence of large scale topographic relaxation. This has been independently confirmed by thermo-chemical evolution models (where the crust is formed by partial melting of the mantle) (*Hauck and Phillips*, 2002; *Breuer and Spohn*, 2006), which predict the formation of too thick crusts when using this compositional model. The compositional models of *Treiman et al.* (1987), *Morgan and Anders* (1979) and *Wänke and Dreibus* (1994) give similar initial and present-day amounts of internal heating.

An additional constraint on the radioelement model arises from the surface radioelement concentrations provided by *Taylor et al.* (2006) and *Boynton et al.* (2007) that use Mars Odyssey gamma ray spectrometer (GRS) data that penetrates up to a few centimeters below the surface. The compositional maps (Figure 1.9a for K, Figure 1.9b for Th) show that the radioelements are roughly homogeneously distributed over the Martian surface, though a higher

| Model reference | $K$ [ppm] | $Th$ [ppb] | U [ppb] | $H_0$ [pW kg$^{-1}$] | $H_{4.5}$ [pW kg$^{-1}$] |
|---|---|---|---|---|---|
| *Treiman et al.* (1987) | 160 | 64 | 16 | 17 | 3.7 |
| *Morgan and Anders* (1979) | 62 | 101 | 28 | 21 | 5.0 |
| *Wänke and Dreibus* (1994) | 305 | 56 | 16 | 23 | 4.0 |
| *Lodders and Fegley* (1997) | 920 | 55 | 16 | 49 | 6.1 |

**TABLE 1.1** – Models for radioelement concentrations in the primitive mantle of Mars. $H_0$ and $H_{4.5}$ correspond to initial and present-day amounts of internal heat production by radioelements, respectively.

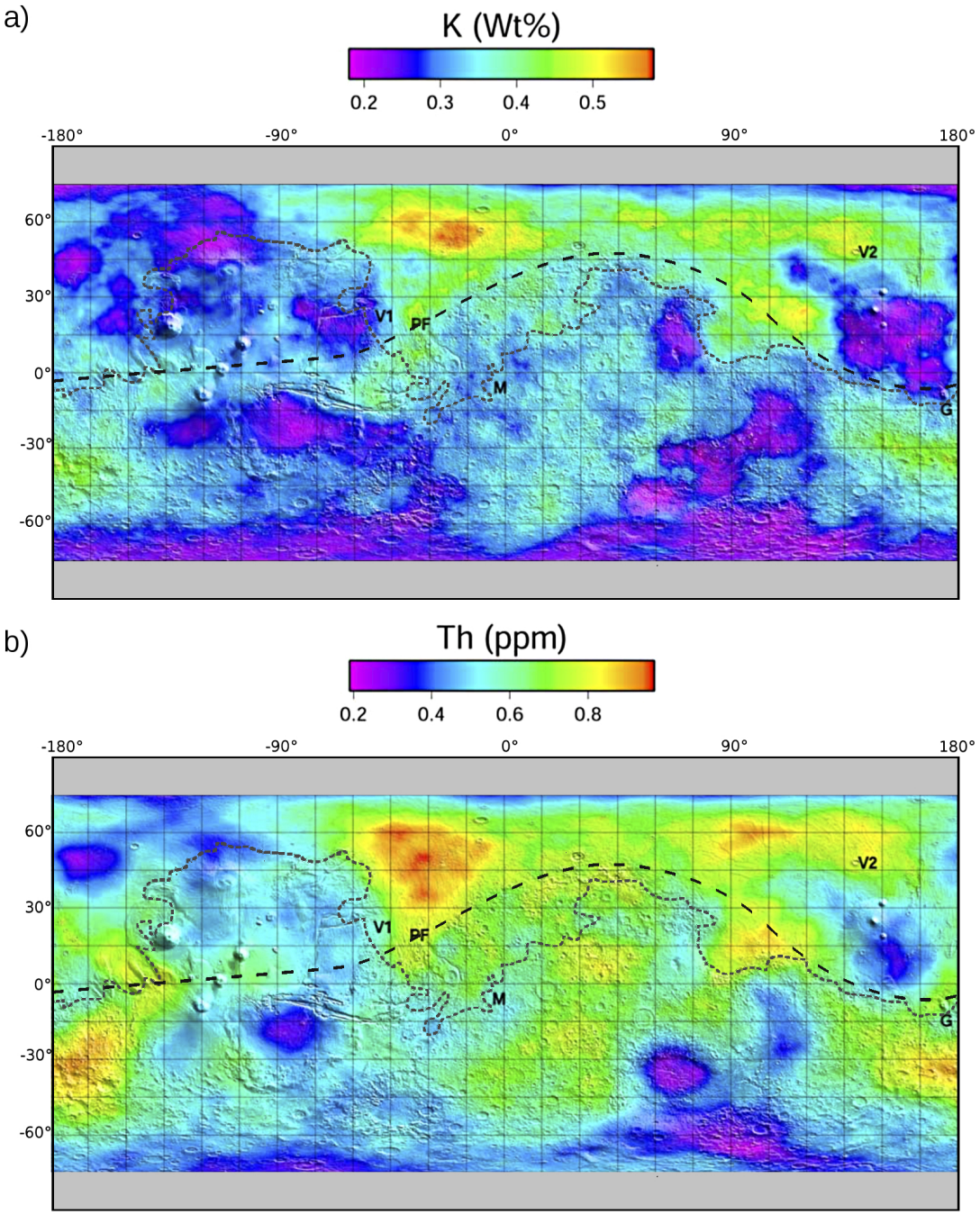


**FIGURE 1.9** – Maps of the surface concentrations of (a) K and (b) Th measured by the Mars Odyssey gamma ray spectrometer (GRS) over a MOLA shaded relief map of Mars (Figures from *Taylor et al.*, 2006). The landing sites of Viking 1 and 2, Pathfinder, Opportunity and Spirit in Gusev crater are indicated by the abbreviations V1, V2, PF, M and G, respectively.

content is observed for both Th and K in a large area located between $-60^{\circ}$E and $\sim 140^{\circ}$E with, however, no obvious correlation with the north/south dichotomy. K and Th surface concentrations are estimated to $2000-6000$ ppm and $0.2-1$ ppm, respectively, and are thus a little higher than the ranges given by SNC meteorite analysis. The ratio of K and Th abundances being well reproduced by the compositional model of *Wänke and Dreibus* (1994), this latter is today widely considered as the reference model for Mars. Given the composition of this model and GRS surface concentrations, some constraints can be put on the crustal enrichment in radioelements with respect to the primitive mantle. *Taylor et al.* (2006) have, for instance, suggested that 50 % of the bulk radioelement content is concentrated in the crust if considering a uniform crust of 57 km and a crustal enrichment factor of 10. However, this percentage strongly depends on the crustal thickness, which remains largely debated, as previously discussed in section 3.1.a.

On the other hand, surface compositions are perhaps not representative of the entire crust and a vertical layering in radioelement concentrations could have been produced by crustal formation processes. Indeed, during the crystallization from bottom to top of the primordial magma ocean, the highly incompatible elements are enriched in the evolved residual liquid, which could concentrate substantial amount of radioelements in the upper most layers of Mars's mantle and primary crust (*Elkins-Tanton et al.*, 2005). A similar process has in particular be invoked to explain the strong enrichment in potassium and rare earth elements of the Procellarum KREEP Terrane on the Moon's nearside (e.g. *Zhong et al.*, 2000). It remains unclear if such process happened on Mars since the higher Martian mantle pressure (due to a larger gravity compared to the Moon) could have led to denser residual melts that could have been trapped deeper in the planet. Another possible source of vertical layering in radioelements arises from the secondary Martian crust, whose enrichment depends on its formation process. Indeed, on Earth, the relatively young basaltic rocks of the oceanic crust are formed by partial melting of a mantle already depleted by previous crustal extraction, implying for those rocks typically low enrichment factors of $\sim 2-5$. For the rocks of the terrestrial continental crust that are produced from the remelting of evolved rocks or from slow differentiation processes in magma chambers, larger enrichments up to 30 could be reached, which depends, however, on the age of the continental crust (the younger, the more enriched) (*Jaupart and Mareschal*, 2003). On Mars, such remelting processes of the crust might have occurred in the thickened and hot early crust of the highlands, which could imply an enrichment in radioelements by differentiation of the southern crust (*Roman and Jaupart*, 2017) (see section 3.2.c).

## 3.3 Conclusion

According to the recent insights on crustal properties provided by both in situ rock analysis and remote-sensing observations, the dichotomy does not seem to be a simple surface feature but probably extends at depth, resulting in structural, and potentially compositional, differences in between the northern and southern Martian crust. Indeed, the inversion of gravity and topography data shows a quasi-bimodal distribution of the northern and southern crustal

thicknesses, with an average value of $57 \pm 24$ km among all studies. However, this average value depends on the crust-mantle density contrast assumed for the inversion and, therefore, on the crustal density, which is still largely unknown. Surface concentration of Fe, Al, Ca, SI and K point to large surface densities ($> 3100$ kg m$^{-3}$ and up to $> 3600$ kg m$^{-3}$), implying a potential very thick southern crust poorly compatible with the absence of viscous relaxation of the dichotomy relief. However, it is unclear if such a large density can be extrapolated to the entire crust. Indeed, felsic rocks excavated from depth in crater rims and crater floors have been detected throughout the highlands by remote-sensing observations and in situ measurements, which suggests the potential presence of a common reservoir enriched in silica and buried within the southern crust. A difference in composition between the northern and southern crusts would also suggest a difference in radioactive element content with, in particular, an enrichment in radioelements if those felsic rocks are produced from evolved melts or from a more primitive mantle. Moreover, the thermal properties of surface rocks might differ in between the two hemispheres. Indeed, the lowlands are covered by compact lava flows, whereas the old southern crust is made of poorly consolidated materials from ancient explosive volcanism, which could imply a lower thermal conductivity for the southern crustal upper layer. As the thermal evolution of a planet largely depends on the crustal properties (thickness, thermal conductivity and enrichment in radiolements) it is therefore essential to investigate the consequences of such large north/south differences in crustal structure and composition on Mars's thermal evolution.

# CHAPTER 2

# MARS'S THERMAL STRUCTURE AND EVOLUTION : MAJOR ISSUES

**Sommaire**

# 1 Summary

In the absence of direct heat flux measurements, indirect evidences have to be considered to constrain the thermal evolution of Mars. The presence of an early Martian internal dynamo constrains the core thermal evolution, whereas Mars's volcanic history and crustal formation chronology give insights on the evolution of the internal conditions required for melt extraction towards the surface, i.e. on internal temperature and lithosphere thickness evolutions.

Another major constraint on Mars's thermal evolution is given by elastic lithosphere estimates that represent a measure of the amount of stress the lithosphere can sustain before yielding. Elastic lithosphere thicknesses being sensitive to the lithosphere thermal structure and rheology, they provide indirect heat flow estimates. On Mars, elastic lithosphere thicknesses are predicted to be low at the Noachian, with a subsequent increase during the evolution due to planetary cooling. Today, they are estimated to reach 161 km below the southern polar cap (though any value greater than 110 km is suitable, *Wieczorek*, 2007), and more than 300 km below the northern one (*Phillips et al.*, 2008). The large present-day value in the north remains today enigmatic and hard to reproduce with thermal models. Indeed, on one hand a wet mantle rheology predicts too low present-day values compared to the northern estimate. On the other hand, if a dry mantle rheology is more consistent with the northern present-day estimate, it is hardly reconciliable with the low Noachian estimates (*Grott and Breuer*, 2008b, 2009). It has been argued that such a unique and large present-day value in the north might be due to lateral variations in elastic lithosphere thicknesses (*Phillips et al.*, 2008; *Grott and Breuer*, 2009, 2010). However, even when accounting in 3-D models for lateral variations in crustal thickness and mantle temperature anomalies, large values $> 300$ km remain especially hard to reach below the northern polar cap (*Plesa et al.*, 2016).

In this thesis, we investigate whether the elastic thickness evolution and other constraints such as recent volcanism can be explained by both a structural and compositional north/south dichotomy in crustal properties. And in the positive case, what are the consequences of such a dichotomy in crustal properties on the thermal evolution and structure of Mars ?

# 2 Introduction

The north/south Martian dichotomy goes beyond to represent a prominent feature of the surface and probably has largely influenced the interior of the planet itself (see chapter 1). Indeed, all the dichotomy formation mechanisms that have been proposed - a large impact event, a degree one convection pattern, plate tectonics or a mantle overturn - should have deeply influenced Mars' internal structure and thermal evolution. Moreover, besides a north/south crustal thickness difference, a dichotomy in crustal thermal properties has also been recently revealed with, in particular, a lower thermal conductivity for the poorly-consolidated upper layer of the Noachian southern crust (*Bandfield et al.*, 2013) and a potential different radioelement content for the felsic component that might be buried in the highlands (*Carter and Poulet*, 2013; *Wray et al.*, 2013; *Baratoux et al.*, 2014; *Sautter et al.*, 2015). In this context, in which extent has this structural and compositional dichotomy influenced the thermal evolution of Mars ? Are those effects still influencing the thermal structure of the planet ?

Mars's thermal structure and evolution is largely unknown, partly due to the lack of direct heat flux measurement at the surface, contrary to the Earth or the Moon. An alternative way to investigate the thermal evolution of Mars is provided by thermal modeling, though many uncertainties have to be considered for the required parameters, as, for instance, for crustal properties (thickness, thermal conductivity) (e.g. *Wieczorek and Zuber*, 2004; *Bandfield et al.*, 2013; *Baratoux et al.*, 2014; *Goossens et al.*, 2017), the radioelement partioning between the crust and the mantle (e.g. *Carter and Poulet*, 2013; *Wray et al.*, 2013; *Baratoux et al.*, 2014; *Sekhar and King*, 2014; *Sautter et al.*, 2015), the crust and mantle rheology, the initial temperature conditions or even the Martian solidus curve (e.g. *Hauck and Phillips*, 2002; *Morschhauser et al.*, 2011). Moreover, the water content being closely linked to mantle and crustal rheological properties, (*Karato and Wu*, 1993; *Mei and Kohlstedt*, 2000a,b) it strongly influences the thermal evolution. Unfortunately, although it is widely accepted that water contributed to shaping the surface (*Carr*, 1996), the early bulk mantle water content, as well as its lost by degassing during the primordial magma ocean stage and since then by subsequent volcanism, are still largely debated.

Given such uncertainties, suitable thermal models should be consistent with :

— **The internal magnetic field evolution**. Indeed, the thermal state of the core, and therefore the existence of a dynamo, is directly linked to mantle cooling (see section 3.2).

— **The crustal formation and volcanic history**, because volcanic extrusions as well as the rate of crustal production are the surface manifestations of the interior thermal state (see section 3.3).

— **The elastic lithosphere thickness evolution**. The base of the elastic portion of the lithosphere (i.e. the crust and the rigid portion of the upper mantle) approximately corresponds to an isotherm, beyond which ductile flow occurs ; the elastic thickness provides thus a clue on the local thermal state (see section 3.4).

— **The tidal dissipation**. The orbital evolution of the two Martian satellites, Phobos and Deimos, being closely linked to the dissipation of tidal energy within Mars's interior, it can be used to constrain the rheological and thermal state of the mantle (e.g. *Nimmo and Faul*, 2013). This has not been considered in this study.

# 3 Mars's thermal evolution : what do we know ?

## 3.1 Mars, a planet in present-day stagnant lid convection

On Earth, plate tectonics causes crustal recycling in subduction zones, which leads to an efficient cooling of its deep interior and a thin lithosphere (*Nimmo and Stevenson*, 2000). Although it remains unclear if plate tectonics occurred during its early stages of evolution (see chapter 1, section 2.3.d for details), Mars is today a one-plate planet, entirely covered by a rigid lithosphere, namely the stagnant lid above the convecting mantle, which does not participate to the convection. For such a stagnant lid convection configuration, the external layers of the planet are preferentially cooled with a thickening of the lithosphere over time (e.g. *Grott and Breuer*, 2008b; *Baratoux et al.*, 2011). The extraction of heat from the deeper interior is less efficient, which implies a relatively stable temperature over time in the well mixed convecting mantle (e.g. *Plesa et al.*, 2015). Using the Gamma Ray Spectrometer (Mars Odyssey) data to analyse the geochemical properties of Hesperian and Amazonian volcanic provinces, *Baratoux et al.* (2011) have highlighted a change in the conditions of melt formation during the evolution : the older the lava flow, the higher the degree of partial melting and the shallower the melt was formed. This gives some constraints on the cooling rate of Mars, which is thus characterized by a lithosphere thickening of $17-25$ km/Gyr and an average temperature decrease of $30-40$ K/Gyr. Due to the absence of plate tectonics, Mars's cooling is thus less efficient than that of the Earth, which is estimated to $50-100$ K/Gyr during the last 3.5 Gyr (*Herzberg et al.*, 2010).

## 3.2 Magnetic field history constraint

### 3.2.a Existence of an early core dynamo

No planetary magnetic field of global scale has been detected by Mars Global Surveyor (*Acuna et al.*, 1999). However, some regions of the crust are strongly magnetized and show anomalies sometimes comparable to or even greater than the highest common values found in Earth's crust, which likely result from acquired magnetic remanence while an early strong core dynamo was active (*Acuna et al.*, 1999). Those magnetic anomalies are mostly concentrated in the Noachian southern terrains (*Acuna et al.*, 1999; *Connerney et al.*, 2005), while they are nearly absent in the younger lowlands' surface. However, weak magnetic anomalies are visible over some large regions of the northern hemisphere, which indicates a potential magnetization of the underlying crust buried after the resurfacing of the northern plains (*Connerney et al.*, 2005). Probably because the heating due to impacts demagnetized the crust (*Hood et al.*, 2003),

there are no anomalies resolvable from orbit in the major Martian impact basins, which suggests that the dynamo ceased before they formed, probably at the late Noachian or early Hesperian (*Stevenson*, 2001). However, although most studies suggest that the dynamo was active early, there is no consensus on the exact timing : *Lillis et al.* (2013) or *Acuna et al.* (1999) propose a cessation at $4.1 - 4$ Gyr, whereas *Milbury et al.* (2012) suggests it occurred latter, at 3.6 Gyr.

### 3.2.b Implications for thermal models

On Mars, geophysical constraints predict the presence of a dense and metallic core with a radius of $1500 - 1800$ km (e.g. *Folkner et al.*, 1997), that is likely mainly liquid (*Bills et al.*, 2005), potentially because of a high content in light chemical elements like sulphur (e.g. *Khan and Connolly*, 2008; *Baratoux et al.*, 2014). The existence of an internal dynamo requires the convection of conductive fluids in the liquid part of the core, which must, therefore, lose its heat to an efficiently cooling mantle.

The presumed $\sim 0.5$ Gyr duration of the dynamo implies to sustain a sufficient temperature gradient between the core and the mantle during this period (*Nimmo and Stevenson*, 2000; *Williams and Nimmo*, 2004). In the case of an early stagnant lid convection, such a temperature gradient could be obtained with thermal models for the right duration with an initially overheated core (e.g. *Breuer and Spohn*, 2003). Core overheating is indeed expected for the early evolution, due to the concentration into the core of a large part of the energy brought by impact events (*Canup*, 2004) and to the release of gravitational energy associated to core formation. The early overheating of the Martian core is estimated at several hundreds of kelvins, and perhaps even at $\sim 1000$ K (*Ke and Solomatov*, 2006; *Ke and Solomatov*, 2009), which is enough to initiate the dynamo during the early Noachian (*Breuer and Spohn*, 2003).

Alternatively, the dynamo, and thus the high temperature gradient between the core and the mantle, could result from plate tectonics and a subsequent evolution towards a one-plate planet (*Breuer and Spohn*, 2003; *Zhang and O'Neill*, 2016). Nevertheless, plate tectonics models are less compatible with the volcanic history than the models associating a stagnant lid and an overheated core as they predict a peak in volcanic activity after plate tectonics has stopped, which is not observed (see section 3.3 for details on volcanism and crustal formation chronologies) (*Breuer and Spohn*, 2003).

Another potential explanation for a dynamo initiation and its duration is provided by the overturn of a gravitationally unstable primary mantle, i.e. one of the mechanisms proposed to explain the dichotomy formation (*Elkins-Tanton et al.*, 2003, 2005) (see chapter 1, section 2.3.c). Indeed, by carrying the upper cold materials close to the CMB, this overturn would adiabatically cool the lower layers of the mantle and thus create a large temperature gradient between the core and the lower mantle of $\sim 1000$ K (*Elkins-Tanton et al.*, 2003, 2005), thereby promoting core cooling. However, this mantle overturn would also concentrate close to the CMB the radioelements initially contained in the upper most layers and thus stop the convection

early (*Elkins-Tanton et al.*, 2003, 2005; *Plesa et al.*, 2014), which is incompatible with the observation of recent volcanism (*Plesa et al.*, 2014).

## 3.3 Volcanic history and crustal formation constraints

### 3.3.a Conditions for melt extraction

Two major issues for thermal models are to suitably reproduce the crustal formation timing (especially a crustal formation roughly achieved at 4 Gyr) as well as to be consistent with Tharsis formation and a recent volcanic activity (the reader is referred to the chapter 1, section 3.2.a for the detailed chronologies of volcanism and crustal formation). Crustal formation and volcanic eruptions are both due to mantle melt formation and extraction processes that directly depend on the internal temperature and lithosphere thickness, respectively. Indeed, the hotter the mantle, the more melt is formed and the thinner the lid, the more efficient its extraction towards the surface is. After a certain time of evolution, though melt could still be produced at depth, lithosphere thickening induced by planetary cooling could prevent melt from rising.

Models coupling thermal and crustal evolution (e.g. *Hauck and Phillips*, 2002; *Breuer and Spohn*, 2006; *Morschhauser et al.*, 2011) have shown that a wet mantle rheology combined with a low initial mantle temperature is more consistent with a fast bulk crustal formation as well as with the volumes of melt that are required to reproduce the average crustal thickness estimates (see chapter 1, section 3.1.a for values). However, a trade-off between the viscosity and the initial mantle temperature is observed. Indeed, a wet mantle rheology is weak, which implies a vigorous convection, efficient heat transfer through the mantle and thus a thin lithosphere that favours melt extraction. But if the initial mantle temperature is too high, it leads to the production of too large amount of crust. Conversely, a dry mantle rheology is also compatible with the crustal formation chronology if associated with hotter initial temperatures, and can, therefore, not be excluded.

Contrary to crustal formation process that involves large areas of melt extraction, the persistence of recent volcanic activity is restricted to very localized areas, i.e. Elysium and Tharsis, in which favourable conditions for magma extrusion are met. Localized melt extraction can result from decompression melting in mantle plumes heads (*Zuber*, 2001; *Li and Kiefer*, 2007; *Grott and Breuer*, 2010) or be promoted by the thermal insulation of a thick crust (*Montési and Zuber*, 2003; *Schumacher and Breuer*, 2006).

### 3.3.b Tharsis formation

One of the major challenges for dynamical models is to form the Tharsis bulge, i.e. the stable production of huge amounts of mantle melt during at least 3 Gyr (*Werner*, 2009). A vigorous long-lived mantle upwelling below Tharsis is thus likely (e.g. *Zuber*, 2001; *Roberts and Zhong*, 2006; *Zhong*, 2009; *Šrámek and Zhong*, 2010). But in a stagnant lid planet like Mars,

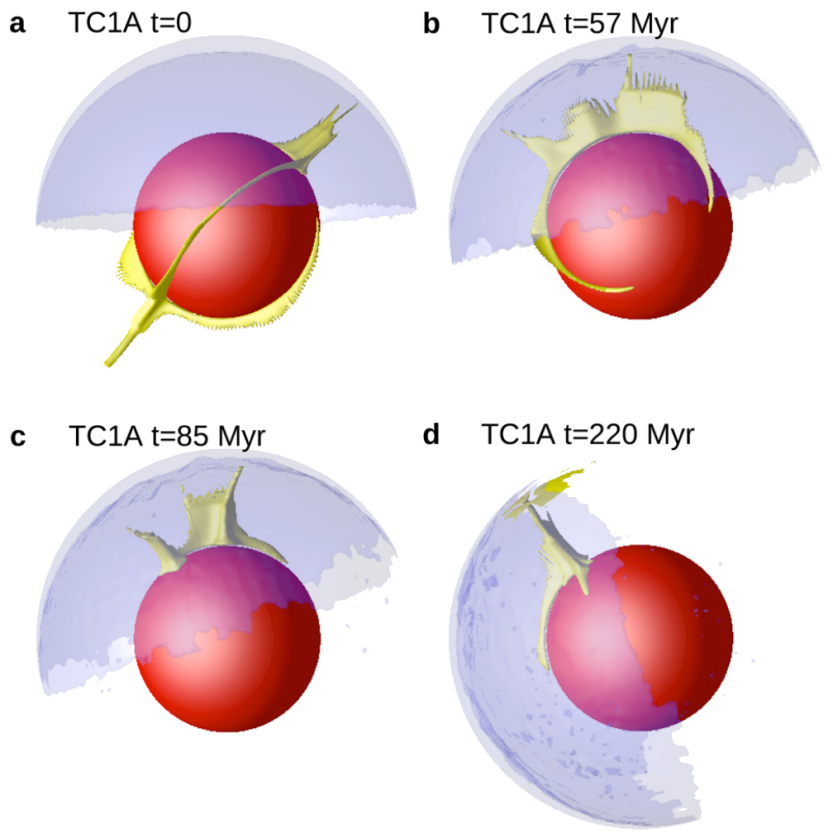


**FIGURE 2.1** – Model example for Tharsis formation (model *TC1A* of *Šrámek and Zhong*, 2010). In this model the presence of a thickened lithospheric keel in the southern hemisphere - resulting from the dichotomy - leads to a differential rotation between the lithosphere and the underlying plume, which is then stabilized at the dichotomy boundary. The captions are shown between 0 Myr and 220 Myr with a lithospheric keel representated in blue (residual non-dimensional composition isosurface at $C = -0.07$), whereas the residual non-dimensional temperature $T = +0.07$ corresponds to the yellow isosurface. This model has been obtained with a viscosity contrast of 25 through the mantle and has shown a differential separation rate of 0.66°/Myr.

how did mantle plumes form and stabilize at a fixed location ? Indeed, on Earth plate tectonics has strongly influenced the mantle convection pattern, which is characterized by multiple hot mantle plumes and cold slab downwellings in subduction zones (*Schubert et al.*, 2001). On Mars, in contrast, the distribution of mantle plumes and downwellings is not imposed by the pattern of plate tectonics and might thus be dominated either by the presence of a strong single plume in the case of a degree-one convection (e.g. *Zuber*, 2001; *Roberts and Zhong*, 2006; *Zhong*, 2009), or by multiple upwellings (e.g. *Li and Kiefer*, 2007; *Grott and Breuer*, 2010; *Plesa et al.*, 2016) depending on the radioelement vertical distribution (*Sekhar and King*, 2014) and on the viscosity contrast within the mantle (*Zhong and Zuber*, 2001; *Roberts and Zhong*, 2006). Phase changes in the deep mantle have also been shown to promote degree-1

mantle convection (*Harder and Christensen*, 1996; *Breuer et al.*, 1997; *Roberts and Zhong*, 2006). However, the current persistence of Martian hot plumes is debated, the present-day core temperature being perhaps too low to destabilize the lower most mantle layer. But if a mantle plume still exists below Tharsis, how can we explain its stable location over several gigayears ?

*Šrámek and Zhong* (2010) and *Zhong* (2009) have shown that the processes involved in the formation of the dichotomy as well as Tharsis, i.e. two large-scale structures, might actually be linked. Indeed, in their models the dichotomy induces the existence of a large mantle plume under the southern hemisphere, allowing the formation of a vast partial melting zone of several hundreds of kilometers wide, which forms a thickened lithospheric keel when cooling. According to the initial conditions (thickness of the lithospheric keel, viscosity contrast through the mantle), a differential movement can be observed between the entire single-plate lithosphere and the underlying mantle plume, which leads to the migration of this latter, and then its stabilization at the transition zone between the thickened lithosphere of the highlands and the lowlands' one (Figure 2.1). In this model, the long-term stability of the plume location not only provides a convincing explanation for the huge amount of magma production required to built the Tharsis bulge, but also explains the location of this latter at the dichotomy boundary (*Zhong*, 2009). In this coupled formation process for Tharsis and the dichotomy, keels $> 200$ km thick are required to obtain a migration rate of the plume - and thus of Tharsis - consistent with the observations, i.e. in a a few hundreds of millions of years. But how can such an early thickened lithospheric keel have formed in the south ? If *Šrámek and Zhong* (2010) argue for an initial degree-one convection pattern, the recent study of *Citron et al.* (2018) shows that it might result from the formation of a large mantle plume in the southern hemisphere in response to a large impact event in the northern one.

## 3.4 Elastic thickness estimate

### 3.4.a Theoretical background

Elastic thickness is defined by the depth range over which stresses are supported elastically within the lithosphere. As the strength of the lithosphere largely depends on its temperature structure, elastic thickness estimates thus give an indirect measurement of lithospheric heat flux. Indeed, the lithosphere propensity to deform under an applied stress indicates the amount of stress that can be supported before yielding, either by brittle deformation in the cold upper lithosphere, or by ductile flow in the hot lower one, at the transition with the asthenospheric mantle. Given the rheology and the thermal state of the lithosphere it is possible to build ductile and brittle deformation envelopes for the crust and the lithospheric mantle (*Goetze and Evans*, 1979) and therefore, by determining which one dominates at a given depth, to obtain the resulting strength envelope (*McNutt*, 1984) (Figure 2.2). This latter indicates the stress over which yielding occurs : when a given stress is applied to the lithosphere, the elastic layers thus correspond to the portions of the crust and the lithospheric mantle that are within the strength envelope. The global elastic lithosphere thickness is different if the crustal and lithospheric

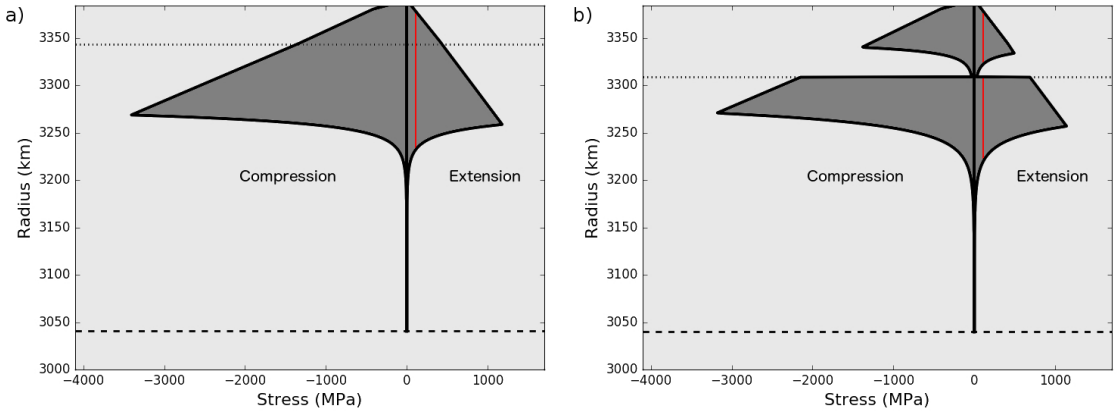


**FIGURE 2.2** – Schematic yield strength envelopes of a two-layer lithosphere (the dotted lines represent the crust-mantle transition, the larger dashed line the lithosphere depth). In (a) the crust and the lithospheric mantle are welded and act as a single plate. The shaded area corresponding to the elastic core of the lithosphere, the elastic thickness (in red) is thus directly given in this case by the depth that is within the strength envelope when a given stress is applied. Once the amount of stress that can be supported by the lithosphere is excedeed (i.e. the critical yield stress) yielding occurs either by brittle deformation in the shallow regions or by ductile flow in the hotter and deeper lithosphere. However, an incompetent layer could exist in the lower part of the crust (b). In this case, the elastic portions of the lithospheric mantle and the crust (in red) are decoupled and the total elastic thickness is lower than when they are welded.

mantle layers are welded (Figure 2.2a) or decoupled by an incompetent crustal layer that reduces the total strength of the lithosphere (Figure 2.2b).

On Earth, the oceanic and continental lithospheres having distinct compositional and physical evolutions, their elastic thicknesses are controled by different processes. Indeed, the thin oceanic lithosphere has a single-layer rheology and its elastic thickness roughly follows the depth of an isotherme of $700 - 850$ K reflecting lithosphere strengthening as it cools (*Watts*, 1978; *Caldwell and Turcotte*, 1979; *McNutt and Menard*, 1982). However, for the more complex multi-layer continental lithosphere, the relation between the elastic thickness and the temperature is not so straightforward (e.g. *McNutt et al.*, 1988) and also depends on the distribution and thickness of the different competent layers (*Burov and Diament*, 1995). That implies large spatial variations of the elastic thicknesses over continental areas, but with an average increase over time due to lithosphere cooling (*Watts*, 1992; *Grott and Breuer*, 2008a).

### 3.4.b Methods for elastic thickness estimation on Mars

On Mars, most elastic thickness estimates have been derived from gravity and topography data, in particular, below large volcanic loads (*McGovern et al.*, 2004; *Kiefer*, 2004; *Belleguic et al.*, 2005; *Hoogenboom and Smrekar*, 2006; *Wieczorek*, 2008; *Grott et al.*, 2011; *Ritzer and Hauck*, 2009). This approach consists in considering that the lithosphere behaves as an

elastic plate overlying a fluid mantle and modeling the lithosphere deformations produced by topographic and/or internal density anomalies. The resulting gravity anomalies depend on parameters such as the elastic lithosphere thickness. However, some Martian geological features allows for other more direct estimation methods. In particular, *Phillips et al.* (2008) have estimated the elastic lithosphere thickness below the two polar caps by comparing their models of lithospheric deflection (due to polar cap loading) to that measured by the Shallow Radar on board the Mars Reconnaissance orbiter. Furthermore, geomorphological features such as rift uplift (*Barnett and Nimmo*, 2002; *Grott et al.*, 2005; *Kronberg et al.*, 2007) or estimates of the seismogenic layer thickness on thrust faults (*Grott et al.*, 2007; *Ruiz et al.*, 2008; *Schultz and Watters*, 2001) have also provided clues on local elastic lithosphere thickness.

One of the major difficulty is to assess an age to elastic thickness estimates. Indeed, lithosphere flexure under a load is acquired when lithosphere temperatures are sufficiently hot, and is then "freezed" during the subsequent cooling. As a result, the age of the elastic lithosphere thickness is generally assumed to correspond to the age of the deformed surface or load. However, this assumption is not always valid, especially below the large volcanoes as they have been active throughout a large part of the planet history. Indeed, while the loading by Tharsis volcanoes was mainly emplaced during the Noachian and probably achieved by the end of the Hesperian, very recent lava flows have been detected on their slopes (*Hartmann et al.*, 1999; *Hauber et al.*, 2011; *Neukum et al.*, 2004; *Susko et al.*, 2017; *Werner*, 2009), implying a large uncertainty ($\sim$ 3 Gyr) for the ages of these estimates. Moreover, as stresses in the lithosphere decay as a function of time due to viscous relaxation, especially for multi-layer rheologies (*Brown and Phillips*, 2000), the lithospheric flexure is determined by a competition between loading rate and lithospheric cooling. Therefore, the present-day elastic thickness does not always correspond to the deformations induced by the total load and care must be taken when interpreting the thermal state derived from loading models.

### 3.4.c Implications for Mars's thermal evolution

Elastic thickness having been estimated for different ages, it thus provides an overview of Mars's thermal evolution (Figure 2.3b), especially in the southern hemisphere and below the large volcanoes, since estimates in the northern lowlands are sparse due to topography eradication (*Tanaka et al.*, 2003) (Figure 2.3a). Elastic thicknesses were very low during the Noachian ($\sim$ 20 km, except at Isidis Planitia), reflecting the high lithospheric temperatures that prevailed at the earliest times of Mars. Due to the later progressive cooling of the planet, the elastic thicknesses increased during the Hesperian and the Amazonian (*Grott and Breuer*, 2008b), reaching a present-day value of 161 km below the southern polar cap (though any value greater than 110 km could fit the observations, *Wieczorek*, 2008), whereas a significantly higher value of $>$ 300 km is observed below the northern pole (*Phillips et al.*, 2008).

The transition from the strong lithosphere to a weak asthenosphere - and thus the elastic lithosphere thickness - not only depends on the lithospheric temperature profile, but also on

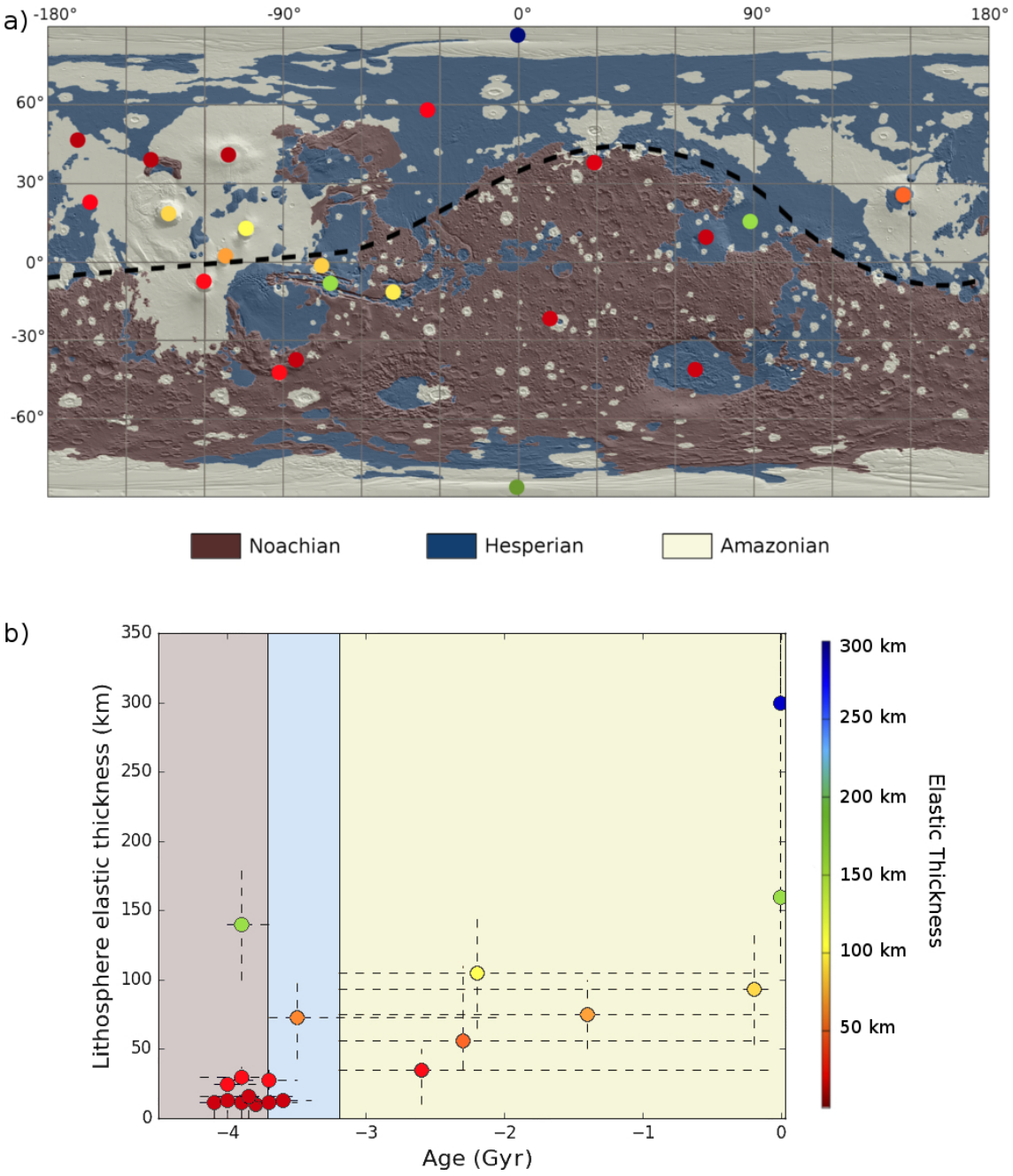


**FIGURE 2.3** – Elastic thickness estimates on Mars previously compiled by *Grott et al.* (2013). (a) Location of those estimates over a Mars Orbiter Laser Altimeter-shaded topographic map. The major Martian geological epochs are derived from the chronostratigraphic map of *Tanaka et al.* (2014). The estimates represented on (a) are given in a color code that corresponds to the elastic thickness value, and are plotted on (b) as a function of age. The dashed lines indicate the errorbarrs for each estimate.

the crust and mantle rheologies that are largely influenced by the water content. Indeed, in the case of a wet mantle rheology the convection is vigorous and efficiently transports the internal heat to the upper layers of the mantle, which implies a thin lithosphere and a fast cooling of the planet. On the contrary, since heat transfers are less efficient in the case of a dry mantle rheology, the upper layers are colder and a thick lithosphere is present at the surface. To explain the very low Noachian elastic thickness estimates, *Grott and Breuer* (2008b) has thus invoked a wet mantle rheology, the dry mantle rheology leading to too large elastic thickness values. On the other hand, *Grott and Breuer* (2008b) and *Guest and Smrekar* (2007) have explained the potential rapid increase of elastic thickness estimates during the Hesperian-Early Amazonian (see Figure 2.3b) by a weak wet crustal rheology. Indeed, in this case an incompetent crustal layer is more likely present at the beginning of the evolution and then vanishes during the lithosphere cooling, which leads to a jump in the total elastic thickness when the crustal and mantle competent layers get coupled. Another alternative explanation might be a transition from an early rheologically wet mantle to a dry one by extraction of volatile elements through volcanism and crust formation (*Guest and Smrekar*, 2007).

But what remains unexplained is the large difference between the two present-day elastic thickness estimates, that means 161 km below the southern polar cap (*Wieczorek*, 2008) and $>$ 300 km below the northern one (*Phillips et al.*, 2008) (see Figure 2.3b). Moreover, such a large global present-day value of 300 km is especially hard to reach without making strong assumptions on the mantle volatile content, the crustal thickness, the radioelement content as well as its vertical distribution between the crust and the mantle (*Grott and Breuer*, 2009; *Plesa et al.*, 2016). Indeed, if a wet mantle rheology is assumed, a sub-chondritic bulk radioelement content is required (*Phillips et al.*, 2008; *Grott and Breuer*, 2009), which is hardly compatible with the concentrations given by meteorite analysis. Furthermore, such a low radioelement content would lead to too low present-day Martian temperatures and prevent recent volcanic emissions, contrary to what is observed (*Grott and Breuer*, 2009). On the other hand, if a present-day dry mantle rheology might be more conciliable with the high value of *Phillips et al.* (2008) below the northern polar cap, it is hardly consistent with the low Noachian estimates. As for the rapid increase of the elastic thickness between the Noachian and the early Amazonian, a potential explanation might be a transition from a wet mantle rheology to a latter dry one (*Morschhauser et al.*, 2011). However, though Mars is today a stagnant lid planet, spatial heterogeneities of the elastic thicknesses probably exist and the high value below the northern polar cap is perhaps not representative of the entire planet (*Phillips et al.*, 2008; *Grott and Breuer*, 2010). Such spatial differences of elastic thickness could be due to heterogeneities in the thermal structure and thickness of the lithosphere across the planet, resulting either from the presence of mantle plumes that decrease the thickness of the lithosphere over geological time-scale (*Kiefer and Li*, 2009; *Grott and Breuer*, 2010; *Plesa et al.*, 2016), or from lateral variations of the crustal properties (thickness, enrichment in radioelements, thermal conductivity). However, even when using 3-D models that account for lateral variations in crustal thickness and the presence of mantle plumes and downwellings, large values $>$ 300 km remain especially hard to reach below the northern polar cap (*Plesa et al.*, 2016).

# 4 Some outstanding questions

If during the past decades significative progresses have been realized on our understanding of Mars's thermal evolution, some problematics remain. A non-exhaustively list is summarized below.

— **How can mantle reservoirs be preserved since the beginning of Mars's evolution ?**
Geochemical analysis of the SNC meteorites shows the existence of three to four separate and isotopically distinct silicate reservoirs on Mars (*Lee and Halliday*, 1997; *Brandon et al.*, 2000; *Foley et al.*, 2005), which have been preserved over the entire evolution (*Jagoutz*, 1991; *Papike et al.*, 2009). Two of those reservoirs are depleted in incompatible elements and are most likely located in the mantle, whereas the third one is, on the contrary, enriched and probably situated in the crust (*Foley et al.*, 2005). The volcanic history suggests the persistence of mantle plumes during at least a large part of Mars's evolution (see section 3.3.b). But how to preserve the reservoirs, especially the two separate mantle ones, if there is an efficient mantle mixing by convection ? A solution might be to have a mantle reservoir located in the lithosphere that is thus not recycled into the convecting mantle. However, this implies a significant lithosphere thickness from the very early evolution : is it consistent with the low Noachian elastic lithosphere thickness estimates ?

— **How was Tharsis formed ?**
It is today widely accepted that Tharsis formation results from the existence of a long-term mantle plume that remained stable for at least during 3 Gyr (section 3.3.b). If the models of *Zhong* (2009) and *Šrámek and Zhong* (2010) provide a plausible explanation for such a stabilization, the mechanism that they propose raise some issues. Indeed, in their models the presence of an initial hemispheric thickened keel of lithosphere is required to stabilize the plume at the transition zone between the lowlands and the highlands. But how could such an early hemispheric thickened keel have formed ? Is it directly related to the dichotomy formation as argued by *Šrámek and Zhong* (2010) or *Citron et al.* (2018) ? Moreover, is this thickened lithosphere consistent with the low Noachian elastic thickness estimates in the southern hemisphere ?

— **How to explain the elastic lithosphere thickness evolution ?**
The evolution of the Martian elastic thickness estimates raises fundamental challenges for thermal models (see section 3.4.c). Indeed, on one hand the low Noachian values are rather explained by a wet mantle rheology (*Grott and Breuer*, 2008b), whereas, on the other hand, the present-day large value $>$ 300 km estimated below the northern polar cap by *Phillips et al.* (2008) is more consistent with a rheologically dry mantle. But even in this case, strong assumptions have to be made on the radioelement content and its vertical distribution (*Grott and Breuer*, 2009). In this context, how can such a large value $>$ 300 km become consistent with thermal models ? And, moreover, can we reconcile this large value with the low Noachian estimates ?

— **What is the influence of the vertical distribution of the radioelements on Mars's thermal evolution ?**
If the effects of the bulk radioelement content on Mars's thermal evolution have often been investigated (e.g. *Grott and Breuer*, 2008a, 2009; *Sekhar and King*, 2014), only a few studies have considered the consequences of potential vertical and lateral variations in radioelement distribution. However, such variations may have large implications for Mars's thermal evolution and, therefore, on the elastic lithosphere thickness evolution, as well as on the magnitude of past and recent volcanism (*Sekhar and King*, 2014). But, how can we constrain the vertical and lateral partitioning of the radiolements given the lack of heat flow measurements and the small number of samples (see chapter 1, section 3.2) ?

## 5 PhD motivations

In the view of recent insights on crustal properties (see chapter 1, section 3), lateral and vertical variations in the distribution of radioelements related to the north/south dichotomy might exist and must be investigated. Indeed, a potentially large felsic component might be buried in the southern crust (*Belleguic et al.*, 2005; *Pauer and Breuer*, 2008; *Carter and Poulet*, 2013; *Wray et al.*, 2013; *Baratoux et al.*, 2014; *Sautter et al.*, 2015; *Sautter et al.*, 2016), which could imply a difference in radioelement enrichment compared to the northern crust (see chapter 1, section 3.2). Moreover, other potential differences in crustal thickness (e.g. *Wieczorek*, 2007) or thermal conductivity (*Bandfield et al.*, 2013) related to the dichotomy have also to be investigated. Considering the constraints that we have on the thermal evolution of Mars (volcanic history and elastic thickness estimates), can we determine if the dichotomy is associated to such north/south distinct crustal properties and, in the positive case, which ones ? And as a corollary, what are the consequences of such a dichotomy in crustal properties on the thermal evolution and structure of the planet ?

To answer these questions, 3-D dynamical thermal models being too time-consuming to investigate a large range of crustal parameters, we will derive in chapter 3 appropriate scaling laws for 1-D parametrized thermal models when considering cooling planets in a stagnant lid regime, like Mars. In chapter 4, we will adapt this 1-D model by considering distinct crustal properties for the two Martian hemispheres and determine which of those crustal properties can well fit the constraints that we have on Mars's thermal history (elastic thickness evolution, recent volcanism). The InSight mission being predicted to land on Mars in November 2018, we will discuss the implications of our best crustal models on the measured heat flux value by the heat flow probe $HP^3$. Finally, we will investigate the implications of our favored models on the seismic signals that will be measured by the seismometer *SEIS*, in particular, on surface wave propagation and dispersion in chapter 5.

# CHAPTER 3

# SCALING LAWS OF CONVECTION

## Sommaire

# 1 Summary

Since 3-D thermal models are too time-consuming to perform the extensive parameter study required to investigate which properties of the northern and southern crusts are compatible with the constraints on Mars's thermal evolution, we have to run 1-D thermal models. However, scaling laws used in 1-D parametrized thermal models to describe the cooling of planets have mainly been derived from convection models with a constant heating. Here, fully dynamic models are performed for terrestrial planet conditions - strong temperature-dependent viscosity, mixed heating mode with radioelement decay, spherical geometry - and compared with parametrized models to derive scaling laws valid for their entire evolution.

In planetary mantles, the thicknesses of the stagnant lid and the upper thermal boundary layer (TBL) must be determined accurately, as they influence the heat transport out of the underlying mantle. In scaling laws derived from a boundary layer stability analysis, the upper TBL thickness depends on the Rayleigh number to the power $\beta^u$, while the lid base temperature is often determined from the mantle temperature and the rate of viscosity change with temperature multiplied by a prefactor $a_{rh}$. In Monte Carlo simulations, by ranging $\beta^u$ and $a_{rh}$, we find that, although the heating conditions change as a function of time, the thermal evolution of a cooling planet in a stagnant lid regime can be represented by one set of parameters. Suitable fits are found for different values of $a_{rh}$ and $\beta^u$ that vary depending on the model parameters, such as the thickness of the convecting layer, the surface temperature, the initial mantle temperature and the viscosity parameters. The observed relationship between suitable values of $a_{rh}$ and $\beta^u$ is explained by a trade-off between the lid and the TBL thicknesses. When considering a specific definition of the stagnant lid thickness in Mars's 3-D simulation, a best combination of $a_{rh} = 2.16$ and $\beta^u = 0.345$ is found for a stagnant lid defined by the intersection between the depth axis and the tangent to the velocity profile at the depth corresponding to the maximum velocity gradient. This combination remains valid when varying some critical parameters such as mantle aspect ratio, surface and internal temperatures, presence of a crust or pressure-dependence of the viscosity.

# 2 Motivation

To find which parameters of the northern and southern crusts (thickness, density, thermal conductivity and enrichment in radioelements) can fit the available constraints on Mars's thermal evolution (elastic lithosphere thickness evolution, recent volcanism...), a large number of thermal models is required. While 3-D dynamical thermal models are most appropriate for studies of mantle convection in the terrestrial planets, they require a considerable computational time, too large to perform such an extensive parameter study. On the other hand, if 2-D dynamical models of mantle convection represent an attractive alternative because of their lower computational time, they generally underestimate the planetary cooling rate (*Plesa et al.*, 2015). In this context, 1-D parametrized models have long been used to reconstruct the thermal history of terrestrial planets (e.g. *Sharpe and Peltier*, 1978; *Schubert et al.*, 1979; *Stevenson et al.*, 1983; *Schubert et al.*, 2001; *Grott and Breuer*, 2008b; *Morschhauser et al.*, 2011). In such models, the physics of the convection is collapsed into a single scaling law relating the non-dimensional Rayleigh number - $Ra$, which represents a measure of the convection vigor - to the heat flux (*Townsend*, 1964), with the aim of reproducing the average thermal evolution of the 3-D convective model and experiments.

However, in terrestrial planets in a stagnant lid regime, the pattern of mantle convection is not imposed by plate tectonics and depends on several parameters that are poorly constrained and, moreover, vary among the different terrestrial planets such as, for instance, the Rayleigh number, the aspect ratio between the core and planetary radius or the heating mode. While the Rayleigh number increases, heat transfer through the mantle is more efficient and the plumes become more numerous and narrower (Figure 3.1a, b and c for $Ra = 10^5$, $Ra = 10^6$ and $Ra = 10^7$ - i.e. close to the typical values of Mercury, the Moon and Mars -, respectively). Similarly, increasing the aspect ratio of the shell results in a stronger bottom heating and the formation of a large number of hot mantle plumes. Therefore, several plumes are present for Mercury's high aspect ratio of 0.8 (Figure 3.1e), whereas a spherical harmonic degree 1 distribution, with only one mantle plume, is observed for a low aspect ratio of 0.3 close to that of the Moon (Figure 3.1d). Finally, the flow pattern is especially sensitive to the relative amount of bottom (from the hot core) and internal heating (due to the decay of radioelements and tidal heating) (e.g. *Travis and Olson*, 1994; *Sotin and Labrosse*, 1999; *McNamara and Zhong*, 2005; *Deschamps et al.*, 2012). For given values of $Ra$ and aspect ratio, increasing the volumetric heating rate reduces the vigor of the hot mantle plumes and results in higher average temperature of the bulk interior (see Figure 3.1a, f, g for bottom heating and non-dimensional internal heating rates of $Ra_Q/Ra = 0$, $Ra_Q/Ra = 10$ and $Ra_Q/Ra = 30$, respectively, with $Ra_Q$ the Rayleigh number for internal heat sources.) (*Labrosse*, 2002; *Deschamps et al.*, 2012).

As illustrated in Figure 3.1, the large uncertainties that we have on the typical parameters of Mars, as well as the strong variations among the terrestrial planets, result in strong variations in the mantle convection pattern. In this context, is it feasible to define a unique scaling law between the Rayleigh number and the heat flux for all those model set-up ? Moreover, does a potential unique scaling law remain valing during the entire planet thermal evolution, since

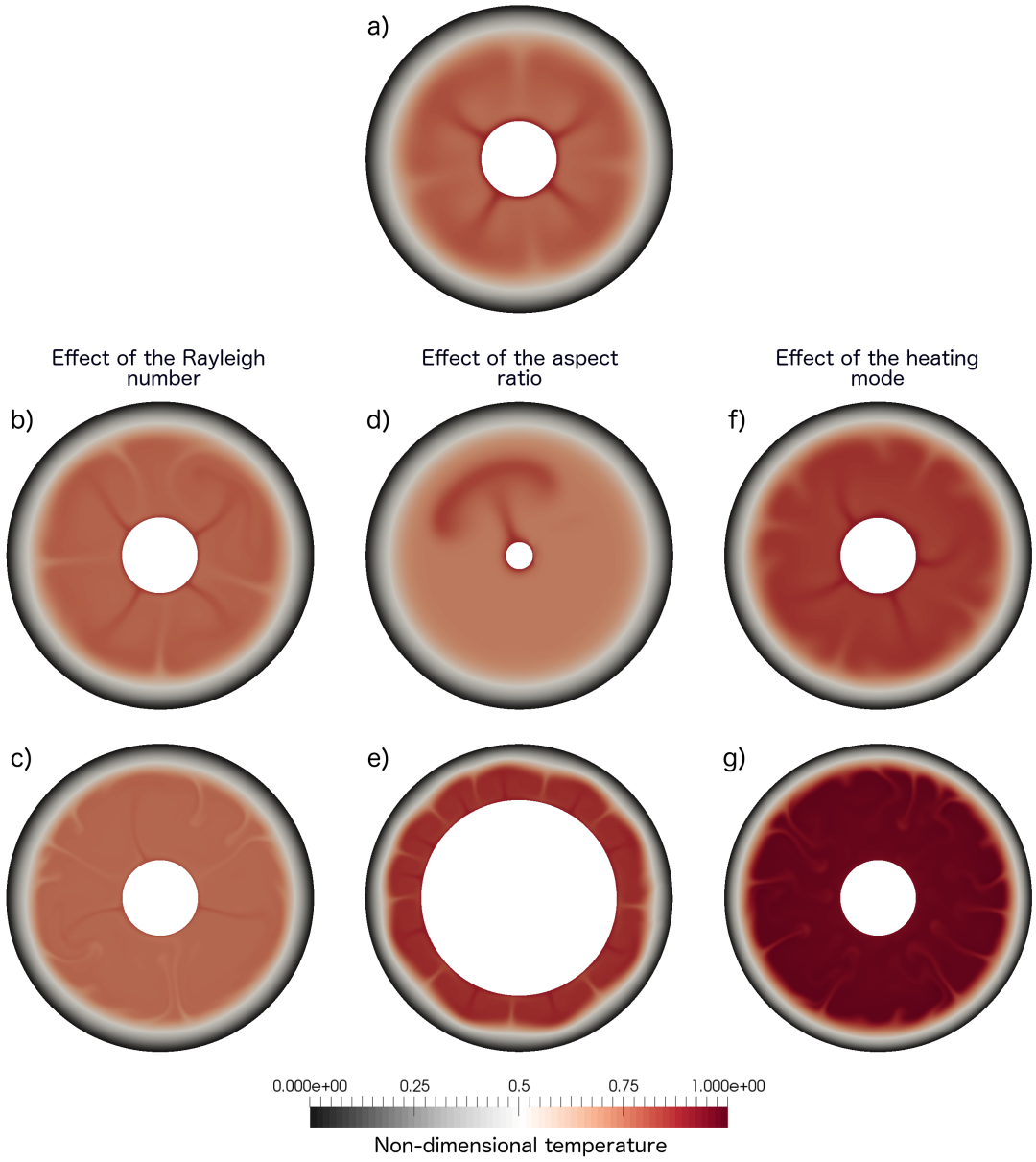


**FIGURE 3.1** – Effect of different parameters on 2-D Mantle convection. The reference 2-D model shown in (a) is in a stagnant lid regime and is characterized by an aspect ratio between the core and planetary radius of 0.5, basal heating from the core and a Rayleigh number of $Ra = 10^5$. From this reference model, we systematically change one parameter to test separately the effect of varying the Rayleigh number in (b) and (c) ($Ra = 10^6$ an $Ra = 10^7$, respectively) and the aspect ratio in (d) and (e) (0.3 and 0.8, respectively). In (a) we only consider basal heating and add internal heating in (f) and (g) with non-dimensional constant internal heating $Ra_Q/Ra = 10$ and $Ra_Q/Ra = 30$, respectively (representative of those observed for Mars at the middle and at the beginning of the evolution). The snapshots are taken after 1 Gyr of evolution, when a steady-state convection is reached. Since the heat flux at the CMB is overestimated for 2-D cylindrical models compared to 3-D spherical models, the ratio between CMB and planetary radius is corrected following *van Keken* (2001) in the Gaia code.

parameters such as the Rayleigh number and the relative amount of bottom and internal heating evolve with time because of planetary cooling and radioelement decay ?

With the aim of investigating the effects of the northern and southern crustal parameters on Mars's thermal evolution with 1-D parametrized models, we define in this chapter appropriate scaling laws for planetary bodies in stagnant lid convection such as Mars, Mercury and the Moon.

# 3 Scaling laws of convection for cooling planets in a stagnant lid regime

This section presents the manuscript that was published in the *Physics of the Earth and Planetary Interior* (*Thiriet et al.*, 2018b). The Annexe and Supplementary Figures have been, however, included in the main text and slight adjustements in the notations have been introduced for a better reading.

## 3.1 Introduction

The thermal evolution of a cooling planet is controlled by the efficiency of mantle convection and, in the case of a stagnant lid regime, by the thickness of its lid, which both vary in time. Highly resolved convection models in 3-D spherical geometry represent thus the most appropriate way to compute planetary thermal evolution as they self-consistently account for temporal as well as spatial variations. Although computational power has largely increased over the past years, such numerical calculations are still extremely time consuming and therefore inappropriate to explore variations of a large set of parameters and physical properties such as different rheological laws, bulk radioelement content or radioelement partition between the crust and mantle. In this context, scaling laws have been largely used in 1-D parametrized models based on heat balance equations for the core and mantle to reconstruct planetary thermal evolution (e.g., *Sharpe and Peltier*, 1978; *Schubert et al.*, 1979; *Davies*, 1980; *Turcotte and Schubert*, 1982; *Stevenson et al.*, 1983; *Schubert and Spohn*, 1990; *Hauck and Phillips*, 2002; *Grott and Breuer*, 2008b; *Morschhauser et al.*, 2011; *Deschamps et al.*, 2012).

The viscosity of mantle silicate strongly depends on temperature and, to a lesser extent, on pressure. If the viscosity contrast across the mantle is high enough ($> 10^4$, *Solomatov*, 1995), laboratory experiments (*Booker and Stengel*, 1978; *Richter et al.*, 1983; *Davaille and Jaupart*, 1993) and numerical models (*Christensen*, 1984; *Ogawa et al.*, 1991; *Moresi and Solomatov*, 1995; *Solomatov*, 1995) all show the formation of a rigid and cold stagnant lid at the surface, where heat transfer occurs solely by conduction. The temperature increase across the stagnant lid leads to a drop in viscosity of several orders of magnitude, while in the convection layer below the lid the viscosity varies only by about one order of magnitude and is almost isoviscous (e.g., *Nataf and Richter*, 1982; *Morris and Canright*, 1984; *Fowler*, 1985; *Davaille*

*and Jaupart*, 1993, 1994; *Solomatov*, 1995). In the case of basal or mixed heating, two thermal boundary layers (TBL) are present, one at the bottom of the convecting layer and another one at its top, below the stagnant lid. The lower and upper TBLs thicken by conduction until they reach a critical thickness and, then, destabilize into hot mantle plumes and cold downwellings, respectively (*Howard*, 1966). When a stagnant lid develops, or in the case of significant internal heating, the dynamics of the upper TBL largely controls the mantle thermal evolution.

Two different approaches for the parametrization of heat transport in the stagnant lid regime with a strongly temperature-dependent viscosity can be used. In the first approach (e.g., *Solomatov*, 1995; *Moresi and Solomatov*, 1995; *Reese et al.*, 1999), a scaling law for the heat flow or so-called Nusselt number, $Nu$, is derived for the whole layer, i.e., the convecting part and the stagnant lid. The Nusselt number at the surface is then defined as (e.g., *Solomatov and Moresi*, 2000) :

$$Nu_{surf} = \frac{q_s}{k\frac{\Delta T}{D}} = a\theta^{-\gamma} Ra_i^{\beta_t} \tag{3.1}$$

where $q_s$ is the surface heat flux, $D$ the shell thickness, $\Delta T$ the temperature difference across the shell and $k$ the thermal conductivity. $a$, $\gamma$ and $\beta_t$ are constants and $\theta$ is the Frank-Kamenetskii parameter, which is the natural logarithm of the viscosity contrast across the mantle

$$\theta = ln(\Delta\eta) \tag{3.2}$$

$Ra_i$ is the internal Rayleigh number :

$$Ra_i = \frac{\rho_m g \alpha \Delta T D^3}{\eta\kappa} \tag{3.3}$$

where $\alpha$ is the thermal expansion coefficient, $\rho_m$ the mantle density, g gravity, $\kappa$ the mantle thermal diffusivity and $\eta$ the viscosity.

In the second approach, the mantle is divided into a convecting layer and a stagnant lid on top (e.g., *Davaille and Jaupart*, 1993; *Grasset and Parmentier*, 1998). A scaling law is determined for the heat flow from the convecting layer into the lid, which is similar to the scaling of a flow with constant viscosity :

$$Nu_m = \frac{q_m}{k\frac{\Delta T_{conv}}{D_{conv}}} = a_m Ra^{\beta_m} \tag{3.4}$$

where $q_m$ is the heat flux through the upper TBL, $a_m$ and $\beta_m$ are constants, and Ra is the Rayleigh number of the convecting mantle :

$$Ra = \frac{\rho_m g \alpha \Delta T_{conv} D_{conv}^3}{\eta\kappa} \tag{3.5}$$

$D_{conv}$ is the thickness of the convecting layer and $\Delta T_{conv}$ is the temperature difference across the convecting part of the mantle.

Using experiments on a cooling convecting fluid with a stagnant lid, *Davaille and Jaupart* (1993) have demonstrated that the temperature difference across the upper TBL is proportional to a viscous temperature scale $\Delta T_\nu$ that represents the rate of viscosity change with temperature and that is equivalent to the inverse of the Frank-Kamenetskii parameter in the case of an Arrhenius type rheology :

$$\Delta T_{rh} = -a_{rh} \frac{\eta(T_m)}{d\eta/dT|_{T_m}} = a_{rh} \Delta T_\nu \tag{3.6}$$

where $a_{rh}$ is a coefficient of proportionality. During the major part of planetary evolution $\Delta T_{conv} \sim \Delta T_{rh}$ since the temperature difference across the lower TBL is negligible compared to that across the upper TBL. To obtain the thermal structure and surface heat flow of the coupled system, i.e. the convecting mantle and the lid, the thickness of the stagnant lid is determined by equating the heat flux through the conductive lid to the heat flux from the underlying convecting layer into the lid.

The values of $\beta$ obtained for the above-mentioned scaling laws depend on the approach and can be as low as $\beta_t = 0.2$ for the first whole-layer approach (*Reese et al.*, 1999; *Deschamps and Sotin*, 2000) while for the second approach the value of $\beta_m$ is often found to be close to $1/3$ (e.g., *Davaille and Jaupart*, 1993). However, for both approaches, the different constants $a/a_m$, $\gamma$ and $\beta$ depend on the model set-up and heating mode, which evolves during planetary thermal history. It is therefore not obvious if constant values of the scaling parameters could satisfactorily fit 3-D thermal models over the entire evolution of a planet.

In the case of an isoviscous fluid in a Cartesian geometry, the boundary layer stability analysis predict a value $\beta_m = 1/3$ and convection models show a value close to $1/3$ for free slip boundary conditions (e.g., *Christensen*, 1984; *Hansen and Yuen*, 1993; *Deschamps and Sotin*, 2000). The value of $\beta_m$ is smaller, i.e., $\beta_m = 0.25$ for rigid boundary conditions (e.g., Table 1 of *Deschamps and Sotin*, 2000). Similarly, for a temperature dependent viscosity, the value of $\beta_t$, as well as that of $a$, seem to depend on the model set-up : model geometry (Cartesian box or spherical shell) (*Vangelov and Jarvis*, 1994; *Jarvis et al.*, 1995; *Iwase and Honda*, 1998; *Reese et al.*, 1999, 2005; *Shahnas et al.*, 2008; *Wolstencroft et al.*, 2009) or heating mode (basal, internal or mixed heating) (*Morris and Canright*, 1984; *Grasset and Parmentier*, 1998; *Dumoulin et al.*, 1999; *Sotin and Labrosse*, 1999; *Reese et al.*, 2005). For instance, values as low as $\beta_t = 1/5$ in association with $\gamma \sim 1$ have been proposed for stagnant lid convection (*Fowler*, 1985; *Reese et al.*, 1998) and likely correspond to a steady-state regime of convection (*Dumoulin et al.*, 1999). In the time-dependent oscillatory regime, that is more appropriate to describe stagnant lid mantle convection of a cooling planet, values of $\beta_t \sim 1/3$, consistent with the boundary layer stability analysis and associated to $\gamma = 1 + \beta_t$ have been favoured both for numerical simulations (*Doin et al.*, 1997; *Grasset and Parmentier*, 1998; *Trompert and Hansen*, 1998; *Dumoulin et al.*, 1999) and laboratory experiments (*Davaille and Jaupart*, 1993). However, discrepancies remain between the scaling laws that have been derived for time-dependent convection that could partially be due to different model conditions (e.g., *Grasset and Parmentier*, 1998)

and to intermediate convection regime between steady-state and fully time-dependent (*Trompert and Hansen*, 1998). Therefore, extensive work has been made to determine appropriate values of $\beta$ and $a/a_m$ for different model set-up.

In the present study, we consider the scaling law for the heat flow through the upper TBL into the lid and determine separately the temperature profile and thickness of the stagnant lid. The separation of the convective mantle from the stagnant lid is more practical if considering different thermal properties for the crust and mantle. The other scaling approach that accounts for the entire system is more problematic because, for instance, inhomogeneous distribution of heat sources between mantle and crust cannot self-consistently be accounted for.

We search for an appropriate set of values for the scaling parameters $\beta_m$ and $a_{rh}$ by comparing, in Monte Carlo simulations, the thermal evolution predicted by 1-D parametrized convection models using such scaling laws with those of reference 3-D models in spherical geometry. We employ realistic terrestrial planetary conditions using a fluid with a strongly temperature-dependent viscosity, heated from the core and by decaying sources and undergoing secular cooling. Our models start with a superheated core. The initial temperature difference at the core-mantle boundary (CMB) is reduced during the thermal evolution and the heating conditions change from bottom to mainly internal heating as a function of time. Nevertheless, we show that the entire thermal evolution can be represented by a range of combinations of the scaling parameters $\beta_m$ and $a_{rh}$ and provide a best fit valid for all the terrestrial planets considered here (Mars, the Moon and Mercury).

## 3.2 Modeling

### 3.2.a 2-D and 3-D mantle convection models

Fully dynamical models are the best way to compute the thermal evolution of a terrestrial planet and are used as reference models. We employ the finite-volume code Gaia in 3-D spherical and 2-D cylindrical geometry (*Hüttig and Stemmer*, 2008; *Hüttig et al.*, 2013) with free-slip boundary conditions at the top and bottom, and consider an incompressible, Boussinesq fluid

| Planet | U [ppb] | Th [ppb] | K [ppm] | $Q_0$ [pW kg$^{-1}$] | $Q_{4.5}$ [pW kg$^{-1}$] | Model |
|---|---|---|---|---|---|---|
| Mars | 16 | 56 | 305 | 23 | 4 | *Wänke and Dreibus* (1994) |
| Moon | 33 | 125 | 83 | 25 | 7 | *Taylor* (1982) |
| Mercury | 28 | 50 | 400 | 33 | 5 | *Tosi et al.* (2013) |

**TABLE 3.1** – Models for radioelement concentration in the primitive mantle of Mars, the Moon and Mercury. $Q_0$ and $Q_{4.5}$ correspond to initial and present-day rates of internal heating by radioelement decay.

with Newtonian rheology and infinite Prandtl number. The following non-dimensional conservation equations of mass, linear momentum, and thermal energy are thus solved (*Christensen and Yuen*, 1985) :

$$\nabla \cdot \vec{v} = 0 \tag{3.7}$$

$$\nabla \cdot \left[\eta'(\nabla\vec{v} + (\nabla\vec{v})^T)\right] - \nabla p + Ra_i T \vec{e}_r = 0 \tag{3.8}$$

$$\frac{DT}{Dt} = \nabla^2 T + \frac{Ra_Q}{Ra_i} \tag{3.9}$$

where $\vec{v}$ is the velocity vector, $T$ the temperature, $p$ the dynamic pressure, $t$ the time, $\eta'$ the viscosity, all made dimensionless, $\vec{e}_r$ is the radial unit vector. The temperature scale is the temperature drop across the shell $\Delta T$ at the beginning of the simulations, the length scale is the thickness of the shell $D$ and the time scale is the diffusive time $D^2/\kappa$.

An Arrhenius law for diffusion creep is used to compute the viscosity $\eta$ as a function of temperature (*Karato and Wu*, 1993) :

$$\eta(T) = \eta_0 \exp\left[\frac{A}{R}\left(\frac{1}{T} - \frac{1}{T_{ref}}\right)\right] \tag{3.10}$$

where $A$ is the activation energy, $R$ the gas constant and $T_{ref} = 1600$ K the reference temperature at which a reference viscosity $\eta_0$ is reached. A dry mantle rheology with the reference viscosity $\eta_0 = 1 \times 10^{21}$ Pa s is used in our reference case for Mars (*Mars1*), the Moon (*Moon1*) and Mercury (*Mercury1*), though we also test the effect of weaker rheologies (*Karato and Wu*, 1993) with $\eta_0 = 1 \times 10^{20}$ Pa s. The activation energy $A$ depends on the dominant deformation mechanism in the mantle. We use a value of 300 kJ mol$^{-1}$ representative of diffusion creep (*Karato and Wu*, 1993) and test the effect of a higher activation energy $A = 450$ kJ mol$^{-1}$ as well as a lower one $A = 150$ kJ mol$^{-1}$. The latter is used to mimic dislocation creep by dividing the activation energy by the stress exponent $n$ (*Christensen*, 1983).

| Parameter | Notation | Value | Unit |
|---|---|---|---|
| Reference temperature | $T_{ref}$ | 1600 | K |
| Critical Rayleigh number | $Ra^u_{crit}$ | 450 | |
| Core density | $\rho_c$ | 7200 | kg m$^{-3}$ |
| Mantle thermal conductivity | $k$ | 4 | W m$^{-1}$ K$^{-1}$ |
| Mantle thermal diffusivity | $\kappa$ | $1 \times 10^{-6}$ | m$^2$ s$^{-1}$ |
| Mantle heat capacity | $C_m$ | 1142 | J kg$^{-1}$ K$^{-1}$ |
| Core heat capacity | $C_c$ | 840 | J kg$^{-1}$ K$^{-1}$ |
| Thermal expansion coefficient | $\alpha$ | $2.5 \times 10^{-5}$ | K$^{-1}$ |
| Gas constant | $R$ | 8.3144 | J K$^{-1}$ mol$^{-1}$ |

**TABLE 3.2** – Parameters that are constant in all simulations.

| Case | Geometry | $R_p$ [km] | $R_c$ [km] | $T_s$ [K] | $T_{m_0}$ [K] | $T_{c_0}$ [K] | $\eta_0$ [Pa s] | $A$ [kJ mol$^{-1}$] | $g^u$ [m s$^{-2}$] | $\rho_m$ [kg m$^{-3}$] | $\beta^u$ | $a_{rh}$ |
|---|---|---|---|---|---|---|---|---|---|---|---|---|
| 3-D reference models | | | | | | | | | | | | |
| *Mars1* | 3-D | 3400 | 1700 | 250 | 1750 | 2250 | $10^{21}$ | 300 | 3.7 | 3500 | 0.345 [0.332 – 0.360] | 2.16 [2.25 – 2.00] |
| *Moon1* | 3-D | 1740 | 390 | 250 | 1750 | 2000 | $10^{21}$ | 300 | 1.6 | 3300 | 0.346 [0.331 – 0.355] | 2.44 [2.55 – 2.35] |
| *Mercury1* | 3-D | 2440 | 2010 | 440 | 1750 | 2000 | $10^{21}$ | 300 | 3.7 | 3500 | 0.349 [0.339 – 0.362] | 2.56 [2.60 – 2.51] |
| Best combination | | | | | | | | | | | 0.335 [0.313 – 0.342] | 2.54 [2.63 – 2.38] |
| 2-D models (parameter study) | | | | | | | | | | | | |
| *Mars2* | 2-D | 3400 | 1700 | 250 | 1750 | 2250 | $10^{21}$ | 300 | 3.7 | 3500 | 0.316 [0.309 – 0.329] | 2.47 [2.62 – 2.32] |
| *PS1* | 2-D | 3400 | 2840 | 250 | 1750 | 2250 | $10^{21}$ | 300 | 3.7 | 3500 | 0.298 [0.292 – 0.310] | 2.54 [2.63 – 2.45] |
| *PS2* | 2-D | 3400 | 1100 | 250 | 1750 | 2250 | $10^{21}$ | 300 | 3.7 | 3500 | 0.307 [0.303 – 0.325] | 2.54 [2.58 – 2.33] |
| *PS3* | 2-D | 3400 | 1500 | 250 | 1750 | 2250 | $10^{21}$ | 300 | 3.7 | 3500 | 0.317 [0.308 – 0.330] | 2.48 [2.63 – 2.34] |
| *PS4* | 2-D | 3400 | 1700 | 450 | 1750 | 2250 | $10^{21}$ | 300 | 3.7 | 3500 | 0.307 [0.298 – 0.314] | 2.60 [2.75 – 2.47] |
| *PS5* | 2-D | 3400 | 1700 | 750 | 1750 | 2250 | $10^{21}$ | 300 | 3.7 | 3500 | 0.289 [0.281 – 0.300] | 2.88 [3.05 – 2.80] |
| *PS6* | 2-D | 3400 | 1700 | 250 | 1750 | 2000 | $10^{21}$ | 300 | 3.7 | 3500 | 0.304 [0.296 – 0.320] | 2.65 [2.73 – 2.48] |
| *PS7* | 2-D | 3400 | 1700 | 250 | 1850 | 2250 | $10^{21}$ | 300 | 3.7 | 3500 | 0.313 [0.309 – 0.328] | 2.49 [2.60 – 2.32] |
| *PS8* | 2-D | 3400 | 1700 | 250 | 1750 | 2250 | $10^{20}$ | 300 | 3.7 | 3500 | 0.311 [0.304 – 0.322] | 2.64 [2.78 – 2.48] |
| *PS9* | 2-D | 3400 | 1700 | 250 | 1750 | 2250 | $10^{21}$ | 150 | 3.7 | 3500 | 0.334 [0.325 – 0.335] | 1.82 [1.89 – 1.82] |
| *PS10* | 2-D | 3400 | 1700 | 250 | 1750 | 2250 | $10^{21}$ | 450 | 3.7 | 3500 | 0.312 [0.298 – 0.334] | 2.85 [3.19 – 2.49] |
| Best combination | | | | | | | | | | | 0.319 [0.304 – 0.340] | 2.47 [2.70 – 2.25] |

**TABLE 3.3** – Parameters considered in dynamical thermal models. 3-D reference models for Mars, the Moon and Mercury correspond to the three first lines, whereas other cases are used for parameter study in section 3.3.d by varying at each time one parameter from the reference 2-D case of Mars, *Mars2*. $R_p$ is the planetary radius, $T_{m_0}$ and $T_{c_0}$ correspond to the initial mantle and CMB temperatures of the start-up simulations with no internal heating. The best combinations of $\beta^u$ and $a_{rh}$ are indicated for each model set-up. They correspond to the best fit between 1-D parametrized models and 2-D/3-D simulations when comparing the temperature profiles, the CMB and surface heat flux, and the temperature at the base of the lid. Here, this latter is defined by the intersection between the tangent to the velocity profile at the depth corresponding to the maximum velocity gradient and the radius axis (see Figure 3.7). The best combination for the 3-D reference models corresponds to the lowest error for all the planets (Mars, the Moon and Mercury) when summing their Monte Carlo simulations (see Figure 3.14b). The best combination for the 2-D models is that which shows the lowest cumulative error when summing all the Monte Carlo results of the 2-D models (see Figure 3.9g). For each case the range of suitable values of $\beta^u$ and $a_{rh}$ are indicated in square brackets and correspond to the combinations that show an additional error $< 10$ % compared to the best combination. Note that the ranges of $a_{rh}$ values are in decreasing order to match their corresponding values of $\beta^u$.

The Rayleigh-Roberts number based on internal heating rate $Q$ is given by :

$$Ra_Q(Q,t) = \frac{\rho_m^2 g \alpha Q D^5}{\eta k \kappa} \tag{3.11}$$

The internal heating rate $Q$ produced by radioelement decay decreases with time and is computed from the compositional models of *Wänke and Dreibus* (1994) for Mars, *Taylor* (1982) for the Moon and *Tosi et al.* (2013) for Mercury (see Table 3.1).

Since the shell is also heated from below by the core, we adopt a cooling condition at the CMB. The core is assumed adiabatic with a constant density and heat capacity, which allows to calculate the evolution of the CMB temperature $T_c$ using a one-dimensional energy balance for the core (e.g. *Ke and Solomatov*, 2009) :

$$\rho_c C_c V_c \frac{dT_c}{dt} = -q_c A_c \tag{3.12}$$

where $\rho_c$, $C_c$, $V_c$ and $A_c$ are respectively the density, heat capacity, volume and area of the core. $q_c$ is the heat flux at the CMB. The values of all the parameters used in equations 3.8-3.12 are listed in Tables 3.2 and 3.3.

We verify that all our simulations are in the stagnant lid regime, which has been proposed to be characterized by a small nondimensional surface velocity ($< 1$) as well as a ratio $< 0.01$ between the surface velocity and that in the well-mixed interior (e.g., *Tackley*, 2000; *Stein et al.*, 2013; *Guerrero et al.*, 2018).

### 3.2.b Parametrized convection model

We compare the results of 2-D/3-D calculations with that of a 1-D parametrized convection model similar to that of *Grott and Breuer* (2008b) except that we use a time-dependent heat

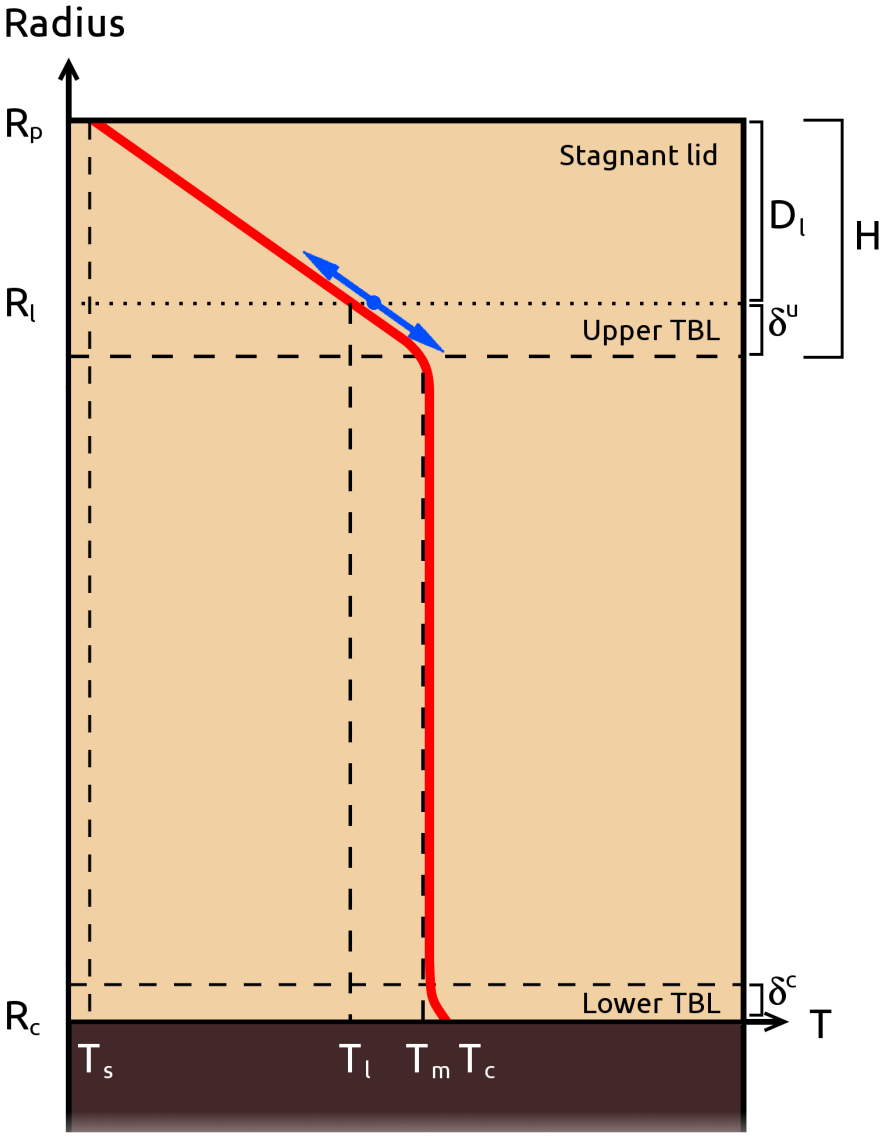


**FIGURE 3.2** – Sketch of the parametrized model set-up used in this study (not to scale), where the upper thermal boundary layer (TBL), located below the rigid stagnant lid that does not participate to convection, destabilizes into cold downwellings (e.g. *Davaille and Jaupart*, 1993; *Grasset and Parmentier*, 1998). In the case of basal heating, hot mantle plumes are formed by the destabilization of the lower TBL at the CMB. A phenomenological temperature profile is indicated in red. The absence of a clear distinction between the upper TBL and the stagnant lid in 3-D models is symbolized by the blue arrow, indicating that the limit in between those two layers (black spotted line) can move along the temperature profile.

conduction equation in the lid rather than a steady-state one. Temperature variations are mostly observed in the TBLs (including the stagnant lid), whereas the rest of the mantle is well mixed (see Figure 3.2) : mantle heat transfer is thus mainly controlled by the thicknesses of these layers for which appropriate scaling laws have to be used.

Starting from the initial temperature profil of our 3-D reference model, we compute the thermal evolution up to the present-day by solving the energy balance equations for the core, the mantle and the stagnant lid. Energy conservation for the core is given by equation 3.12, where the heat flux conceded by the core to the mantle $q_c$ is given by :

$$q_c = k\frac{T_c - T_m}{\delta^c} \tag{3.13}$$

where $\delta^c$ is the thickness of the lower TBL.

In parallel to the heat provided by the core, the energy balance for the mantle also depends on the internal heat production rate by radioelement decay, $Q$, and on the heat that is conceded by the mantle to the base of the stagnant lid $q_m$ :

$$\rho_m C_m V_m \frac{dT_m}{dt} = q_c A_c - q_m A_m + Q(t)V_m \tag{3.14}$$

where $C_m$ is the heat capacity of the mantle, $A_m$ the surface area at the lid-mantle boundary and $V_m$ the volume of the convecting mantle. $q_m$ corresponds to the conductive heat flux through the upper TBL and is computed using

$$q_m = k\frac{T_m - T_l}{\delta^u} \tag{3.15}$$

with $\delta^u$ the thickness of the upper TBL and $T_l$ the temperature at the base of the lid.

The heat production rate is computed from :

$$Q(t) = \sum_i Q_i exp(-\lambda_i t) \tag{3.16}$$

where the sum extends over the four long-period radiogenic species - $^{40}K$, $^{232}Th$, $^{235}U$ and $^{238}U$ - which have a specific initial heating rate $Q_i$ and a decay constant $\lambda_i$.

The rate of stagnant lid growth is computed using an energy balance at the base of the lid that depends on the heat provided by the convecting mantle and the heat which is conducted away towards the surface :

$$\rho_m C_m (T_m - T_l)\frac{dD_l}{dt} = -q_m - k\left.\frac{\partial T}{\partial r}\right|_{r=R_l} \tag{3.17}$$

where $D_l$ is the stagnant lid thickness and $r$ the radial distance. We consider a time-dependent heat conduction equation in the lid, which is more appropriate for the thick stagnant lids of Mars, Mercury and the Moon (*Michaut and Jaupart*, 2004) :

$$\rho_m C_m \frac{\partial T}{\partial t} = \frac{1}{r^2}\frac{\partial}{\partial r}\left(r^2 k \frac{\partial T}{\partial r}\right) + Q(t) \tag{3.18}$$

To solve this equation in the case of a moving lower boundary, we introduce a change of variable $r = R_p - yD_l$. In the framework of an implicit numerical scheme, this allows to keep a fixed number of grid points between two fixed boundaries $y = 0$ and $y = 1$ for all time steps.

For time-dependent convection, the boundary layer stability analysis provides the theoretical background for TBL thickness computation (*Turcotte and Schubert*, 2002) :

$$\delta^{u,c} = (R_l - R_c)\left(\frac{Ra^{u,c}_{crit}}{Ra^{u,c}_{rh}}\right)^{\beta^{u,c}} \tag{3.19}$$

where $R_l$ is the radius of the stagnant lid base, $R_c$ is the core radius and the subscript $u, c$ denotes the upper TBL or lower core TBL, respectively. For simplicity, we drop the index $m$ in $\beta$ the scaling parameter for the heat flow through the upper TBL into the lid. $Ra^{u/c}_{rh}$ is given by :

$$Ra^{u/c}_{rh}(T) = \frac{\alpha \rho_m g^{u/c} \Delta T^{u/c} (R_l - R_c)^3}{\kappa \eta(T^{u/c})} \tag{3.20}$$

In $Ra^{u}_{rh}$, since we do not consider the adiabatic temperature increase in 2-D and 3-D models, we use $\Delta T^u = T_c - T_l$, the surface gravity $g^u$ and the viscosity at the temperature $T_m$ at the top of the convecting mantle. Note that $\Delta T^u \sim T_m - T_l$ as the temperature difference across the lower TBL is negligible during the major part of planetary evolution compared to that across the upper TBL, except at the beginning when the mantle is significantly heated by the core. In $Ra^{c}_{rh}$ we use $\Delta T^c = T_c - T_m$, the gravity at the core-mantle boundary $g^c$, the viscosity at the temperature $(T_c + T_m)/2$ corresponding to the middle of the lower TBL. In our modelling we consider an isoviscous fluid below a stagnant lid, and the value of $\beta^u$ is in particular sensitive to the boundary condition at the interface of the lid and the convecting mantle, i.e. $\beta^u$ is $1/3$ for free slip and $\sim 0.25$ for rigid boundary condition (e.g., *Deschamps and Sotin*, 2000). In addition, the heating mode of the mantle between basal and internal heating may change during planetary evolution because of core cooling, radioelement decay and secular cooling. Therefore, we test a large range of possible values of $\beta^u$ between 0.2 and 0.38. On the contrary, for the lower TBL, which should not be strongly affected by internal heating and viscosity changes, we adopt a value $\beta^c = 1/3$ in equation 3.19.

For stagnant lid thickness computation, we follow the approach of *Davaille and Jaupart* (1993), where convection is driven by the temperature difference across the upper TBL :

$$T_l = T_m - a_{rh}\Delta T_v = T_m - a_{rh}\frac{RT_m^2}{A} \tag{3.21}$$

In this study, we consider the stagnant lid and the upper TBL separately and estimate the heat flux $q_m$ through the upper TBL at the radius $r = R_l$. As discussed in the introduction, most scalings have determined the heat flux at the surface instead of below the lid, which makes a comparison between their $\beta^u_t$ values and the values of $\beta^u_m$ found in this study not

straightforward. Considering equations 3.1 and 3.6 the surface heat flow can be written in the form :

$$q_s = akD^{3\beta_t^u - 1} \left( \frac{\alpha \rho_m g}{\kappa \eta} \right)^{\beta_t^u} \Delta T_v^{\gamma} \tag{3.22}$$

where $\gamma$ is usually equal to $\gamma = 1 + \beta_t^u$. Assuming there is no internal heating and small transient effects in the lid

$$q_m \approx q_s \left( \frac{R_p}{R_l} \right)^m \tag{3.23}$$

where $R_p$ is the planetary radius, $m = 0$, 1 or 2 for a cartesian, cylindrical or spherical geometry, respectively. Rewriting equations 3.23 with 3.22, 3.15 and 3.6 and assuming that $\beta_m^u = \beta_t^u = \beta^u$ leads to :

$$a_{rh} = \left[ a \left( \frac{D}{R_l - R_c} \right)^{3\beta^u - 1} Ra_{crit}^{u\beta^u} \left( \frac{R_p}{R_l} \right)^m \right]^{\frac{1}{1+\beta^u}} \tag{3.24}$$

which allows to compute equivalent values of $a_{rh}$ for studies which consider the surface heat flow of the entire mantle, and then to compare them with our best parameters $a_{rh}$ and $\beta^u$.

| $a$ | $\beta_t^u$ | $a_{rh}$ | Geometry | Heating mode | Method | Reference |
|---|---|---|---|---|---|---|
| 0.47 | $1/3$ | 2.24 | 3-D cartesian | cooling from above | experiment | 1 |
| 0.53 | $1/3$ | $\sim 2.2$ | 2-D cartesian | internal heating | numerical | 2 |
| 0.52 | $1/3$ | 2.82* | 2-D cartesian | bottom heating | numerical | 3 |
| 0.54 | $1/3$ | 2.90* | 2-D cartesian | bottom heating | numerical | 4 |
| 0.67 | $1/3$ | 3.2 | 3-D spherical | internal heating | numerical | 5 |
| $2.8 \pm 1.7$ | $0.21 \pm 0.06$ | $6.5 \pm 4.6$ | 3-D spherical | internal heating | numerical | 6 |
| 0.39* | $1/3$ | 2.44 | 3-D spherical | mixed heating | numerical | this study |
| 0.41* | 0.335 | 2.54 | 3-D spherical | mixed heating | numerical | this study |

References are (1) *Davaille and Jaupart* (1994), (2) *Solomatov and Moresi* (2000), (3) *Dumoulin et al.* (1999), (4) *Doin et al.* (1997) (5) *Reese et al.* (2005), (6) *Reese et al.* (1999).

**TABLE 3.4** – Scaling parameters $a$, $\beta^u$ and $a_{rh}$ determined by other studies. To make a comparison we indicate one of our best fits for Mars's 3-D model ($\beta^u = 1/3$ and $a_{rh} = 2.44$), and for the three planets ($\beta^u = 0.335$ and $a_{rh} = 2.54$). The symbol * indicates the values of $a_{rh}$ and $a$ that have been respectively computed with equation 3.24 for the studies of *Dumoulin et al.* (1999) and *Doin et al.* (1997), and equation 3.25 for our results. The values of $a$ that are calculated with equation 3.25 are however underestimated due to the presence of internal heat sources. The equivalent values of $a_{rh}$ and $a$ are here computed for $Ra_{crit}^u = 450$ (the value we use in equation 3.19) given the parameters of Mars 3-D reference model : $R_p = 3400$ km and the typical value of stagnant lid thickness for this simulation, at the time corresponding to the shift between planetary heating and cooling (see Table 3.5 for values).

Conversely, we can compute equivalent values of $a$ for our combinations of $a_{rh}$ and $\beta^u$ using

$$a = a_{rh}^{1+\beta^u} \left( \frac{D}{R_l - R_c} \right)^{1-3\beta^u} Ra_{crit}^{u-\beta^u} \left( \frac{R_l}{R_p} \right)^m \tag{3.25}$$

Note that the presence of internal heat sources leads to underestimate the equivalent value of $a$ (see Table 3.4 for values).

The critical Rayleigh number $Ra_{crit}$ depends on the boundary conditions and on the ease of destabilization of the TBLs. For the upper TBL, we assume the theoretical value of $Ra^u_{crit} = 450$. With transient cooling experiments *Davaille and Jaupart* (1993) have found a value of $a_{rh} = 2.24$. However, $a_{rh}$ depends on the model set-up (heating mode, system geometry) and higher values as high as 3.4 to 4 have also been reported for 3-D spherical shells heated from within (*Reese et al.*, 2005). Here, we consider values between 1 and 6.

Determining $Ra^c_{crit}$ is less straightforward than $Ra^u_{crit}$ since the lower TBL is both influenced by basal heating from the core and internal heat production. If the internal heating rate is high, the lower TBL is very thin, weak and hardly gives rise to instabilities. In this case, the hot mantle plumes do not interact with the upper TBL (*Vilella and Deschamps*, 2018). However, the dynamics of the lower TBL probably depends on that of the upper one. Indeed, for a convecting fluid with a low or moderate Rayleigh number ($Ra < 10^9$), cold downwellings from the upper TBL could interact with the dynamics of the lower TBL and play a role in the development of new hot instabilities (*Labrosse*, 2002; *Moore*, 2008). These interactions are even expected to be stronger in the case of a more viscous upper TBL. Since typical values of $Ra^u_{rh}$ considered here are relatively low ($10^4$ to $10^7$ for Mercury, the Moon and Mars), this implies that the dynamics of the lower TBL is not independent of those of the upper layers and that the value of $Ra^c_{crit}$ is linked to $\beta^u$ and $a_{rh}$. Therefore, we only vary the values of $\beta^u$ and $a_{rh}$, and use the description of *Deschamps and Sotin* (2000) for $Ra^c_{crit}$ computation. A recent study proposed different scalings laws for the lower TBL (*Yao et al.*, 2014). However, the model set-up used by *Yao et al.* (2014) is significantly different than the set-up considered here, and therefore their scaling law is difficult to adopt for our study. In the description of *Deschamps and Sotin* (2000), the heat flux at the core-mantle boundary is determined from a scaling relation between the lower critical Rayleigh number $Ra^c_{crit}$ and the internal Rayleigh number $Ra_i$ (equation 3.3) :

$$Ra^c_{crit} = 0.28 Ra_i^{0.21} \tag{3.26}$$

Since this law was established for a fluid in a 2-D Cartesian geometry, with a strongly temperature-dependent viscosity and a mixed heating mode, we check a posteriori its validity for a 3-D spherical geometry.

### 3.2.c Comparison method between 1-D and 2-D/3-D thermal models

The thermal evolution of 3-D spherical models is used as reference to search appropriate scaling parameters for the thicknesses of the two TBLs as well as of the stagnant lid in 1-D

parametrized models. The less time consuming 2-D cylindrical simulations are used to investigate the effects of parameters such as the shell aspect ratio, the surface temperature, initial internal temperatures, the activation energy or the reference viscosity (see section 3.3.d).

One of the difficulties of comparing 1-D and 2-D/3-D thermal models over the entire planet evolution is the delay of a few tens to hundred of Myr before the development of a fully convecting system with identifiable TBLs in the dynamical simulations, while in parametrized models scaling laws for mantle convection apply from the beginning. Thus, to compare the models, we first run 2-D/3-D-simulations with the same geometry and parameters (initial temperature, surface temperature, rheology parameters) but no internal heating until a steady temperature profile is reached. We then use this fully convecting system as the initial velocity field condition at $t = 0$ Gyr. From that time, cooling of the core and radioelement decay is considered. The effect of such an initial startup-simulation on our results is discussed in section 3.3.c.

For the comparison between parametrized and dynamical thermal models we consider the temperature profiles that provide error on the absolute values of the temperature. Since slight errors on the temperature profile near the boundary of the shell could lead to large errors in heat flux, we also compare CMB heat flux and surface heat flux between 1-D and 3-D models. The temperature at the base of the stagnant lid can be used in addition to better constrain the suitable scaling parameters. In 2-D/3-D models the quantities of these parameters are laterally averaged over the shell and compared with those obtained with 1-D parametrized models every 10 Myr over the 4.5 Gyr of planetary evolution. At a given time step, the error on the temperature profile is estimated every kilometer and then averaged over the entire profile using the corresponding shell volume as a weight. A major issue is to suitably compare the goodness of fit for distinct comparison parameters with different units. In order to have comparable errors, we define a weighting scale ($W_{scale}$) for each parameter that represents our acceptable misfit between 1-D and 2-D/3-D models. The weighted error ($W_{error}$, in %) is given by the absolute value of the difference between 1-D and 2-D/3-D models divided by the weighting scale of the corresponding parameter, averaged over the entire evolution of the planet.

$$W_{error} = \frac{1}{N} \sum_{N} \frac{\left| parameter^{3-D} - parameter^{1-D} \right|}{W_{scale}} \tag{3.27}$$

where $N$ is the total number of time steps. We adopt a weighting scale of 3 mW m$^{-2}$ for the surface and CMB heat flux and of 20 K for temperatures, though using different values does not change our results as discussed in section 3.3.b. Using Monte Carlo simulations, we first look for the combined values of $\beta^u$ (equation 3.19 for the upper TBL thickness) and $a_{rh}$ (equation 3.21 for the stagnant lid thickness) that best fit the time evolution of 3-D models and give the lowest total weighted error on surface heat flux, CMB heat flux and temperature profiles. Second, we use the temperature at the lid base as another constraint in Monte-Carlo inversion.

## 3.3 Results for a Mars size planet

In this section, best fitting scaling parameters for 1-D parametrized models have been obtained when considering the 3-D dynamical case of Mars as a reference (*Mars1*, see Table 3.3 for parameters).

### 3.3.a 1-D vs 3-D thermal evolution

**— Mars typical thermal evolution with 3-D models**

Initially, the core is superheated compared to the lower mantle implying a large cooling rate and CMB heat flux. During the first $\sim$ 1.5 Gyr of Mars's evolution the average mantle temperature increases due to radiogenic heating and a large heat flux from the core (Figure 3.3a). The associated viscosity decrease leads to an efficient heat transfer to the uppermost layers of the fluid, which results in an increase in surface heat flux (Figures 3.3c). Due to the large initial rate of internal heating and the subsequent temperature rise in the mantle, core cooling quickly becomes less efficient and the core is even slightly heated by the mantle during $\sim$ 1 Gyr. After $t >$ 1.5 Gyr to 2 Gyr, the planet slowly cools down : the average temperature of the mantle progressively decreases. Below the lid, the mantle temperature remains relatively constant (Figure 3.3d).

**— 1-D thermal evolution**

To reproduce the 3-D thermal evolution with 1-D parametrized models, the parameters $a_{rh}$ and $\beta^u$ - that determine the thickness of the upper TBL and stagnant lid (see equations 3.19 and 3.21) - have to be fixed. Assuming the value of $\beta^u = 1/3$ predicted by the boundary layer stability analysis for basal heating (*Turcotte and Schubert*, 1982), we find the best fit to the 3-D thermal parameters (surface and CMB heat flux, temperature profiles) when considering $a_{rh} = 2.44$ with a total weighted error of 2.1 (green dashed lines, Figure 3.3). In particular, there is a good agreement between predicted mean mantle temperature from parametrized models with 3-D results (average difference of $\sim$ 11 K, see Figure 3.3a). Nonetheless, the 1-D model slightly overestimates the mean temperature between $\sim$ 1.5 and 3 Gyr, i.e. after the switch between the first stage of mantle heating and the subsequent progressive cooling of the planet. This shift in mantle evolution is indeed particularly hard to reproduce accurately with 1-D thermal models, for which the beginning of planet cooling generally occurs with a little delay. A similar shift between 1-D and 3-D models is also retrieved for the surface heat flux evolution (Figure 3.3c) that is slightly underestimated before 2 Gyr and then on the contrary too high, with an average heat flux difference of $\sim$ 1 mW m$^{-2}$. The beginning of planet cooling occurs on the contrary too early in 1-D models when considering a steady-state temperature profile in the lid compared to 3-D. We note that 1-D thermal evolution models with a steady-state conduction in the lid provide much less satisfactory fits to the 3-D surface heat flux (average difference of 4.5 mW m$^{-2}$). Since this time lag is also comparable to the time-scale of heat transport through the lid (*Choblet and Sotin*, 2000, 2001) it could thus arise from differential secular cooling of the lid in between 1-D and 3-D models and in particular from a slightly

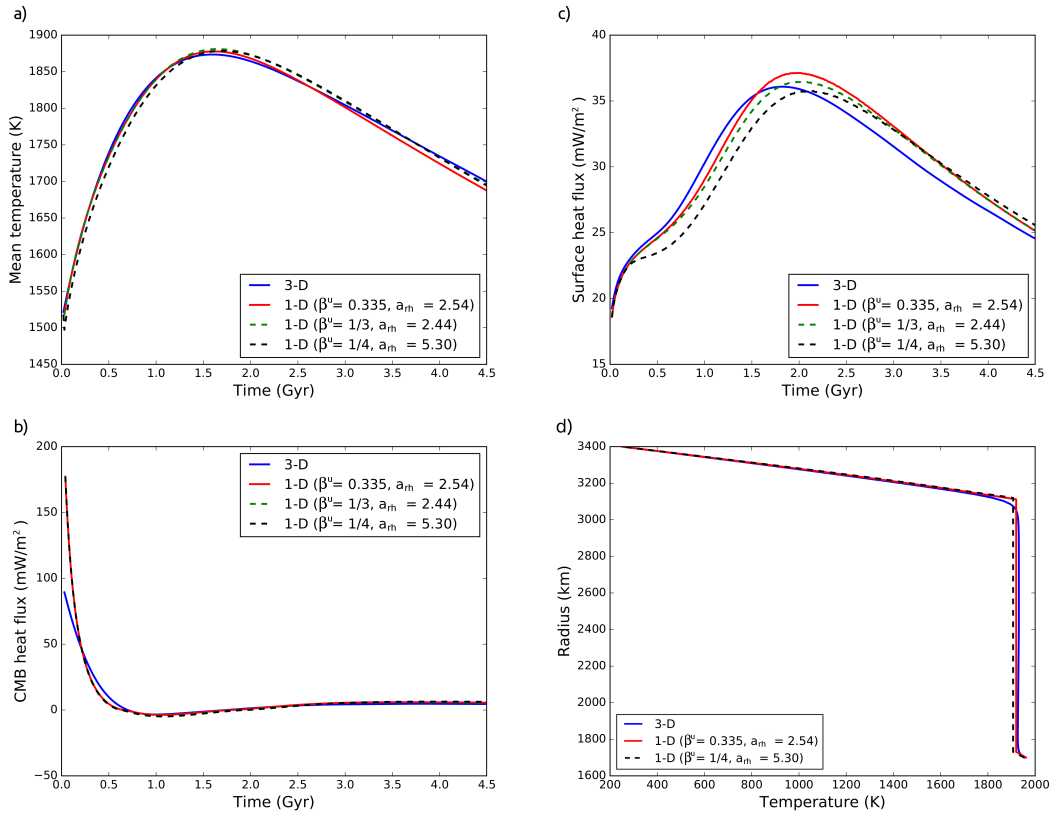


**FIGURE 3.3** – Mars thermal evolution : (a) temperature averaged over the whole mantle, (b) heat flux at the CMB, (c) surface heat flux and (d) temperature profile at the present-day. 3-D thermal evolution (blue lines) corresponds to the Mars reference convection model (case *Mars1* in Table 3.3), whereas 1-D thermal evolution models have been obtained considering some of our best scaling parameter combinations $\beta^u = 1/3$ and $a_{rh} = 2.44$ (green dashed lines in (a), (b) and (c), red line in (d), indistinguishable from the thermal evolution obtained with $\beta^u = 0.335$ and $a_{rh} = 2.54$), $\beta^u = 1/4$ and $a_{rh} = 5.3$ (black dashed lines) and $\beta^u = 0.335$ and $a_{rh} = 2.54$ our best combination for the three planets (red solid lines). For $Ra^c_{crit}$ we consider the description of *Deschamps and Sotin* (2000) (equation 3.26).

larger transient effect when accounting for a time-dependent conduction in the lid. However, due to the so-called thermostat effect (*Plesa et al.*, 2015; *Breuer et al.*, 2016), the surface heat flux and average mantle temperature from 1-D models converge to a specific value at present-day, which is similar to the value obtained in the 3-D model. The CMB heat flux depends on $Ra^c_{crit}$, that determines the lower TBL thickness (equation 3.19), as well as on the efficiency of mantle heat transfer, which is linked to the values of $\beta^u$ and $a_{rh}$. If the global thermal evolution of the planet is well reconstructed with appropriate values of $\beta^u$ and $a_{rh}$, the $Ra^c_{crit}$ description of *Deschamps and Sotin* (2000) provides an excellent fit to the 3-D CMB heat flux evolution although the CMB heat flux values are initially largely overestimated when the overheated core cools rapidly (Figure 3.3b). We note, however, that the lower TBL is very thin ($\sim$ 20 km) and accommodates strong temperature variations ($\sim$ 300 K) during this period : a little

underestimation of its thickness thus results in large heat flux differences that does not affect the quality of the fit of the global thermal evolution.

Similar results to those previously described for $\beta^u = 1/3$ and $a_{rh} = 2.44$ can also be obtained when considering for instance $\beta^u = 1/4$ and $a_{rh} = 5.3$ (Figure 3.3, black dashed lines), which implies that values of $\beta^u$ different from $1/3$ can be used to model a cooling planet in a stagnant lid regime of convection if the value of $a_{rh}$ is changed accordingly. A slightly higher total weighted error of 2.4 is, however, obtained with this combination due to a higher underestimation of the surface heat flux and average mantle temperature during the first part of the evolution.

### 3.3.b Monte Carlo simulation results

**— Upper TBL and stagnant lid thicknesses ($\beta^u$ and $a_{rh}$)**

Using Monte Carlo simulations, we find a trade-off between $\beta^u$ and $a_{rh}$ for a large range of parameters. In addition to ($\beta^u = 1/3$, $a_{rh} = 2.44$) and ($\beta^u = 1/4$, $a_{rh} = 5.3$), a range of combinations (Figure 3.4b) provides a suitable fit to the 3-D thermal evolution with a total weighted error between $\sim 2$ and 2.4 (see section 3.2.c for error computation). All the tested range of $\beta^u$ $(0.2 - 0.38)$ could in fact provide suitable results if $a_{rh}$ is adopted accordingly, though the lowest errors are obtained when considering high values of $\beta^u$ ($> 0.32$). Note that very similar trade-offs between $\beta^u$ and $a_{rh}$ are observed in the Monte Carlo simulations for all the comparison parameters between 1-D and 3-D models (surface and CMB heat flux, temperature profiles, see Figure 3.5a-c). This implies that considering different weighting scales for the temperatures and the heat flux - as for instance 50 K and 1 mW/m$^2$, respectively - does not change our results.

We interpret the observed negative correlation between suitable values of $\beta^u$ and $a_{rh}$ (red zone on Figure 3.4b) as the trade-off between the possible thickness of the upper TBL and that of the rigid lid : if $a_{rh}$ increases, the temperature at the base of the lid is colder (equation 3.21) implying a thinner stagnant lid thickness and a thicker upper TBL, hence a smaller value of $\beta^u$ (equation 3.19). In fact, this trend is representative of the linear conductive temperature profile in the whole upper layer : as $\beta^u$ decreases and $a_{rh}$ increases the limit between the upper TBL and the rigid lid (dotted line in Figure 3.2) moves up along the conductive temperature profile. Continuity of heat flux at the interface gives :

$$\frac{T_m - T_l}{\delta^u} \approx \frac{T_l - T_s}{D_l} \tag{3.28}$$

with $T_s$ the surface temperature and $D_l$ the stagnant lid thickness.

Over most of the thermal evolution, excluding the first hundreds of Myrs, when the core is superheated, $T_c \sim T_m$ and $\Delta T^u = T_c - T_l \sim T_m - T_l$ to first order in equation 3.20. In this case, by rewriting equation 3.28 with equations 3.19, 3.20 and 3.21, we obtain an analytic expression for the relation between $a_{rh}$ and $\beta^u$ :

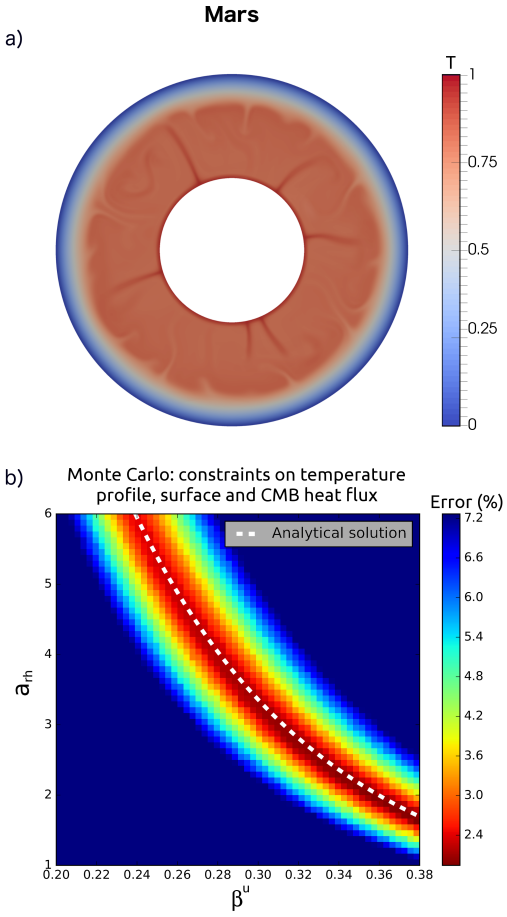


**FIGURE 3.4** – Results of Monte Carlo simulations comparing the 3-D run and 1-D parametrized models in the case of Mars. A snapshot at $t = 0.1$ Gyr of the 3-D dynamical reference model *Mars1* is given in (a), where the colorscale corresponds to the non-dimensional temperature $T$. Monte Carlo results are shown in (b) in the case where the 1-D temperature profiles, the CMB and surface heat flux are compared to those of the 3-D reference run every 10 Myr. Errors are shown in a colorscale and correspond to the cumulative weighted differences between 1-D and 3-D models (in %, see section 3.2.c for the detailed methodology). The white dashed line shows the relation between $\beta^u$ and $a_{rh}$ predicted with equation 3.29, given typical mantle temperature $T_m$ and stagnant lid thickness $D_l$ of the 3-D model that are estimated at the time corresponding to the shift between planetary heating and cooling.

$$a_{rh}(\beta^u) \sim \left[ \frac{T_m - T_s}{H} \frac{1}{\Delta T_v} (R_l - R_c)^{1-3\beta^u} \left( \frac{Ra^u_{crit} \kappa \eta(T_m)}{\alpha \rho g \Delta T_v} \right)^{\beta^u} \right]^{\frac{1}{1+\beta^u}} \tag{3.29}$$

where $H = \delta^u + D_l$ (Figure 3.2) and $\Delta T_v$ is given by $\Delta T_v = RT_m^2/A$. This relation depends in fact on the temperature gradient in the conductive layers of the fluid $(T_m - T_s)/H$, the convective layer thickness $R_l - R_c$ (if $\beta^u \neq 1/3$) and the mantle viscosity. We can indeed retrieve pairs of $a_{rh}$ and $\beta^u$ (white dashed line in Figure 3.4b) that are in excellent agreement with the trend

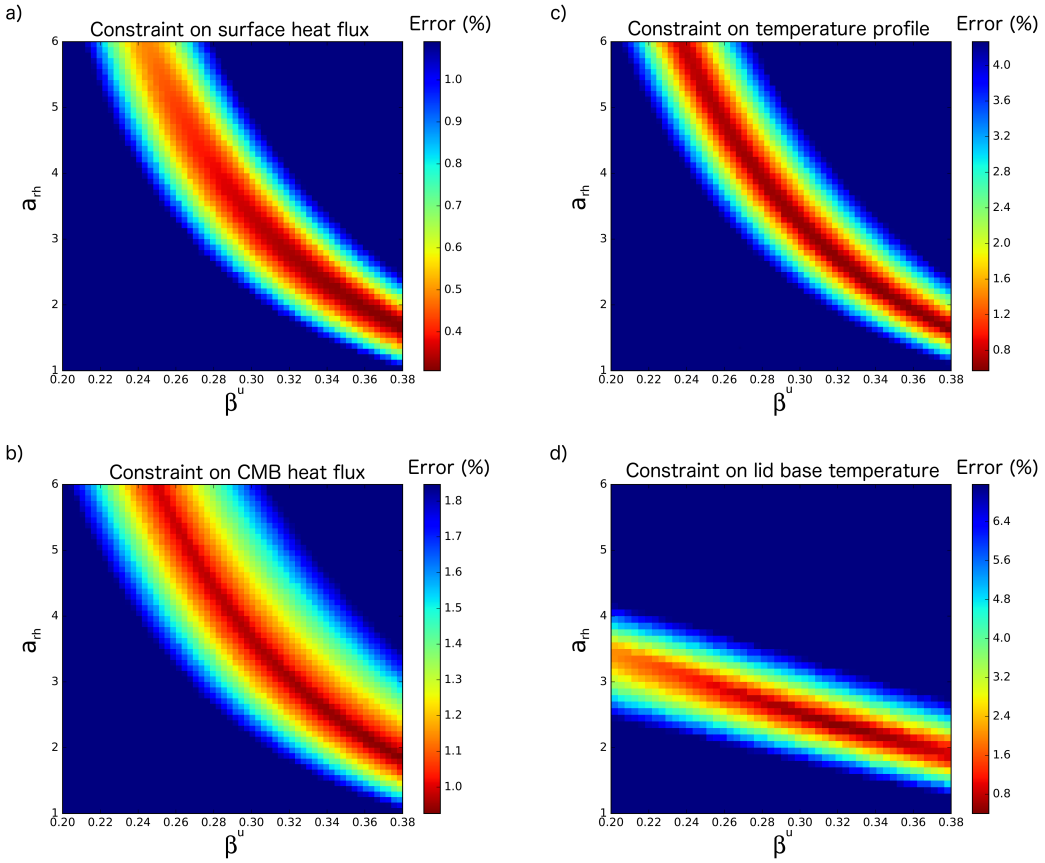


**FIGURE 3.5** – Detailed results of Monte Carlo simulations comparing the 3-D run and 1-D parametrized models in the case of Mars. Weighted errors (see section 3.2.c for details) are shown in (a) for the surface heat flux, in (b) for the heat flux at the CMB, in (c) for the temperature profile and in (d) for the temperature at the base of the stagnant lid when the depth of this lid is calculated using method 1 in dynamical thermal models (see Figure 3.7).

found with Monte Carlo simulation, confirming our interpretation. For this excellent agreement, we use the mantle temperature and stagnant lid thickness values in equation 3.29 at the time where a quasi steady-state is achieved, i.e. at the time corresponding to the shift between planetary heating and cooling from the 3-D reference model (see Table 3.5 for values).

— **Lower TBL thickness ($Ra^c_{crit}$)**

To fix appropriate scaling relations for $\beta^u$ and $a_{rh}$, we have considered in section 3.3.b the relation of *Deschamps and Sotin* (2000) (equation 3.26) to compute the lower TBL thickness. For our best fits, we observe that the values of $Ra^c_{crit}$ computed with this relation are rather stable during the entire evolution ($Ra^c_{crit} \sim 19$), which implies that a constant value of $Ra^c_{crit}$ could give at first order a good estimation of the lower TBL thickness. By varying $Ra^c_{crit}$ between 1 and 1000, we tested the influence of this parameter on the thermal evolution of the upper layers of the fluid and, thus, on the best combinations of $\beta^u$ and $a_{rh}$ that was determined in section 3.3.b. As expected, $Ra^c_{crit}$ mainly affects the evolution of the lower layers close to

| Case | Geometry | $T_m$ [K] | $D_l$ [km] | $\eta$ [Pa s] |
|---|---|---|---|---|
| 3-D reference models | | | | |
| *Mars*1 | 3-D | 2050 | 180 | $7.3 \times 10^{18}$ |
| *Moon*1 | 3-D | 1950 | 290 | $1.8 \times 10^{19}$ |
| *Mercury*1 | 3-D | 1950 | 160 | $1.7 \times 10^{19}$ |
| 2-D models (Parameter study) | | | | |
| *Mars*2 | 2-D | 2075 | 182 | $5.8 \times 10^{18}$ |
| *PS*1 | 2-D | 2125 | 170 | $4.0 \times 10^{18}$ |
| *PS*2 | 2-D | 2090 | 190 | $4.2 \times 10^{18}$ |
| *PS*3 | 2-D | 2085 | 190 | $5.3 \times 10^{18}$ |
| *PS*4 | 2-D | 2090 | 170 | $5.1 \times 10^{18}$ |
| *PS*5 | 2-D | 2105 | 135 | $4.4 \times 10^{18}$ |
| *PS*6 | 2-D | 2055 | 230 | $6.7 \times 10^{18}$ |
| *PS*7 | 2-D | 2090 | 180 | $5.1 \times 10^{18}$ |
| *PS*8 | 2-D | 1920 | 150 | $2.3 \times 10^{18}$ |
| *PS*9 | 2-D | 2095 | 200 | $7.0 \times 10^{19}$ |
| *PS*10 | 2-D | 2010 | 175 | $1.0 \times 10^{18}$ |

**TABLE 3.5** – Typical values of mantle temperature $T_m$, stagnant lid thickness $D_l$ (calculated using method 1, see Figure 3.7) and viscosity $\eta$ for 2-D and 3-D models. The values are taken at the time corresponding to the shift between planetary heating and cooling.

the CMB : although heat transfer in the upper mantle directly influences the thermal evolution at the CMB, the value of $Ra^c_{crit}$ does not play a substantial role on its evolution. The error on the surface heat flux remains constant over the entire range of $Ra^c_{crit}$, while error variations are observed for the other thermal parameters (CMB heat flux and temperature profiles) that are essentially linked to the quality of the CMB temperature fit. The latter is indeed particularly sensitive to the thickness of the lower TBL (and thus to $Ra^c_{crit}$), which determines the efficiency of heat transfer at the CMB and core cooling.

Although the relation of *Deschamps and Sotin* (2000) was obtained for a 2-D Cartesian geometry, it provides an excellent agreement to the thermal evolution observed in a 3-D spherical geometry with a total weighted error of 2.1. In particular, for the thermal evolution of the lower layer of the shell we observe an error of 7 K for the CMB temperature (see Figure 3.6) and an average difference of 4 mW m$^{-2}$ for the CMB heat flux that is predominantly due to an overestimation of it by the parametrized models at the beginning of the simulations. However, during the rest of the evolution the agreement between the CMB heat flux predicted by 1-D and 3-D models is excellent.

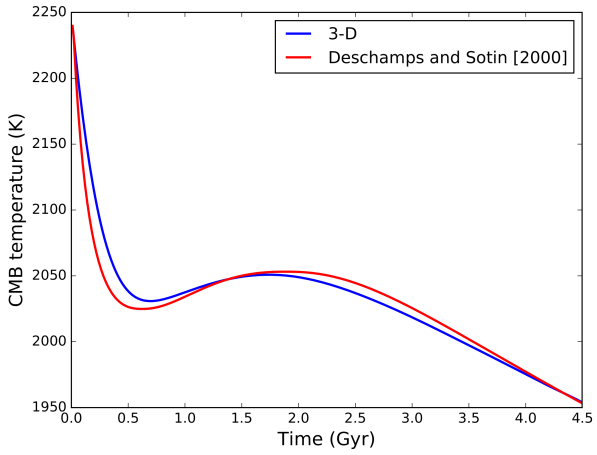


**FIGURE 3.6** – The CMB temperature evolution is represented for Mars 3-D reference model (in blue) and 1-D parametrized models assuming the $Ra^c_{crit}$ definition of *Deschamps and Sotin* (2000) (red curve) for our best combination for the 3-D model of Mars ($\beta^u = 0.345$ and $a_{rh} = 2.16$).

### 3.3.c Temperature at the base of the stagnant lid

Given that all the best fit pairs of $\beta^u$ and $a_{rh}$ show a similar thermal evolution but differ in their predicted thicknesses for the upper TBL and stagnant lid, suitable parameter combinations could be further limited if constraints on the stagnant lid thickness are given. Moreover, considering a stagnant lid definition would lead to more realistic values of the upper TBL and lid thicknesses that could be, otherwise, physically inappropriate. However, the estimation of the stagnant lid thickness is not straightforward in 3-D convection models because the boundaries between the stagnant lid, the upper TBL and the convecting layer are not clear. Different methods have been used to estimate the stagnant lid thickness, that is defined as the portion of the shell where heat flux by conduction dominates and the velocity field tends to zero. We first use the method of *Reese et al.* (2005), where the bottom of the stagnant lid is defined by the intersection between the depth axis and the tangent to the velocity profile at the depth corresponding to the maximum velocity gradient (Figure 3.8 a). Figures 3.3c and 3.8a-b show that the stagnant lid thickness evolution is closely linked and inversely correlated to that of the surface heat flux (the thinner the lid, the larger the surface heat flux) and decreases during the first 2 Gyr before slowly growing during the subsequent evolution.

When considering the temperature at the base of the lid as an additional constraint with a weighting scale of 20 K in our Monte Carlo simulation comparing 1-D and 3-D models (Figure 3.5d), values of $\beta^u$ need to be $\gtrsim 1/4$ and we obtain best fits between $\beta^u = 0.33 - 0.36$, while $a_{rh} \lesssim 3.5$ with best fits between 2 and 2.25 (Figure 3.8e). Best fits show a cumulative error $< 2.7$ that accounts for the error on the temperature at the base of the lid with a weighting scale of 20 K. Considering the relation of *Deschamps and Sotin* (2000) for $Ra^c_{crit}$, we find that

scaling parameters $\beta^u = 0.345$ and $a_{rh} = 2.16$ provide a best-fit for Mars's thermal evolution. Our results show suitable fits to the evolution of the stagnant lid thickness and the temperature at the base of the lid with average errors of 25 km and 10 K, respectively (red dotted dashed lines on Figure 3.8a and c). Those errors are mainly due to an underestimation of the stagnant lid thickness during the second part of planetary evolution (Figure 3.8a), resulting also in an overestimation of the surface heat flux. Note that the fit of the other thermal parameters (heat flux at the surface and at the CMB, temperature profiles) are similar to those obtained with the parameter combination $\beta^u = 1/3$ and $a_{rh} = 2.44$ (green dashed lines in Figure 3.3 and 3.8a). The startup-simulation used in the dynamical models (see section 3.2.c) leads to a thick stagnant lid at the beginning of the thermal evolution and is probably not representative for the conditions present during early history. To test the sensitivity of our results to the initial conditions, we ran an additional case with no startup-simulation for the dynamical thermal evolution model. We found that an initial stagnant lid thickness of only 50 km does not affect our Monte Carlo results.

Another stagnant lid definition leads to slightly different best combinations. Considering, for instance, the value of 1% of the maximum velocity as a threshold value to define the rigid portion of the mantle, implies a thinner stagnant lid (see Figure 3.8b) and shifts therefore the best combinations to higher values of $a_{rh}$ ($a_{rh} = 2.63 - 2.81$) and slightly lower values of $\beta^u$ ($\beta^u = 0.325 - 0.340$) (Figure 3.8f). Although similar good fits to the 3-D thermal evolution

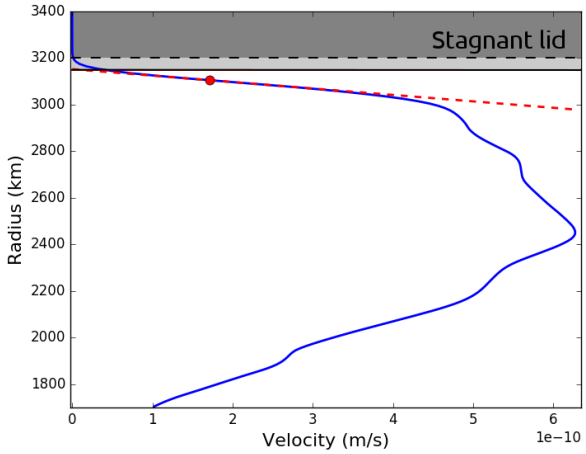


**FIGURE 3.7** – Methods used for stagnant lid thickness estimation in 2-D and 3-D dynamical thermal models. The base of the lid has been calculated using either method 1 : the intersection between the tangent to the velocity profile (averaged over the entire shell, blue solid line) at the depth corresponding to the maximum velocity gradient (red dashed line) and the radius axis (black line, same method as *Reese et al.*, 2005), or method 2 : the depth where a fraction of the maximum velocity is reached (for instance 1%, black dashed line).

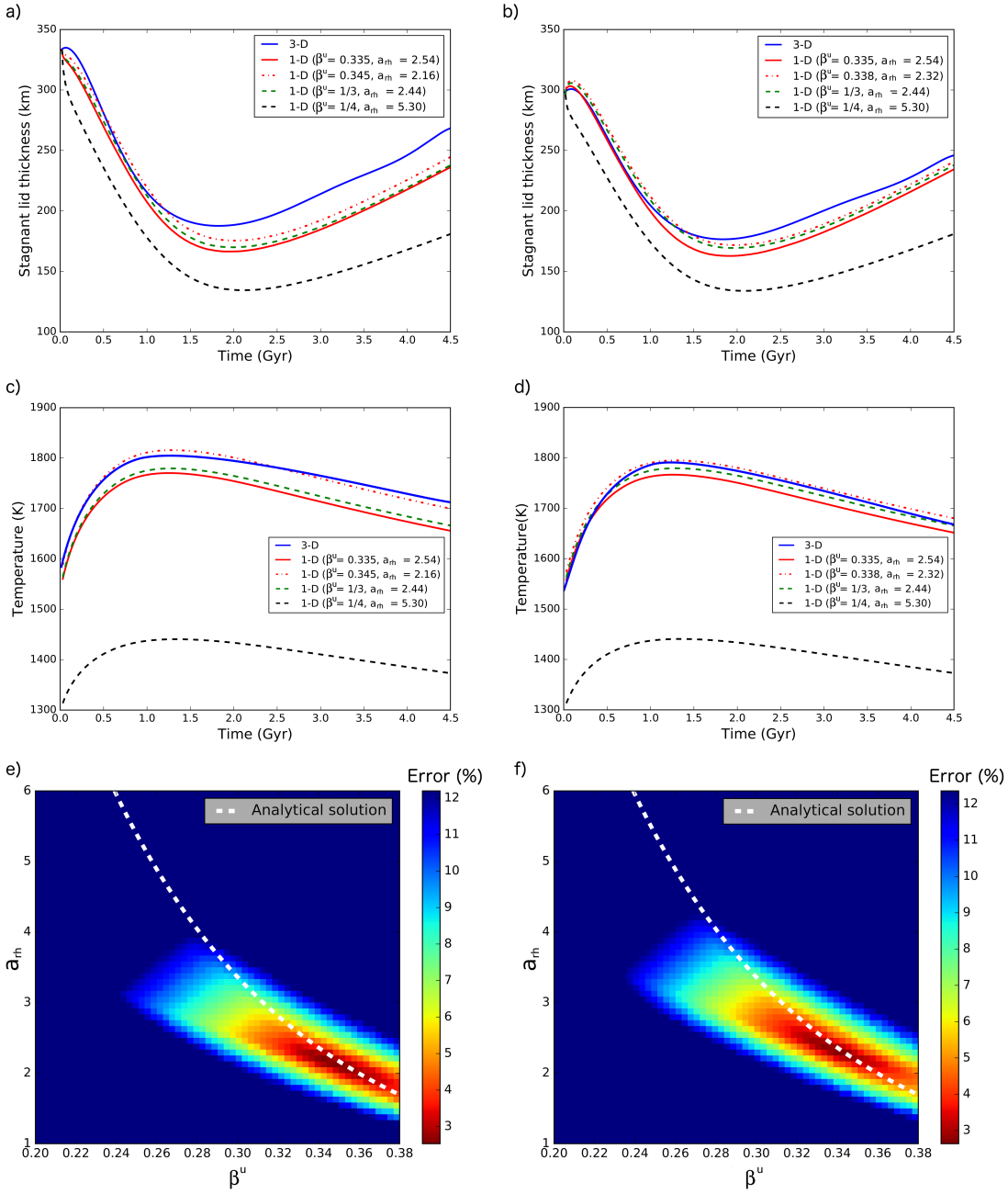
a)
b)
c)
d)
e)
f)
Stagnant lid thickness (km)
Temperature (K)
Temperature(K)
Time (Gyr)
3-D
1-D (β^u= 0.335, a_rh = 2.54)
1-D (β^u= 0.345, a_rh = 2.16)
1-D (β^u= 1/3, a_rh = 2.44)
1-D (β^u= 1/4, a_rh = 5.30)
1-D (β^u= 0.338, a_rh = 2.32)
Analytical solution
Error (%)
a_rh
β^u

FIGURE 3.8

**FIGURE 3.8** – Stagnant lid thickness evolution for Mars and implications for the Monte Carlo results. The stagnant lid thickness evolution obtained for Mars's 3-D model is shown in blue : in (a) if the base of the lid is defined by the intersection between the tangent to the velocity profile at the depth corresponding to the maximum velocity gradient and the radius axis (method 1, *Reese et al.*, 2005), in (b) if it corresponds to the depth where 1% of the maximum velocity is reached (method 2, see Figure 3.7 for details). The temperature at the lid depth is shown in (c) for method 1 and in (d) for method 2. We obtain best fits when considering in 1-D models $\beta^u = 0.345$ - $a_{rh} = 2.16$ for method 1 and $\beta^u = 0.338$ - $a_{rh} = 2.32$ for method 2 (red dotted dashed lines). Stagnant lid thickness evolution for 1-D models are also shown for some of our best scaling parameter combinations $\beta^u = 1/3$ and $a_{rh} = 2.44$ (green dashed lines), $\beta^u = 1/4$ and $a_{rh} = 5.3$ (black dashed lines) and $\beta^u = 0.335$ and $a_{rh} = 2.54$ (our best combination for the three planets, red solid lines). When the temperature at the stagnant lid depth from 1-D models is also compared to that of the 3-D one, Monte Carlo results are shown in (e) for method 1, in (f) for method 2. Errors are shown in a colorscale and correspond to the cumulative weighted differences between 1-D and 3-D models (in %, see section 3.2.c for the detailed methodology). The white dashed line shows the relation between $\beta^u$ and $a_{rh}$ predicted with equation 3.29, given typical mantle temperature $T_m$ and stagnant lid thickness $D_l$ of the 3-D model that are estimated at the time corresponding to the shift between planetary heating and cooling.

are found with the two different stagnant lid definitions assumed here, in the following we will consider the method of *Reese et al.* (2005) since it seems physically more robust than an arbitrary percentage of the velocity.

### 3.3.d Effect of planetary parameters on the relation between $\beta^u$ and $a_{rh}$

In the following, we test the sensitivity of the best fit parameters when varying the aspect ratio, the surface temperature, the initial mantle temperature, the reference viscosity and the activation energy. These parameters have been identified to influence the relation between $\beta^u$ and $a_{rh}$ (see equation 3.29). To this end, we run 2-D simulations as an extensive parameter study since 3-D thermal models are too time-consuming. We calculate a reference model (case *Mars2* in Table 3.3) in a 2-D cylindrical geometry equivalent to the 3-D one (case *Mars1*). Though the ratio between CMB and planetary radii is corrected following *van Keken* (2001) for 2-D models in the Gaia code, we find, in agreement with *Plesa et al.* (2015), that bottom heating from the core is still overestimated in 2-D models compared to 3-D simulations. This leads to a less efficient cooling resulting in an overestimation of the surface heat flux (by $\sim 2$ mW m$^{-2}$) and of the average mantle and CMB temperatures (by $\sim 40$ K and $\sim 50$ K, respectively) associated to a too thin stagnant lid (by $\sim 25$ km). The differences between 2-D and 3-D results observed here are due to the different geometries used (i.e., cylindrical vs. spherical geometry). Although these differences could be smaller for a 2-D spherical annulus geometry (e.g., *Nakagawa and Tackley*, 2010) or 2-D axisymmetric geometry, no 2-D model will accurately reproduce the 3-D results (*Hernlund and Tackley*, 2008). This leads to a shift of the best parameter combinations to lower values of $a_{rh}$ ($a_{rh} = 2.2$ for $\beta^u = 1/3$ for instance) with a difference that increases as $\beta^u$ decreases (Figure 3.9a). This discrepancy should be kept in mind when choosing best fit values in parametrized convection models.

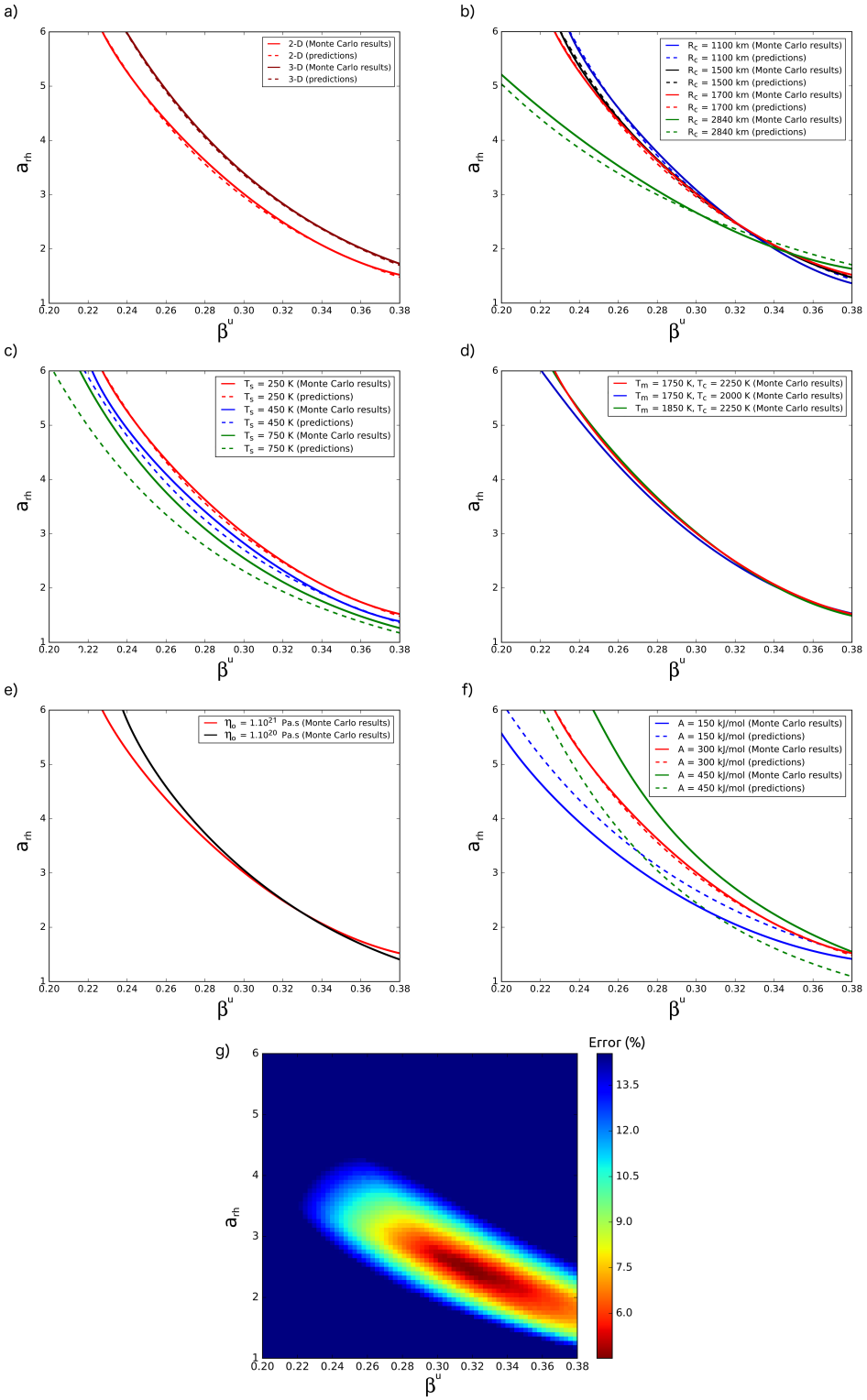
a)
2-D (Monte Carlo results)
2-D (predictions)
3-D (Monte Carlo results)
3-D (predictions)
b)
$R_c$ = 1100 km (Monte Carlo results)
$R_c$ = 1100 km (predictions)
$R_c$ = 1500 km (Monte Carlo results)
$R_c$ = 1500 km (predictions)
$R_c$ = 1700 km (Monte Carlo results)
$R_c$ = 1700 km (predictions)
$R_c$ = 2840 km (Monte Carlo results)
$R_c$ = 2840 km (predictions)
c)
$T_s$ = 250 K (Monte Carlo results)
$T_s$ = 250 K (predictions)
$T_s$ = 450 K (Monte Carlo results)
$T_s$ = 450 K (predictions)
$T_s$ = 750 K (Monte Carlo results)
$T_s$ = 750 K (predictions)
d)
$T_m$ = 1750 K, $T_c$ = 2250 K (Monte Carlo results)
$T_m$ = 1750 K, $T_c$ = 2000 K (Monte Carlo results)
$T_m$ = 1850 K, $T_c$ = 2250 K (Monte Carlo results)
e)
$\eta_o$ = $1.10^{21}$ Pa.s (Monte Carlo results)
$\eta_o$ = $1.10^{20}$ Pa.s (Monte Carlo results)
f)
A = 150 kJ/mol (Monte Carlo results)
A = 150 kJ/mol (predictions)
A = 300 kJ/mol (Monte Carlo results)
A = 300 kJ/mol (predictions)
A = 450 kJ/mol (Monte Carlo results)
A = 450 kJ/mol (predictions)
g)
Error (%)
13.5
12.0
10.5
9.0
7.5
6.0
$a_{rh}$
$\beta^u$

FIGURE 3.9

**FIGURE 3.9** – Effect of different parameters on the Monte Carlo best trend. For computational reasons, we consider here a reference 2-D model for Mars (red solid line, case *Mars2* in Table 3.3). The difference with the trend obtained for the reference 3-D model *Mars1* (dark red solid line) is shown in (a). We compare the trend obtained for the reference 2-D model with those of other simulations where only one parameter is changed, to test separately the effect of (b) core radius (cases *PS1*, *PS2* and *PS3*), (c) surface temperature (cases *PS4* and *PS5*), (d) initial temperatures (core temperature in case *PS6*, mantle temperature in case *PS7*), (e) reference viscosity (case *PS8*) and (f) activation energy (cases *PS9* and *PS10*). We also show the predicted relation with equation 3.29 (dashed lines), in which we use the mantle temperature and stagnant lid thickness from our reference 2-D case *Mars2* and compute the viscosity $\eta(T_m)$ from equation 3.10 and $\Delta T_v$ from equation 3.21. The average error for the Monte Carlo simulations of all the 2-D models (*Mars2* and *PS1* to *PS10*) is shown in (g) with a lowest global error for $\beta^u = 0.319$ and $a_r h = 2.47$ (including the error on the temperature at the lid depth when considering a stagnant lid definition similar to *Reese et al.*, 2005). Errors are shown in a colorscale and correspond to the cumulative weighted differences between 1-D and 2-D models (in %, see section 3.2.c for the detailed methodology).

We further calculate the relation between $\beta^u$ and $a_{rh}$ predicted by equation 3.29 when varying the aspect ratio, rheology parameters and surface conditions. We use the typical values of mantle temperature and stagnant lid thickness for the reference 2-D simulation, at the time corresponding to the shift between planetary heating and cooling (see Table 3.5 for values), and compute the viscosity $\eta(T_m)$ from equation 3.10 and $\Delta T_v$ from equation 3.21. The computed combinations of $a_{rh}$ and $\beta^u$ from equation 3.29 (dashed lines on Figure 3.9) predict the shift in direction of the trend well but not its amplitude : the results of Monte-Carlo simulations (solid lines on Figure 3.9) are not perfectly fitted since the values of the mantle temperature and stagnant lid thickness we use in equation 3.29 are characteristic of the reference 2-D simulation. The fits are perfect if we use the mantle temperature and stagnant lid thickness of each run at the time corresponding to the shift between planetary heating and cooling.

— **Effect of the aspect ratio**

The aspect ratio between the core and planetary radius of a planet is typically not well known and also varies among the terrestrial planets. Recent studies have investigated the effect of the aspect ratio on the average temperature and bottom heat flux for stagnant lid simulations (*Yao et al.*, 2014; *Guerrero et al.*, 2018). However, these studies solely consider basal heating and their scaling depends on the Frank-Kamenetskii viscosity contrast of the mantle and are not directly comparable with the set-up used in this study. The effects of the aspect ratio are most pronounced in a basal heated scenario. A small aspect ratio leads to a colder interior compared to a large aspect ratio because of the higher effective Rayleigh number and more efficient heat transport in the former case compared to the latter (*Yao et al.*, 2014). We note, however, that the consideration of heat sources in a thermal evolution scenario would relax these conclusions since the total amount of internal heating increases with the volume of the mantle and, thus, with a decreasing aspect ratio (see Figure 3.10).

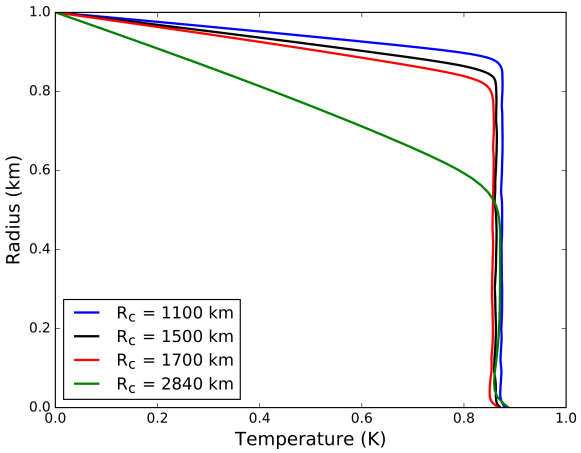


**FIGURE 3.10** – Nondimensional average temperature profiles at the end of the evolution for the 2-D simulations accounting for the Martian planetary radius value of $R_p = 3400$ km and different core radius values of $R_c = 1100$ km (in blue), $R_c = 1500$ km (in black), $R_c = 1700$ km (in red) and $R_c = 2840$ km (in green).

To investigate the effect of the aspect ratio on the relation between $\beta^u$ and $a_{rh}$ in a thermal evolution scenario, where an Arrhenius rheology is used and the mantle is heated both from below and from within, we vary the core radius and keep the planetary radius fixed at the Martian value. We consider aspect ratios of 0.32 and 0.83 representative of those of the Moon and Mercury (cases *PS2* and *PS1*, respectively, see Table 3.3) as well as a potential value of 0.44 for Mars (case *PS3* in Table 3.3) versus 0.5 for the reference model.

As expected from equation 3.29, Monte Carlo results show that the relation between $\beta^u$ and $a_{rh}$ strongly depends on the aspect ratio of the shell, and in particular on the convective layer thickness as the stagnant lid thickness is about the same in all simulations (Figure 3.9b, solid lines). Indeed, if the convecting layer is thinner, the vigor of convection decreases and the trend between suitable combinations of $\beta^u$ and $a_{rh}$ is less steep characterizing a relatively thicker lid (equation 3.29). Nevertheless, all the Monte Carlo simulation trends converge to values of $a_{rh} \sim 1.7-2.4$ for $\beta^u \sim 0.32-0.36$ (Figure 3.9b), i.e. values that minimize the dependency between $a_{rh}$ and the thickness of the convecting layer in the term $(R_l - R_c)^{(1-3\beta^u)/(1+\beta^u)}$ of equation 3.29. Moreover, such values of $\beta^u$ correspond to the values that are obtained when adding the criteria on the temperature at the lid base in our misfit computation between parametrized and dynamical thermal models (see section 3.3.c).

— **Effect of the surface and initial mantle temperatures**

The relation between $\beta^u$ and $a_{rh}$ also depends on the temperature gradient in the upper conductive layers of the fluid, and thus on the surface and mantle temperatures (see equation 3.29).

In cases *PS4* and *PS5* we consider $T_s = 450$ K and $T_s = 750$ K, respectively, and $T_s = 250$ K in the reference case *Mars2* (see Table 3.3). For higher surface temperatures, the Monte Carlo simulation trend is shifted to lower values of $a_{rh}$ (see Figure 3.9c, solid lines) - i.e. thinner stagnant lid - for a given $\beta^u$. In this case, there is no convergence of the different trends to a unique combination of the scaling parameters $\beta^u$ and $a_{rh}$. However, such trends represent an arbitrary choice of the best error value and are in fact very close for values of $\beta^u$ of $\sim 0.32 - 0.36$ that are obtained when considering the temperature at the base of the lid as an additional constraint in the Monte Carlo simulations.

We also test the effect of changing initial mantle and CMB temperatures for cases *PS6* and *PS7* (see Table 3.3 for detailed parameters). After a few hundreds of million years, differences in temperature profiles are typically leveled out by the so-called thermostat effect, which balances mantle cooling through the strong temperature-dependence of the viscosity (e.g., *Tozer*, 1970; *Breuer et al.*, 2016). Thus, Monte Carlo trends of the best-fit are only slightly influenced by the initial temperature distribution (see Figure 3.9d).

— **Effect of the rheology**

Mantle rheology parameters are important for thermal evolution as they determine the efficiency of heat transfers and remain poorly constrained for terrestrial planets. We first investigate the effect of assuming a lower reference viscosity of $\eta_0 = 10^{20}$ Pa s in equation 3.10 (case *PS8*, see Table 3.3), compared to $\eta_0 = 10^{21}$ Pa s in the reference case. The resulting lower viscosity leads to a more efficient heat transfer and a faster cooling of the planet through a thinner stagnant lid that implies a higher temperature gradient in the conductive layers. Though the trend obtained with Monte Carlo simulations for the case *PS8* (Figure 3.9e, black solid line) is steeper than that of the reference model, it is close and converge to the same values of $a_{rh}$ for values of $\beta^u \sim 0.31 - 0.35$, which minimizes the effect of the stagnant lid thickness.

Similarly, we test the effect of varying the activation energy $A$ in equation 3.10 by assuming $A = 150$ kJ mol$^{-1}$ and $A = 450$ kJ mol$^{-1}$ in cases *PS9* and *PS10*, respectively, compared to $A = 300$ kJ mol$^{-1}$ in the reference case *Mars2* (see Table 3.3). A lower activation energy implies a higher viscosity at a given temperature and thus a less efficient mantle heat transfer associated with a higher internal temperature and a thicker stagnant lid. This leads to lower values of $a_{rh}$ for a given value of $\beta^u$ on *PS9* Monte Carlo trend (blue solid line in Figure 3.9f). Conversely, for the higher activation energy assumed in case *PS10*, the Monte Carlo trend (green solid line in Figure 3.9f) shows values of $a_{rh}$ that are higher than those of the reference model for a given value of $\beta^u$, caused by a higher cooling rate and a thinner stagnant lid. As for the variation of some of the other parameters, the best-fit values differ the least for large values of $\beta^u$, corresponding to thinner upper TBL. It should be noted that although $a_{rh}$ is a constant

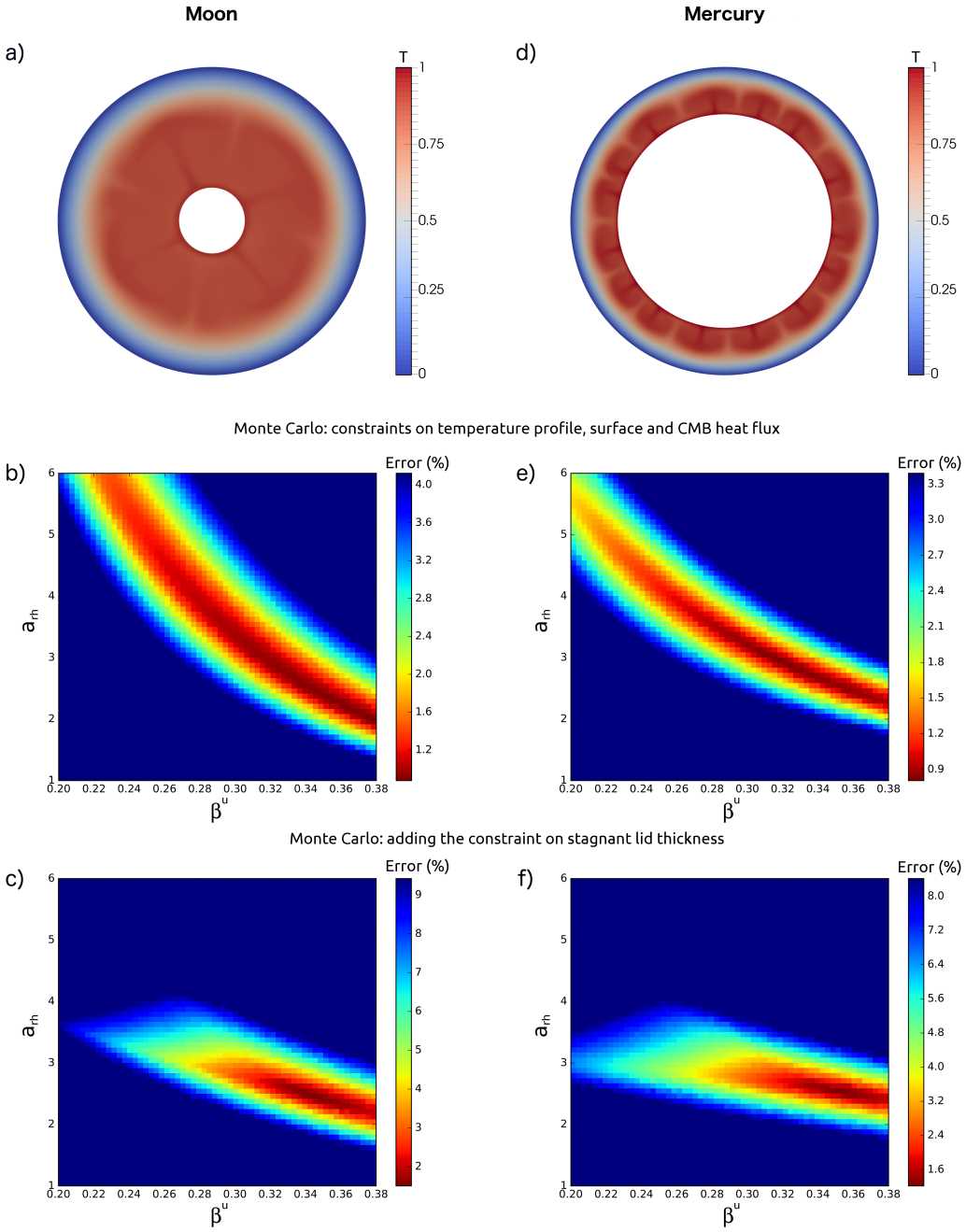
Moon
Mercury
a)
d)
T
1
0.75
0.5
0.25
0
Monte Carlo: constraints on temperature profile, surface and CMB heat flux
b)
e)
Error (%)
$a_{rh}$
$\beta^u$
Monte Carlo: adding the constraint on stagnant lid thickness
c)
f)

FIGURE 3.11

**FIGURE 3.11** – Results of Monte Carlo simulations comparing 3-D models and 1-D parametrized ones in the case of the Moon and Mercury. Snapshots at $t = 0.1$ Gyr of the 3-D dynamical reference models *Moon1* and *Mercury1* are given in (a) and (d), respectively, where the colorscale corresponds to the non-dimensional temperature $T$. Monte Carlo results are shown in (b) for the Moon, and (e) for Mercury in the case where the 1-D temperature profiles, the CMB and surface heat flux are compared to those of the reference 3-D runs every 10 Myr. Monte Carlo results are shown in (c) for the Moon and (f) for Mercury if the temperature at the stagnant lid depth from 1-D models is also compared to that of the 3-D runs (stagnant lid definition similar to that of *Reese et al.*, 2005). Errors are shown in a colorscale and correspond to the cumulative weighted differences between 1-D and 3-D models (in %, see section 3.2.c for the detailed methodology).

(see equation 3.6), our results, also confirmed by the scaling of equation 3.29, show that it depends on the activation energy. The cause is likely the Arrhenius viscosity, which we used for the 2-D and 3-D models instead of the simplified Frank-Kamenetskii approximation. Thus, different values of $a_{rh}$ have been found for different values of the activation energy. This is also the case for the dependence of $a_{rh}$ on the reference viscosity and on the surface temperature.

**— Best combination for 2-D simulations**

To determine the parameter combination that minimizes the global error for all the 2-D simulations considered in the parameter study (*Mars2*, *PS1* to *PS10* models), we sum the Monte Carlo results of all these models when considering the differences between 1-D parametrized models and 2-D simulations in temperature profiles, CMB and surface heat flux, and temperature at the lid base (Figure 3.9g) (see Table 3.3 for the best parameter combinations of each model). The lowest global error is obtained for $\beta^u = 0.319$ and $a_{rh} = 2.47$, which is almost similar to the best combination $\beta^u = 0.316$ and $a_{rh} = 2.47$ of Mars's 2-D reference model *Mars2*, inducing, therefore, a negligible additional error for this model set-up. Similarly, minor additional weighted errors ($< 0.15$) are obtained for most of the other 2-D models. Indeed, the best trends shown in Figure 3.9a-f represent an arbitrary definition of the acceptable error between parametrized and dynamical thermal models. This implies that the discrepancies observed between the majority of the trends are in fact slight, especially for the values of $\beta^u \sim 0.32 - 0.36$ that are typically retrieved when considering the temperature at the lid base as an additional comparison parameter between 1-D and 2-D thermal models. However, a few models show very different best trends inducing a large error. Indeed, as discussed in section 3.3.d, changing the surface temperature results in a shift of the best scaling parameters to lower values of $a_{rh}$ for a given value of $\beta^u$. Since this shift becomes significant for high surface temperatures of about $T_s = 750$ K (case *PS5*, green line in Figure 3.9c), considering the global best combination $\beta^u = 0.319$ and $a_{rh} = 2.47$ leads to underestimate the stagnant lid thickness and overestimate the cooling rate with a too low internal temperature by $\sim 15$ K. Similar errors are also observed for the case *PS1* (simulation with Mercury's aspect ratio, green line in Figure 3.9b). While such slight errors remain acceptable, the underestimation of the cooling rate is more significant for *PS9* (case with a low activation energy, blue line in Figure 3.9f) for which it results in a too low internal temperature by $\sim 50$ K.

## 3.4 Generalization for terrestrial planets

For modeling the thermal evolution of other planets with parametrized convection, the same scaling parameters are usually chosen (e.g., $\beta^u = 1/3$ and $a_{rh} = 2.24$ of *Davaille and Jaupart* (1993, 1994)), although the interior structure, composition and thermal evolution of each planet likely differs. In this section, we determine the best-fit parameters obtained for the Moon and Mercury (cases *Moon1* and *Mercury1* in Table 3.3), using the same methodology as for Mars in section 3.3.

### 3.4.a The Moon

Compared to Mars, the Moon has a higher cooling rate due to both a smaller core - associated to a lower basal heating and only a few hot mantle plumes (Figure 3.11a) - and a lower Rayleigh number ($\sim 10^6$) linked to a thinner convecting layer. Other main differences concern surface gravity and mantle density that are lower as well for the Moon (case *Moon1*, Table 3.3).

Given these differences, the thermal evolution of the Moon is similar in many ways to that of Mars (see Figure 3.12). After a first $\sim 2$ Gyr phase of mantle heating marked by an increase in the average mantle temperature and surface heat flux, a global cooling is observed. However, the present Moon is colder than Mars with a stagnant lid thicker by $\sim 100$ km associated to a lower surface heat flux. 1-D parametrized models can satisfactorily fit this 3-D typical thermal evolution with average misfits of $\sim 8$ K for the temperature profiles and $\sim 0.3$ mW m$^{-2}$ for both surface and CMB heat flux. The values of $Ra^c_{crit}$ ($\sim 11$) computed with the law of *Deschamps and Sotin* (2000) (equation 3.26) thus suitably describe the thermal evolution of the layers close to the CMB. As is observed for Mars, the most critical part is to suitably reproduce the timing of the transition between planetary heating and cooling at $\sim 2$ Gyr, which occurs slightly too late in 1-D models accounting for transient effects in the lid. Moreover, during the cooling period, the stagnant lid is thinner by $\sim 20$ km in the 1-D models compared to the 3-D models.

As for Mars, when comparing temperature profiles, surface and CMB heat flux between 1-D and 3-D models in Monte Carlo simulations (see section 3.2.c for the detailed methodology), results show a similar trend between $\beta^u$ and $a_{rh}$ marked by lower errors for values of $\beta^u > 0.27$ (Figure 3.11b). This trend is slightly more gradual than that of Mars (Figure 3.14a, blue solid line). This difference results from both a lower internal temperature and a thinner convecting layer (see section 3.3.d). By using the typical thermal parameters of *Moon1* at the time corresponding to the shift between planetary heating and cooling (see Table 3.5) in equation 3.29, we find combinations of $\beta^u$ and $a_{rh}$ that are in excellent agreement with the Monte Carlo trend (Figure 3.14a, blue dashed line). When the temperatures at the base of the stagnant lid are also compared between 1-D and 3-D models (Figure 3.11c, definition similar to that of *Reese et al.* (2005), see section 3.3.c), we find that suitable combinations of scaling parameters are much more constrained, converging to values of $\beta^u = 0.33 - 0.355$ and $a_{rh} = 2.35 - 2.55$ (global weighted error of $< 1.6$) with a best fit for $\beta^u = 0.346$ and $a_{rh} = 2.44$. The range of $\beta^u$ is thus close to that obtained for Mars, whereas slightly higher values of $a_{rh}$ are found.

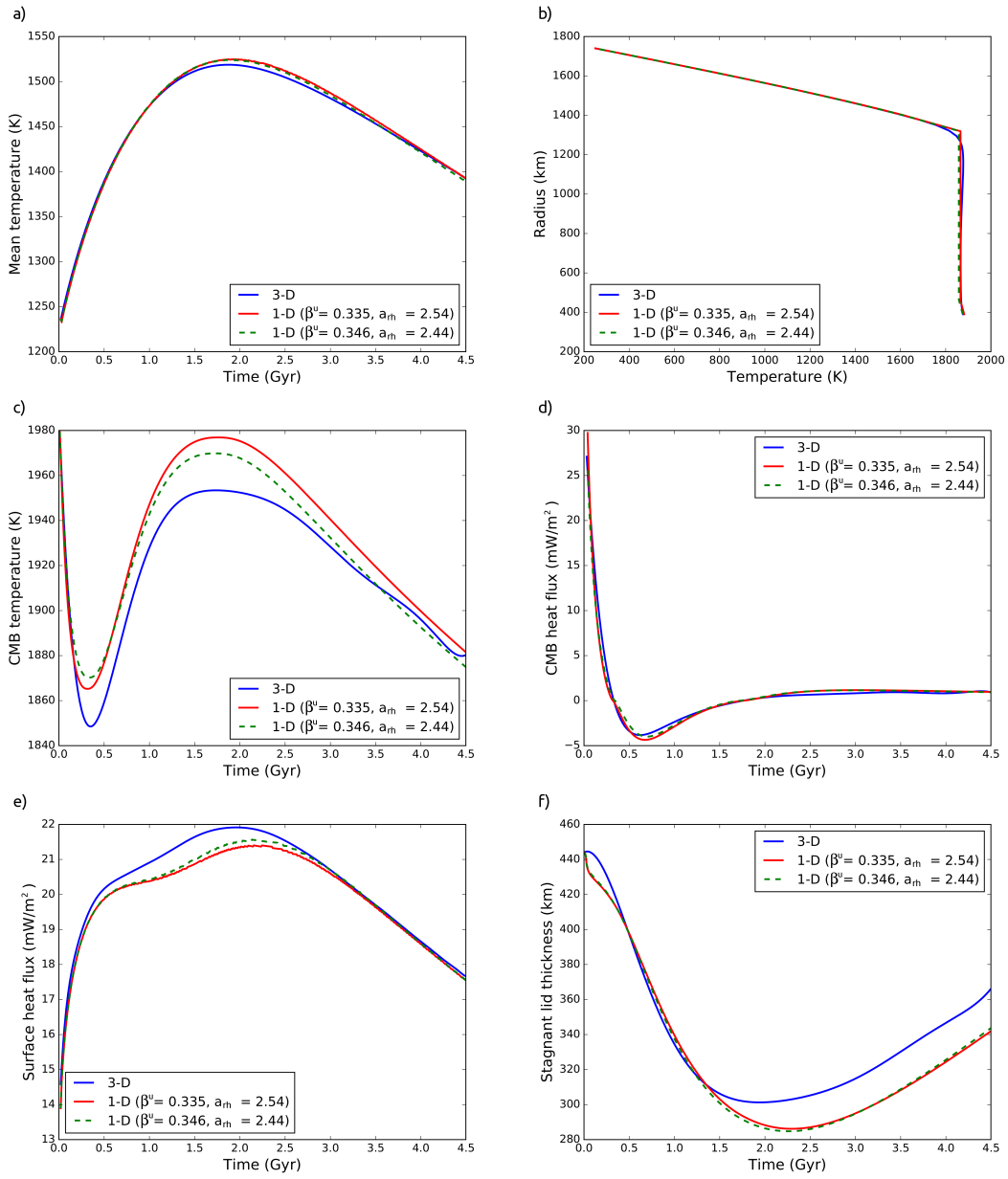


**FIGURE 3.12** – Moon's typical thermal evolution : (a) temperature averaged over the whole mantle, (b) temperature profile at the present-day, (c) temperature at the CMB, (d) heat flux at the CMB, (e) surface heat flux and (f) stagnant lid thickness. Results are shown for the reference 3-D model of the Moon (blue solid lines, case *Moon1* in Table 3.3) and for 1-D models considering $\beta^u = 0.346$ and $a_{rh} = 2.44$, the combination that minimizes cumulative weighted error on surface and CMB heat flux, temperature profiles and temperature at the base of the lid for the Moon's 3-D case (green dashed lines, stagnant lid definition similar to that of *Reese et al.*, 2005), and $\beta^u = 0.335$, $a_{rh} = 2.54$, our best combination for the three planets (red solid lines).

### 3.4.b Mercury

The prominent aspect ratio between Mercury's core and planetary radius results in a thin convective layer where many mantle plumes are present, at least during the first stages of evolution (Figure 3.11d). Due to the larger CMB surface area, basal heating is more important than for Mars and the Moon. Another major difference is a higher surface temperature than for the Moon and Mars that should influence the conductive heat transfer through the stagnant lid.

The thermal history of Mercury (Figure 3.13) is mainly influenced by its thin mantle : the Rayleigh number is low ($\sim 10^4$) and convection even stops at $\sim 2.5$ Gyr, when conductive heat transfer becomes dominant. Indeed, after $\sim 300$ Myr of slight warm up, the planet rapidly cools as the internal heat production is not sufficient to compensate for heat loss at the surface. The stagnant lid thickens during Mercury's entire evolution, while the surface heat flux, initially high, progressively decreases. As the mantle temperature rapidly decreases, the core and the CMB temperature efficiently cool down without any phase of heating by the mantle. The scaling laws for 1-D parametrized thermal models being only valid when the convection is well developed, we limit the comparison between 1-D and 3-D thermal models to the first 2 Gyr. Given this restriction, thermal evolution scenarios that fit 3-D ones can be retrieved with parametrized models when considering single combinations of $\beta^u$, $a_{rh}$ and the law of *Deschamps and Sotin* (2000) for $Ra^c_{crit}$ computation ($Ra^c_{crit} \sim 5$), especially those that minimize errors on heat flux ($\sim 0.2$ mW m$^{-2}$ and $\sim 0.7$ mW m$^{-2}$ at the surface and the CMB, respectively). Though the error on temperature profiles remains good, with an average of 9 K, the agreement between 1-D and 3-D models is better in the conductive part of the mantle as significant differences are observed in the convective layer, especially during the last stages of comparison. Indeed, 1-D models do not predict sufficient cooling. This might be explained by the poorly developed convective system after 2 Gyr of evolution. At that time heat transfer through Mercury's mantle predominantly occurs by conduction and the scaling laws of mantle convection used in 1-D models are not appropriate anymore to retrieve the 3-D thermal evolution (see Figure 3.13b).

When comparing 1-D and 3-D temperature profiles, surface and CMB heat flux in Monte Carlo simulations, we find again a similar trend between $\beta^u$ and $a_{rh}$ as those observed for Mars and the Moon (Figure 3.11e). However, Mercury's trend is less steep, which is clearly linked to its much thinner convecting layer (section 3.3.d and Figure 3.9b). Contrary to the other planets, the trend predicted by equation 3.29 considering the typical thermal parameters of *Mercury1* simulation at the time corresponding to the shift between planetary heating and cooling ($\sim 0.3$ Gyr, see Table 3.5 for values) is not in perfect agreement with the Monte Carlo one (green lines in Figure 3.14). This might be because convection is too weak and cannot be modelled sufficiently well with parametrized scaling laws. However, considering one of the combinations of $\beta^u$ and $a_{rh}$ from the predicted trend rather than the best Monte Carlo combinations leads to reasonable additional errors of $\sim 10$ K, $\sim 0.7$ mW m$^{-2}$ and $\sim 0.7$ mW m$^{-2}$ on temperature profiles, CMB and surface heat flux, respectively. When the temperature at the stagnant lid base is included in misfit computation (definition similar to that of *Reese et al.*,

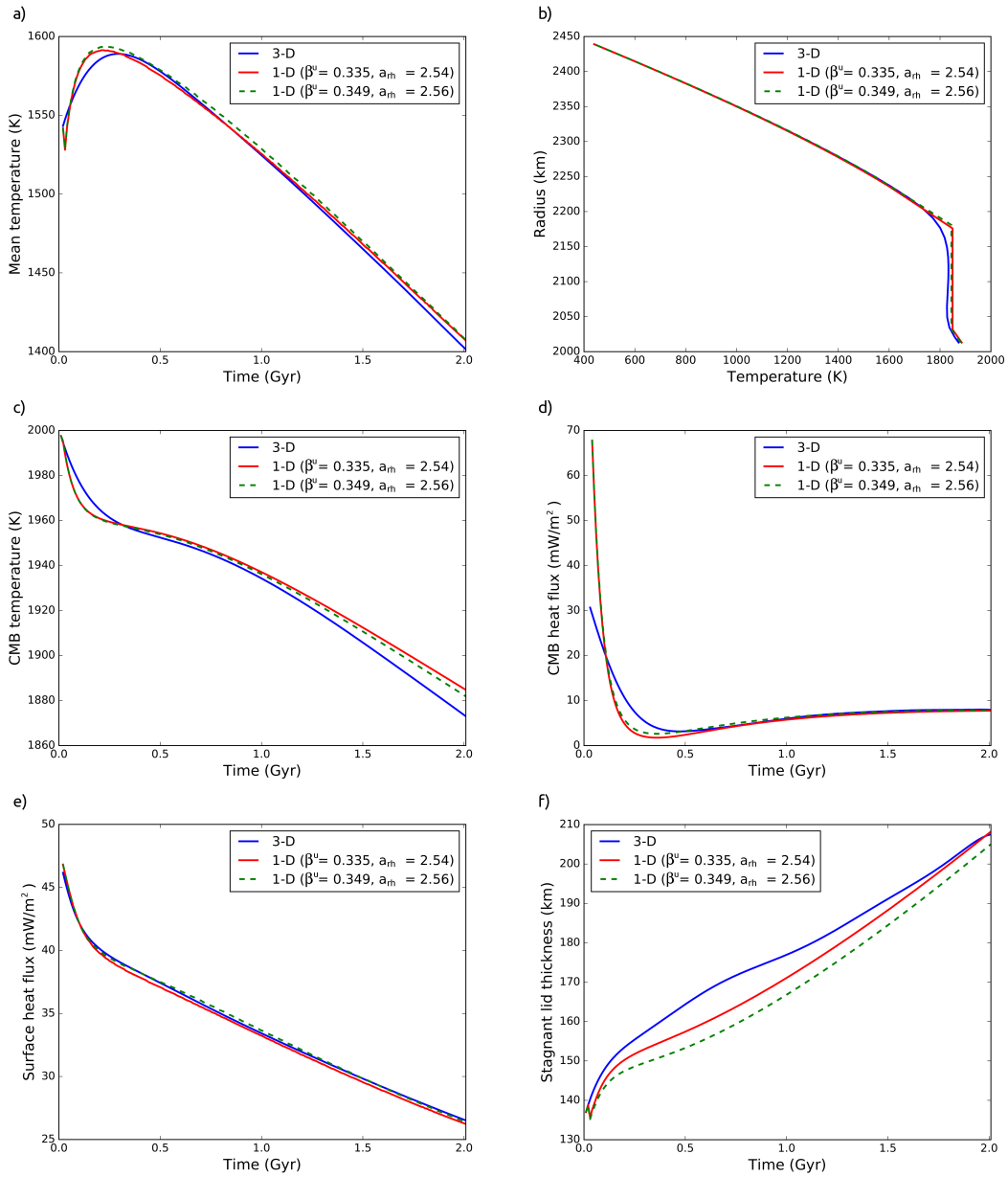


**FIGURE 3.13** – Mercury's typical thermal evolution : (a) temperature averaged over the whole mantle, (b) temperature profile at the end of the comparison period between 1-D and 3-D models, after 2 Gyr of evolution, (c) temperature at the CMB, (d) heat flux at the CMB, (e) surface heat flux and (f) stagnant lid thickness. Results are shown for the reference 3-D model of Mercury (blue solid lines, case *Mercury1* in Table 3.3) and for 1-D models considering the combination $\beta^{u} = 0.338$ and $a_{rh} = 2.47$ that provides the lowest cumulative weighted error on surface and CMB heat flux, temperature profiles and temperature at the base of the lid for the Mercury's 3-D case (green dashed lines, stagnant lid definition similar to that of *Reese et al.*, 2005), and $\beta^{u} = 0.335$, $a_{rh} = 2.54$, our best combination for the three planets (red solid lines).

2005), suitable combinations of $\beta^u$ and $a_{rh}$ are much more constrained with a Monte Carlo best fit for $\beta^u = 0.349$ and $a_{rh} = 2.56$ associated to a weighted average error of 1.22 (Figure 3.11f). The range of $\beta^u$ values ($0.34 - 0.36$) is almost similar to those obtained for Mars and the Moon, which further confirms that the relative importance of basal and internal heating does not affect the value of $\beta^u$ in stagnant lid convection. The range of $a_{rh}$ is similarly much more constrained to values between 2.5 and 2.6 that are thus higher than those of Mars but close to the values retrieved for the Moon, although the best combinations of $\beta^u$ and $a_{rh}$ for Mercury show a flatter trend due to its thinner mantle.

### 3.4.c Best combination for terrestrial planets

Since differences in convective layer thickness and surface temperature are observed among Mars, the Moon and Mercury, their Monte Carlo trends differ, which leads to different best parameter combinations for each planet (Figure 3.14a and Table 3.3). However, when considering the Monte Carlo results obtained for the 3-D reference models of Mars, the Moon and Mercury, we observe a convergence to a best combination $\beta^u = 0.335$ and $a_{rh} = 2.54$ when summing their errors on surface and CMB heat flux, temperature profiles and temperature at the base of the lid (Figure 3.14b). Considering this best combination rather than those predicted for each planet (see Table 3.3 for parameter values) leads to non-significant additional errors for the Moon and Mercury (see Figures 3.12 and 3.13, red lines). However, this average best value of $a_{rh}$ is located above the best trend of Mars (Figure 3.14a, in red), involving a slightly too thin stagnant lid and, therefore, too large rate of cooling for the interior (additional errors of $\sim 10$ km and $\sim 5 - 10$ K, respectively, see Figures 3.8a and 3.3a), which, however, still remains acceptable.

## 3.5 Discussion

### 3.5.a Best combination for 3-D models

Considering the best parameter combination $\beta^u = 0.335$ and $a_{rh} = 2.54$ in 1-D parametrized models gives a good fit to the thermal evolution observed for the 3-D reference models of Mars, the Moon and Mercury. However, for these 3-D models we did not examine an extensive parameter study on core radius, surface temperature and viscosity.

The parameter study that we performed with 2-D models for computational reasons (see section 3.3.d) shows that the best combinations of $a_{rh}$ and $\beta^u$ depends on the aspect ratio of the mantle. This dependence was also previously reported in other studies, although it mainly arises from a difference in total internal heating rather than from a difference in curvature (e.g., *Yao et al.*, 2014; *Guerrero et al.*, 2018). More unexpectedly, our best parameter combinations also vary when changing the activation energy, the reference viscosity and the surface temperature, which is likely due to the non-linear evolution of the viscosity with temperature when computing it with an Arrhenius law, as previously mentioned in section 3.3.d (see equation 3.10). However, despite the differences observed between all the trends, we showed that the thermal

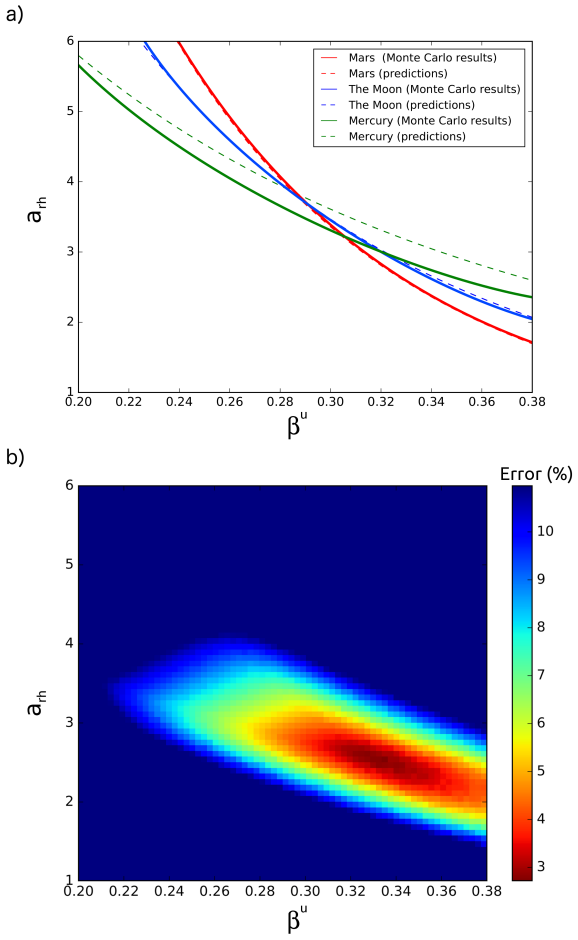


**FIGURE 3.14** – Best combinations of $\beta^u$ and $a_{rh}$ for the 3-D reference models of the three planets. (a) Best trends observed between $\beta^u$ and $a_{rh}$ in Monte Carlo simulations for Mars (red solid line), the Moon (blue solid line) and Mercury (green solid line) among 1-D parametrized models that minimize the difference with 3-D thermal parameter evolution (temperature profiles, surface and CMB heat flux). Equation 3.29 is used to predict these trends (dashed lines) given typical mantle temperature $T_m$ and stagnant lid thickness $D_l$ that are estimated at the time corresponding to the shift between planetary heating and cooling in 3-D models (see Table 3.5 for values). These predictions are in excellent agreement with Monte Carlo results, especially for Mars and the Moon, whereas predicted values of $a_{rh}$ are slightly overestimated for Mercury. (b) Average error of the Monte Carlo simulations for the 3-D reference models of the three planets (including the error on the temperature at the base of the lid, definition similar to that of *Reese et al.*, 2005). Errors are shown in a colorscale and correspond to the cumulative weighted differences between 1-D and 3-D models (in %, see section 3.2.c for the detailed methodology). The best combination minimizing the differences between 1-D models and 3-D simulations corresponds to $\beta^u = 0.335$ and $a_{rh} = 2.54$.

evolution of all 2-D simulations can be well retrieved when using a given combination of $\beta^u$ and $a_{rh}$ (respectively equal to 0.319 and 2.47), except if a low activation energy of $A = 150$ kJ mol$^{-1}$ is considered to mimic dislocation creep. A similar convergence to a unique best combination should thus be also retrieved with 3-D simulations. Therefore, the pair $\beta^u = 0.335$ and $a_{rh} = 2.54$ represents certainly the best choice for 3-D simulations and should remain valid for different model set-ups as long as diffusion creep is considered.

### 3.5.b Comparison with other studies

It should be noted that a comparison with most other scalings from the literature is not directly possible. As a reminder, we decouple the convecting mantle from the lid above, use the scaling representing an isoviscous fluid and determine the heat flow from the convecting mantle into the lid. Instead, the other approach considers the coupled system, i.e., the convecting mantle including the lid, and determines the heat flow at the surface. $\beta^u$ is typically not the same for both approaches. However, if one assumes a small transient effect and no internal heating in the lid, $\beta^u_m \sim \beta^u_t$ and equivalent values of $a_{rh}$ can be computed for given $a$ values (see section 3.2.b for the method used to derive equivalent values of $a_{rh}$ for other studies and Table 3.4 for the values computed with equation 3.24).

For a similar value of $\beta^u$, our best combination for 3-D models predicts a value of $a_{rh} = 2.54$ that is slightly higher than that found by *Davaille and Jaupart* (1993) ($\beta^u = 1/3$ and $a_{rh} = 2.24$, see Table 3.4). Considering this combination implies thus a too thick stagnant lid and a too low cooling rate due to an underestimation of the surface heat flux. Most other previous studies (see Table 3.4) have suggested slightly higher values of $a_{rh}$ for $\beta^u = 1/3$, which implies, conversely, a too thin stagnant lid leading to too high surface heat flux and cooling rate. For instance, the parameter pair $\beta^u = 1/3$ and $a_{rh} = 2.90$ retrieved by *Doin et al.* (1997) leads to an average increase of the stagnant lid thickness error by $\sim 30$ km and too low internal temperatures by $\sim 40$ K for the three planets in comparison with our best combination.

Our result fits to the 3-D thermal evolution for all the tested range of $\beta^u$ values ($0.2 - 0.38$) if the parameter $a_{rh}$ is changed accordingly, including the values of $\beta^u = 1/3$ and $\beta^u = 0.25$ that have been proposed to correspond to isoviscous flow with either free slip or rigid boundary conditions, respectively (*Deschamps and Sotin*, 2000). The corresponding value of $a_{rh}$ then implies a different thickness of the stagnant lid, which can also be interpreted as a different kinematic boundary condition at the base of the lid. Note that the finding of the large parameter range is only valid if we do not constrain the thickness of the stagnant lid but simply the thermal evolution with temperature profile and surface and core heat flow.

If accounting for the lid thickness defined by the temperature at the base of the lid in our Monte Carlo simulations, the suitable combinations of $a_{rh}$ and $\beta^u$ are more restricted, but with values that depend on the lid definition. Although $\beta^u$ larger than $1/3$ is also possible for the definition corresponding to the tangent to the velocity profile (see section 3.3.c for details),

we find values of $\beta^u$ that are close to $1/3$ for the two methods that define the base of the lid and have been considered in this study. In particular, our best value for the three terrestrial planets of $\beta^u = 0.335$ is almost equal to $\beta^u = 1/3$ since it minimizes the shell size effect on the relation between the values of $\beta^u$ and $a_{rh}$ (equation 3.29). Interestingly, this value is lower than those obtained for individual planets ($\beta^u \sim 0.345 - 0.349$), that certainly provide a better approximation of the isoviscous convection below a stagnant lid assumed in our approach, while still not depending so much on the convecting layer thickness (still close to $1/3$).

In any case, our results (when fitting also the lid thickness) comprise the value $\beta^u = 1/3$ predicted by the boundary layer stability analysis in the case of an isoviscous fluid in a Cartesian geometry heated from below and free slip boundary condition (*Turcotte and Schubert*, 1982). This result demonstrates that, in agreement with previous studies, the relation between the heat flux and Rayleigh number is independent of the heating mode in stagnant lid convection (e.g., *Reese et al.*, 2005; *Choblet and Parmentier*, 2009) and that the spherical geometry gives similar scaling laws to those obtained for a Cartesian box (*Iwase and Honda*, 1998; *Reese et al.*, 1999, 2005; *Choblet*, 2012). However, our best value of $\beta^u = 0.335$ is surprisingly high and more representative of a free-slip boundary condition.

### 3.5.c Limitations of the present study

The derived scaling law considers purely the thermal evolution of a planet but partial melting and the effects of intrusive and extrusive magmatism, i.e. the so-called heat pipe mechanism (*Moore and Webb*, 2013), may influence the evolution. While such processes could significantly affect the thermal evolution and cooling history of the Earth, Venus and Io (*Moore and Webb*, 2013; *Lourenço et al.*, 2018), they most likely played a limited role for Mars, Mercury and the Moon. For the latter, the bulk of the crust has been built during the first Gyrs and only limited amounts of melt have been produced thereafter (e.g., *Greeley and Schneid*, 1991; *Byrne et al.*, 2016; *Hiesinger et al.*, 2003). Furthermore and more important, we do not expect a significant difference in the derived scaling parameters, i.e. in the values of $a_{rh}$ and $\beta^u$, because in principle the volcanic heat transport can be introduced in the mantle energy equation as an additional sink (e.g., *Morschhauser et al.*, 2011). However, this needs to be tested in future studies.

We do not consider chemical heterogeneities in the planetary interior. Parametrized thermal evolution models cannot self-consistently account for the formation and evolution of mantle geochemical reservoirs, but assume instead a well-mixed interior. A simple approach to consider compositional buoyancy due to melting in parametrized models has been introduced for Mars by *Fraeman and Korenaga* (2010). However, in that approach the density contrast due to composition is approximated with an equivalent temperature contrast (*Korenaga*, 2009), which shows a different convective and cooling behavior in contrast to using fully dynamical model that consider melting (*Plesa et al.*, 2014). We note that geochemical reservoirs in the mantle of terrestrial planets have been proposed to explain the surface composition of Mercury (e.g.,

*Weider et al.*, 2015), the isotopic signatures of Martian meteorites (e.g., *Papike et al.*, 2009), and the asymmetric distribution of mare basalts on the surface of the Moon (e.g., *Hiesinger et al.*, 2003). Nevertheless, the location, size, and evolution of chemical anomalies is poorly understood, and so far, a homogeneous mantle seems to reproduce at best the observations related to the thermochemical history of Mars, Mercury and the Moon (e.g., *Breuer et al.*, 2016; *Tosi et al.*, 2013; *Laneuville et al.*, 2013).

It has been argued by *Choblet and Sotin* (2000) that an initial stage up to 1 Gyr cannot be described by the stagnant lid parametrization, which is based on steady-state convection models. During that initial transitional stage the mantle cools by conduction until the upper thermal boundary layer becomes unstable due to increased mantle temperatures and reduced viscosities, and convection sets in. Thus, the cooler the early planet the longer it takes for convection to start. In general, however, it is assumed that planets have temperatures close to the solidus due to the energy released during accretion and core formation (one even assumes early magma oceans). Under these conditions, convection starts in less than 1 Myr and the scaling laws can be applied even for the early planetary evolution.

Parametrized thermal evolution models are also often used to constrain the magnetic field history of a planet because the magnetic field generation in the iron-rich core of a planet is strongly coupled to its thermal evolution (e.g., *Stevenson et al.*, 1983; *Breuer and Moore*, 2015). In the present thermal evolution models we have considered the energy balance of the core to account for the heat flow from the core into the mantle and to calculate the core temperature as a function of time - although we did not consider the potential growth of an inner solid core which would require a modified energy equation of the core (e.g., *Stevenson et al.*, 1983). Our results show that there is an excellent agreement of the CMB heat flux and the CMB temperature between the parametrized and the 2D-3D convection models. Only in the early evolution we typically observe a larger error with values of about 25 K for the CMB temperature (Figure 3.6) and an average difference of 17 mW $m^{-2}$ for the CMB heat flux that is predominantly due to an overestimation of the CMB heat flux by the parametrized models. Thus, the parametrized models may slightly overestimate the strength of a thermal dynamo because the field strength scales with 1/3 of the heat loss relative to the heat flow along the adiabat (e.g., *Stevenson et al.*, 1983). Furthermore, the onset time for inner core growth is overestimated - if the temperature decreases below the core melting temperature - because the core temperatures are initially too low. However, the general thermal and chemical evolution of the core including the magnetic field generation will not vary too much between the models, as the differences will quickly balance each other out.

## 3.6 Conclusion

Comparison of 3-D models of mantle convection with 1-D parametrized thermal models show that the latter can well reproduce the thermal evolution of a cooling planet in a stagnant lid regime with the same set of scaling parameters $\beta^{u}$ and $a_{rh}$ that parametrize the heat flux from

the convecting mantle into the base of the stagnant lid. Several combinations of the scaling parameters provide in fact a good description of the planet's thermal evolution. Those combinations are distributed along a negative correlation between suitable values of $\beta^u$ and $a_{rh}$ : if $\beta^u$ increases the upper TBL is thinner, which implies a thicker stagnant lid and a lower value of $a_{rh}$. The shape of this best-fit curve depends on surface temperature, mantle characteristics - rheology and size of the convecting layer - and hence varies for the different terrestrial planets. However, for a stagnant lid defined by the intersection between the tangent to the velocity profile at the depth corresponding to the maximum velocity gradient and the depth axis, they converge for our 3-D models for Mars, the Moon and Mercury to similar values of $a_{rh} = 2.54$ and $\beta^u = 0.335$.

# 4 Validity of the scaling laws for more realistic models

In the previous section 3, we consider simplified models that do not account for all the complexities of planetary mantles, especially for the presence of an enriched crust in radioelements, an adiabatic temperature gradient in the mantle or the pressure-dependence of the viscosity. In this section we run 2-D models accounting for such additional parameters (see Table 3.6 for detailed parameters) to investigate their effects on the best combination of $\beta^u$ and $a_{rh}$ for 2-D models (values of 0.319 and 2.47, respectively, see section 3.3.d).

## 4.1 Effect of additional parameters

### 4.1.a Adiabatic temperature gradient

We consider here a model with the same parameters than the reference 2-D model for Mars (case *Mars2* in Table 3.3), except that we assume an adiabatic temperature gradient in the mantle (red and blue lines on Figure 3.15b, respectively). In the Gaia code the following

| Case | d [km] | $\Lambda$ | Adiabatic gradient | $V$ [cm$^3$/mol] | $\beta^u$ | $a_{rh}$ | $Ra^c_{crit}$ |
|---|---|---|---|---|---|---|---|
| *Mars2* | - | - | no | 0 | 0.316 | 2.47 | 19 |
| *Adiab* | - | - | yes | 0 | 0.321 | 2.40 | 19 |
| *Crust* | 50 | 10 | no | 0 | 0.321 | 2.41 | 19 |
| *Vact* | - | - | no | 6 | 0.312 | 2.5 | 19 |
| *ACV* | 50 | 10 | yes | 6 | 0.310 | 2.56 | 19 |

**TABLE 3.6** – Parameters considered in the additional 2-D dynamical thermal models (section 4). The other parameters (thickness of the convective mantle, initial temperature, reference viscosity and activation energy...) are those of the referent 2-D model *Mars2* (see Table 3.3 for details). The best parameter combination of $\beta^u$ and $a_{rh}$ is indicated for each model, when comparing surface and CMB heat flux, temperature profiles and temperature at the base of the lid between 1-D and 2-D models. For each model we consider the best value of $Ra_{crit} = 19$ obtained for the case *Mars2*.

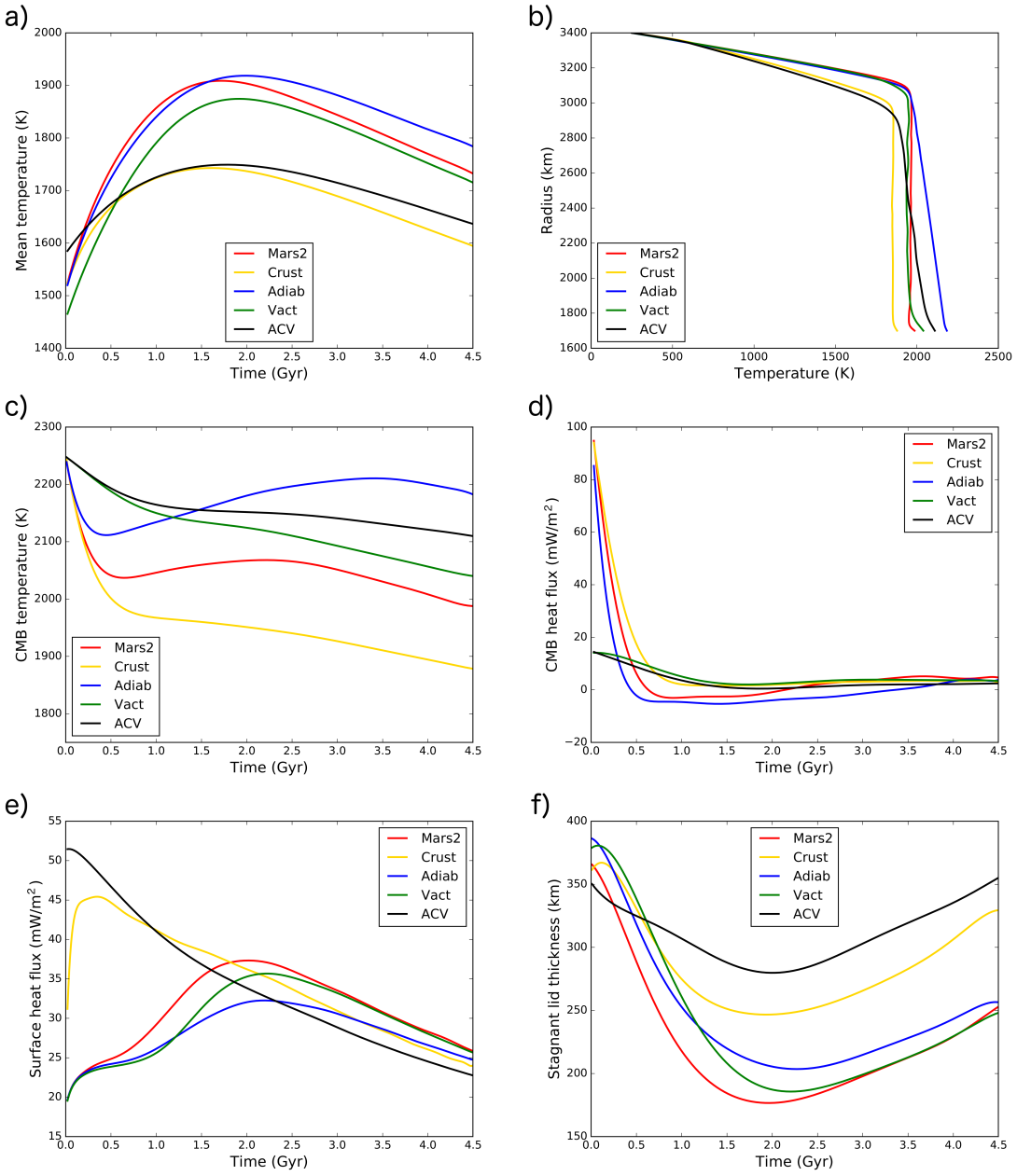


**FIGURE 3.15** – Thermal evolution of the case *mars2* and the additional 2-D dynamical models considered in section 4 (see Table 3.6 for details) : (a) temperature averaged over the whole mantle, (b) temperature profile at the present-day, (c) temperature at the CMB, (d) heat flux at the CMB, (e) surface heat flux and (f) stagnant lid thickness.

non-dimensional conservation equations of linear momentum and thermal energy are solved (e.g. *Christensen and Yuen*, 1985) :

$$\nabla \cdot \left[\eta'(\nabla\vec{v} + (\nabla\vec{v})^T)\right] - \nabla p + Ra_i \alpha T \vec{e}_r = 0 \tag{3.30}$$

$$\frac{DT}{Dt} = \nabla^2 T + Di\alpha(T + T_s) + \frac{Di}{Ra_i}\Phi + \frac{Ra_Q}{Ra_i} \tag{3.31}$$

where $\Phi \equiv \underline{\tau} : \underline{\dot{\varepsilon}}/2$ is the viscous dissipation, with $\underline{\tau}$ and $\underline{\dot{\varepsilon}}$ corresponding to the deviatoric stress and strain rate tensors, respectively. The dissipation number $Di$ is given by :

$$Di = \frac{\alpha g D}{C_p} \tag{3.32}$$

When accounting for the adiabatic gradient in 1-D parametrized models, the temperature $T_b$ at the bottom of the convecting mantle is higher than $T_m$ (see Figure 4.3, in chapter 4), contrary to the case *Mars2* in which $T_b = T_m$ (see Figure 3.2). However, this adiabatic temperature gradient does not participate to the dynamics of the convection, which implies that $\Delta T^u = T_c - T_b + T_m - T_l$ in $Ra^u_{rh}$ computation (equation 3.20) with $T_b$ given by :

$$T_b = T_m + \frac{\alpha g T_m}{C_m}(R_l - R_c - \delta^u - \delta^c) \tag{3.33}$$

Assuming an adiabatic temperature gradient in the mantle does not much influence the thermal evolution of the upper layers of the mantle, which implies minor differences between the surface heat flux and stagnant lid thicknesses observed for the cases *Adiab* and *Mars2* (Figure 3.15e and f). 1-D parametrized models can thus very satisfactorily fit the 2-D evolution of the upper layers of the mantle with similar errors than those reported for the case *Mars2* ($\sim$ 1 mW/m$^3$ for the surface heat flux and $\sim$ 8 km for the stagnant lid thickness). Inversely, the temperature difference between the bottom of the mantle and the core being considerably reduced by the adiabatic temperature increase with depth, the core is particularly inefficiently cooled in the case *Adiab*, which leads to higher CMB temperatures by $\sim$ 200 K at the present day compared to the case *Mars2* (Figure 3.15c). Moreover, after a first phase of fast cooling, the core becomes even colder than the bottom layers of the mantle : a very slight negative heat flux is then present at the CMB, which means that the core is heated by the mantle between 0.5 and 3.5 Gyr (Figure 3.16a and b). This phase of core heating is not well captured by 1-D models that overestimate the CMB temperature during this period because of a too large heat flux towards the core (average errors of $\sim$ 40 K and $\sim$ 6 mW/m$^2$ for CMB temperature and heat flux, respectively). This likely results from the computation of the lower TBL thickness in parametrized models (equation 3.19) : when the heat flux at the CMB becomes negative, the TBL is located in the core and its thickness does not, therefore, depend on $\Delta T^c = T_c - T_b$ ; using equation 3.19 is then not appropriate anymore. However, when the core becomes again hotter

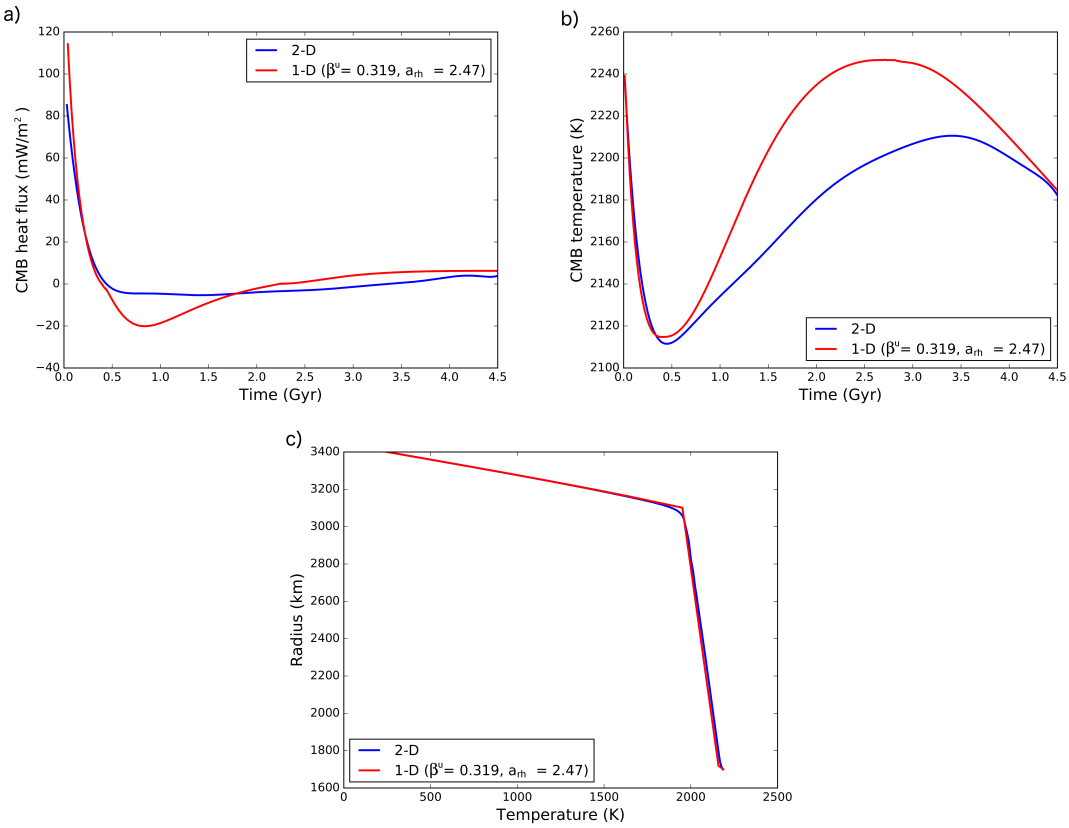


**FIGURE 3.16** – 2-D and 1-D thermal evolution models accounting for the adiabatic temperature gradient in the mantle (case *Adiab* in Table 3.6) : (a) heat flux at the CMB (b) temperature at the CMB and (c) temperature profile at the present-day. Results are shown for the 2-D model *Adiab* (in blue, see Table 3.6) and for a 1-D model considering the best combination for the 2-D models of the section 3.3.d, $\beta^u = 0.319$ and $a_{rh} = 2.47$ (in red), indistinguishable from the thermal evolution obtained with the best parameter combination for the case *Adiab*, $\beta^u = 0.321$ and $a_{rh} = 2.40$.

than the mantle the 1-D temperature at the CMB fastly converges to that of the 2-D model with similar present-day values.

When comparing 1-D and 2-D temperature profiles, surface and CMB heat flux in Monte Carlo simulations, we find a trend between the best values of $\beta^u$ and $a_{rh}$ (green solid line in Figure 3.17a) that is almost indistinguishable from that of the reference 2-D case (red solid line in Figure 3.17a). This was expected since the thermal evolution of the upper layers (that is directly linked to the values of the scaling parameters) is comparable in the two simulations *Mars2* and *Adiab*. Consequently, the best parameter combination for the case *Adiab* is almost the same than that of the case *Mars2* (see Table 3.6 for values) and considering the best parameter combination for 2-D models of $\beta^u = 0.319$ and $a_{rh} = 2.47$ (see section 3.3.d, black star in Figure 3.17a) leads to an excellent agreement with the thermal evolution of the case *Adiab*,

except, again, for the lowermost layers of the mantle and the core. A better parametrization needs thus to be found for the thermal evolution of the core when the overlying mantle heats it up.

### 4.1.b Crust

In the reference 2-D model *Mars2*, the distribution of the radioelements is uniform within the shell, though a vertical layering in internal heat source concentrations has been proved to strongly influence the mantle convection pattern and the thermal evolution of a planet (e.g. *Grott and Breuer*, 2009; *Sekhar and King*, 2014). In this section we compare the results of *Mars2* with that of a model accounting for the presence of a crust that concentrates half of the

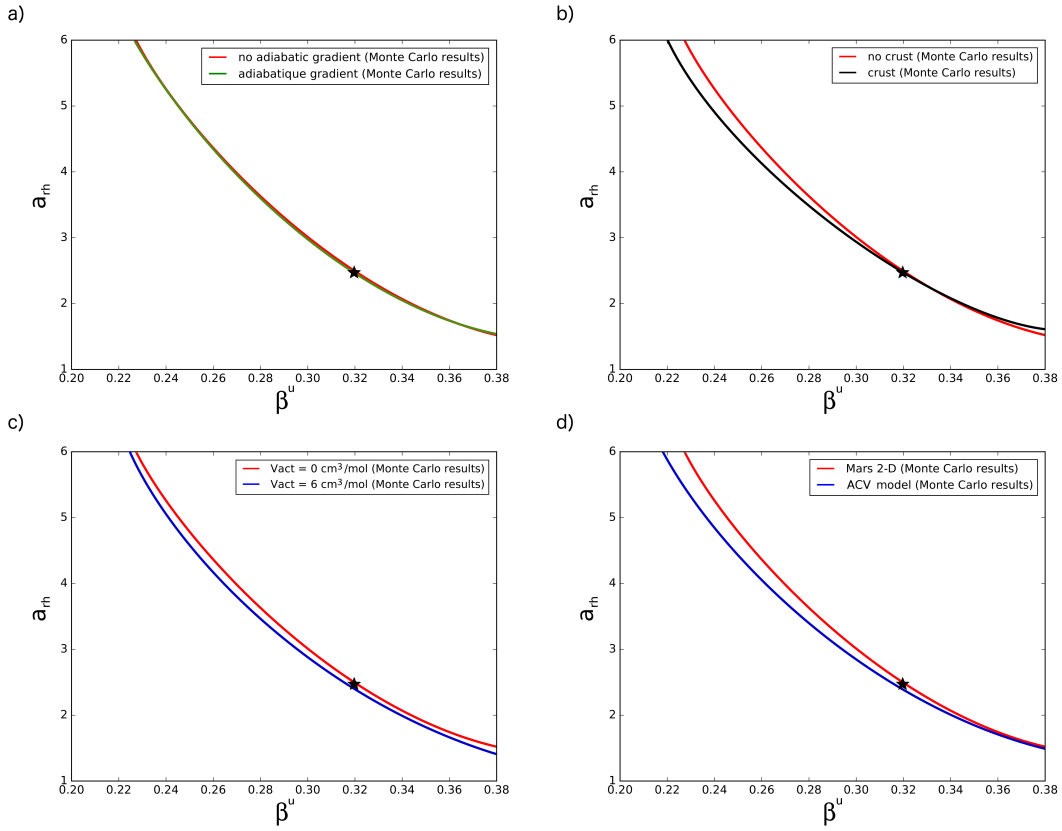


**FIGURE 3.17** – Best Monte Carlo trends between $\beta^u$ and $a_{rh}$ for the additional 2-D models considered in section 4. The trend of the reference 2-D model of Mars (red line, case *Mars2* in Table 3.3) is compared with those obtained if considering an adiabatic temperature increase in the mantle in (a) (case *Adiab* in Table 3.6), a crust that concentrates half of the radioelements in (b) (case *Crust* in Table 3.6), the pressure-dependence of the viscosity in (c) (case *Vact* in Table 3.6) and a model accounting for all those complexities (crust, adiabatic temperature gradient, pressure-dependence of the viscosity, case *ACV* in Table 3.6) in (d). The best combination for all the 2-D simulations considered in section 3.3.d is represented by the black star ($\beta^u = 0.319$ and $a_{rh} = 2.47$).

bulk radioelement content (crustal thickness of $d = 50$ km, enrichment factor in radioelements of $\Lambda = 10$ compared to the primitive mantle, case *Crust* in Table 3.6).

In the case *Crust*, since large amounts of radioelements are concentrated in the upper layers, the internal heat production is easily conducted away towards the surface, which implies a high surface heat flux during the first stages of the evolution when the heat sources are the most abundant (Figure 3.15e). In parallel, the internal heat production in the mantle is lower, which results at the present day in colder temperatures in the well mixed interior by $\sim 120$ K and in a thicker stagnant lid by $\sim 80$ km compared to the case *Mars2* (Figure 3.15a and f). In this configuration, the hot core is thus efficiently cooled and no phase of negative heat flux at the CMB is observed.

Given these differences, 1-D parametrized models can very satisfactorily fit the thermal evolution of the simulation *Crust* if assuming the best combination for 2-D models ($\beta^u = 0.319$ and $a_{rh} = 2.47$, see section 3.3.d) with average errors of 0.7 mW/m$^2$, 2 mW/m$^2$ (but mostly at the beginning, as for the case *Mars2*), 4 K and 8 km for surface and CMB heat flux, temperature profiles and stagnant lid thickness, respectively. Indeed, Figure 3.17b shows that the trends of the cases *Mars2* and *Crust* converge for values of $\beta^u = 0.31 - 0.35$, which includes the best combination for 2-D models (black star). However, as previously reported for the cases where a relatively thicker lid is observed (for instance cases *PS*1 and *PS*6 in section 3.3.d, Figure 3.9b and d, respectively), the Monte Carlo trend of the case *Crust* is steeper than that of the reference 2-D model.

### 4.1.c Pressure-dependence of the viscosity

For the reference case *Mars2*, the viscosity is computed with equation 3.10 in which the temperature increase with depth leads to a decrease of the viscosity. However, while dominant, this decrease is in reality partly counteracted by the pressure effect on the viscosity : the deeper in the shell, the higher the viscosity at a given temperature is. Here, we introduce the model *Vact* that has the same parameters than the model *Mars2* (see Table 3.3 for details), except that we use a more realistic Arrhenius law in which the viscosity depends on temperature and pressure for both the upper and lower TBL (see equations 3.19 and 3.20) :

$$\eta(T,P) = \eta_0 exp\left(\frac{A+PV}{RT} - \frac{A+P_{ref}V}{RT_{ref}}\right) \tag{3.34}$$

where $V$ is the activation volume and $P_{ref} = 3 \times 10^9$ Pa a reference pressure at which the reference viscosity $\eta_0$ is reached. For the case *Vact* we consider an activation volume of $V = 6$ cm$^3$/mol representative of diffusion creep (*Karato and Wu*, 1993).

The pressure-dependence of the viscosity mostly affects the thermal evolution of the lower layers of the mantle, especially those close to the CMB, which implies in particular a thicker lower TBL (Figure 3.15b, see equations 3.19 and 3.20 for thickness computation). Since the heat flux at the CMB decreases when the lower TBL thickness increases (see equation 3.13

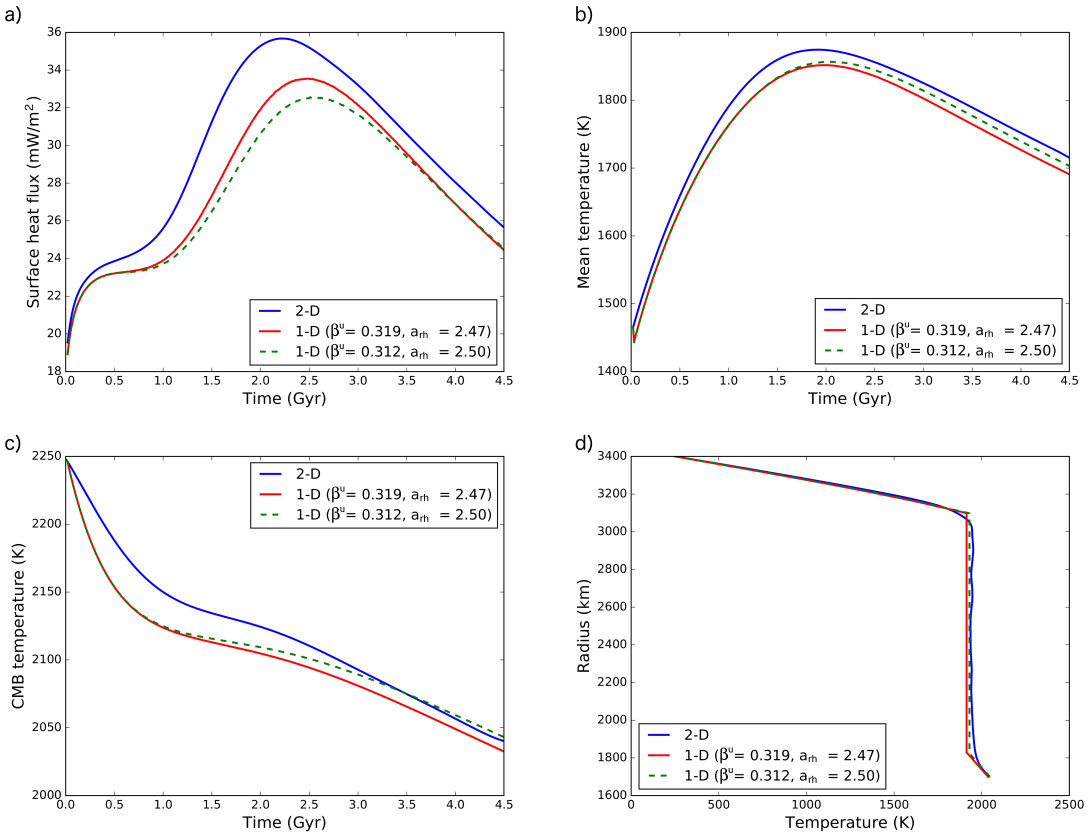


**FIGURE 3.18** – 2-D and 1-D thermal evolution models accounting for the pressure-dependence of the viscosity (case *Vact* in Table 3.6) : (a) surface heat flux, (b) temperature averaged over the whole mantle, (c) temperature at the CMB and (d) present-day temperature profile. Results are shown for the 2-D model *Vact* (blue solid line), for 1-D models considering the best combination for 2-D models ($\beta^u = 0.319$ and $a_{rh} = 2.47$, red solid line) or the best Monte carlo combination for the case *Vact* ($\beta^u = 0.312$ and $a_{rh} = 2.50$, green dashed line).

and Figure 3.15d) the cooling of the core is less efficient, which leads to a higher temperature at the CMB by $\sim$ 100 K on average compared to the case *Mars2*, without any phase of core heating by the overlying mantle (Figure 3.15c). Conversely, the thermal evolution of the rest of the shell - i.e. stagnant lid thickness, average temperature and surface heat flux - is only slightly different to that of the case *Mars2*. Indeed, the pressure effect on the viscosity is lower for the upper TBL than for the lower TBL that is located deeper in the mantle. However, when considering the best combination for the case *Vact* (see Table 3.6 for values), parametrized models underestimate the temperature of the well mixed interior and the surface heat flux by $\sim$ 15 K and $\sim$ 2 mW/m$^2$ on average, which implies a resulting too low temperature at the CMB by $\sim$ 15 K (Figure 3.18a-c, green dashed lines). The best trend of the simulation *Vact* is shifted for a given value of $\beta^u$ to lower values of $a_{rh}$ by $\sim$ 0.1 (Figure 3.17c, blue line) compared to the best trend of the reference case and to the best combination for 2-D simulations (red line and black star in Figure 3.17c, respectively). Considering the value of $a_{rh}$ of the best

combination for 2-D simulations implies thus a thinner stagnant lid (see equation 3.21) and a larger underestimation of the internal temperature of $\sim$ 25 K (Figure 3.18b, red solid line). On the other hand, the thinner lid leads to a higher surface heat flux slightly more consistent with that of the 2-D model (Figure 3.18a, red solid line).

## 4.2 Towards a more realistic model for Mars

Including additional parameters in the reference case *Mars2* (see Table 3.3 and section 3.3.d) introduces non-negligible misfits between 1-D and 2-D models, as described in the previous section 4.1. In particular, when the core is heated by the overlying mantle layers the negative heat flux at the CMB leads to an overestimation of the temperature at the CMB, whereas the global cooling rate of the planet is overestimated for the model accounting for the pressure-dependence of the viscosity. In this context, to what extent can parametrized models reproduce the thermal evolution of a 2-D dynamical model accounting for all the additional parameters introduced in the previous section 4.1 ? Is still the best combination for 2-D models $\beta^u = 0.319$ and $a_{rh} = 2.47$ appropriate ? In the following, we thus consider a more realistic 2-D model for Mars (case *ACV* in Table 3.6), which assumes an adiabatic temperature gradient in the mantle, the pressure-dependence of the viscosity (equation 3.34) and the presence of an enriched crust that concentrates the half of the radioelements.

The differences observed between the thermal evolution of the cases *Mars2* and *ACV* result from a combination of the additional parameters assumed in this latter model (Figure 3.15). Indeed, as previously described in section 4.1, since the crust concentrates large amounts of radioelements in the model *ACV*, the surface heat flux is high during the first stages, whereas the temperature averaged over the whole shell is colder by $\sim$ 100 K, which induces a thicker stagnant lid by $\sim$ 100 km compared to the case *Mars2*. On the other hand, because of the adiabatic temperature increase with depth and the pressure-dependence of the viscosity, the core and the lower layers of the mantle are less efficiently cooled, which leads to higher temperatures at the CMB (by up to 150 K at the present-day). However, contrary to the case *Adiab*, there is no phase of core heating by the overlying mantle since the internal temperatures are cooler, due to the presence of a crust enriched in radioelements. We finally observe that the switch between the initial mantle warming and the subsequent cooling of the planet is slightly delayed by $\sim$ 0.5 Gyr compared to the case *Mars2*, which arises from the less efficient heat extraction from the lower layers of the mantle.

The trend between $\beta^u$ and $a_{rh}$ in Monte Carlo simulations for the case *ACV* (Figure 3.17d, blue line) directly reflects the tendancies of those of the cases *Crust* and *Vact* (Figure 3.17 b and c, in black and blue, respectively) and is therefore less steep and slightly shifted compared to that of the case *Mars2*. When considering the temperature at the base of the lid as an additional constraint in the Monte Carlo simulations, a best parameter combination of $\beta^u = 0.31$ and $a_{rh} = 2.56$ is obtained, which is associated to a surprisingly low weighted error of 1.53 (versus 2.64 for the best fit of the case *Mars2*, see section 3.2.c for error computation). This error is mainly

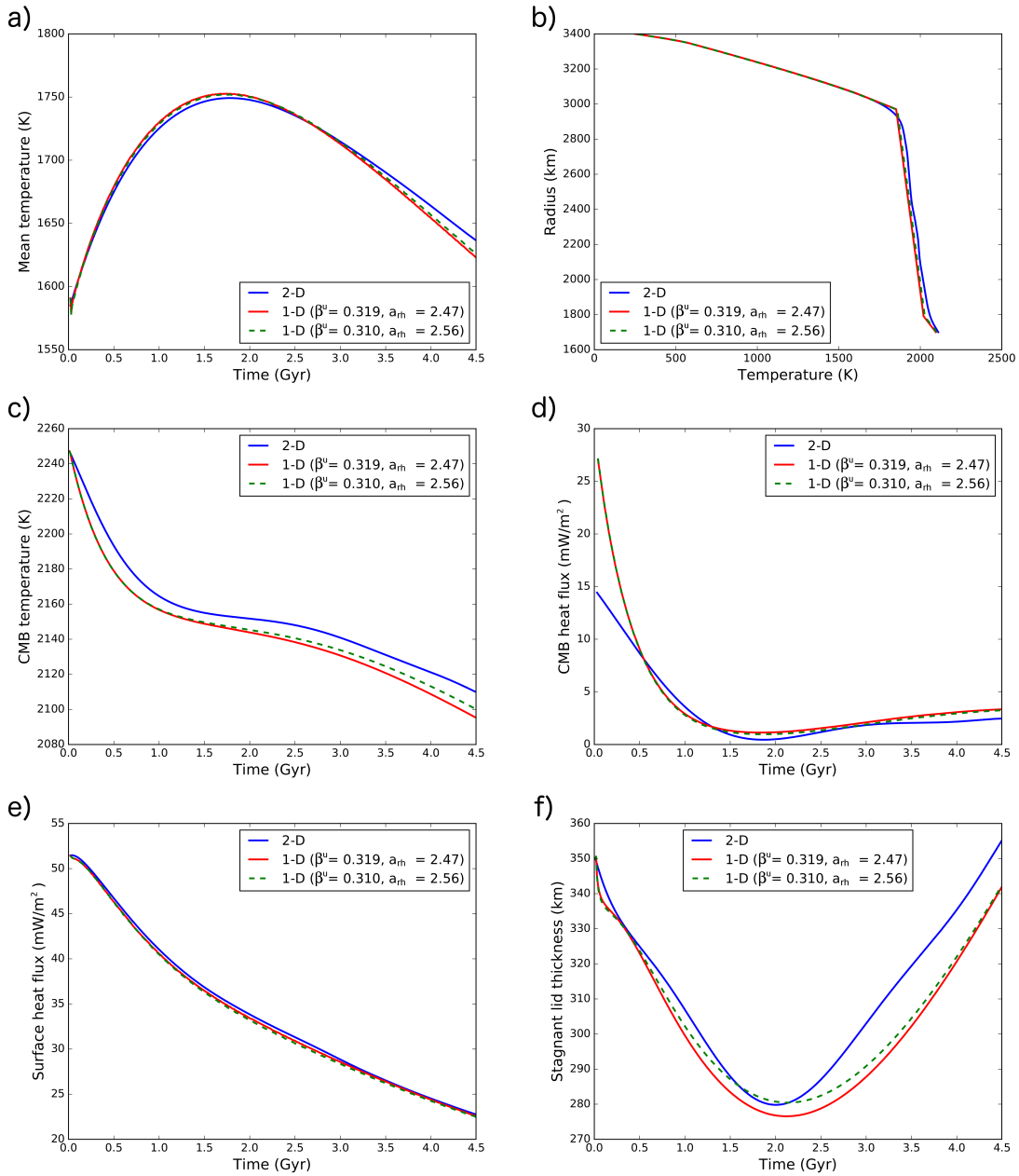


**FIGURE 3.19** – 2-D and 1-D thermal evolution models accounting for a crust, an adiabatic temperature gradient in the mantle and a pressure-dependence of the viscosity (case *ACV* in Table 3.6) : (a) temperature averaged over the whole shell (including the crust), (b) temperature profile at the present-day, (c) temperature at the CMB, (d) heat flux at the CMB, (e) surface heat flux and (f) stagnant lid thickness (estimation with the same method as *Reese et al.* (2005) in the 2-D model, see section 3.3.c). Results are shown for the reference 2-D dynamical model *ACV* (blue solid lines) and for 1-D models considering $\beta^u = 0.319$ and $a_{rh} = 2.47$ (the best combination for 2-D models defined in section 3.3.d, red solid lines) and $\beta^u = 0.310$ and $a_{rh} = 2.56$, the best combination for the *ACV* case (green dashed lines).

due to a slight underestimation of the stagnant lid thickness and of the internal temperatures, both at the CMB and in the convecting layer (green dashed lines in Figure 3.19). Since the best trend of the model *ACV* is close to the best combination for 2-D models, $\beta^u = 0.319$ and $a_{rh} = 2.47$, using this set of parameters in 1-D models also well fits the 2-D thermal evolution. Minor additional misfits are indeed observed on the stagnant lid thickness and the temperature at the CMB (red lines in Figure 3.19), with a global weighted error of only 1.65 when considering $\beta^u = 0.319$ and $a_{rh} = 2.47$. This error value remains very satisfactory regarding the large impact the presence of a crust, the pressure-dependence of the viscosity and the adiabatic temperature increase have on the global thermal evolution.

## 4.3 Conclusion

The thermal evolution of more complex 2-D thermal models considered in this section is generally well reproduced by parametrized model, especially for the models *Crust* (addition of a crust compared to the case *Mars2*) and *ACV* (addition of a crust, pressure-dependence of the viscosity and adiabatic temperature gradient in the mantle) for which only slight misfits are reported. Moreover, the best parameter combinations for all models are similar, or only slightly different from the best set of values previously defined in section 3.3.d for 2-D models ($\beta^u = 0.319$ and $a_{rh} = 2.47$), which gives us confidence in the robustness of this specific combination to describe the thermal evolution of 2-D models. This implies that the best parameter combination $\beta^u = 0.335$ and $a_{rh} = 2.54$ obtained for 3-D models in section 3.4.c should be valid for more complex model set-up accounting for a vertical layering in radioelements, an adiabatic temperature gradient in the mantle and the pressure-dependence of the viscosity.

# CHAPTER 4

# EFFECT OF THE NORTHERN AND SOUTHERN CRUSTAL PROPERTIES ON MARS'S THERMAL EVOLUTION

**Sommaire**

# 1 Summary

Estimates of the Martian elastic lithosphere thickness suggest small values of $\sim 25$ km during the Noachian for the southern hemisphere and a potentially large present-day difference below the two polar caps ($\geq 300$ km in the north and $> 110$ km in the south with a best fit of 161 km). In addition, young lava flows indicate that Mars has been volcanically active up to the recent past.

We investigate whether a north/south hemispheric dichotomy in crustal properties and composition can explain these constraints. Using 1-D parametrized thermal evolution models in Monte Carlo simulations, our results suggest two main categories of suitable crustal models. The first one (Uniform Crustal Models, UCM) is characterized by a large north/south difference in crustal thickness, the southern crust being thicker and equally or slightly more enriched in radioelements than the northern one. An alternative category of models is represented by some Non-Uniform Crustal Models (NUCM) cases that present a smaller north/south difference in crustal thickness with a southern crust that is less dense (up to 480 kg/m$^3$) than the northern one and migh contain a non-negligible proportion of felsic rocks. For such models, the southern crust is also much more enriched (enrichment factor up to $\sim 21$) than the rest of the crust (enrichment factor of 10). All the models indicate that $55-65$ % of the bulk radioelement content are in the crust, and most of it ($43-51$ %) in the southern one. Our models predict a dry mantle and a wet or dry crustal rheology today, which is consistent with a mantle depleted in radioelements and volatiles. At the present day, we retrieve north/south surface heat flux of $17.1-19.5$ mW/m$^2$ and $24.8-26.5$ mW/m$^2$, respectively, and a large difference in lithospheric temperatures between the two hemispheres ($170-304$ K in the shallow mantle).

To validate the results obtained with parametrized models, we perform 3-D simulations accounting for representative properties of the suitable UCM and NUCM cases. For each case, the thermal evolutions of the 3-D and 1-D models are in good agreement and predict, in particular, similar stagnant lid thicknesses and temperature profiles at the present day. The 3-D simulations for the UCM and NUCM cases show similar convection patterns characterized by a potential north/south asymmetry linked to the crustal dichotomy with mantle plumes preferentially located in the northern hemisphere and below the dichotomy boundary.

## 2 Motivation

The evolution of the Martian elastic lithosphere thickness estimates remains still enigmatic (see chapter 2). Indeed, the large present-day value estimated below the northern polar cap ($>$ 300 km, *Phillips et al.*, 2008) is hardly compatible with the lower present-day estimate below the southern polar cap ($>$ 110 km with a best fit of 161 km, *Wieczorek*, 2008) and, moreover, with the low Noachian estimates ($\sim$ 25 km) (e.g. *Grott and Breuer*, 2009; *Grott et al.*, 2013). Noting that all the Noachian estimates are located in the southern hemisphere, we investigate in this chapter whether a north/south dichotomy in crustal structure and/or composition could reconcile the low elastic thickness estimates that have been made for the southern hemisphere with the present-day large value below the northern polar cap.

## 3 Hemispheric Dichotomy in Lithosphere Thickness on Mars Caused by Differences in Crustal Structure and Composition

This section corresponds the article that was published in the *Journal of Geophysics research* (*Thiriet et al.*, 2018).

### 3.1 Introduction

In the absence of direct heat flux measurements, the thermal and geodynamic history of Mars still remains enigmatic. Indirect evidence for the evolution of the Martian heat flux with time is offered by elastic lithosphere thickness estimates. They represent a measure of the amount of stress the lithosphere can sustain before yielding, either by brittle deformation in the upper cold part of the lithosphere or by ductile deformation in the hotter lower one. Elastic lithosphere thicknesses are sensitive to the lithosphere thermal structure providing heat flow estimates. They have been mainly derived by local analysis of topography and gravity data, in particular below large volcanic loads (*Belleguic et al.*, 2005; *McGovern et al.*, 2004; *Kiefer*, 2004; *Hoogenboom and Smrekar*, 2006; *Wieczorek*, 2008; *Ritzer and Hauck*, 2009; *Grott et al.*, 2011). Other methods have also been used. In particular, elastic lithosphere thicknesses have been estimated for the polar regions by modeling the deflexion under the cap load and comparing it with the deflexion measured by the Shallow Radar onboard the Mars Reconnaissance orbiter (*Phillips et al.*, 2008). Finally indications on local elastic lithosphere thicknesses have been derived from local geomorphological features such as rift uplift (*Barnett and Nimmo*, 2002; *Grott et al.*, 2005; *Kronberg et al.*, 2007) or from estimates of the seismogenic layer thickness on thrust faults (*Schultz and Watters*, 2001; *Grott et al.*, 2007; *Ruiz et al.*, 2008). As elastic thicknesses have been estimated for different ages - the age of the deformed surface or load - they provide an overview of Mars thermal evolution.

Elastic lithosphere thicknesses on Mars were very low ($\sim$ 20 km) during the Noachian, and increased above 50 km during the Hesperian to finally reach values between 40 and 150 km in the Amazonian, reflecting a progressive cooling of the planet (*Grott and Breuer*, 2008b; *Grott*

*et al.*, 2013). However, the very large present-day thickness of $\geq$ 300 km estimated below the north polar cap (*Phillips et al.*, 2008) seems hard to reconcile with these other values. Using a 1D parametrized thermal model, *Grott and Breuer* (2009) showed that present-day values $\geq$ 300 km can only be explained if Mars has a sub-chondritic bulk composition for a moderate crustal enrichment in heat sources. They also found that present-day melt formation below large volcanoes (*Hartmann et al.*, 1999; *Hartmann and Malin*, 2000; *Neukum et al.*, 2004; *Werner*, 2009) requires either a strongly pressure dependent mantle viscosity or endothermic phase transitions in the case of a dry mantle rheology, or large mantle water contents of the order of 1000 ppm if a wet mantle rheology is considered. In the framework of a 1D model, such a large present-day elastic thickness is incompatible with the very small Noachian values (*Grott and Breuer*, 2009). Moreover the north pole value is significantly larger than the present-day elastic lithosphere thickness suggested below the southern polar cap (only 161 km, though any value higher than 110 km could fit the observations, *Wieczorek*, 2008).

This discrepancy between different estimates of elastic lithosphere thickness was attributed to spatial variability that cannot be resolved with classical 1D thermal models (*Grott and Breuer*, 2009). *Grott and Breuer* (2010) provided an explanation for the large present-day elastic thickness by including the effects of thermal anomalies in a 1D parametrized model. However, their model relies on a number of assumptions related to mantle thermal anomalies. 2D and 3D thermal models by *Kiefer and Li* (2009) and *Plesa et al.* (2016) allow to investigate these spatial variations selfconsistently, but are extremely time consuming and therefore inappropriate to explore a large range of parameters. In addition, the elastic thickness is very sensitive to lithosphere thermal structure and thus to crustal thermal properties (enrichment in radioelements, thermal conductivity), which can show spatial variations. Furthermore, Mars bulk content in radioelements and their distribution between the mantle and crust remain poorly constrained but play a major role in the planet thermal evolution (*Grott and Breuer*, 2009; *Sekhar and King*, 2014). It seems therefore essential to investigate the potential effect of spatial differences in crustal enrichment and properties on elastic lithosphere thickness evolution.

As a potential source of spatial crustal differences, the hemispheric dichotomy of Mars is a major candidate. The southern highlands are characterized by sharp reliefs more craterized and superficially older than the northern lowlands covered by extensive lava plains. These latter are very flat and lower in altitude by $\sim$ 6 km compared to the southern hemisphere. At the dichotomy boundary, the large volcano complexes of Tharsis and Elysium rise are present. As the dichotomy predates the formation of the volcanic regions, their belonging to one of the two hemispheres remains uncertain. *Andrews-Hanna et al.* (2008) argue for a location in the northern hemisphere and a lowland surface fraction of 42 %.

The origin of this surface dichotomy remains debated and various formation mechanisms have been proposed such as a heterogeneous fractionation of an early magma ocean (*Solomon et al.*, 2005), a mantle overturn (*Elkins-Tanton et al.*, 2005), a degree 1 mantle convection pattern (*Roberts and Zhong*, 2006; *Yoshida and Kageyama*, 2006) or an impact origin either in the north (*Andrews-Hanna et al.*, 2008; *Marinova et al.*, 2008) or in the south (*Reese et al.*,

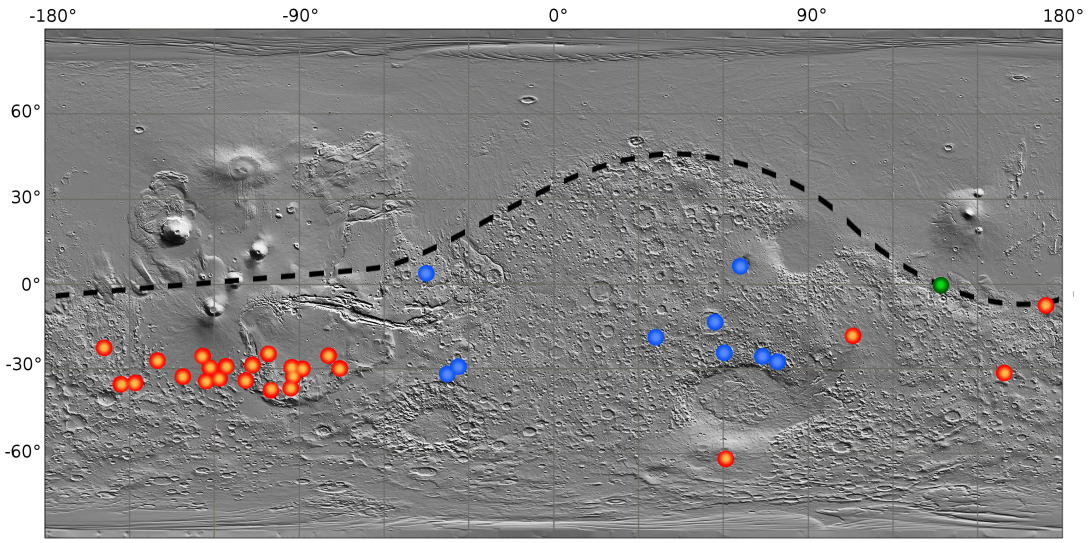


**FIGURE 4.1** – Indications of potential north/south differences in crustal properties over a MOLA shaded relief topographic map. The boundary of the north/south dichotomy proposed by *Andrews-Hanna et al.* (2008) is represented by the dashed line. Red points indicate ancient volcanoes detected by *Xiao et al.* (2012) and *Huang and Xiao* (2014). Blue points show the localization of felsic rocks detected by *Carter and Poulet* (2013) and *Wray et al.* (2013). Felsic rocks very similar to that characterizing the early terrestrial continental crust have been detected with the Curiosity rover in the Gale crater (green point, *Sautter et al.*, 2015). All these detections are located in the southern highlands.

2010; *Golabek et al.*, 2011; *Leone et al.*, 2014). In any case, the dichotomy formation would probably date back to the early stages of Mars evolution, between 4.5 and 4 Gyr (*Nyquist et al.*, 2001; *Nimmo and Tanaka*, 2005; *Frey*, 2008; *Bottke and Andrews-Hanna*, 2017; *Brasser and Mojzsis*, 2017). The dichotomy in topography is likely compensated by a difference in crustal thickness and/or density.

Despite the large north/south dichotomy, the surface of Mars seems nearly homogeneous in composition. The analysis of SNC meteorites (*McSween et al.*, 2006; *Aoudjehane et al.*, 2012; *Humayun et al.*, 2013; *Agee et al.*, 2013) and spectroscopic investigations of the surface (*Christensen et al.*, 2005; *Mustard et al.*, 2005; *Baratoux et al.*, 2011) point to a basaltic composition. The surface distribution in radioelements seems roughly uniform (*Taylor et al.*, 2006), with no clear north/south difference. These observations lead to the traditional Mars crustal model where the crust has uniform properties except that the southern one is thicker to compensate for its higher altitude, implying a higher bulk radioelement content and thus a hotter lithosphere in the south.

However, recent studies have shown that the southern and northern crusts could potentially have different properties. In particular, evidence of felsic rocks, such as anorthosites and granodiorites, has been found by remote-sensing techniques (*Carter and Poulet*, 2013; *Wray et al.*, 2013) or in situ analysis in the Gale crater (*Sautter et al.*, 2015). This felsic material is located

in the southern hemisphere (see Figure 4.1), and has been identified in rocks excavated from depth in crater rims and crater floors, suggesting the potential presence of a reservoir enriched in silica and buried within the southern crust (*Pauer and Breuer*, 2008; *Carter and Poulet*, 2013; *Wray et al.*, 2013; *Baratoux et al.*, 2014; *Sautter et al.*, 2015). Furthermore, the bulk crustal density is largely debated. While *Goossens et al.* (2017) has estimated a very low average density of $2582 \pm 209$ kg m$^{-3}$, *Baratoux et al.* (2014), on the contrary, proposed a value larger than 3100 kg m$^{-3}$. Such a large value would imply a very thick southern crust, hardly reconciliable with geoid-to-topography ratios without the existence of a less dense component in the south (*Baratoux et al.*, 2014). A difference in composition between the northern and southern crusts would also suggest a difference in radioactive element content. In particular, Mars' anorthosites could result from magmatic processes that produce highly evolved melts, implying a larger radioelement enrichment in the southern buried felsic component. Moreover, a recent study suggested that the thermal properties of surface rocks vary with their age (*Bandfield et al.*, 2013). The north is covered by compact lava flows (*Xiao et al.*, 2012; *Bandfield et al.*, 2013; *Huang and Xiao*, 2014), while the old surface of the southern hemisphere is made of fine-particulate and poorly consolidated materials from ancient explosive volcanism or widespread ejecta deposition following a large impact (Figure 4.1). Due to the presence of these porous materials, thermal conductivity in the southern hemisphere could be lower (*Piqueux and Christensen*, 2009a,b) than that in the north over several kilometers. This difference in thermal conductivity might disappear at depth by compaction.

Here we test two plausible crustal models : one with a southern crust potentially less conductive for its upper part, enriched in radioelements and silica rocks compared to that of the northern hemisphere, and a more traditional one where the north and south have the same crustal properties except that the southern crust is thicker. Using 1D parametrized thermal evolution models of Mars accounting for two hemispheres with different crustal models in Monte Carlo simulations, we constrain the thermal parameters of the northern and southern crusts (thickness, radioelement enrichment and density) that allow to fit elastic lithosphere thickness estimates at different ages.

## 3.2 Constraints on the thickness of the elastic lithosphere

In this study, we use elastic lithosphere thickness ($T_e$) estimates, previously compiled by *Grott and Breuer* (2008b) and *Grott et al.* (2013), as the main constraints for the parameters of our models (Figure 4.2b). First we distinguish between estimates in the northern or southern hemispheres. We notice that the low values in the Noachian reported by *Grott and Breuer* (2008b) are mostly located in the southern hemisphere. These estimates are all in the range 10 to 37 km, although values in the range 0 and 50 km between 4.2 and 3.5 Gyr can fit given error bars and age scattering (*McGovern et al.*, 2004; *Grott et al.*, 2013). Elastic thickness estimates in the Noachian are not well constrained in the northern hemisphere. On the one hand *Hoogenboom and Smrekar* (2006) provide very low estimates, comparable to those in the south, that are likely associated to large uncertainties as they are based on topography and

gravity data analyses in a region where evidence of past topography has mostly been erased. On the other hand, *Ritzer and Hauck* (2009) retrieve a range estimate of $100-180$ km at Isidis Planitia, at the edge of the highlands/lowlands boundary. Elastic thicknesses at this location could be influenced by the properties of both hemispheres but are more representative of the larger values of the north (*Plesa et al.*, 2016). Given this wide range of values, we do not include any constraint in the Noachian in the north. We will see indeed that our results cover a large range of potential $T_e$ in the north during this period (see section 3.4.a).

Elastic thicknesses have also been evaluated below large volcanoes. However, although a large fraction of these edifices, e.g., Tharsis and Elysium, has probably been emplaced during the Noachian, their construction lasted several Gyr. Recent lava flows have indeed been detected on the slopes of Tharsis and Elysium (*Hartmann et al.*, 1999; *Neukum et al.*, 2004; *Werner*, 2009; *Hauber et al.*, 2011; *Susko et al.*, 2017), introducing a large error bar for the ages of these estimates ($\sim 3$ Gyr). In addition, Tharsis is located close to the dichotomy boundary (*Neumann et al.*, 2004; *Andrews-Hanna et al.*, 2008). In this study, we therefore do not account for $T_e$ estimates below large volcanoes. We rather consider present-day estimates obtained under the two polar caps as their age is well constrained. A mean value of 161 km has been obtained below the south polar cap, although any value greater than 110 km could fit the observations (*Wieczorek*, 2008). Below the north polar cap, *Phillips et al.* (2008) have obtained values larger than 300 km. We notice that *Phillips et al.* (2008) have estimated a lower bound of $275-300$ km for the elastic thickness below the south polar cap noting that this value could reflect the substrate topography noise. Thus we use the less severe restriction of $T_e > 110$ km by *Wieczorek* (2008) (Figure 4.2b).

We use Monte Carlo simulations to select suitable thermal models, defined in terms of the northern and southern crustal thermal properties (see section 3.3.c), that are compatible with these three constraints on elastic lithosphere thicknesses (i.e. low $T_e$ in the Noachian, present-day $T_e$ values larger than 300 km for the north and higher than 110 km for the south).

To assess the likelihood of each model, scores on our constraints are defined. Suitable southern Noachian values are between 0 and 50 km with a best fit at 22 km. We choose an asymmetric gaussian probability law representative of this distribution (Figure 4.2c) at an age of 3.85 Gyr (the mean age of Noachian estimates), normalized between 0 and 1 point. We use another asymmetric gaussian score for the constraint on the present-day southern elastic thickness, with a maximum of 1 point at 161 km (Figure 4.2c). Concerning the elastic thickness constraint in the northern hemisphere, we assign the maximal score of 1 for a model that predicts $T_e \geq 300$ km in the lowlands (*Phillips et al.*, 2008). Nevertheless, this estimate is perhaps not valid for the entire hemisphere. In 3D thermal models, lateral variations in $T_e$ of 20 km and $30-40$ km could be observed in the lowlands with and whitout present-day mantle plumes, respectively (*Plesa et al.*, 2016) : we thus choose a gaussian shape representative of this uncertainty (Figure 4.2c). We assume the same weight for the three constraints on $T_e$, which implies a maximal total score of 3 for a model.

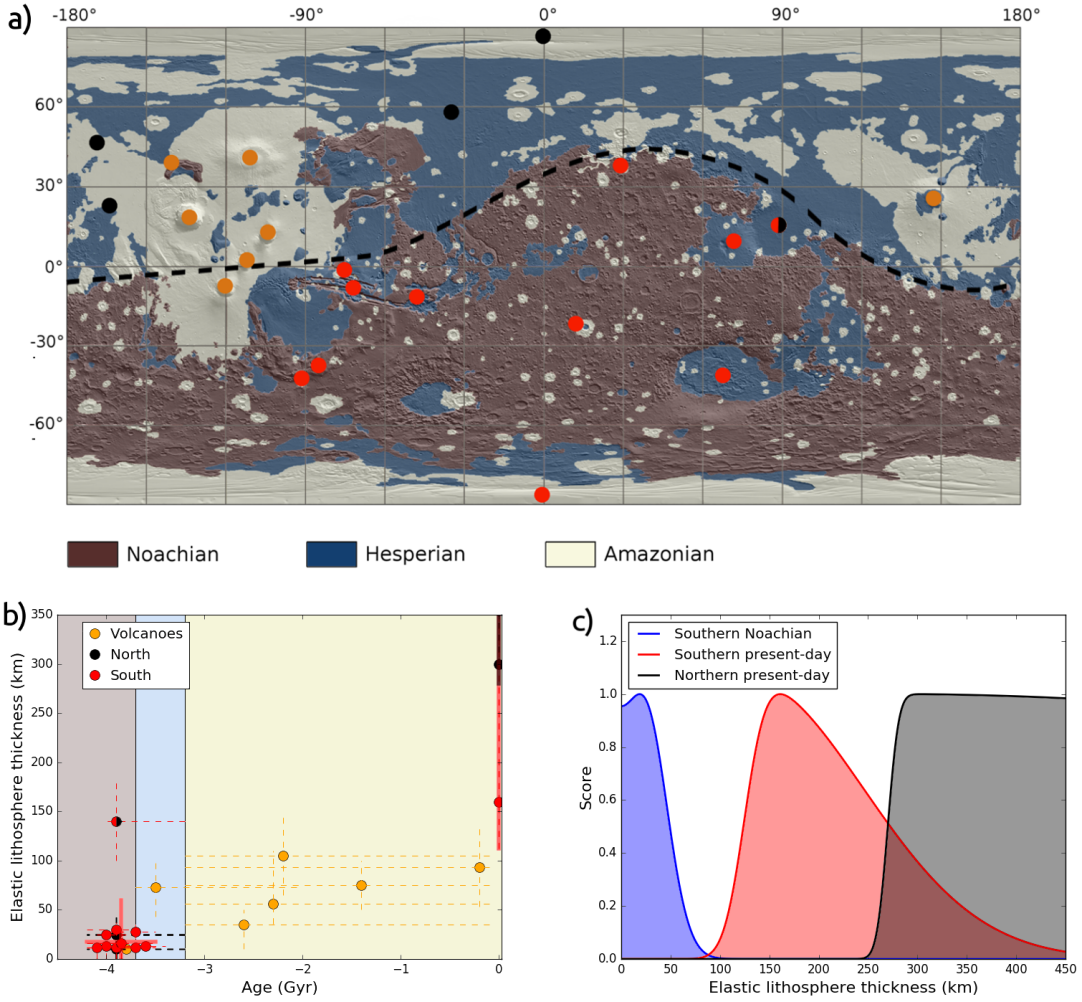


**FIGURE 4.2** – Constraints on elastic lithosphere thickness ($T_e$). a : localization of $T_e$ estimates, previously compiled by *Grott et al.* (2013), over a MOLA shaded topographic map. The major Martian geological epochs are taken from the chronostratigraphic map of *Tanaka et al.* (2014). The north/south dichotomy of *Andrews-Hanna et al.* (2008) is shown with a dashed line. In this study we make the distinction between southern and northern values : red points are localized in the highlands, black ones in the lowlands. The orange points correspond to estimations below the large volcanoes situated close to the dichotomy. b : $T_e$ estimates represented on (a) are here plotted as a function of age. Errorbars are represented in dashed line for each estimate. Bold lines correspond to the three major $T_e$ constraints considered : in the Noachian in the south and at the present day below the two polar caps. c : scores given as a function of the computed value of the elastic lithosphere thickness. Asymetric gaussian distributions are used for the constraints in the Noachian south (blue), at the present day below the south polar cap (red) and below the northern one (black).

## 3.3 Method and modeling

### 3.3.a Thermal model

We adopt the 1D parametrized model of stagnant lid convection of *Grott and Breuer* (2008b) and consider distinct crustal properties for the two hemispheres of Mars. One dimensional parametrized convection models are based on scaling relationships between heat flux through boundary layers and the Rayleigh number, which describes the vigor of convection (*Grasset and Parmentier*, 1998) :

$$Ra_{rh}^{N/S}(T) = \frac{\alpha \rho_m g \Delta T (R_l^{N/S} - R_c)^3}{\kappa \eta(T)} \tag{4.1}$$

where $\alpha$ is the coefficient of thermal expansion, $\rho_m$ mantle density, $g$ gravity, $\kappa$ mantle thermal diffusivity, $R_c$ core radius and $\Delta T$ the temperature difference across the boundary layers. The subscript $N/S$ indicates that a parameter differs between the northern and southern hemispheres. In our model, we observe a north/south difference in the Rayleigh number as the lithosphere thickness and thus the radius of the mantle-lithosphere boundary $R_l^{N/S}$ are different between the lowlands and the highlands. The mantle viscosity $\eta$ strongly depends on temperature which leads to the formation of a rigid lid at the surface that does not participate to the convection, the so-called stagnant lid. We use an Arrhenius law to describe the viscosity as a function of temperature and pressure :

$$\eta(T,P) = \eta_0 exp\left(\frac{A+PV}{RT} - \frac{A+P_{ref}V}{RT_{ref}}\right) \tag{4.2}$$

where $A$ and $V$ are the activation energy and volume, respectively, for a linear rheology ; $R$ is the gas constant, $\eta_0$ the reference viscosity at a reference temperature $T_{ref} = 1600$ K and a reference pressure $P_{ref} = 3 \times 10^9$ Pa.

Beside temperature and pressure, the viscosity depends on mantle water content (*Mei and Kohlstedt*, 2000a,b) and deformation mechanism. Geochemical analysis of SNC meteorites suggests that the mantle may contain large amounts of water (*Médard and Grove*, 2006; *McSween, Jr et al.*, 2001). *Grott and Breuer* (2008b) also found that the small $T_e$ observed during the Noachian period are in good agreement with a wet mantle rheology. However, there is no indication that water has been retained in the mantle during accretion ; in addition, water could have been lost since then by dehydration due to mantle melting. We therefore consider both cases in our simulations using a reference viscosity of $10^{21}$ Pa s at a reference temperature $T_{ref}$ of 1600 K for a dry mantle rheology, and $10^{19}$ Pa s for a wet rheology (*Karato and Wu*, 1993). We also consider wet and dry rheologies for the crust.

Viscosity also depends on the deformation mechanisms at play in the mantle. On Earth, dislocation creep is predicted to dominate in the upper mantle, whereas diffusion creep is the major deformation mechanism in the lower mantle (*Karato and Wu*, 1993). Nevertheless, the exact style of deformation depends on grain size, which is poorly constrained in planetary mantles. Therefore, even if on Mars the gravity is lower than on Earth leading to lower pressures

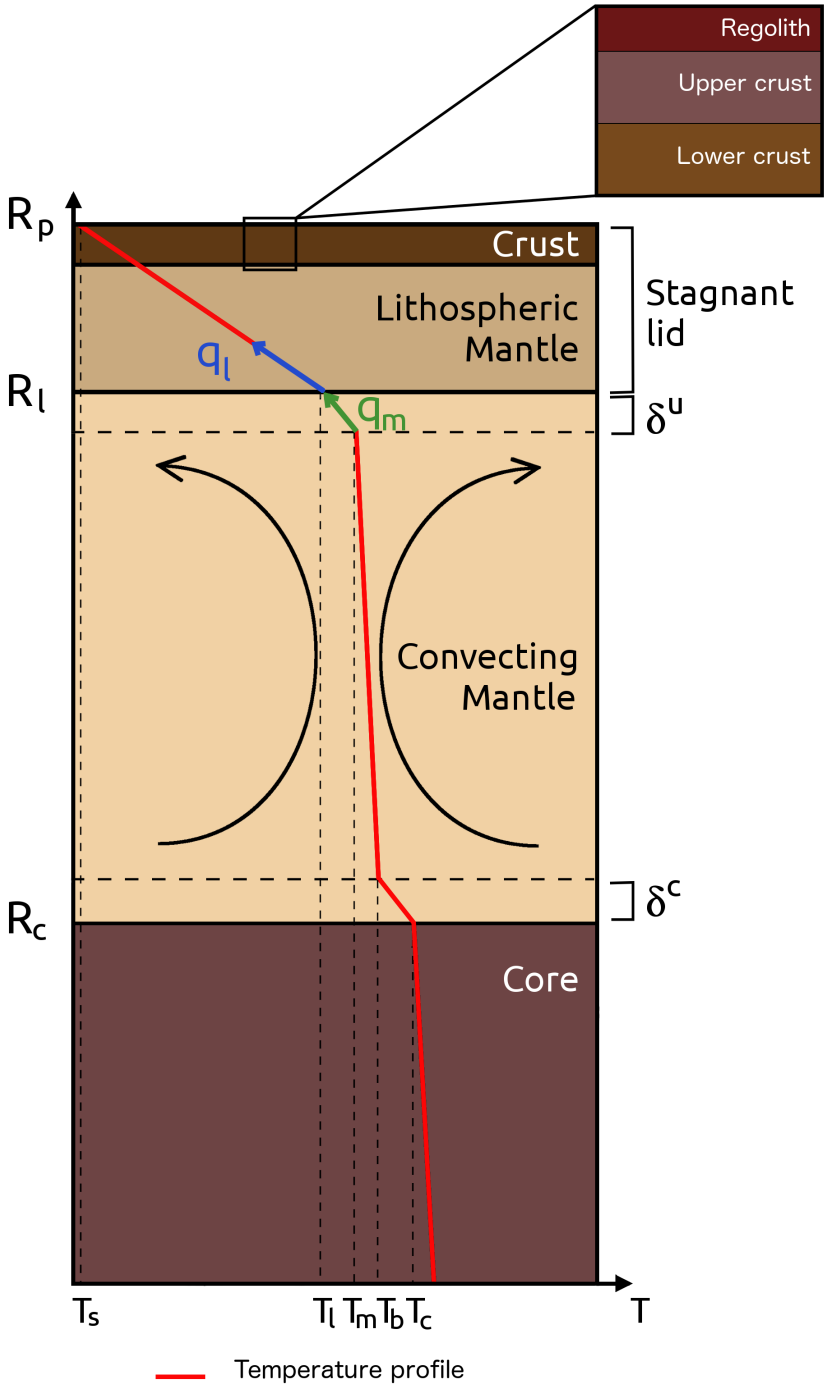


**FIGURE 4.3** – Sketch of the thermal parametrized model used in this study (not to scale). A phenomenological temperature profile is indicated in red. Lithosphere growth results from the difference between $q_m$, the heat flux out of the convecting mantle to the base of the stagnant lid, and $q_l$ the heat which is conducted away towards the surface by conduction through the stagnant lid. The heat flux $q_l$ is computed considering a time-dependent conduction equation 4.14.

in the Martian mantle, diffusion creep could still be the dominant deformation mechanism. We use representative values of the linear diffusion rheology in viscosity computation (equation 4.2) with $A = 300$ kJ mol$^{-1}$ and $V = 6$ cm$^3$ in the case of a dry mantle rheology, and $A = 240$ kJ mol$^{-1}$ and $V = 5$ cm$^3$ in the case of a wet mantle rheology (*Karato and Wu*, 1993). We also test the effect of dislocation creep by assuming an activation volume of $V = 7$ cm$^3$ and lower activation energies of $A = 200$ kJ mol$^{-1}$ (dry mantle rheology) or $A = 157$ kJ mol$^{-1}$ (wet mantle rheology) in the simplified Newtonian viscosity law (equation 4.2), which results from the dislocation creep activation energy and volume being divided by the stress exponent $n$ in order to produce an equivalent temperature dependence (*Christensen*, 1983).

The Martian mantle is heated both internally through the decay of radioelements and from below by the core. The mantle heat balance is thus determined by the internal heating and the heat flow across the two conductive boundary layers situated at the bottom and below the surface stagnant lid, which rapidly forms due to the strong temperature dependence of the viscosity. In the mantle (excluding the boundary layers), the temperature gradient is assumed adiabatic (see Figure 4.3 for a sketch of the model and Table 4.1 for the parameters). The boundary layer theory suggests that the thickness of the boundary layers evolves as :

$$\delta^{u,c} = (R_l^{N/S} - R_c)\left(\frac{Ra_{crit}^{u,c}}{Ra_{rh}^{u,c}(T_m)}\right)^{\beta} \tag{4.3}$$

where we use $\beta = 1/3$ (*Turcotte and Schubert*, 2002) and the subscript $u,c$ denotes the upper boundary layer or core mantle boundary layer. In $Ra_{rh}^{u}$ we use $\Delta T^u = T_m - T_l + T_c - T_b$ - where $T_l$ is the temperature at the base of the stagnant lid, $T_m$ the temperature at the top of the convecting mantle, $T_c$ the temperature at the core-mantle boundary and $T_b$ the temperature at the base of the convecting mantle (see Figure 4.3) -, the surface gravity $g^u$, the viscosity at the temperature $T_m$ and the pressure at the base of the upper thermal boundary layer. Note that $\Delta T^u = T_m - T_l$ if $T_b > T_c$, which arises when the mantle heats the core during thermal evolution. In this case the temperature difference between $T_b$ and $T_c$ becomes negative and does not contribute to convection anymore. In $Ra_{rh}^{c}$ we use $\Delta T^c = T_c - T_b$ (Figure 4.3), the gravity at the core-mantle boundary $g^c$, a viscosity at the temperature $(T_c + T_b)/2$ (*Richter*, 1978) and the pressure at the top of the lower thermal boundary layer. $Ra_{crit}^{u,c}$ is the critical Rayleigh number at which this layer destabilizes. For the upper boundary layer we use $Ra_{crit}^{u} = 450$ while, for the lower boundary layer we use the local description of *Deschamps and Sotin* (2000) that depends on $Ra_{rh}^{u}$ :

$$Ra_{crit}^{c} = 0.28(Ra_{rh}^{u})^{0.21} \tag{4.4}$$

Starting from an initial temperature profile in the planet, which requires an assumption on the initial mantle and core temperatures, the thermal evolution of the planet up to the present day is computed by solving the energy balance equations for the core, the mantle and the stagnant lid. Assuming that the core is well-mixed and that the temperature difference across the thermal boundary layer on the core side of the CMB is negligible, energy conservation in the core can be computed as follows (*Ke and Solomatov*, 2009) :

$$\rho_c C_c V_c \varepsilon_c \frac{dT_c}{dt} = -q_c A_c \tag{4.5}$$

where $A_c$, $\rho_c$, $C_c$ and $V_c$ are respectively the surface area, the density, the heat capacity and the volume of the core, $t$ is time, $\varepsilon_c \sim 1.1$ is the ratio between the average core temperature and the temperature at the core-mantle boundary $T_c$ (*Stevenson et al.*, 1983). The heat flux out of the core and into the mantle $q_c$ is calculated from :

$$q_c = k_m \frac{T_c - T_b}{\delta^c} \tag{4.6}$$

where $\delta^c$ is the lower boundary layer thickness and $k_m$ the mantle thermal conductivity. The temperature at the base of the convecting mantle, $T_b$, is calculated from $T_m$ and the adiabatic temperature gradient in the mantle :

$$T_b = T_m + \frac{\alpha g T_m}{C_m}(R_l - R_c - \delta^u - \delta^c) \tag{4.7}$$

In parallel, the mantle concedes heat to the stagnant lid with a heat flux $q_m$ ; its energy balance is thus given by :

$$\rho_m C_m V_m \varepsilon_m \frac{dT_m}{dt} = q_c A_c - q_m A_m + Q_m V_m \tag{4.8}$$

with $C_m$ the heat capacity of the mantle, $Q_m$ the mantle heat production rate. $\varepsilon_m$ is the ratio between the mean temperature of the convecting mantle and $T_m$, and is computed at each time step. The volume of the convecting mantle $V_m$ is computed from :

$$V_m = \frac{4}{3}\pi \sum_{N/S} F^{N/S}(R_l^{N/S^3} - R_c^3) \tag{4.9}$$

with $F^{N/S}$ the surface fractions of the north and south, which are 42% and 58%, respectively, if considering the dichotomy boundary of *Andrews-Hanna et al.* (2008), where Tharsis is located in the north (see Figure 4.2a). Nevertheless, the crust under large volcanoes is particularly thick and thus more similar to the southern crust of our model. We therefore vary the southern surface fraction between 60 % (our reference model) and 70 %. The total surface area $A_m$ at the lid-mantle boundary is given by :

$$A_m = 4\pi \sum_{N/S} F^{N/S} R_l^{N/S^2} \tag{4.10}$$

The heat flux $q_m$ out of the mantle and into the base of the stagnant lid is computed from :

$$q_m = k_m \frac{T_m - T_l}{\delta^u} \tag{4.11}$$

The base of the stagnant lid is defined by its temperature $T_l$, which depends on mantle temperature $T_m$ and on the rate of viscosity change with temperature (*Davaille and Jaupart*, 1993) :

$$T_l = T_m - 2.21\frac{\eta(T_m)}{d\eta/dT|_{T_m}} = T_m - 2.21\frac{RT_m^2}{A} \tag{4.12}$$

The rate of stagnant lid growth is determined by an energy balance at the base of the lid, i.e. by the difference between $q_m$, the heat transferred from the convecting mantle to the base of the stagnant lid, and the heat which is conducted away towards the surface through the lid (*Grott and Breuer*, 2008b) :

$$\rho_m C_m (T_m - T_l)\frac{dD_l^{N/S}}{dt} = -q_m - k_m \left.\frac{\partial T^{N/S}}{\partial r}\right|_{r=R_l^{N/S}} \tag{4.13}$$

where $D_l^{N/S}$ is the stagnant lid thickness, $T^{N/S}$ is the temperature in the lid and $r$ the radial distance from the planet center. Contrary to *Grott and Breuer* (2008b), we consider time-

| Parameter | Notation | Value | Unit |
|---|---|---|---|
| Mean planetary radius | $R_p$ | $3390 \times 10^3$ | m |
| Core radius | $R_c$ | $1700 \times 10^3$ | m |
| Regolith thickness | $d_r$ | 10 | m |
| North-south mean altitude difference | $dh$ | $6 \times 10^3$ | m |
| Northern hemisphere surface fraction | $F^n$ | $0.3 - 0.4$ | |
| Mantle density | $\rho_m$ | 3500 | kg m$^{-3}$ |
| Core density | $\rho_c$ | 7200 | kg m$^{-3}$ |
| Regolith thermal conductivity | $k_r$ | 0.1 | W m$^{-1}$ K$^{-1}$ |
| Mantle thermal conductivity | $k_m$ | 4 | W m$^{-1}$ K$^{-1}$ |
| Surface temperature | $T_s$ | 220 | K |
| Reference temperature | $T_{ref}$ | 1600 | K |
| Initial mantle temperature | $T_{m_0}$ | 1800 | K |
| Initial core temperature | $T_{c_0}$ | 2050 | K |
| Critical Rayleigh number | $Ra^u_{crit}$ | 450 | |
| Mantle heat capacity | $C_m$ | 1142 | J kg$^{-1}$ K$^{-1}$ |
| Core heat capacity | $C_c$ | 840 | J kg$^{-1}$ K$^{-1}$ |
| Ratio of the mean and upper core temperature | $\varepsilon_c$ | 1.1 | |
| Surface gravity | $g^u$ | 3.7 | m s$^{-2}$ |
| Core-mantle boundary gravity | $g^c$ | 3.4 | m s$^{-2}$ |
| Gas constant | $R$ | 8.3144 | J K$^{-1}$ mol$^{-1}$ |
| Thermal expansion coefficient | $\alpha$ | $2.5 \times 10^{-5}$ | K$^{-1}$ |
| Activation energy | $A$ | $1.5 - 3 \times 10^5$ | J mol$^{-1}$ |
| Activation volume | $V$ | $5 - 7$ | cm$^3$ mol$^{-1}$ |
| Reference pressure | $P_{ref}$ | $3 \times 10^9$ | Pa |
| Strain rate (convection) | $\dot{\varepsilon}$ | $10^{-17}$ | s$^{-1}$ |
| Strain rate (glacial loading ) | $\dot{\varepsilon}_{cap}$ | $10^{-14}$ | s$^{-1}$ |
| Impact temperature increase | $\Delta T_i$ | 100 | K |

**TABLE 4.1** – Model parameters.

dependent rather than steady-state heat conduction in the lid, which is more appropriate for a thick lithosphere (*Michaut and Jaupart*, 2004) :

$$\rho_j^{N/S} C_j \frac{\partial T^{N/S}}{\partial t} = \frac{1}{r^2}\frac{\partial}{\partial r}\left(r^2 k_j^{N/S}\frac{\partial T^{N/S}}{\partial r}\right) + Q_j^{N/S} \tag{4.14}$$

In our model, we assume that the whole mantle is well-mixed. In particular the heat flow out of the mantle, $q_m$, and the temperature at the base of the lid, $T_l$, are the same in both hemispheres, which is reasonable in the absence of large mantle plumes (*Plesa et al.*, 2016). Nevertheless, the rate of stagnant lid growth and the temperature profile are expected to differ between both hemispheres, as they depend on crustal properties (thermal conductivity, crustal thickness and enrichment factor) that vary between the north and south. $Q_j^{N/S}$, $\rho_j^{N/S}$ and $k_j^{N/S}$ represent respectively the volumetric heat production rate, the density and the thermal conductivity in the $j$ different layers of the stagnant lid, i.e. the regolith, upper crust, lower crust and lithospheric mantle (Figure 4.3). The distinct crustal layers, of volume $V_{cr_j}^{N/S}$, can show distinct radioelement enrichment $\Lambda_j^{N/S}$ with respect to the primitive mantle. Heat production is thus computed from :

$$Q_{cr_j}^{N/S} = \sum_i Q_i exp(-\lambda_i t)\frac{M_{silicate}}{V_{silicate}}\Lambda_j^{N/S} \tag{4.15}$$

where the sum extends over the 4 radiogenic species - $^{40}K$, $^{232}Th$, $^{235}U$ and $^{238}U$ -, which have a heat production rate $Q_i$ decreasing with time depending on their respective half-lives $\lambda_i$. $M_{silicate}$ and $V_{silicate}$ are the mass and volume of the silicate bulk. Mantle heat production $Q_m$ is then computed from mass balance.

A Runge-Kutta numerical scheme of order 4 is used to solve the ordinary differential equations 4.5, 4.8 and 4.13. Equation 4.14 is solved using an implicit numerical scheme and a change of variable $r = R_P^{N/S} - D_l^{N/S} y$, which allows to keep a fixed number of grid points between two fixed boundaries $y = 0$ and $y = 1$, and to adapt the grid distance according to the stagnant lid thickness that varies at each iteration. Note that the planetary radius differs between the two hemispheres with an average value of 3390 km and a north/south altitude difference $dh = 6$ km.

### 3.3.b Elastic thickness computation

Given the temperature structure and the rheology of the lithosphere, ductile and brittle deformation envelopes can be retrieved. By determining which deformation mechanism dominates at a given depth, it is then possible to build the strength envelope (*McNutt et al.*, 1988).

The brittle deformation $\sigma_B$ - or frictional sliding - is related to the effective vertical stress $\sigma_v$, or lithostatic pressure (*Mueller and Phillips*, 1995). It is essentially independent of temperature, strain rate, and in most cases, rock composition (*Byerlee*, 1978). It occurs as soon as a stress in

extension exceeds

$$\sigma_B = \begin{cases} 0.786\sigma_v & if\ \sigma_v \leq 529.9MPa \\ 56.7MPa + 0.679\sigma_v & if\ \sigma_v > 529.9MPa \end{cases} \tag{4.16}$$

or when a compressive stress becomes greater than

$$\sigma_B = \begin{cases} -3.68\sigma_v & if\ \sigma_v \leq 113.2MPa \\ -176.6MPa - 2.12\sigma_v & if\ \sigma_v > 113.2MPa \end{cases} \tag{4.17}$$

In the lower hot lithosphere, yield strength is limited by intracrystalline ductile creep $\sigma_D$. Unlike brittle deformation it depends on the temperature profile $T(r)$ in the lithosphere, the strain rate $\dot{\varepsilon}$ and lithospheric rheological parameters like the stress exponent $n$, the prefactor $B$ and the activation energy $A_n$ for a non-linear rheology (*Durham and Goetze*, 1977a,b)

$$\sigma_D = \left(\frac{\dot{\varepsilon}}{B}\right)^{\frac{1}{n}} e^{A_n/nRT} \tag{4.18}$$

The choice of these parameters is therefore crucial to determine an elastic thickness. We use rheological parameters suitable for wet and dry olivine rheology in the mantle (*Karato and Wu*, 1993), and wet (*Caristan*, 1982) and dry diabase (*Mackwell et al.*, 1998) in the crust (see Table 4.2). The strain rate $\dot{\varepsilon}$ in the lithosphere is usually due to underlying convection. Since Mars convection is less vigorous than on Earth, the strain rate is assumed to be low, with a value of $\sim 10^{-17}$ s$^{-1}$ (*McGovern et al.*, 2004). However, Martian polar caps have been emplaced a few million years ago and the strain rate at those latitudes is related to the timescale of obliquity changes that are believed to have driven the ice cap deposition (*Laskar et al.*, 2004). We thus consider a strain rate of $10^{-14}$ s$^{-1}$, which allows a direct comparison between our present-day elastic thickness estimations and those of *Phillips et al.* (2008) and *Wieczorek* (2008) below the two polar caps. Note that this low strain rate only applies below the polar caps at the present-day, but not to the entire hemisphere, which implies different present-day estimations according to the location. In order to determine elastic lithosphere thickness from its strength envelope, one needs to evaluate the stress undergone by the lithosphere, induced by mantle convection, i.e. the bounding stress $\sigma_y$. This is a decisive parameter as it sets the temperature at which ductile failure occurs, and hence the thickness of the elastic lithosphere :

$$T(\sigma_y) = \frac{A_n}{R}\left[ln\left(\frac{\sigma_y^n B}{\dot{\varepsilon}}\right)\right]^{-1} \tag{4.19}$$

In this study, we assume a bounding stress of 15 MPa as in *Burov and Diament* (1995).

The rheologies differ between the crust and the lithospheric mantle : their elastic thicknesses, respectively $T_{e,c}$ and $T_{e,m}$, have therefore to be computed separately. We assume a non-flexed plate, with zero bending moment. In this way the modeled $T_e$ could directly be compared to estimations made under the present-day polar caps or during the Noachian, for which a non-flexed lithosphere is a good approximation. Depending on the rheology and the temperature profile, $T_{e,c}$ and $T_{e,m}$ could be welded and the elastic thickness $T_e$ is given by

| Rheology | $B$ [Pa$^{-n}$ s$^{-1}$] | $A_n$ [kJ mol$^{-1}$] | $n$ [K] | Reference viscosity $\eta_0$ [Pa s] |
|---|---|---|---|---|
| Dry olivine | $2.4 \times 10^{-16}$ | 540 | 3.5 | $10^{21}$ |
| Wet olivine | $3.9 \times 10^{-15}$ | 430 | 3.0 | $10^{19}$ |
| Dry diabase | $1.1 \times 10^{-26}$ | 488 | 4.7 | - |
| Wet diabase | $3.1 \times 10^{-20}$ | 276 | 3.05 | - |

TABLE 4.2 – Rheological parameters. The parameters characterizing the rheology of dry and wet olivine for dislocation creep are those of *Karato and Wu* (1993). For the crust, parameters characterizing the rheology of dry diabase are from *Mackwell et al.* (1998), and of wet diabase from *Caristan* (1982).

$$T_e = T_{e,c} + T_{e,m} \tag{4.20}$$

or separated by an incompetent crustal layer, in which case $T_e$ is given by

$$T_e = (T_{e,c}^3 + T_{e,m}^3)^{\frac{1}{3}} \tag{4.21}$$

### 3.3.c Crustal models and parameters

According to the recent discoveries related to crustal properties (Figure 4.1) that could potentially mark differences in composition between the two hemispheres of Mars, we consider two different crustal models (Figure 4.4) : one - referred to as the Non-Uniform Crustal Model (NUCM) - accounting for north/south differences in crustal properties, and a more traditional one, referred to as the Uniform Crustal Model (UCM). The latter model is defined by no north/south differences in crustal properties : both crusts have the same density and thermal parameters ; but there is a hemispheric difference in crustal thickness. In particular, an Airy isostatic compensation of the 6 km difference in altitude between the two hemispheres induces a thick southern crustal root whose thickness depends on crustal density and northern crustal thickness. For the NUCM case, the northern and southern primary crusts are first assumed to be the same, resulting for instance from the crystallization of the primordial magma ocean and subsequent early evolution of Mars (*Elkins-Tanton et al.*, 2003, 2005). The dichotomy formation is then modeled by an instantaneous removal of the entire primary northern crust due to a large impact and the resetting of the lithosphere thickness to that of the new northern secondary crust formed after this event. Compared to the primary crust, this secondary one is assumed to be more mafic with a higher density along with a lower radioelement content due to the depletion of the parent mantle compared to the primitive one. The radioelements of the primary northern crust as well as the energy of the impact are injected in the well-mixed mantle. The energy released by the impact into the mantle is challenging to estimate. *Marinova et al.* (2008) have evaluated an impact energy of 3 to $6 \times 10^{29}$ J, one third of it being estimated to contribute to a dramatic local heating at the impact side (Kai Wünnemann, personal communication). A large part of the impact energy is also consumed by melting and the formation of a new crust,

limiting the temperature increase to a couple of hundred Kelvins. Temperature anomalies in the north may persist for $> 100$ Myr (*Roberts and Arkani-Hamed*, 2014), while the southern hemisphere is not immediatly heated (*Arkani-Hamed and Olson*, 2010). Nevertheless, the temperature increase is later homogenized by convection. Here we assume a simplified scenario in which the temperature rises by $\sim 100 - 200$ K in the entire mantle following the impact. We also suppose that the injection of radioelements and impact energy into the mantle results in the production of high flows of hot and buoyant basaltic melt that could, as observed on Earth, reach the southern surface and form an upper thin crustal layer in the south, of the same type as that in the north. This would explain the absence of a large difference in surface composition between hemispheres. We thus assume the instantaneous formation of a surficial crustal layer in the south of the same composition as the secondary northern crust, but with a thermal conductivity that can be lower, consistent with porous materials formed by pyroclastic volcanism (*Bandfield et al.*, 2013). In both crustal models, we do not account for crustal formation by mantle partial melting. As the bulk of the crust is supposed to have formed within the first Gyr of evolution (*Hartmann et al.*, 1999; *Hartmann and Malin*, 2000; *Grott*, 2005; *Hauber et al.*, 2009; *Werner*, 2009) we do not expect that this would have a strong effect on our results, especially at the present day. Nevertheless, we range the age of the dichotomy formation between 4.5 and 4 Gyr, and choose 4.4 Gyr in our nominal model).

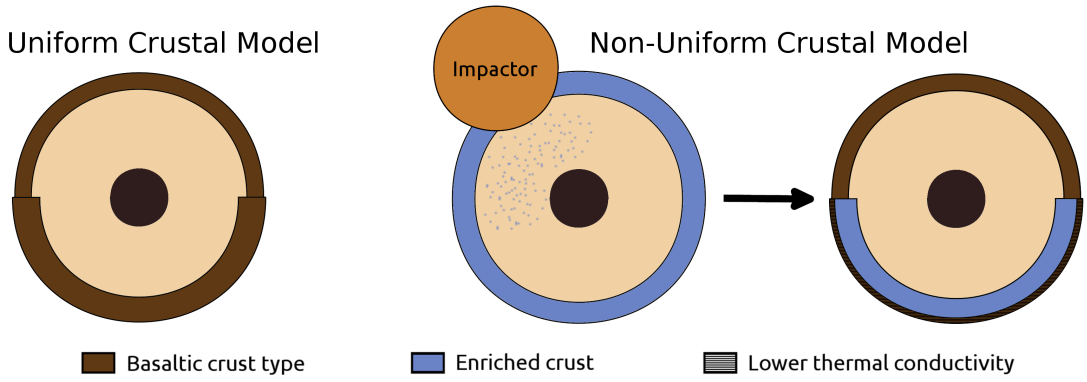


**FIGURE 4.4** – Sketchs of the two different crustal models (not to scale). Left : in the Uniform Crustal Model (UCM) the northern and southern crusts have the same properties (thermal conductivity, enrichment in radioelements, density) but the southern one is thicker by Airy isostatic compensation of the 6 km north/south difference in altitudes. Right : In the Non-Uniform Crustal Model (NUCM), the two crusts are the same initially. After a large impact remixes the northern primary crust in the mantle at $4.5 - 4$ Gyr, a new secondary crust forms instantaneously in the north with distinct properties (composition, enrichment in radioelements and thickness). In this crustal model the impact injects energy in the mantle as well as the additional radioelements of the primary northern crust, which triggers the formation of an upper layer of 10 km in the south with a composition similar to the northern secondary crust. This thin upper layer in the south can have a different thermal conductivity as proposed by *Bandfield et al.* (2013).

Constraints on crustal thickness are mainly derived from topography and gravimetry data (*Zuber et al.*, 2000; *Neumann et al.*, 2004; *Wieczorek and Zuber*, 2004), or from the absence of large scale relaxation of the topography (*Nimmo and Stevenson*, 2001). Assuming a uniform crustal density of 2900 kg $m^{-3}$, *Neumann et al.* (2004) retrieved average crustal thicknesses of 32 and 58 km in the lowlands and highlands, respectively. Nevertheless, other crustal models considering higher crustal densities up to 3200 kg $m^{-3}$ found thicker crusts both in the north and in the south (with averages as high as 60 and 110 km, respectively) that could fit the topography and gravity data (*Wieczorek and Zuber*, 2004; *Plesa et al.*, 2016). By evaluating the global chemical composition of the Martian surface and meteorites, *Baratoux et al.* (2014) have reestimated crustal grain density to values higher than 3100 kg $m^{-3}$. Assuming therefore that the 32 km of *Neumann et al.* (2004) is a lower bound, we use the range $30-60$ km for the northern crustal thickness in our two crustal models. For the UCM simulations, we consider a basaltic crust with a density between 2900 and 3200 kg $m^{-3}$, whereas for the NUCM simulations we assume a density of 3100 kg $m^{-3}$ for both the northern crust and the upper basaltic part of the southern one. The latter is assumed to have a thickness of 10 km, which is coherent with the detection of outcrops of different thermal inertia by *Bandfield et al.* (2013) along with the excavation depth of felsic material estimated by *Carter and Poulet* (2013). The density of the buried part of the southern crust is varied between 2500 and 3100 kg $m^{-3}$ for the NUCM simulations, representing compositions ranging from felsic to basaltic. In the two crustal models the southern crustal thickness is computed considering isostatic compensation of the higher topography (with an average of $\sim 6$ km) of the south. Though it is not expected to have an effect on the global thermal structure and evolution, we also account for a 10 m thick regolith layer at the surface (*Warner et al.*, 2017) that could influence the stagnant lid temperature profile. Finally we check that all our simulations are compatible with Mars' moment of inertia (*Konopliv et al.*, 2006).

In some models, at the beginning of the thermal evolution, the stagnant lid could become thinner than the crust, which would lead to crustal recycling. This process is favored by thick and insulating crusts, highly enriched in radioelements, that drive high crustal temperatures. Such a recycling is incompatible with the SNC geochemical characteristics (*Jagoutz*, 1991; *Papike et al.*, 2009) and with the north/south isostatic equilibrium that we impose at the beginning of our simulations : we thus rule these models out.

The Martian crust is supposed to be mainly composed by compact volcanic materials. The thermal conductivity of this type of rocks is estimated between 1.5 and 3.5 W $m^{-1}$ $K^{-1}$ at ambient conditions and decreases when temperature increases (*Clauser and Huenges*, 1995; *Seipold*, 1998). Many uncertainties remain, however, when considering real Martian conditions : the structure of crustal rocks such as their porosity and percentage of ice cement could lower the thermal conductivity (*Mellon et al.*, 2004) ; a hydrothermal circulation in the upper crust could on the contrary significantly increase it (*Parmentier and Zuber*, 2007). We assume a thermal conductivity of 3 W $m^{-1}$ $K^{-1}$ for the entire crust with the exception of the upper southern layer for the NUCM simulations where we vary it between 2 and 3 W $m^{-1}$ $K^{-1}$ to account for the poorly compacted materials pointed out by *Xiao et al.* (2012), *Bandfield et al.*

(2013) and *Huang and Xiao* (2014) (see section 3.1). The thermal conductivity of the lower southern crust is supposed to be the same as that in the northern crust, as the rocks are being compacted with depth. In the fractured and poorly compacted regolith we assume a lower value of 0.1 W $m^{-1}$ $K^{-1}$ (*Gagnepain-Beyneix et al.*, 2006). See Table 4.3 for a summary of UCM and NUCM crustal parameters.

### 3.3.d Heat production

The choice of the bulk radioactive element content is crucial as it determines heat production and thermal evolution. While the compositional model of *Wänke and Dreibus* (1994) is today widely accepted, the distribution of radioelements between the crust and mantle remains unfortunately poorly constrained on Mars. The latter is a crucial parameter of our model since heat produced in the crust is easily conducted away towards the surface, while the heat produced into the mantle is harder to evacuate. Crustal radioactivity enrichment factors relative to the primitive mantle between 4 (*Nimmo and Stevenson*, 2001) and 10 (*Schumacher and Breuer*, 2006; *Grott and Breuer*, 2009) have been previously considered. Given Gamma-Ray Spectroscopy (GRS) observations, *Taylor et al.* (2006) have suggested that about half of the bulk radioelement content is situated in the crust if an average crustal thickness of 57 km is considered, which corresponds to a crustal enrichment factor of 10. In this study, as crustal

| | **UCM** | **NUCM** |
|---|---|---|
| **Northern crust** | | |
| $d^N$ [km] | 30 – 60 | 30 – 60 |
| $\rho^N$ [kg $m^{-3}$] | 2900 – 3200 | 3100 |
| $k^N$ [W $m^{-1}$ $K^{-1}$] | 3 | 3 |
| $\Lambda^N$ | 5 – 15 | 10 or 5 – 15 (section 3.7.a) |
| | | |
| **Southern crust** | | |
| $d_1^S$ [km] | 0 | 10 |
| $d^S$ [km] | 65 – 127 | 39 – 112 |
| $\rho_1^S$ [kg $m^{-3}$] | 2900 – 3200 | 3100 |
| $\rho_2^S$ [kg $m^{-3}$] | 2900 – 3200 | 2500 – 3100 |
| $k_1^S$ [W $m^{-1}$ $K^{-1}$] | 3 | 2 – 3 |
| $k_2^S$ [W $m^{-1}$ $K^{-1}$] | 3 | 3 |
| $\Lambda_1^S$ | 5 – 15 | 10 or 5 – 15 (section 3.7.a) |
| $\Lambda_2^S$ | 5 – 15 | 5 – 30 |

**TABLE 4.3** – A priori range of crustal parameters considered in each hemisphere for the two crustal models. For the southern crust, the index 1 corresponds to the upper layer of 10 km ($= d_1^S$) and $j = 2$ to the lower one whose thickness is $d_2^S = d^S - d_1^S$. The subscript N/S relates to the northern or southern hemisphere respectively ; $d$ is the thickness, $\rho$ the density, $k$ the thermal conductivity and $\Lambda$ the enrichment factor in radioelements with respect to the primitive mantle.

thicknesses vary over a wide range of values, we vary the crustal enrichment factor between 5 and 15 for the UCM simulations. For the NUCM simulations the enrichment factor of the northern crust and the upper part of the southern one is set equal to the average value of 10. In a second set of NUCM simulations (NUCM2, section 3.7.a), we also vary the northern crustal enrichment factor and consider the same range as for the UCM case, i.e. 5 to 15. For the buried part of the southern crust, which may have formed very early by primary differentiation processes, we use a wider range of enrichment factors : from 5 to 30.

### 3.3.e Initial conditions

The initial mantle temperature $T_{m_0}$ is largely uncertain, but it is constrained by the solidus and liquidus temperatures, which are respectively 1600 and 2300 K (*Takahashi*, 1990). Indeed an initial mantle temperature lower than the solidus is not consistent with early crustal formation. On the other hand, an initial temperature higher than the liquidus would imply a long persistence of the primordial magma ocean (*Schubert and Spohn*, 1990). Crustal thicknesses are also predicted to be too large if high initial temperatures, close to the liquidus, are considered (*Hauck and Phillips*, 2002; *Breuer and Spohn*, 2006; *Parmentier and Zuber*, 2007). Following *Grott and Breuer* (2009), we consider an inital mantle temperature of 1800 K. We discuss briefly the effect of this parameter in section 3.5.d. The initial core temperature $T_{c_0}$ is estimated using an adiabatic temperature increase from $T_{m_0}$ through the mantle. We do not assume an initial superheating of the core.

## 3.4 Results

We first show in this section a sample result for a dry mantle and wet crust in association with diffusion creep, our favored rheology. Other rheologies are discussed in section 3.5.c and 3.7.b.

### 3.4.a Reference model

We present here a reference model for the elastic lithosphere thickness evolution obtained with one of our thermal models that best fits the three constraints on elastic thickness defined in section 3.2 (Figure 4.5a and b, bold lines, red for the south, black for the north). This evolution corresponds to a Non-Uniform Crustal Model that considers north/south thicknesses of 32/70 km (including the upper layer thickness of 10 km in the south), enrichment factors of 10/13.1, densities of 3100/3003 kg $m^{-3}$, respectively, and a thermal conductivity of 2 W $m^{-1}$ $K^{-1}$ in the upper southern layer.

There is a large difference in elastic lithosphere thickness evolution between the two hemispheres. Before the dichotomy-forming impact at 4.4 Gyr, both hemispheres show a similar evolution since the crust is everywhere the same. Thereafter, north and south elastic lithosphere

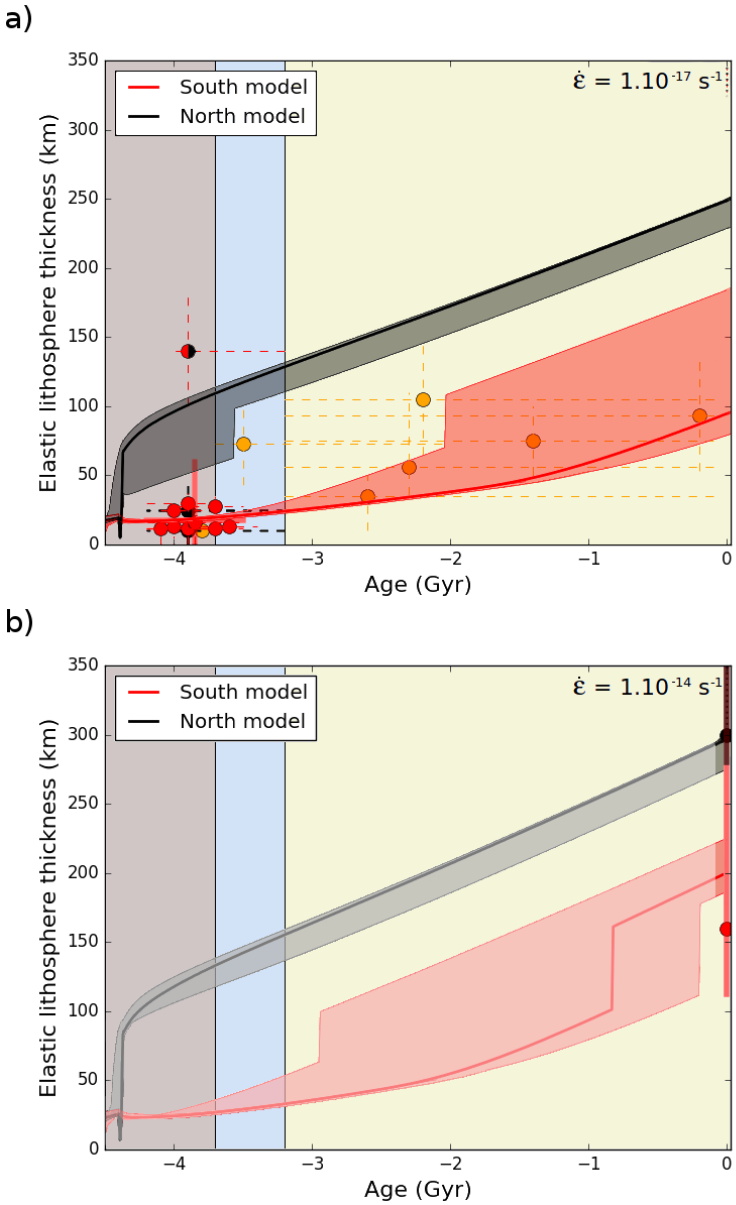


**FIGURE 4.5** – Elastic lithosphere thickness evolution as a function of age for the models that fit all four constraints, including present-day volcanism, in the south (red) and north (black), (a) for $\dot{\varepsilon} = 10^{-17}$ s$^{-1}$, a strain rate representative of the time scale of mantle convection, and (b) for $\dot{\varepsilon} = 10^{-14}$ s$^{-1}$ below the two polar caps, where the strain rate is representative of the time scale of polar cap deposition. Note that the elastic lithosphere thickness calculated in (b) should only be applied below the polar caps at the present day, but not to the entire hemisphere. Our reference model (Non-Uniform Crustal Model, see section 3.4.a for crustal properties) is represented by bold lines, whereas shadowed areas show the range of $T_e$ evolution that we obtain for the models showing the best scores (between 2.5 and 2.91) for both the UCM and NUCM cases.

thicknesses diverge with very low values in the southern hemisphere that fit $T_e$ estimates during the second part of the Noachian era (Figure 4.5a). The subsequent evolution is characterized by a slow increase in thickness in the south, reaching only 80 km at the present day for $\dot{\varepsilon} = 10^{-17}$ $s^{-1}$ because, for this strain rate, an incompetent weak crustal layer is still present, decoupling the elastic upper crust from the elastic upper mantle. Nevertheless, for a higher strain rate of $\dot{\varepsilon} = 10^{-14}$ $s^{-1}$, a value representative of cyclic ice loading, this weak layer disappears, leading to an elastic thickness equal to 193 km below the southern polar cap at the present day (Figure 4.5b). This is higher than the 161 km best estimate of *Wieczorek* (2008) but suits our southern present-day constraint (Figure 4.2b and c). In the north, after the formation of a new, thinner and more depleted secondary crust at 4.4 Gyr, the elastic lithosphere thickness quickly rises to high values of $\sim 100$ km at 3.9 Gyr, interestingly close to $T_e$ estimates of $100-180$ km at Isidis Planitia. Our model predicts higher Noachian northern elastic thicknesses than those estimated by *Hoogenboom and Smrekar* (2006) even though other models are close to the upper bound of these estimates (shaded areas on Figure 4.5a). The discontinuity at $\sim 4.3$ Gyr in $T_e$ evolution is due to the disappearance of the incompetent crustal layer in the north, which occurs much earlier in the lowlands because of its thinner and colder crust. The Hesperian and Amazonian periods show a regular increase in $T_e$, more pronounced than in the southern hemisphere due to the lower radioelement content. Values of the order of 250 km for $\dot{\varepsilon} = 10^{-17}$ $s^{-1}$ are finally reached during the last stages of evolution, implying a north/south difference of 180 km in $T_e$ (Figure 4.5a). Below the northern polar cap, at the present day and for $\dot{\varepsilon} = 10^{-14}$ $s^{-1}$, the elastic thickness reaches 293 km, in good agreement with our constraint (Figure 4.5b).

Similarly, good fits to our three main constraints can be obtained when considering the Uniform Crustal Model. During the earlier stages, north/south $T_e$ evolution curves diverge from the beginning since the crustal dichotomy is already emplaced. Shaded areas on Figure 4.5a and b represent the range of $T_e$ evolution that we obtain from the simulations - from both the UCM and NUCM cases - that best fit $T_e$ constraints. These models are presented in section 3.4.c.

### 3.4.b Monte Carlo simulation results

**— Uniform Crustal Model (UCM)**

For the Uniform Crustal Model, we test the influence of three main parameters on $T_e$ evolution : the thicknesses of the northern and southern crusts (which are closely linked to their densities), and the crustal radioactivity enrichment factor.

As expected, the present-day value of $T_e$ below the northern polar cap is a strong constraint, that can be fitted only when considering large crustal radioelement contents, either with thick southern crusts relatively poorly enriched compared to the primitive mantle, or with thinner crusts more enriched in radioelements (Figure 4.6c). Suitable models for this constraint - i.e. with a score $> 0.5$ - predict a southern crustal thickness of 65 to 103 km, a northern one of 30 to 58 km, a crustal density of 2900 to 3170 kg $m^{-3}$ and an enrichment factor between 7.6

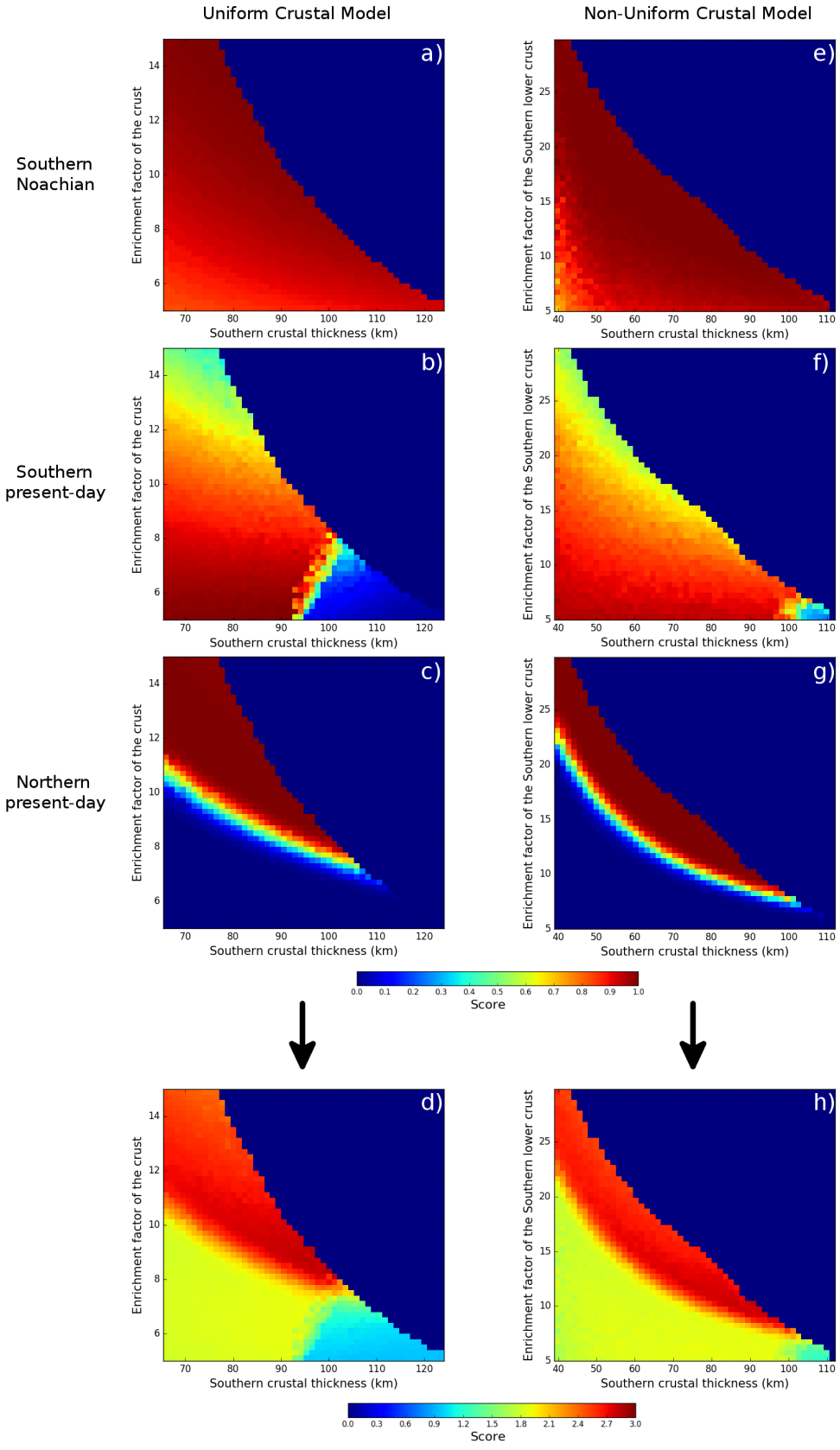
Uniform Crustal Model
Non-Uniform Crustal Model
Southern Noachian
Southern present-day
Northern present-day
a)
b)
c)
d)
e)
f)
g)
h)
Enrichment factor of the crust
Enrichment factor of the Southern lower crust
Southern crustal thickness (km)
Score

FIGURE 4.6

**FIGURE 4.6** – Results of the Monte Carlo simulations for the UCM (a, b, c and d) and NUCM (e, f, g and h) cases. Scores are represented in a color scale as a function of the southern crust thickness and radioelement enrichment factor for each $T_e$ constraint : from top to bottom in the Noachian in the south, at the present-day in the south and in the north, as well as for these 3 constraints altogether (d and h). See Figure 4.2c for score definition and main text for detailed parameter ranges.

and 14.7. The low southern Noachian elastic thicknesses are fitted with a wide range of values for all parameters and do not provide a strong constraint for crustal parameters (Figure 4.6a). Indeed, a wet crustal rheology implies a weak crust with an incompetent layer, at least during the early evolution, which decouples the elastic upper crust and lithospheric mantle inducing a low effective $T_e$ in agreement with observations. We note, however, that the crustal parameters for which the best scores for the northern present-day constraint are obtained, (i.e. relatively thin southern crusts and high bulk enrichment factors), deliver also the best scores for the Noachian $T_e$ constraint. This is not the case for the present-day value of $T_e$ below the southern polar cap (Figure 4.6b) for which the best fits are obtained for a similar crustal thickness but a much lower enrichment factor (bulk enrichment factor of $\sim 5-7$). This discrepancy between the crustal enrichment factor predicted by the two present-day constraints is due to the fact that if a lot of radioelements are present in the mantle, this latter is hotter and therefore allows to fit a low $T_e$ under the southern polar cap. On the opposite, if a large amount of radioelements is concentrated in the crust, the mantle is colder and high present-day $T_e$ could be reached in the northern hemisphere. In return, the $T_e$ in the south are also high but still in agreement with the $>$ 110 km constraint. In general, models with a thick southern crust and a low enrichment factor are characterized by present-day values of $T_e$ that are too low, both in the north ($<$ 280 km) and in the south ($<$ 110 km). On the contrary, models with large crustal thicknesses and strong radioelement enrichments might lead to crustal recycling, which is associated to a score equal to 0 and is responsible for the clear limit between areas with a high score and areas having a score equal to 0 (Figure 4.6d).

— **Non-Uniform Crustal Model (NUCM)**

Even though we test the effect of more parameters in this crustal model - thicknesses of the two crusts, enrichment in radioelements, density of the lower southern crust layer and thermal conductivity of the upper one - results for the Non-Uniform Crustal Model are similar in many ways to those for the Uniform Crustal Model : the range of parameters required to fit the southern Noachian and northern present-day constraints are in good agreement (Figure 4.6e and 4.6g), while the range of parameters required to fit the southern present-day $T_e$ constraint predicts poorly enriched southern crusts (Figure 4.6f). For the NUCM simulations our best scores, i.e. simulations fitting our three $T_e$ constraints (red zone on Figure 4.6h), are obtained when considering a southern crustal thickness between 39 and 99 km (including the 10 km basaltic upper crust), and a southern lower crustal enrichment factor ranging from 7.8 to 29.8, while we use a value of 10 for the northern crust. The clear negative trend between the southern crustal thickness and enrichment factor, shown by models with best scores, illustrates the need to have a large amount of radioelements in the crust in order to get a cold northern hemisphere

and fit the northern present-day constraint. The crustal radioelements need to be concentrated in the south, to provide low elastic thicknesses in agreement with the two constraints in the south. The southern crustal radioelement content is however limited by crustal delamination processes in the case of a thick southern crust, which is illustrated by the abrupt boundary between high score and zero score models in Figure 4.6h. In the case of a thin and highly enriched southern crust, this boundary is due to parameter combinations requiring more radioelements than those actually available in the planet inventory, as, before the impact, the northern primary crust has the same characteristics as the southern one. The northern crustal thickness as well as the thermal conductivity of the southern upper crust and the density of the southern lower crust are not constrained : the entire proposed range of values are suitable. The lower southern crustal density correlates positively with the crustal thickness (the denser, the thicker) and hence negatively with the enrichment factor (the denser, the less enriched). Interestingly for the NUCM simulations, very thin southern crusts (lower than 50 km) could fit the constraints if they are very enriched in radioelements (up to 30 compared to the primitive mantle).

### 3.4.c Accounting for recent volcanism

The range of suitable crustal parameters can be further constrained by Mars' volcanic activity. Recent volcanism, in the form of lava flows that might be as young as a few tens of Myr, has been observed in the large volcanic complexes of Tharsis (*Hartmann et al.*, 1999; *Neukum et al.*, 2004; *Werner*, 2009; *Hauber et al.*, 2011) and Elysium (*Vaucher et al.*, 2009; *Susko et al.*, 2017). This implies melt formation under Mars present-day mantle conditions, probably in mantle plumes localized under the large volcanoes (*O'Neill et al.*, 2007; *Li and Kiefer*, 2007). These mantle plumes likely originate at the core-mantle boundary, with a temperature $T_c$ characteristic of this depth. During their rise they cool adiabatically and their temperature at the depth $z$ is given by :

$$T_{plume}(z) = T_c - \frac{\alpha g T_c z}{C_m} \tag{4.22}$$

In order to test if current melt formation is feasible in our models, we compare the temperature profile in plumes $T_{plume}(z)$ with the solidus temperature $T_{solidus}(z)$ of a peridotite given by the parametrization of *Takahashi* (1990) from laboratory experiments :

$$T_{solidus}(P) = 1409 + 134.2P - 6.581P^2 + 0.1054P^3 \tag{4.23}$$

where $P$ is the pressure in GPa and $P(z) = \rho(z)g(z)z$. $\rho(z)$ and $g(z)$ are density and gravity. Suitable models are those where melt is formed at the base of the lid beneath large volcanoes. These volcanoes are located in the south because such provinces have a thick crust, similar to the southern one of our model. Since large plumes penetrate and erode the stagnant lid, we allow for plume penetration in the stagnant lid over a height of 100 km, which is reasonable given present-day stagnant lid thickness range of $260-480$ km. This means that we compare $T_{solidus}$ and $T_{plume}$ up to a depth $z = D_l^S - 100$ km in the south, where the temperatures are higher.

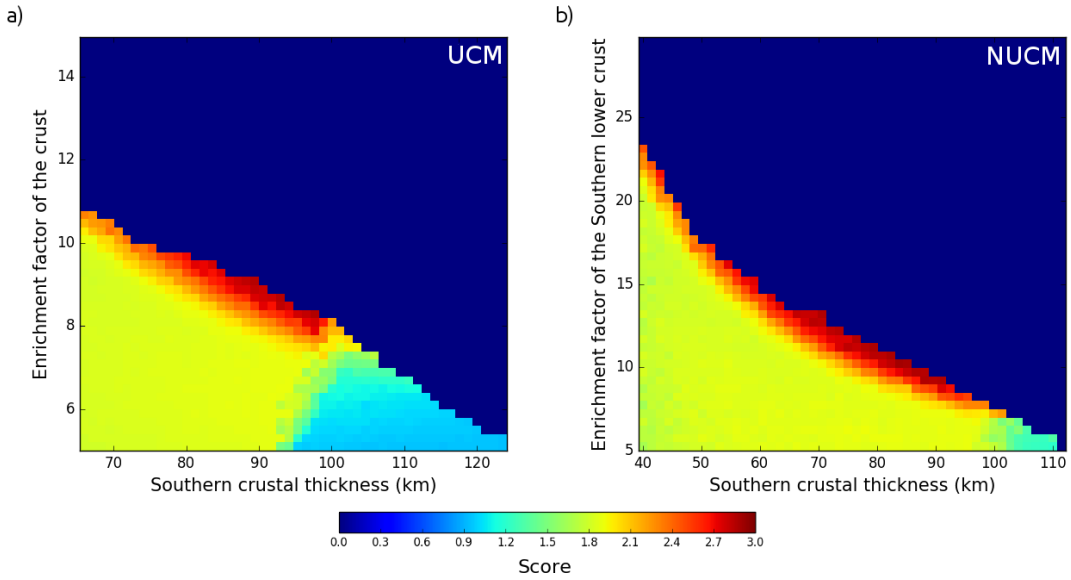


**FIGURE 4.7** – Results of the Monte Carlo simulations using the constraints on present-day volcanism in the south, for the UCM (a) and the NUCM (b) simulations. Scores are represented in a color scale as a function of the southern crust thickness and enrichment factor in radioelements. See Table 4.4 and Figure 4.10 for detailed parameter ranges.

Models that present a rather thin southern crust strongly enriched in radioelements concentrate the heat production near the surface, which is easily conducted away : these models cool too efficiently to be compatible with present-day melt formation. For the Uniform Crustal Model, enrichment factors higher than 9.7 for the entire crust and southern crustal thicknesses lower than 78 km are no longer suitable (Figure 4.7a). For the Non-Uniform Crustal Model, the properties of the southern lower crust are also more constrained with a crustal thickness of $43-96$ km (for a minimum density of 2620 kg m$^{-3}$) and an enrichment factor limited to values $< 21.7$ (Figure 4.7b). The northern crustal thickness is also constrained to values of $30-45$ km for both UCM and NUCM simulations. We note however that taking into account the lower solidus of *Kiefer et al.* (2015) rather than that provided by *Takahashi* (1990) would make melt formation easier and thus extend the range of admissible parameters to thinner southern crusts more enriched in radioelements. Finally, we observe that none of our suitable models predicts present-day melt formation in the north, in good agreement with observations. These results are summarized in Figure 4.10 and Table 4.4.

## 3.5 Discussion

In the following best models refer to those that fit the three constraints on elastic thickness with a score higher than 2.5 and current melt formation in the southern hemisphere.

### 3.5.a Model predictions on radioelement concentrations

GRS measurements give surface concentrations of 2000 – 6000 ppm for K and 0.2 – 1 ppm for Th (*Taylor et al.*, 2006). Using the compositional model of *Wänke and Dreibus* (1994), our best UCM cases predict a crustal enrichment factor of 7.8 – 9.7 resulting in concentrations of 2380 – 2960 ppm for K and 0.44 – 0.54 ppm for Th, in good agreement with GRS data. Similarly, our NUCM cases showing the best scores are in the range of GRS measurements for surface concentrations where we assume $\Lambda^N = 10$. Even though the potentially more enriched southern lower crust is buried and might not influence surface measurements, we obtain K

| | UCM | NUCM | NUCM2 |
|---|---|---|---|
| **Northern crustal parameters** | | | |
| $d^N$ [km] | 30 – 41 | 30 – 45 | 30 – 55 |
| $\rho^N$ [kg m$^{-3}$] | 3040 – 3170 | 3100 | 3100 |
| $k^N$ [W m$^{-1}$ K$^{-1}$] | 3 | 3 | 3 |
| $\Lambda^N$ | 7.8 – 9.7 | 10 | 5 – 13.5 |
| Northern *PBR* [%] | 11.1 – 13.8 | 12.7 – 19 | 6.4 – 20.3 |
| **Southern crustal parameters** | | | |
| $d_1^S$ [km] | 0 | 10 | 10 |
| $d^S$ [km] | 78 – 99 | 43 – 96 | 40 – 96 |
| $\rho_1^S$ [kg m$^{-3}$] | 3040 – 3170 | 3100 | 3100 |
| $\rho_2^S$ [kg m$^{-3}$] | 3040 – 3170 | 2620 – 3100 | 2530 – 3100 |
| $k_1^S$ [W m$^{-1}$ K$^{-1}$] | 3 | 2 – 3 | 2 – 3 |
| $k_2^S$ [W m$^{-1}$ K$^{-1}$] | 3 | 3 | 3 |
| $\Lambda_1^S$ | 7.8 – 9.7 | 10 | 5 – 13.5 |
| $\Lambda_2^S$ | 7.8 – 9.7 | 8 – 21.7 | 7.7 – 26.8 |
| Southern *PBR* [%] | 42.7 – 46.6 | 44.5 – 51.2 | 42.6 – 56.8 |
| **Present-day predictions** | | | |
| Northern SLT [km] | 443 [434 – 459] | 445 [433 – 471] | 445 [431 – 479] |
| Southern SLT [km] | 337 [321 – 349] | 347 [326 – 371] | 346 [313 – 373] |
| Difference in temperature [K] | 268 [229 – 301] | 246 [170 – 304] | 249 [168 – 327] |
| Northern SHF [mW m$^{-2}$] | 17.6 [17.1 – 18.1] | 18.2 [17.1 – 19.5] | 17.1 [15.1 – 19.9] |
| Southern SHF [mW m$^{-2}$] | 25.2 [24.8 – 25.6] | 25.8 [25.0 – 26.5] | 26.5 [24.6 – 27.8] |

**TABLE 4.4** – Range of crustal parameters and characteristics of the present-day thermal structure predicted by the models that fit the 4 constraints, including present-day melt formation in the south. For the NUCM2 simulations the enrichment factor of the northern crust is allowed to vary between 5 and 15 (see section 3.7.a). Notations are similar to those used in Table 4.3 and PBR corresponds to the fraction of the bulk radioelement content contained in the crust. We provide the average and range of values (in square brackets) of our predictions concerning the present-day thermal structure in the north and south, i.e. the stagnant lid thickness (SLT), surface heat flux (SHF), and the north/south differences in temperature at a depth of 150 km.

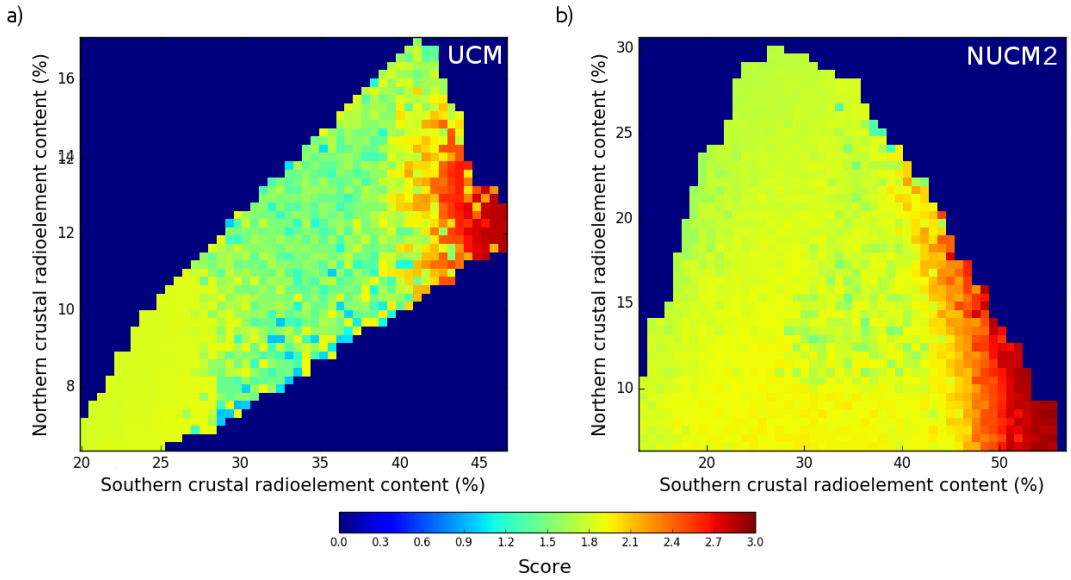


**FIGURE 4.8** – Results of the Monte Carlo simulations using the constraints on present-day volcanism in the south. Scores are represented in a color scale as a function of the radioelement contents of the two hemispheres, for the UCM (a) and the NUCM2 (NUCM where we vary the northern crustal enrichment factor, see section 3.7.a) (b) simulations. See Table 4.4 for detailed parameter ranges.

content of $2440 - 6620$ ppm, and Th concentrations of $0.45 - 1.2$ ppm for this layer, which remains in good agreement with surface data. In general our results lie close to the upper bound of the enrichment factors usually taken for the Martian crust (*Nimmo and Stevenson*, 2001; *Schumacher and Breuer*, 2006; *Taylor et al.*, 2006; *Grott and Breuer*, 2008b, 2009), although they can be much higher if the north and south differ (NUCM simulations), consistent with a smaller degree of partial melting for crustal production, though still remaining in good agreement with the constraints we have on radioelement concentrations.

Our models suggest that the crust concentrates $55 - 65$ % of the bulk radioelement content of the planet, with more than 42 % in the southern crust (see Figure 4.8 and Table 4.4), implying an important mantle depletion in radioelements. Since the partition coefficients of water and heat sources are similar (*Morschhauser et al.*, 2011), a significant mantle depletion in water is also expected. Our mantle depletion is stronger than the 50 % suggested by *Taylor et al.* (2006) although the surface concentration in radioelements is similar. This difference can be explained by the thicker average crust needed to explain the constraints of the elastic lithosphere thickness. Note that for the NUCM simulations, more radioelements ($70 - 80$ %) are contained in the crust before the impact because both the northern and southern crusts have then a high radioelement content and thickness, implying a mantle even more depleted. Such a depletion could be explained by extraction of radioelements through basaltic volcanism with a low degree of partial melting or could result from initial magma ocean solidification as crystallization

proceeded from the bottom up (*Elkins-Tanton et al.*, 2003), resulting in a high concentration of incompatible radioelements near the surface. A large depletion in radioelements is necessary to retrieve very large present-day elastic lithosphere thickness in the north, whereas the low Noachian and present-day southern $T_e$ constraints could be fitted either with a large southern crustal radioelement content or with a hot and poorly depleted mantle. Among all models, the best scores are thus obtained for the highest southern radioelement content that are feasible without crustal delamination (Figure 4.8a and b). In those models, the northern crust contains few radioelements, due to either a thin crust in both UCM and NUCM simulations, or to a low enrichment factor for the NUCM2 ones (see section 3.7.a).

*Sekhar and King* (2014) have shown that a prominent degree-two structure of convection is observed at $\sim 4$ Gyr if a lot of heat sources (100 % in their simulations) are concentrated into the crust. Such a planform of mantle convection could explain the generation of large plumes below Tharsis and Elysium Mons. Nevertheless the authors also note that present-day volcanism requires a higher content of radioelements in the mantle. Our Non-Uniform Crustal Model could represent an alternative scenario to explain this apparent paradox on crustal radioelement content. Indeed, before the impact a large part of the radioelements are contained in the crust (up to 80 %) : during this early stage a two-degree convection structure may have formed. As the secondary crust is less enriched in radioelements, the impact reinjects the additional radioelements of the northern primary crust into the mantle resulting in a more enriched mantle, which could explain the longstanding volcanic activity.

### 3.5.b Crustal thickness and density predictions

We find an average range of $40-75$ km for the global crustal thickness, with a similar average thickness of 35 km in the north for both the UCM and NUCM simulations, whereas the estimations in the south are more scattered. In this hemisphere an average of 80 km is retrieved, but significantly thinner southern crusts can not be ruled out as 5 % of the NUCM best cases show values $< 60$ km (see Table 4.4 for the total ranges). *Neumann et al.* (2004) obtained the same bimodal distribution of crustal thicknesses but with thickness peaks at 32 and 58 km, whereas *Wieczorek and Zuber* (2004) found values of 38 and 62 km. There is thus a close agreement with the values that we retrieve in the north, but not in the south where our models generally predict thicker crusts. This is due to the larger crustal densities of our best models compared to those of *Neumann et al.* (2004) and *Wieczorek and Zuber* (2004). The quite large crustal densities of most of our best models would be more compatible with estimates of *Baratoux et al.* (2014) for a porosity of $5-10$ % in the crust, but a few models that consider high radioelement enrichment factors in the south ($> 18$) are coherent with the low average crustal thickness value of 42 km given by *Goossens et al.* (2017). However, we observe that these latter models do not fit the present-day volcanism constraint if the southern surface fraction is increased to values of $65-70$ %.

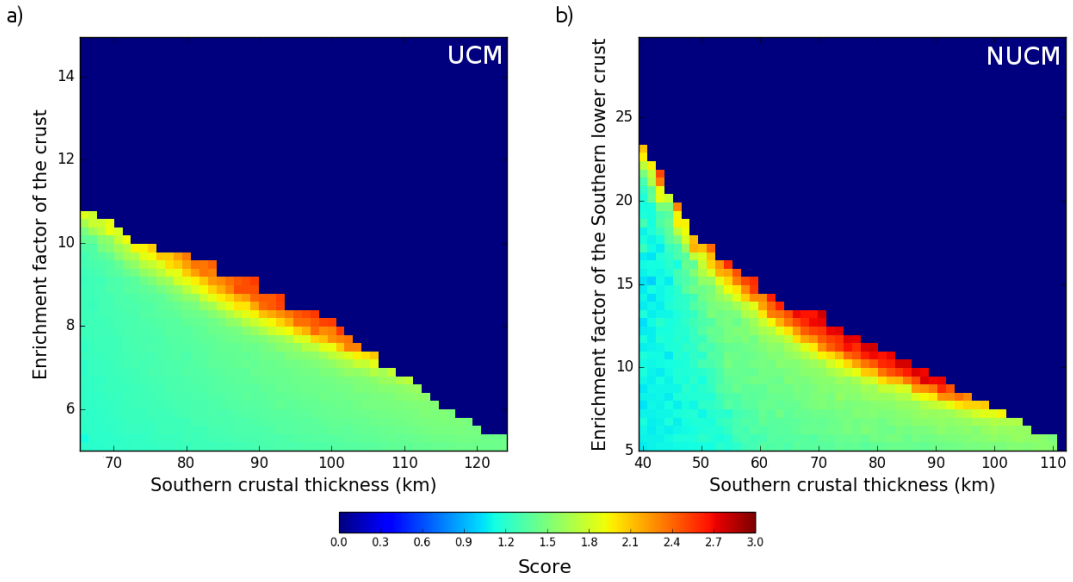


**FIGURE 4.9** – Results of the Monte Carlo simulations using a dry mantle and dry crustal rheology for the UCM (a) and the NUCM (b) simulations. Scores are represented in a colorscale as a function of the southern crust thickness and enrichment factor. See section 3.7.b for detailed parameter ranges.

### 3.5.c Effect of the mantle and crustal rheology

The rheology of mantle and crust has a large impact on the elastic thickness calculations, and depends on the mantle and crustal water contents as well as on the deformation mechanism, which are poorly constrained. In the previous sections, we have presented results for a dry mantle and wet crustal rheology along with diffusion creep. Assuming instead a dry mantle and dry crustal rheology provides similar results to the dry mantle and wet crustal one, except that the low Noachian $T_e$ cannot be fitted by the UCM simulations. This finding is similar to *Grott and Breuer* (2009) and *Morschhauser et al.* (2011) who argue that a wet crust is necessary to explain the low elastic thickness in the Noachian. However, for the NUCM simulations the situation is slightly different as it shows that a dry crust is compatible with the observation although values of the elastic lithosphere thicknesses in the Noachian are in the upper range of permissible values (see section 3.7.b and Figure 4.9). In addition, we find that none of our simulations with a wet olivine mantle rheology could retrieve suitable fit to our three $T_e$ constraints (see section 3.7.a). In particular, the present-day north elastic thicknesses are much lower than the $\geq$ 300 km constraint. With a wet mantle rheology, *Grott and Breuer* (2009) could retrieve higher global $T_e$, close to 300 km, if they consider a large crustal radioelement content $>$ 80 %, but they use a steady-state temperature profile in the stagnant lid. In fact, transient effects caused by heat transport in a thick stagnant lid should be large (*Michaut and Jaupart*, 2004). The time-dependency of the conductive temperature profile leads to higher temperatures in the lithosphere, inducing lower elastic thicknesses. Moreover a present-day dry mantle rheology

is more consistent with the high crustal radioelement contents obtained by our best models ($>$ 55 % of the bulk heat sources). Indeed, extraction of radioelements due to partial melting of the mantle and crustal formation also implies a similar extraction of volatiles (*Morschhauser et al.*, 2011). Our modeling does not provide a self-consistent way to investigate water depletion as it assumes that the bulk of the crust is formed at the beginning of our simulations. However, using a scenario of crustal formation by mantle partial melting, *Morschhauser et al.* (2011) found that a wet olivine rheology with a low reference viscosity is more compatible with the crustal formation history during the early stages of evolution, whereas the occurrence of present-day volcanism is better fitted with a mantle depleted in water due to crustal formation. Accounting for a more realistic crustal and volatile extraction process by mantle partial melting in our simulations might lead to lower elastic thicknesses during the Noachian period - still in agreement with our constraint - but would probably not significantly change our present-day values.

In our model, we consider diffusion creep deformation mechanisms in the mantle with an activation energy of 300 kJ mol$^{-1}$ for a dry mantle (*Karato and Wu*, 1993). It is however not clear if dislocation creep rather than diffusion creep occurs in the Martian mantle. Simulations with a lower activation energy of 200 kJ mol$^{-1}$ for dislocation creep and a dry olivine mantle rheology (see section 3.3.a) lead to thinner lithospheres. The constraint of present-day melting is thus more easily met and models with even thinner crusts more enriched in radioelements are acceptable. Compared to results obtained with an activation energy of 300 kJ mol$^{-1}$, our best fits for both the UCM and NUCM simulations are obtained when considering thinner crusts by about 10 to 15 km that are less dense and more enriched in radioelements (see Figure 4.10 for detailed ranges of parameters).

### 3.5.d Effect of the initial conditions

In our models the initial mantle temperature has an impact on the present-day elastic thickness in the case of a dry mantle rheology - i.e. large viscosity -, since the large enrichment of radiogenics in the crust and depletion in the mantle can lead to a less pronounced thermostat effect. In this case, the less vigorous convection in the strongly depleted mantle cannot entirely erase the difference in initial temperatures.

1D parametrized models of the coupled crustal and thermal evolution of Mars suggest that the initial mantle temperature would be about 1700 K (*Hauck and Phillips*, 2002; *Morschhauser et al.*, 2011), thus lower than that considered here (1800 K). An initial temperature of 1700 K leads to higher present-day $T_e$ values by $\sim$ 30 km on average and thicker stagnant lids in both hemispheres, hardly compatible with recent volcanism, especially for UCM simulations. Only a few NUCM parameter combinations considering a thick southern crust ($\sim 75-85$ km), moderately enriched in radioelements ($\sim 7.8-9$), fit our four constraints. Conversely, for a higher initial mantle temperature of 1900 K, the four constraints are fitted with a similar mantle depletion as in the models presented in sections 3.5.a and 3.5.b. For the NUCM simulations,

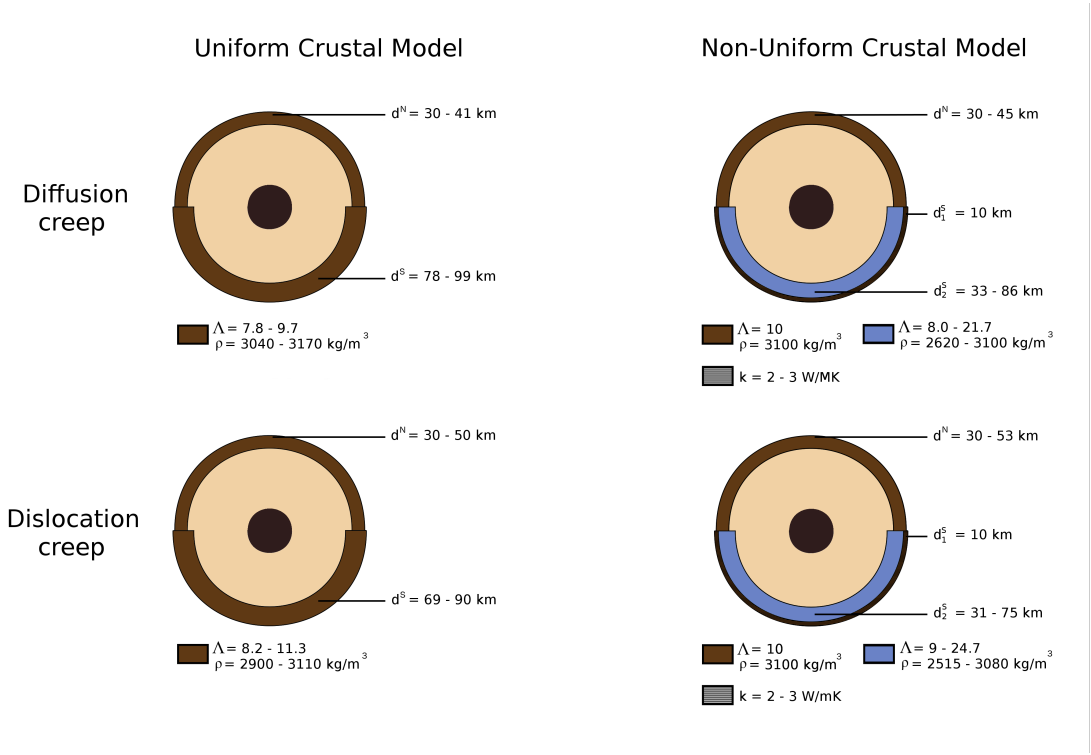


**FIGURE 4.10** – Summary of the crustal properties of our best models, for diffusion creep (top) and dislocation creep (bottom) rheologies.

using a temperature increase of 200 K rather than 100 K following the impact has the same effect as considering $T_{m_0} = 1900$ K. The impact age - ranging from 4.5 to 4 Gyr - has only very little effect on our $T_e$ evolution.

### 3.5.e Predictions on present-day thermal structure

The results of our study suggest that the temperature profiles at the present day might be different in both hemispheres (Figure 4.11). For instance, our NUCM reference model (see section 3.4.a for its crustal parameters, in bold on Figure 4.11) shows a temperature profile that might be higher by $> 300$ K over more than 250 km depth in the southern hemisphere in comparison to the northern one. The surface temperature is considered the same in both hemispheres but the temperature gradient in the southern crust is much larger than in the north because of its larger thickness and radioelement content. The difference in temperature between the two hemispheres reaches its maximum at the depth of the southern crust-mantle transition and remains constant in the entire lithospheric mantle. These predictions on Mars' current thermal structure are quite stable among our best fit models (see Table 4.4 and shadowed areas on Figure 4.11 that represent the dispersion of their temperature profiles).

The future InSight NASA mission will land on Mars in the northern hemisphere, close to the dichotomy boundary in November 2018 and will place a seismometer (SEIS) and a heat flow probe (HP$^3$) on the planet's surface. The north/south differences in thermal structure predicted by our models might thus leave a signature in the seismic signals recorded by the seismometer (*Panning et al.*, 2015). Furthermore, both crustal models predict a similar surface heat flux at the InSight landing site in the north, with a range of 17.1 to 19.5 mW m$^{-2}$ for the best models. Heat flux are predicted to be significantly higher in the south with a range of $24.8 - 26.5$ mW m$^{-2}$ (Table 4.4).

### 3.5.f Model limitations and validation

Our model is limited because crustal properties are assumed to be homogeneous over an entire hemisphere, although spatial differences in thicknesses probably exist (*Neumann et al.*, 2004). We also assume a well-mixed mantle, which does not account for upwellings and downwellings even though they induce spatial variability in lithosphere thickness. In fact, $T_e$ estimates below the two polar caps might not be representative of the entire hemisphere as assumed here.

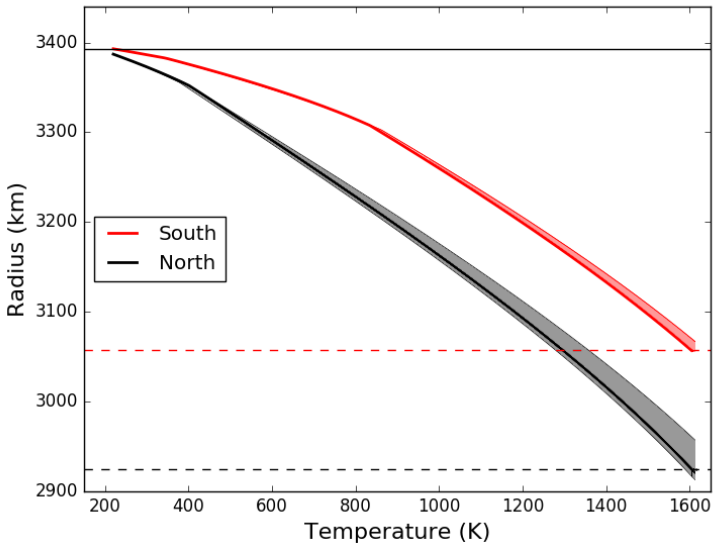


**FIGURE 4.11** – Present-day temperature profile in the stagnant lid, in the north (black) and in the south (red), for models that show the best scores (i.e. that fit all our 4 constraints). The temperature profiles of the reference model (section 3.4.a, Figure 4.5) are shown in bold lines. The southern surface altitude ($r = R_p^S$) is illustrated by the horizontal black line and the base of the stagnant lid by the dashed lines. The shaded areas correspond to the range of temperature profile obtained in the simulations that have the best scores (between 2.5 and 2.91) for both the UCM and NUCM simulations.

To validate our 1D model, we compared our results with those obtained in 3D convection simulations by *Plesa et al.* (2016) in a model set-up accounting for a crustal model comparable to the UCM one presented here (case 25 of *Plesa et al.*, 2016)). Strong mantle plumes cause lateral variations of 40 km for the present-day elastic thicknesses over an hemisphere, which is consistent with the assumptions we made for this study (see section 3.2 and Figure 4.2 c). Furthermore, we found that there is a close agreement between our north/south temperature profiles and those of *Plesa et al.* (2016) averaged over each hemisphere. In particular, *Plesa et al.* (2016) also observe a similar north/south difference in temperature and retrieve present-day surface heat flux in good agreement with ours. Their total range of surface heat flux is larger ($16.2 - 35.3$ mW m$^{-2}$ and 19 mW m$^{-2}$ at the InSight landing site in their case 25, in comparison to a range of $17.1 - 26.5$ mW m$^{-2}$ and 17.1 mW m$^{-2}$ at the InSight landing site for our model), but this is likely due to localized effects of the topography in the 3D thermal simulations that can not be resolved with our 1D model.

## 3.6 Conclusion

The prominent north/south crustal dichotomy might extend at depth and induce distinct lithosphere thicknesses for the two hemispheres. We have therefore distinguished northern and southern $T_e$ estimates and used three main constraints on $T_e$ evolution : low values during the Noachian in the south, and a potentially large north/south present-day difference below the two polar caps ($\geq$ 300 km in the north and $>$ 110 km in the south). As recent volcanic activity has been suggested for the large volcanic centers on Mars, suitable models must also allow for present-day melt formation in the highlands.

In our simulations, a dichotomy in crustal structure and composition was considered with two possible crustal models. The UCM case is characterized by a uniform crustal composition but the southern crust is thicker to compensate for the north/south difference in altitude. In the NUCM case, the southern crust can have distinct properties (conductivity, enrichment in radioelements, density and thickness) compared to the northern one.

Running Monte Carlo simulations with a parametrized thermal evolution model accounting for north/south differences in crustal properties, we find the range of crustal parameters that fit constraints on elastic lithosphere thickness and present-day volcanism. Interestingly both the UCM and NUCM cases converge on similar ranges of values for the northern and southern crustal radioelement contents. In order to fit the large current northern $T_e$, we predict that $55 - 65$ % of the radioelements have to be concentrated in the crust, and more than 42 % in the southern one, which implies a similar mantle depletion in water. In most suitable models, expected crustal thicknesses are higher than those usually assumed in the highlands, with northern and southern averages of 35 and 80 km, respectively, and a bulk average of $40 - 75$ km, with a southern crust that is equally or slightly less dense than the northern one. Enrichment factors in radioelements are in the upper range of values or even slightly higher than in previous studies. However, simulations with two types of crust also show a high score for a

southern crust much more enriched in radioelements than the north (by a factor of 2.2). These models are associated with a southern crust less dense than the northern one by as much as 480 kg $m^{-3}$ (in agreement with *Pauer and Breuer* (2008) and *Baratoux et al.* (2014)), which would suggest the presence of a buried felsic component in the south. Note that all of the results are given for a dry olivine mantle rheology. A present-day wet mantle rheology cannot satisfactorily fit the $\geq$ 300 km northern present-day elastic thickness constraint, which is coherent with the large mantle extraction of radioelements and volatiles predicted by our models. Conversely, both wet and dry diabase crustal rheologies are possible and converge to the same predictions regarding crustal properties.

The future InSight mission is expected to land close to the dichotomy boundary in the northern hemisphere. In our models north/south present-day thermal profiles are expected to differ by 170 to 304 K over more than $250-310$ km depth, which might result in different travel times of seismic waves produced by events occuring in the two hemispheres and leave a signature in the geophysical signals recorded by the SEIS instrument. Surface heat flux should also be very different in between both hemispheres : we predict values as high as $24.8-26.5$ mW $m^{-2}$ in the highlands and low heat flux in the range of $17.1-19.5$ mW $m^{-2}$ in the north (i.e. at the InSight landing site), close to those of *Plesa et al.* (2016) when considering similar crustal properties.

## 3.7 Supplements

### 3.7.a NUCM simulations with a variable northern enrichment factor (NUCM2)

In order to investigate the role of the northern crustal parameters in more detail for the NUCM simulations, we also run Monte Carlo simulations where the northern crustal enrichment factor could vary between 5 and 15. We refer to these simulations as the Non-Uniform Crustal Model 2 (NUCM2). We found suitable parameter combinations, that fit the three $T_e$ constraints and present-day melt formation, when considering northern crustal enrichment factor ranging from 5 to 13.5. However, in order to fit the large present-day elastic thickness in the north, the percentage of radioelements that could be concentrated in the northern crust remains very close to that retrieved by the UCM and NUCM cases (Figure 4.8b and Table 4.4). There is thus a trade-off between the enrichment factor and the thickness of the northern crust : the more enriched, the thinner the crust is. The ranges of enrichment factor retrieved for NUCM2 simulations correspond to surface concentrations of K and Th that are in agreement with GRS data.

### 3.7.b Effect of a wet or dry rheology for the mantle and the crust

Considering a dry mantle and dry crustal rheology also provides a good fit to the three $T_e$ constraints. By using crustal models similar to our UCM one, *Grott and Breuer* (2008b) and *Breuer et al.* (2016) found that a dry mantle and dry crustal rheology is not in agreement

with the Noachian low $T_e$. Indeed a dry crust is stronger and the thinner incompetent bottom crustal layer disappears earlier both in the north and in the south in Mars evolution. Nevertheless they used crustal thicknesses of $30-60$ km and an enrichment factor of $5-10$, lower than the ranges considered here. In our simulations we find that models accounting for thicker crusts more enriched in radioelements could predict low elastic thicknesses during the Noachian period in agreement with our constraint, especially for the NUCM simulations as even more radioelements could be concentrated in the southern crust. The Noachian constraint remains however hard to fit for the UCM simulations where minimal values of 43 km are reached for the elastic thickness in the Noachian, i.e. in the upper bound of Noachian estimates. Interestingly the range of suitable models for the southern Noachian constraint is similar to that fitting the present-day northern $T_e$. The present-day elastic thicknesses and their fit to the constraints remain similar to those for a wet crust and dry mantle. Our best fits for the dry mantle dry crustal rheology predict therefore similar parameters as for the dry mantle and wet crustal one. For the UCM case, simulations with the best scores have crustal thicknesses of $31-39$ km in the north, $89-101$ km in the south, an enrichment factor of $7.9-9.1$ and a crustal density of $3138-3182$ kg m$^{-3}$ (Figure 4.9a). For the NUCM simulations, the northern crust is predicted to have a thickness of $30-45$ km, for a radioelement enrichment of 10, and the southern one is $43-93$ km thick with an enrichment factor of $8.4-21.7$ and a density range of $2620-3100$ kg m$^{-3}$ for its lower part (for 3100 kg m$^{-3}$ in the north) (Figure 4.9b).

We also run Monte Carlo simulations with a wet mantle and a dry or wet crust. In this case, the mantle viscosity is lower and therefore energy transfer by convection is more efficient, resulting in thinner lithosphere thicknesses. In this context many models that were fitting constraints for a dry mantle, are now excluded because they predict crustal delamination due to high mantle temperatures during the early stages of evolution. We note that two parameters favor thin lithosphere thicknesses and delamination processes : a thick crust and/or a high crustal heat production. In UCM simulations, the southern crust is thick (at least 65 km) and therefore none of our simulations prevents crustal delamination. But for NUCM simulations, lower southern crustal thicknesses of $40-45$ km in the south and $\sim 30$ km in the north can be found, which do not lead to delamination. These models have an enrichment factor of $6-8.6$ in the lower south crust (for $\Lambda^N = 10$). In these simulations $T_e$ are much thinner than for a dry mantle and there is therefore a good fit to the Noachian and the present-day southern constraints. Nevertheless none of our simulations with a wet mantle rheology fit the high northern present-day $T_e$, and show maximum values of only 180 km.

# 4 3-D simulations of two representative UCM and NUCM cases

We perform 3-D simulations accounting for the properties predicted by two examples representative of the best UCM and NUCM cases defined in section 3.4.c. Those dynamical thermal models are used in this section to validate the results obtained with parametrized models and to investigate the consequences of the best crustal models on the mantle convection pattern.

## 4.1 3-D mantle convection models

### 4.1.a The *UCMref1* and *NUCMref2* cases

Two main categories emerge among all the best crustal models (score $> 2.5$, see section 3.4.c) that fit the constraints on present-day volcanism in the south and on elastic lithosphere thickness (small values during the Noachian for the southern hemisphere and a large present-day difference below the two polar caps). For both UCM and NUCM cases, most of the suitable models are characterized by a large difference in crustal thickness between the two hemispheres, the southern crust being thicker than the northern one (see Figure 4.7, Table 4.4). In this case, the southern crust is equally or slightly more enriched than the northern crust with moderate values of the radioelement enrichment factor. A second category of suitable models is represented by some NUCM cases that are characterized by a smaller north/south difference in crustal thickness with a southern crust that is significantly less dense than the bulk crust and that contains a non-negligible proportion of felsic rocks. For such models the southern crust is much more enriched (enrichment factor up to $\sim 21$) than the northern one (enrichment factor of 10) whereas the upper most layer of the southern crust can have a lower thermal conductivity.

The *UCMref1* case is a typical example of the first category of crustal models. It is characterized by a southern crust that is almost three times thicker than the northern one and by a uniform and moderate enrichment factor in radioelements of 8.4 (see Table 4.5 for details). The elastic thickness evolution predicted by this model is almost the same as that of the reference NUCM case introduced in section 3.4.a (black and red solid lines on Figure 4.5). In particular, it shows a large present-day contrast in elastic thickness between the northern and southern hemispheres (285 km and 185 km, respectively) associated to one of the highest scores (2.89) among all NUCM and UCM simulations. In contrast, the *NUCMref2* case predicts a smaller north/south present-day difference in elastic thickness (275 and 209 km, respectively), which leads to a lower score of 2.7 though still in the upper range given the errorbars of the elastic lithosphere thickness estimates (see Figure 4.2b). The crustal model *NUCMref2* is characterized by a southern crust only slightly thicker than the northern one but much more enriched in radioelements for its lower part (16 versus 10 in the north). Finally, a lower thermal conductivity of 2.2 mW $m^{-1}$ $K^{-1}$ is assumed in the 10 km thick upper southern crustal layer compared to the rest of the crust (3 mW $m^{-1}$ $K^{-1}$, see Table 4.5 for details).

| | *UCMref1* model | *NUCMref2* model |
|---|---|---|
| **Northern crust** | | |
| $d^N$ [km] | 35 | 33 |
| $\rho^N$ [kg m$^{-3}$] | 3165 | 3100 |
| $k^N$ [W m$^{-1}$ K$^{-1}$] | 3 | 3 |
| $\Lambda^N$ | 8.4 | 10 |
| Northern *PBR* [%] | 11.8 | 13 |
| **Southern crust** | | |
| $d_1^S$ [km] | 0 | 10 |
| $d^S$ [km] | 98 | 55 |
| $\rho_1^S$ [kg m$^{-3}$] | 3165 | 3100 |
| $\rho_2^S$ [kg m$^{-3}$] | 3165 | 2835 |
| $k_1^S$ [W m$^{-1}$ K$^{-1}$] | 3 | 2.2 |
| $k_2^S$ [W m$^{-1}$ K$^{-1}$] | 3 | 3 |
| $\Lambda_1^S$ | 8.4 | 10 |
| $\Lambda_2^S$ | 8.4 | 16 |
| Southern *PBR* [%] | 48 | 53 |
| **Present-day predictions** | | |
| Northern SLT [km] | 458 | 447 |
| Southern SLT [km] | 330 | 362 |
| Difference in Temperature [K] | 310 | 210 |
| Northern SHF [mW m$^{-2}$] | 17.1 | 17.9 |
| Southern SHF [mW m$^{-2}$] | 25.9 | 26 |
| Northern transition SHF [mW m$^{-2}$] | 18 | 18.5 |
| Southern transition SHF [mW m$^{-2}$] | 25.4 | 25.5 |

TABLE 4.5 – Crustal parameters and characteristics of the present-day thermal structure predicted by the *UCMref1* and *NUCMref2* end members among the best *UCM* and *NUCM* crustal models that fit the three constraints on elastic thickness and predict current melt formation in the southern hemisphere (score $> 2.5$, see section 3.4.c). Notations are similar to those used in Table 4.4. Northern and southern transition SHF correspond to the surface heat flux on each side of the transition zone defined in section 4.3 (see Figure 4.14).

### 4.1.b Modeling of the north/south dichotomy in 3-D dynamical models

To investigate the convection patterns induced by the best crustal models obtained with 1-D parametrized models in section 3 we perform 3-D simulations for the *UCMref1* and *NUCMref2* cases with the same parameters than those used for the 1-D models (see Table 4.1). The Gaia code (*Hüttig and Stemmer*, 2008; *Hüttig et al.*, 2013) is used with a radial resolution of 15 km in the first 115 km below the surface and 25 km in the rest of the mantle. 41000 grid points are considered for each radial level, resulting in a lateral resolution of $\sim 45$ km in the mid-mantle.

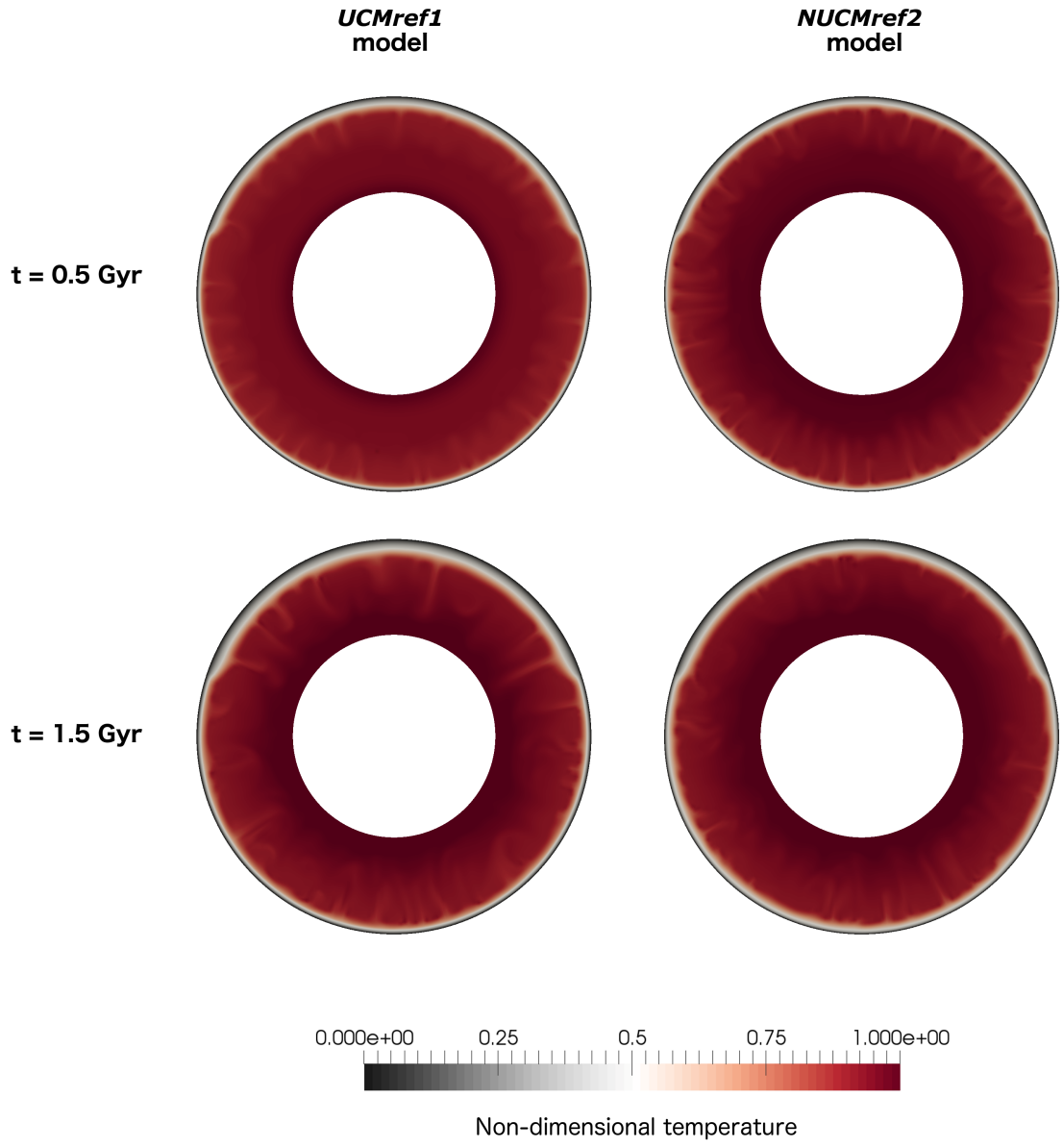


**FIGURE 4.12** – Pole to pole cross sections of the 3-D thermal models accounting for the properties of the *UCMref1* (left) and *NUCMref2* (right) crustal models. Snapshots are given at $t = 0.5$ Gyr (top) and $t = 1.5$ Gyr (bottom). The color-scale represents the non-dimensional temperature $T$ for a temperature scale corresponding to the initial temperature drop across the shell $\Delta T = T_{c_0} - T_s$.

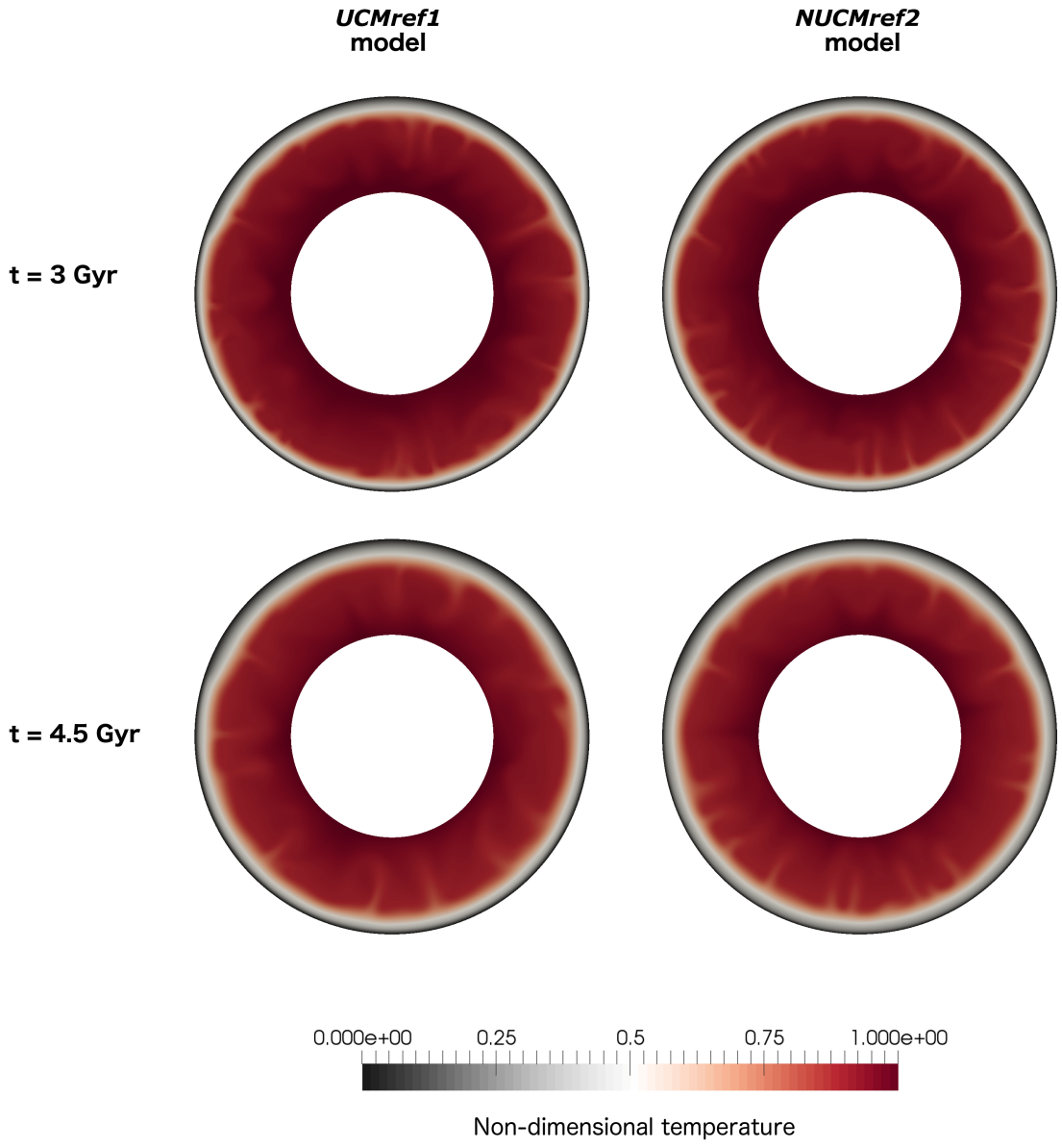


**FIGURE 4.13** – Pole to pole cross sections of the 3-D thermal models accounting for the properties of the *UCMref1* (left) and *NUCMref2* (right) crustal models. Snapshots are given at $t = 3$ Gyr (top) and $t = 4.5$ Gyr (bottom). The color-scale represents the non-dimensional temperature $T$ for a temperature scale corresponding to the initial temperature drop across the shell $\Delta T = T_{c_0} - T_s$.

To be consistent with 1-D parametrized models, we do not account for lateral variations in crustal thickness within a hemisphere. Similarly the long-wavelength topography change over several hundred kilometers observed at the dichotomy boundary (*Watters*, 2003a; *Watters and McGovern*, 2006; *Watters et al.*, 2007) is neglected. To mimic the north/south crustal dichotomy in our dynamical *UCMref1* and *NUCMref2* thermal models, we rather adopt a simplified approach, in which we only consider an abrupt transition between two types of crust representative of purely northern or southern properties (thickness, density, enrichment in radioelements and thermal conductivity, see Table 4.5 for values). Contrary to parametrized NUCM models, these differences are set from the beginning at 4.5 Gyr.

## 4.2 Mantle convection panels

In the *UCMref1* simulation (left snapshots on Figures 4.12 and 4.13), the thickness of the cold stagnant lid (black and white areas) steadily increases and is thus larger in the northern hemisphere than in the southern one from the very beginning. The north/south transition in stagnant lid thickness is large for this crustal model during the entire evolution. At 1.5 Gyr, large downwellings are well-developped in the northern hemisphere, whereas they are narrower and more numerous in the southern mantle. Differences in the convection pattern between hemispheres smooth out with time as the downwellings become more pronounced and spaced in the southern mantle. Mantle upwellings are not well distinguishable given the small initial contrast in temperature at the CMB (see Table 4.1), the intermediate value of activation volume ($V = 6$ cm$^3$/mol) and the high internal heating rate that we use in our models. For the last time steps ($\geq 3$ Gyr), stable mantle upwellings are, nevertheless, distinguishable at the dichotomy boundary : as proposed by *Šrámek and Zhong* (2010) and *Zhong* (2009), the dichotomy boundary might thus stabilize upwellings. However, in our models the mantle plumes located at the north/south transition zone are too numerous and weak to give rise to the major volcanic provinces of Tharsis and Elysium. Those mantle plumes might, nonetheless, generate volcanic activity at the dichotomy boundary where they reach shallow depths because of the presence of hot mantle upwellings below the thin lithosphere of the southern hemisphere.

Although different crustal properties are considered for the *NUCMref2* model compared to the *UCMref1* one, very similar convection patterns are observed for those two 3-D simulations (right and left snapshots, respectively, on Figures 4.12 and 4.13). However, some slight differences are visible. On one hand, the deflection in stagnant lid thickness associated to the transition zone between the northern and southern hemispheres is smoother in the *NUCMref2* simulation because of the lower north/south difference in lithosphere thickness for this model (see Table 4.5). In the *NUCMref2* simulation we impose an initial temperature higher by 100 K to mimic the impact and to be consistent with the 1-D model. At the present day, the *UCMref1* simulation is, however, hotter than the *NUCMref2* one for which more radioelements are concentrated in the shallow crust (65 % versus 60 % for the *UCMref1* simulation). Since lower mantle temperatures are observed at the present day in the *NUCMref2* simulation, the plumes are more distinguishable than for the *UCMref1*. They seem to be mostly concentrated in the

northern hemisphere whereas downwellings are more numerous in the southern hemisphere, which leads to an asymmetric convection pattern directly linked to the north/south crustal dichotomy that is, in fact, visible in all our 3-D simulations. However, those observations are not consistent with the results of previous studies (e.g. *Schumacher and Breuer*, 2006; *Citron et al.*, 2018) that suggest, on the contrary, that the upwellings are preferentially located below the thickened portions of the crust. Since the plumes are not well defined in our simulations, a further step will consist in assuming a higher contrast in temperature at the CMB and a higher value of the activation volume to investigate more in details the trend of our models.

## 4.3 Northern and southern temperature profiles

### 4.3.a North/south transition zone delimitation in dynamical models

Obtaining representative temperature profiles of the northern and southern hemispheres is not straightforward in the dynamical models, though we only consider two types of crust representative of purely northern or southern properties (see section 4.1.b). Indeed, assuming an abrupt transition in crustal thickness between the northern and southern hemispheres in dynamical thermal simulations results in a long-wavelength transition in lithosphere thickness as clearly illustrated by Figure 4.14. The thermal structure of this north/south transition zone is thus not representative of that observed for a purely northern or southern hemisphere. Therefore, we define four distinct zones in the dynamical models : the southern portion (southern crustal properties and average thermal profile of the zone 4, see Figure 4.14), northern portion (northern crustal properties and average thermal profile of the zone 1, see Figure 4.14), and a transition zone divided into northern and southern sides (zones 2 and 3 on Figure 4.14, respectively).

The north/south transition zone is defined as the area where large lateral temperature gradients are observed at the depth corresponding to the base of the stagnant lid (in white on Figure 4.14). Here we assume that each side of the north/south transition zone has a width corresponding to the length scale of conductive heat transfer $\sqrt{\kappa t_{char}}$ ($\sim$ 300 km), where $t_{char}$ is the characteristic time for radioelement decay ($\sim$ 2.5 Gyr). This length scale also corresponds to the thickness scale of the stagnant lid. In the northern and southern sides of the transition zone we assume the crustal properties of the corresponding hemisphere (thickness, enrichment in radioelements and thermal conductivity) and the average temperature of the zones 2 and 3, respectively.

### 4.3.b Validation of the temperature profiles obtained with 1-D models

The results described in section 3.4.c are especially sensitive to the northern and southern present-day stagnant lid thicknesses and, therefore, to the temperature profiles. We thus compare the present-day temperature profiles predicted by the 3-D dynamical models in the purely northern and southern hemispheres with those obtained with 1-D parametrized models and find

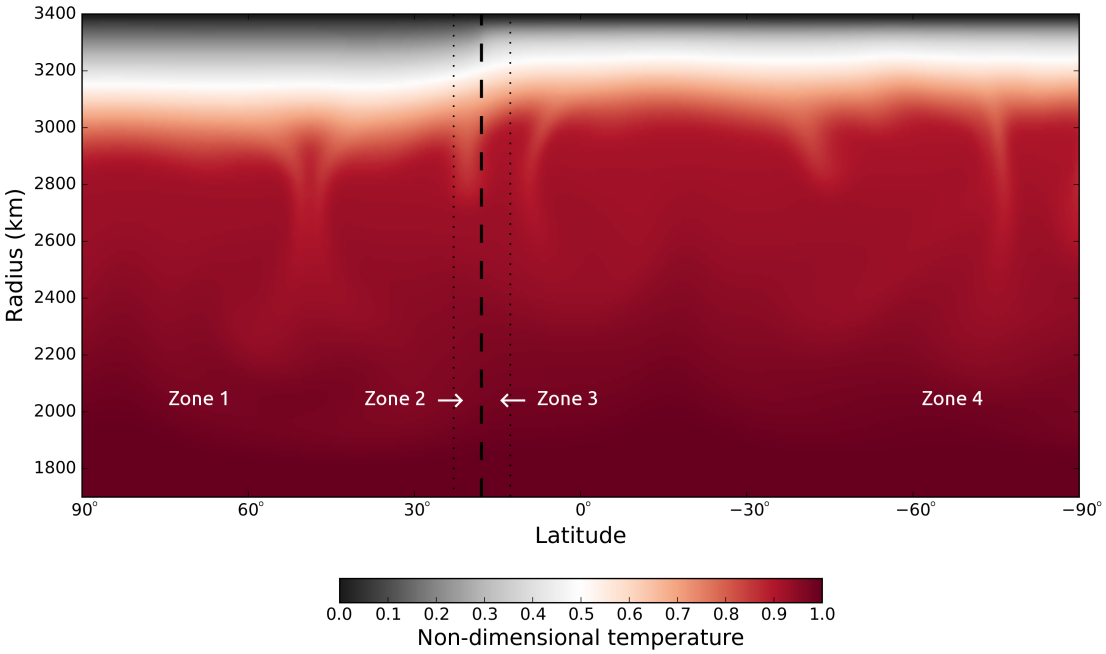


**FIGURE 4.14** – Delimitation of the northern and southern transition zones in dynamical thermal simulations (zones 2 and 3, respectively). The northern and southern hemispheres correspond to the zones 1 and 4. The boundary of the north/south dichotomy (large dashed line) and the limits of the transition zones in the two hemispheres (dotted lines) are represented on a cross section of the mantle at the present-day from 90°N to 90 °S for a 2-D cylindrical simulation considering the *UCMref1* crustal model. The colorscale corresponds to the non-dimensional temperature T.

a good agreement for both the *UCMref1* and *NUCMref2* cases (Figures 4.15 a and b, respectively), which was expected given our first study presented in chapter 3. Although 1-D models slightly overestimate the temperature in the convecting mantle by $\sim$ 10 K on average, the stagnant lid thickness is well described and only slight differences in lithospheric temperature are observable. Such minor differences are likely due to the radial resolution of 15 km used in the upper layers of the dynamical thermal models, which cannot perfectly capture the crustal thickness. The good agreement between the present-day thermal structure predicted by the 1-D and 3-D models gives us good confidence in the results that have been obtained in chapter 4 section 3 with parametrized models since those results are essentially sensitive to the present-day lithospheric thickness and temperature profile.

### 4.3.c Temperature profiles in the north/south transition zone

To account for the large-scale lateral variations in temperature that are observed below the dichotomy boundary, we have defined a transition zone between the two hemispheres divided into northern and southern sides for which we also compute the average temperature profiles (see section 4.3.a and Figure 4.14). The heat produced by radioelement decay in the southern

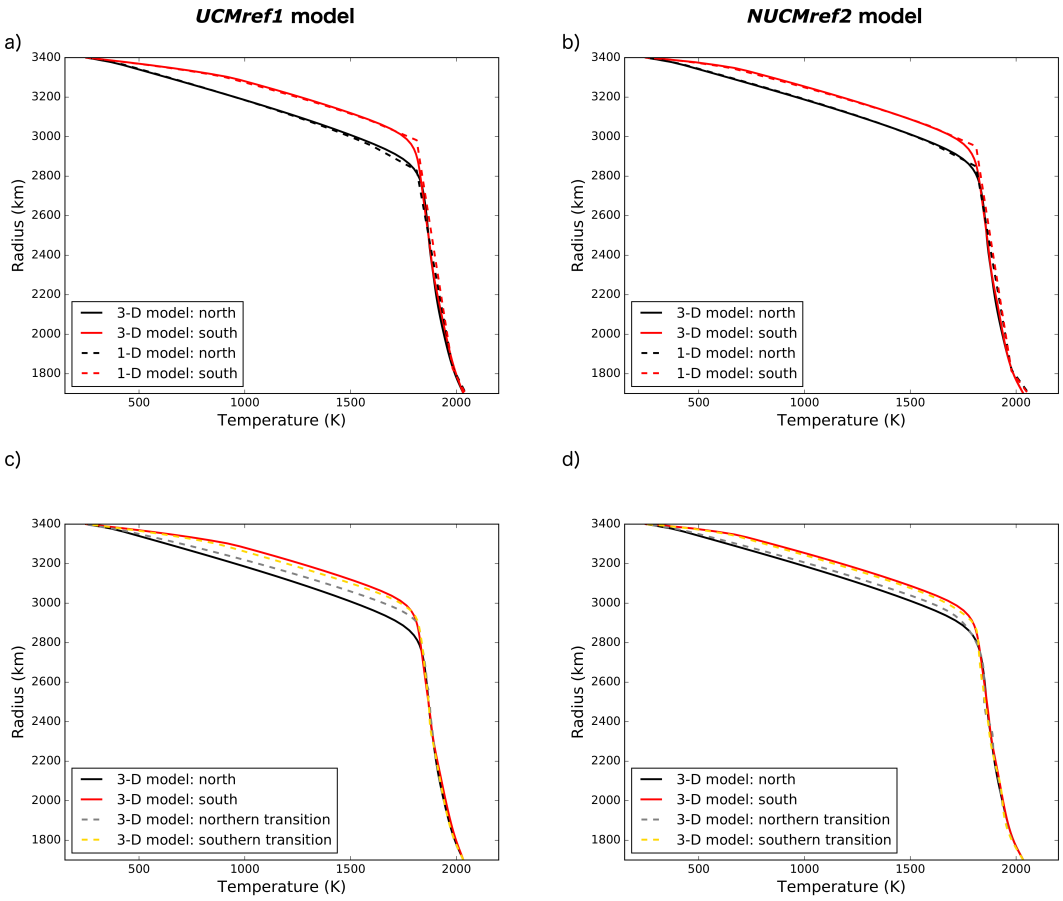


**FIGURE 4.15** – Present-day temperature profiles for the 3-D thermal models accounting for the properties of two of the best NUCM and UCM crustal models defined in section 3.4.c. The northern and southern average temperature profiles of the 3-D models (black and red solid lines, respectively. See Figure 4.14 for the delimitation of the four zones considered here) are compared with those obtained with 1-D parametrized models (black and red dashed lines) for the *UCMref1* crustal model in (a) and for the *NUCMref2* case in (b). They are also compared with the average temperature profiles obtained in the northern and southern sides of the transition zone between the two hemispheres (gray and yellow dashed lines, respectively) in (c) for the *UCMref1* crustal model and in (d) for the *NUCMref2* one.

crust is transported laterally towards the north. As a result the average temperature profile observed in the southern side of this transition zone only slightly differs from that of the southern hemisphere (yellow dashed and red lines, respectively, on Figure 4.15c-d) for both the *UCMref1* and *NUCMref2* crustal models. This is consistent with the smooth transition in stagnant lid thickness on this side of the transition zone (see Figure 4.14). In the north, a higher lateral gradient in stagnant lid thickness is observed : the temperature profile of the transition zone is thus significantly hotter than that of the corresponding hemisphere (gray dashed and black solid lines, respectively, on Figure 4.15c-d), for both the *UCMref1* and *NUCMref2* crustal models.

## 4.4 Conclusion

We performed 3-D simulations accounting for the crustal properties predicted by the *UCMref1* and *NUCMref2* cases that represent two end members among the best crustal models defined in section 3 with parametrized models. We do not account for lateral variations in crustal thickness within a hemisphere and rather adopt a simplified modeling, in which we only consider an abrupt transition between two types of crust representative of purely northern or southern properties. Very similar convection patterns are observed for the 3-D simulations accounting for those two crustal models, though the crustal properties of the *UCMref1* and *NUCMref2* cases (thickness, enrichment in radioelements, thermal conductivity) are largely different, especially in the southern hemisphere. The small contrast in temperature at the CMB as well as the high internal rate of heating assumed in our thermal models make it difficult to clearly discern the mantle convection pattern, although it is slightly more visible for the *NUCMref2* case. However a north/south asymmetrical pattern linked to the crustal dichotomy is observed with well-defined and numerous downwellings predominantly located in the southern hemisphere, whereas the larger mantle plumes concentrate over time in the northern hemisphere and below the north/south transition zone. This trend has to be investigated more in details since it is not consistent with previous studies that suggest the presence of hot plumes below the thick and insulating portions of the crust (e.g. *Schumacher and Breuer*, 2006). A further improvement of our models will be to account for lateral variations in crustal thickness that have been proved to influence the location of mantle plumes. The thermal evolutions predicted by the 3-D thermal simulations are in good agreement with those obtained in section 3 with parametrized models. This gives us confidence in the results presented in section 3, i.e. in the range of crustal parameters and characteristics of the present-day thermal structure predicted by the models that fit the three constraints on elastic thickness and present-day melt formation in the south.

# CHAPTER 5

# IMPLICATIONS OF OUR BEST THERMAL MODELS FOR SURFACE WAVE PROPAGATION

**Sommaire**

# 1 Summary

Since body-wave travel time analysis requires at least three seismic stations for event location and time origin, specific approachs have to be used for the InSight single station that will soon land on Mars. If large enough marsquakes with moment release of $10^{16} - 10^{17}$ Nm occur on Mars, the R1 and R3 arrival times of multiple-orbit Rayleigh surface waves will likely be recorded. This will allow to invert the average group velocity dispersion curve along a great circle to derive a first order S-wave velocity profile independently of assumptions on quake's location and origin time (e.g. *Panning et al.*, 2015). However, group velocities are particularly sensitive to lithospheric properties and, especially, to the crustal thickness that produces a guided effect for surface waves. In this chapter, we thus investigate the effects on Rayleigh wave velocities of the northern and southern properties predicted by two end members among the suitable crustal models in terms of north/south contrast in crustal thickness, lithospheric temperature profile and composition (*UCMref1* and *NUCMref2*, see chapter 4).

In the absence of seismic data on Mars, *a priori* structural models have been developed to prescribe reasonable range of internal composition, density, P and S wave velocities. We consider the DW initial structural model of *Rivoldini et al.* (2011), which is first adapted to the northern and southern crustal properties (thickness, density, composition) of the *UCMref1* and *NUCMref2* models, and then consider the mantle temperature profiles predicted by those two crustal models in addition. Using the MINEOS package, those *a priori* northern and southern structural models are used in a forward problem to compute the group velocities of the Rayleigh wave fundamental mode as a function of period (between 10 and 250 s).

We find that surface wave velocities mostly depend on the crustal thickness and, to a lesser extent, on the crustal composition and lithospheric temperatures. For surface waves traveling in the northern or in the southern hemisphere, the largest differences in velocity are thus observed at periods sensitive to crustal properties ($\lesssim$ 100 s). Along great circle paths the dispersion curves are influenced by the properties of the two hemispheres, but probably mostly by those of the southern one that covers a wider area. If the northern hemisphere is not enough sampled, or if the north/south contrast in crustal thickness is small ($\sim$ 20 km in the *NUCMref2* case), constraining the northern crust's properties might be hard with only surface wave analysis given the uncertainties on the R3 arrival time. The analysis of body waves produced by local events in the north should thus likely be necessary to provide complementary informations on the northern crustal structure.

# 2 Motivation

In chapter 4, we found that the crustal dichotomy might lead to significant north/south differences in lithospheric thickness and thermal structure. The crustal models fitting the evolution of elastic thickness estimates predict, indeed, a large difference in lithospheric temperatures between the two hemispheres of $170 - 300$ K in the shallow mantle. Moreover, the southern crust can be up to three times thicker than the northern one (for instance : *UCMref1* case, see chapter 4, Table 4.5). Alternatively, in some of our best NUCM models the southern crust might contain a non-negligible proportion of felsic rocks (for instance : *NUCMref2* case) and can be up to 480 kg/m3 less dense than the northern one.

Such north/south differences could leave a signature in the geophysical signals measured by the seismometer SEIS on board the InSight (Interior Exploration using Seismic Investigations, Geodesy and Heat Transport) Discovery mission, which results from an international collaboration between the NASA, CNES and IPGP, launched on May 5, 2018, and expected to land on Mars on November 26, 2018. Indeed, seismic wave velocities, and especially surface wave propagation, are sensitive to the crustal structure and lithospheric temperatures. In this chapter, we estimate the effect of the northern and southern crustal properties (temperature profile, crustal thickness and composition) predicted by two end members among our best thermal and crustal models (*UCMref1* and *NUCMref2* cases) on surface wave velocities and dispersion. Conversely, we investigate to what extent the seismological data of SEIS will help to discriminate between our best UCM and NUCM crustal models.

# 3 Introduction

## 3.1 Seismology : a window on planetary body internal structures

Much of our knowledge of the internal structure of planetary bodies is provided by geophysical observations and measurements such as gravity field, rotation and tide analysis obtained by tracking orbiting spacecraft. However, all those observations provide an integrated view of planetary interiors, which does not lead to a unique internal structure. By its potential to detect interfaces and variations in the physical properties of rocks, seismology is the best available geophysical tool to constrain planets' internal structure (e.g. *Lognonné and Johnson*, 2007). Indeed, on Earth, the advent of seismometers in the late 19th and early 20th centuries has led to a revolution of the knowledge of our planet's internal structure, which was prior to that mainly determined from Earth tide analysis (*Thomson*, 1862; *Darwin*, 1882). The first recordings of global scale seismograms led to the discovery of the Earth's core, with the detection of seismic waves refracted at the core-mantle boundary (CMB) (*Oldham*, 1906), and of the inner core (Inge Lehmann in 1936). Seismology has also provided the description of the major discontinuities and mantle phase transitions and, in particular, the crust-mantle discontinuity by Andrija Mohorovičić in 1909.

The Moon is the only other planetary body for which we have, up to now, recorded unambiguous seismic data through the deployment of a network of four seismic stations by the Apollo program between 1969 and 1972 (e.g. *Latham et al.*, 1969). The data that was recorded until 1977 gave first order constraints on the Moon's internal structure and are still being investigated with, in particular, the recent detection of a $\sim$ 350 km in radius core probably with an inner solid part (*Weber et al.*, 2011). To date, there has been no convincing detection of seismological event on Mars since the only seismometer that was operational at its surface (Viking 2 mission in the late 1970s) failed to record any signal originating from the planetary interior during the 19 months of operation (e.g. *Anderson et al.*, 1977). As a consequence, the internal structure of Mars remains poorly known. However, despite the lack of seismological observations on Mars's interior, basic constraints arise from geophysical observations (including the planetary mass, the mean moment of inertia and the $k_2$ tidal Love number) as well as assumptions of bulk chemistry from Martian meteorite analysis, which have allowed for several estimates of the internal compositional and elastic structure of the planet (e.g. *Mocquet et al.*, 1996; *Sohl and Spohn*, 1997; *Gudkova and Zharkov*, 2004; *Khan and Connolly*, 2008; *Rivoldini et al.*, 2011).

Most progress in seismology for the Earth and the Moon has been realized through the concept of networks of multiple seismometers that provide precise determination of source parameters (location and origin time) for recorded quakes. However, such a network requires multiple landers and geophysical instruments and, though previously proposed for Mars (e.g. *Lognonné et al.*, 2000), it has not been considered for expense reasons for the InSight mission. This latter will thus consist in the first single-station geophysical observatory dedicated to the investigation of the deep interior of a planetary body. It will deploy on Mars (at Elysium planitia, see Figure 5.9a for the expected location) the Seismic Experiment for Interior Structure (SEIS) instrument composed by a 3-component broadband Very Broad Band (VBB) and 3 Short Period (SP) seismometers with bandwidths of $0.1 - 1000$ s and $0.025 - 10$ s, respectively. Other instruments are also part of the mission : the previously mentioned HP$^3$ instrument (Heat flow and Physical Properties Probe), the geodetic instrument Rotation and Interior Structure Experiment (RISE), a magnetometer and meteorological sensors.

## 3.2 Potential sources and expected seismicity for Mars

The traditional seismology often relies on body wave travel time analysis, which requires at least three seismic stations for precise event location and origin time. Such analysis is thus not appropriate for the single seismometer of the InSight mission. In this context, it is important to estimate in advance the potential seismic sources and moment magnitudes $M_w$ since they will define the expectations for the types of signals recorded by the InSight mission and, thus, the strategies that will be used to characterize Mars's internal structure.

Despite the lack of unambiguous quake detection by the Viking landers (*Anderson et al.*, 1977), Mars's seismicity is expected to be significant. Indeed, subsequent analysis has shown

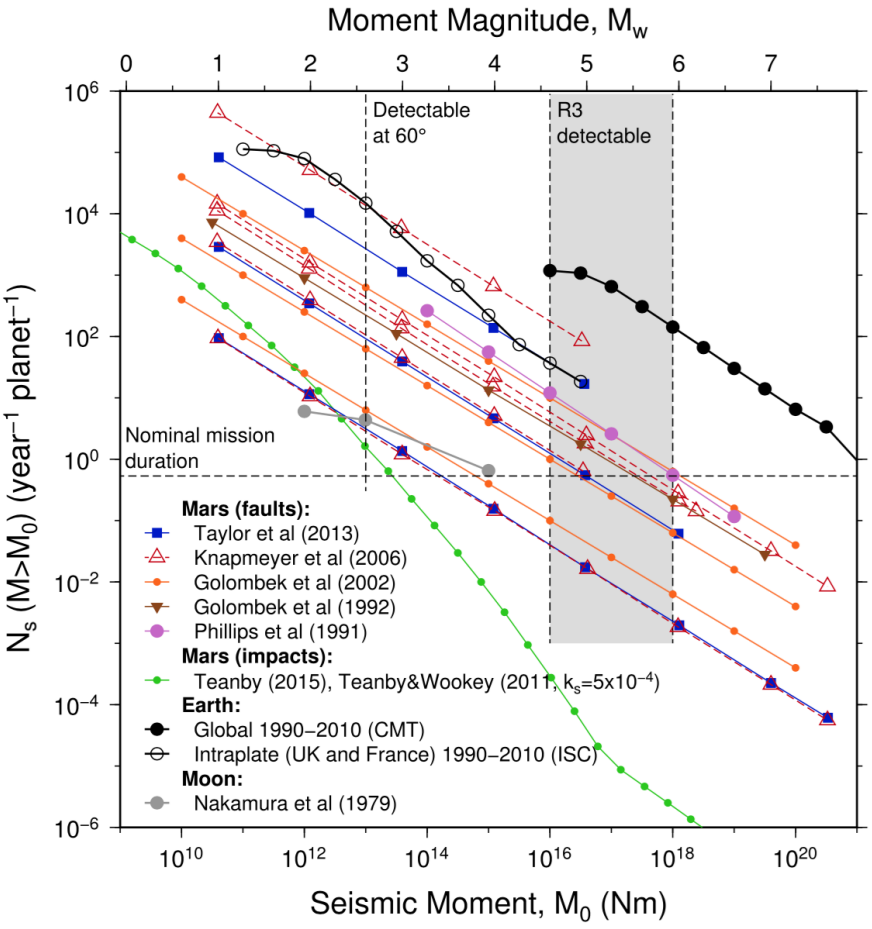


**FIGURE 5.1** – Number of events $N_s$ per Earth year that exceed a given seismic moment as a function of seismic moment $M_0$ and moment magnitude $M_w$ for the telluric bodies (Figure from *Panning et al.*, 2017). Seismic activity is derived from the Harvard CMT catalog and Intraplate settings ISC catalog for the Earth and from the catalog of *Nakamura et al.* (1979) for the Moon. Predictions of Martian seismicity for faults are based on the studies of *Phillips* (1991), *Golombek et al.* (1992), *Golombek* (2002), *Knapmeyer et al.* (2006) and *Taylor et al.* (2013). Impact seismicity is derived from the estimates of *Teanby* (2015). The grey shaded area shows the threshold magnitude for detection of *R*3 (the arrival time of the third orbit surface wave). The horizontal dashed line represents the nominal duration of the InSight mission.

that the mounting of the instrument on top of the Viking 2 lander (*Goins and Lazarewicz*, 1979) and the inadequate sensitivity of the seismometer to wind noise (*Nakamura and Anderson*, 1979) has prevented the detection of any signals originating from the planetary interior (*Anderson et al.*, 1977). Several potential sources of elastic deformation are, however, present on Mars including faulting, meteorite impacts, Phobos tide and atmospheric hum (wind-induced pressure variations, turbulences) (*Golombek*, 2002; *Lognonné and Mosser*, 1993; *Panning et al.*, 2015; *Panning et al.*, 2017). In the absence of plate tectonics on Mars, Earth's intraplate seismic activity level (number of event per year of a given seismic moment, black curve and white

points on Figure 5.1) might represent an upper bound for the Martian seismic activity. A lower bound likely corresponds to the Moon's seismic moment ($10^{15}$ Nm/yr, grey line on Figure 5.1), since this planetary body has a lower cooling rate than Mars. Indeed, in the absence of plate tectonics, faulting due to thermal contraction associated with secular cooling (*Solomon et al.*, 1991; *Phillips*, 1991; *Knapmeyer et al.*, 2006) or to stresses induced by large lithospheric loads such as Tharsis is expected to be the dominant source of seismicity on Mars. In advance of instrumental data, the Martian seismic moment remains largely uncertain but has been estimated to $\sim 10^{17} - 10^{19}$ Nm/yr according to predictions of stress released from thermal modeling (*Phillips*, 1991) and analysis of surface faulting (*Golombek et al.*, 1992; *Golombek*, 2002; *Knapmeyer et al.*, 2006). In particular, Cerberus Fossae represents a potential seismic source since evidences of large and recent marsquakes have been identified in this region, which is only $\sim$ 1500 km from the expected InSight landing site to the north-east (*Taylor et al.*, 2013). Although meteorite impacts produce seismic signals of secondary importance compared to faulting, they will provide reliable informations on the internal structure. Indeed, in this case, accurate locations can be determined using the high resolution cameras of Mars Reconnaissance Orbiter and ExoMars for impact monitoring of the flashes generated by thermal radiation of vaporized target material (*Bouley et al.*, 2012). Again, there are large uncertainties about the number of detectable impacts for the InSight mission duration (2 Earth's years). *Teanby and Wookey* (2011) and *Teanby* (2015) estimated that $\sim 1$ global and $\sim 0.1 - 30$ regional events might be detectable, whereas *Lognonné and Johnson* (2015) estimated a rate of $\sim 10$ per year.

### 3.3 Multiple orbit surface wave-based approach

Depending on the source and seismic moment released by an event, various approaches will be used to analyze the data from the InSight single-station such as normal mode analysis (e.g. *Lognonné et al.*, 1996; *Panning et al.*, 2017), surface wave dispersion analysis (*Panning et al.*, 2015; *Panning et al.*, 2017), receiver functions (e.g. *Phinney*, 1964; *Vinnik et al.*, 2001; *Panning et al.*, 2017) or analysis of $HP^3$ hammering (*Kedar et al.*, 2017). All those methods give complementary informations on Mars's interior since they resolve structures on a wide variety of length scales, from normal modes sensitive to the global Martian structure to near surface techniques providing informations on crustal and regolith properties. Here, we focus on the analysis of surface wave propagation, which will be sensitive to lithospheric properties and thus to the characteristics of the best crustal models defined in chapter 4.

Two types of surface waves exist : Love and Rayleigh waves. In the presence of a free surface, such as the ground-atmosphere interface of planetary bodies, they form through interferences between body waves. They propagate at the surface with a penetration depth that increases with their wavelength, which yields to a maximal amplitude at the surface that strongly decreases with depth (*Bormann et al.*, 2009). In the following, though a similar approach can be conducted for Love waves, we consider Rayleigh waves for which the noise is expected to be lower on the signals recorded by the InSight mission (*Panning et al.*, 2015). Radial variations of shear wave velocity result in a frequency dependence of their horizontal propagation

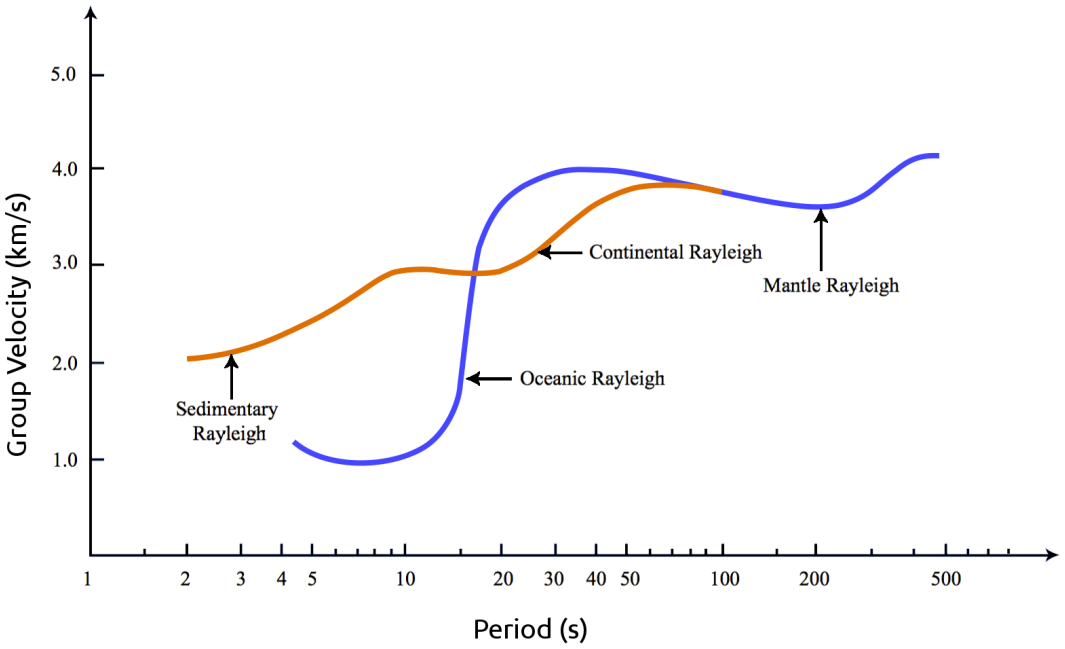


**FIGURE 5.2** – Earth's typical group-velocity dispersion curves as a function of period for the fundamental mode of Rayleigh waves in oceanic and continental areas (Figure based on *Bullen et al.*, 1985).

velocity, called dispersion (e.g. *Bormann et al.*, 2009), which forms long oscillating wave trains in seismograms with a duration that increases with the travelled distance. Therefore, dispersion curve - i.e. the propagation velocity of surface waves as a function of their period - contains structural informations on the velocity-depth structure along the travel path. Since the sample depth increases with the surface wave period, the group velocity, with which the energy of the wave travels, mostly depends on the properties of the shallow crustal structures for short period ($\lesssim 10$ s) and on mantle characteristics for higher periods ($\gtrsim 100-150$ s). For intermediate periods, group velocities are extremely sensitive to the crustal thickness with $\sim 10$ % variations for a crustal thickness difference of 20 km (*Lognonné and Johnson*, 2007). On Earth, the discovery of different surface-wave velocities in oceanic and continental areas was in the 1920s the first indication of structural and compositional differences between the oceanic and continental crusts (blue and brown curves on Figure 5.2, respectively).

The shortest path for a surface wave from a source to a station is along a great circle. At a given frequency, the first surface wave group arrival time R1 at a seismic station will have taken the shorter path along the great circle, while the second arrival R2 has traveled around the major arc path (in green and blue on Figure 5.3, respectively). For large enough seismic events, multiple orbits can be recorded : in this case the arrival time R3 corresponds to surface waves that have traveled around the minor arc plus another great circle path (in red on Figure 5.3). If such multiple orbit surface-waves are recorded during the inSight mission duration, the average group velocity of Rayleigh waves $v_g$ can be derived at a given period along the great

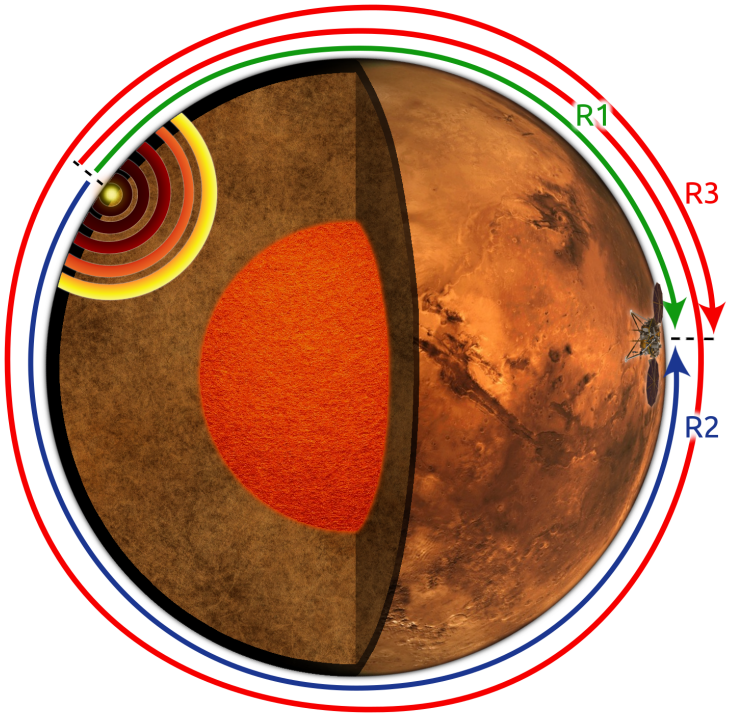


FIGURE 5.3 – Schematic diagram of great circle paths for the first three arrivals of global Rayleigh surface waves at a seismic station (R1, R2 and R3 in green, blue and red, respectively). The location of the epicenter is represented by the yellow point, the simplified travel of body waves by the concentric circles that propagate towards Mars's interior. The global mosaic image of Mars was taken by Viking 1 orbiter (credits NASA/JPL-Caltelch).

circle connecting the station and the epicenter from the difference between R3 and $R1$ (e.g. *Panning et al.*, 2015) :

$$v_g = \frac{2\pi R_p}{R3 - R1} \tag{5.1}$$

The dispersion curve of the Rayleigh wave group velocities can then be inverted to determine a first order S-wave velocity profile (e.g. *Panning et al.*, 2015; *Panning et al.*, 2017).

Such a multiple orbit surface wave-based approach does not rely on assumptions on quake's location and origin time and has thus been proposed to deliver an initial Martian velocity model with the InSight single-station. However, it remains unclear if large enough events will be observed on Mars to allow for the detection of the R3 arrival time that is not easily pickable on seismograms, due to surface wave dispersion and noise measurement. On Earth, multiple orbit surface waves are reliably observable for event of at least $M_w 6$ ($\sim 10^{18}$ Nm in moment release) because of large attenuation effects. A higher quality factor $Q$, and thus a lower attenuation, are expected on Mars, which has a smaller radius and a thermal lithosphere likely thicker than the Earth's one (*Lognonné and Mosser*, 1993; *Nimmo and Faul*, 2013). Events in the range $10^{16} - 10^{17}$ Nm in moment release ($M_w \sim 4.6 - 5.3$) might thus be large enough to detect the

R3 arrival time. While there are large uncertainties, $1-10$ of such large events may potentially be recorded for the InSight mission duration (see Figure 5.1).

The average Rayleigh wave group velocity along a great circle might strongly depend on the lateral variations that are expected on Mars. Though local variations in lithospheric and crustal properties are likely present in the huge volcanic provinces or impact basins, the large-scale variations due to the north/south dichotomy might be at first order dominant on the average surface wave dispersion curve. Here, we investigate the effect of the Martian crustal dichotomy on the average surface wave group velocities along different potential seismic paths, using isotropic *a priori* models for Mars's internal seismic properties (density, temperature, attenuation, S and P-waves velocities) that we correct given the north/south crustal thicknesses and thermal profiles predicted by two reference north/south crustal models (*UCMref1* and *NUCMref2*).

# 4 Seismological models for the northern and southern hemispheres

In the absence of seismic data on Mars, *a priori* structural models are used in the forward problem to compute the group velocity dispersion curves for the fundamental mode as a function of period (here between 10 and 250 s). We use the MINEOS package, which is a normal-mode summation code based on the work of *Gilbert and Dziewonski* (1975), updated by *Woodhouse* (1988) and rewritten by (*Masters et al.*, 2011). In section 4.1 we present the DW initial seismological model of *Rivoldini et al.* (2011), which is considered here as a reference model. To evaluate the seismological manifestations of the lithospheric Low-Velocity Zone (LVZ) present in the DW model, we also consider an initial structural model similar to DW but with no LVZ. In section 4.2 we adapt those two initial *a priori* models given the properties (thermal structure, crustal thickness and composition) of two representative models of our best crustal cases (*UCMref1* and *NUCMref2* models, see chapter 4, section 4). The consequences of considering the EH45 initial seismological model of *Rivoldini et al.* (2011) rather than DW are briefly discussed in section 8.

## 4.1 Initial seismological models for Mars

*A priori* models have been developed to prescribe reasonable range of internal composition, shear and bulk attenuation, density, P and S wave velocities ($v_p$ and $v_s$, respectively) for Mars interior (e.g. *Mocquet et al.*, 1996; *Sohl and Spohn*, 1997; *Zharkov and Gudkova*, 2005; *Rivoldini et al.*, 2011; *Khan et al.*, 2016). They have been constructed to match basic constraints from available geodetic data such as bulk density, inertia momentum, tidal love number and global tidal dissipation. Assuming thermodynamic equilibrium and a known bulk mantle composition derived from isotopic analysis of Martian rocks and early solar-system meteorites (e.g. *Taylor et al.*, 2013), first thermodynamics principles and experimental phase diagrams are used to predict the stability of mineralogical assemblages as a function of pressure and temperature conditions (*Verhoeven et al.*, 2005; *Khan and Connolly*, 2008; *Rivoldini et al.*, 2011). Shear and

bulk attenuation are scaled from a preliminary reference Earth model (PREM, *Dziewonski and Anderson*, 1981) or computed given a specific viscoelastic model. Uncertainties in the assumed bulk chemistry or in core radius as well as the diversity of methods used has yielded to several estimates of the internal elastic and compositional structure of Mars. However, a general good agreement is retrieved for basic characteristics of the velocity structure in terms of approximate velocity gradients and location of phase-transitions (see for instance *Clinton et al.* (2017) for a comparison between the vertical profiles of density and seismic velocities proposed by different studies).

#### 4.1.a The DW model

The DW structural model of *Rivoldini et al.* (2011) is one of the most used. It is based on the compositional model of *Dreibus and Wanke* (1985) constrained by the analysis of SNC meteorites and is thus coherent with the Martian bulk composition assumed for our thermal models in chapters 3 and 4. For this isotropic and spherically symmetric model, three compositionally distinct layers are considered : the core, mantle and crust.

The large value of the love number $k_2$ inferred from solar tides (*Yoder et al.*, 2003) and by Phobos tidal acceleration value responsible of surface deformations indicates the presence of at least an outer liquid core (*Bills et al.*, 2005). Here, the core is assumed to be entirely liquid. A core radius of $R_c = 1755$ km is considered, which is consistent with estimates of inertia momentum (*Yoder et al.*, 2003), but is not critical to study surface wave group velocities that are not sensitive to the exact core size.

In the Earth, significant mantle discontinuities due to phase transition lead to abrupt jumps in seismic wave velocities. Major transitions are those from olivine to wadsleyite (the 410 km discontinuity), from wadsleyite to ringwoodite (the 520 km discontinuity) and from ringwoodite to perovskite and magnesiowüstite (the 660 km discontinuity) (e.g. *Lay and Wallace*, 1995). On Mars, the presence of the first two mantle discontinuities is expected at depths of $\sim$ 1100 and 1400 km, respectively. However, depending on the core size and on the internal temperature, the transition from ringwoodite to perovskite may or may not be present. Because of the lower Martian pressure and temperature and the higher iron mantle content (*Mocquet et al.*, 1996), those transitions might be more progressive and might not produce strong seismic reflections (*Lognonné and Johnson*, 2007) in agreement with the DW model (blue lines on Figure 5.4).

Different structural models have been derived from the basic DW model of *Rivoldini et al.* (2011) accounting for distinct crustal structures and present-day hot and cold temperature profiles from the thermal evolution models of *Plesa et al.* (2016) (cases 10 and 21) (e.g. *Clinton et al.*, 2017; *Panning et al.*, 2017). Here we consider the DWhot model that corresponds to the DW model given a hot temperature profile (blue lines on the right plots of Figure 5.6d). As previously mentioned, the properties of the Martian crust are still largely unknown (e.g *Mocquet*

*et al.*, 2011; *Grott et al.*, 2013). In the DWhot model, the crust is assumed to be vertically and horizontally uniform both in density, thickness (90 km) and velocity (blue curves on Figure 5.4). However, note that the choice of another seismological model derived from the DW one would have lead to similar results since we adjust the DW model with our own temperature profiles and crustal structures.

### 4.1.b The DWnoLVZ model

Seismic velocities generally increase with depth due to material compression. However, a seismological Low-Velocity Zone (LVZ) can be present in the upper mantle and represents a

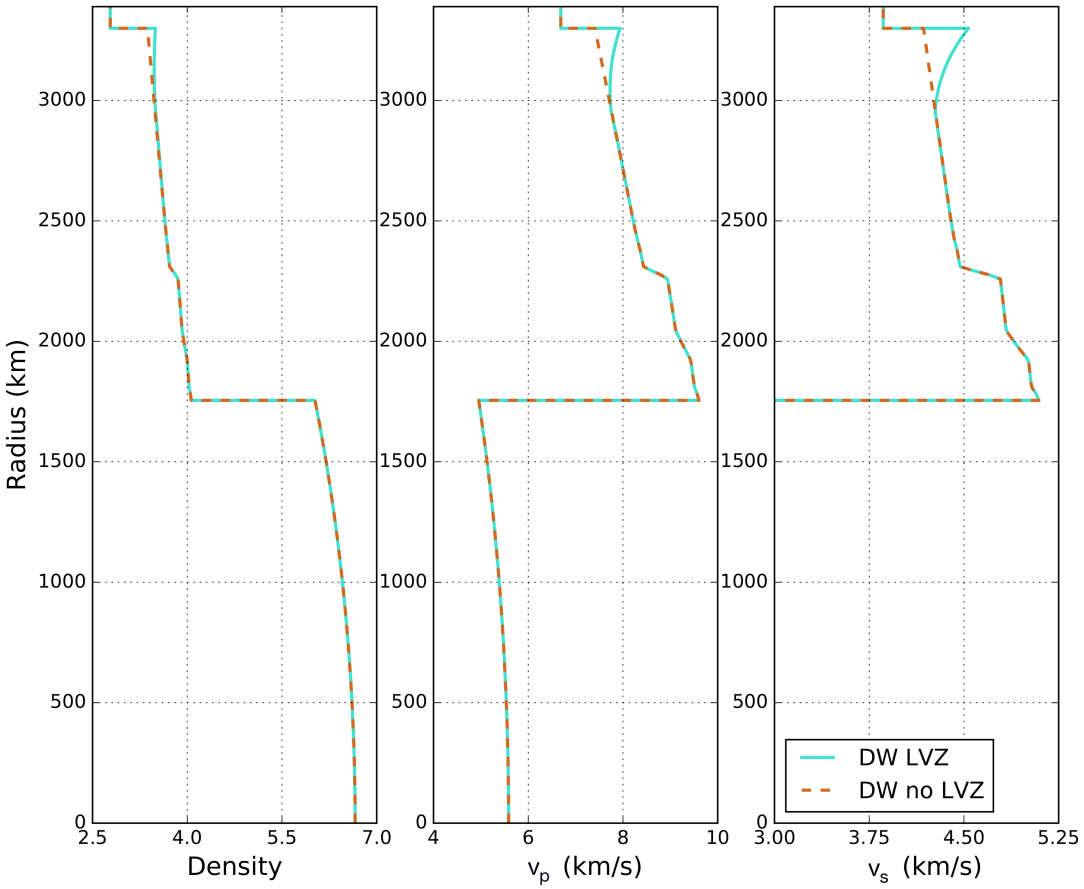


**FIGURE 5.4** – From left to right : vertical profiles of density, P and S-wave velocities for the two reference seismological models considered here. The DW model (blue lines) has been established by *Rivoldini et al.* (2011) given the bulk composition of *Dreibus and Wanke* (1985). To evaluate the effect of the presence of a lithospheric Low Velocity Zone (LVZ) in this model on the Rayleigh-wave group velocities, we also consider a similar model with the same structure below 400 km but with no LVZ and a positive increase in velocity and density with depth in the lithospheric mantle (DWnoLVZ model, dark orange dashed lines).

region for which seismic velocities increase in the downwards but also in the upwards directions. On Earth, the existence of a LVZ was first proposed by *Gutenberg* (1948) and is related to thermal and compositional effects linked to the rheological transition from the lithosphere to the asthenosphere (e.g. *Anderson*, 1989). On Mars, the existence of a LVZ depends on the near-surface temperature gradient and could be amplified by the relatively high iron-content of the mantle (*Mocquet et al.*, 1996). Indeed, high temperature gradients are expected within Mars's lithosphere because of the presence of a stagnant lid (*Mocquet and Menvielle*, 2000; *Rivoldini et al.*, 2011; *Nimmo and Faul*, 2013). In this case, unlike on Earth, the thermal effect on the lithospheric seismic velocities might overcome that of the pressure, which yields to the presence of a LVZ below the crust-mantle boundary (*Nimmo and Faul*, 2013; *Zheng et al.*, 2015). Due to similar mechanisms, the presence of a LVZ was also expected on the Moon and was perhaps detected by (*Nakamura*, 1983). However, its existence has, up to now, not been clearly demonstrated.

Such a lithospheric LVZ is present in the DW model below the crust and extends up to $\sim$ 400 km depth (Figure 5.4). If associated to a large enough decrease in seismic velocities, this LVZ would lead to a shadow zone for direct P and S-waves (*Gutenberg*, 1959; *Zheng et al.*, 2015) and, more specifically for our study on group-velocities, to a delay in the arrival time of long-period surface waves, which usually arrive first. To evaluate the seismological manisfestations of the LVZ assumed in the DW model, we create a similar model with the same structure than DW but with no LVZ in the lithospheric mantle (DWnoLVZ) (dark orange dashed line on Figure 5.4). For this purpose, following *Zheng et al.* (2015), mantle velocity and density gradients are interpolated up to the crust-mantle boundary to produce a positive velocity increase in the lithosphere. Although this seismological model is probably less justifiable on physical grounds than the DW model, it will allow us to investigate the LVZ effects.

## 4.2 Adjustment of the initial seismological models with north/south properties

The DW and DWnoLVZ initial seismological models defined in section 4.1 are adapted given the northern and southern characteristics of the *UCMref1* and *NUCMref2* crustal and thermal models (see Table 4.5 in chapter 4 for detailed characteristics).

### 4.2.a Crustal velocities

Large uncertainties exist for the properties of the crust (composition, density, thickness) and, therefore, for the crustal seismic velocities that have however to be prescribed in *a priori* seismological models. The DW initial seismological model considers uniform properties in the crust (density, seismic velocities) and a crustal thickness of 90 km. Since this is not consistent with the values of the *UCMref1* and *NUCMref2* models that are tested in this chapter, we construct our own vertical profiles of density and seismic velocities in the crust.

| | $v_{p_0}$ [km/s] | $v_{s_0}$ [km/s] | $\partial v_p/\partial T$ [km/(s K) | $\partial v_s/\partial T$ [km/(s K)] | $\partial v_p/\partial P$ [km/(s MPa)] | $\partial v_s/\partial P$ km/(s MPa) |
|---|---|---|---|---|---|---|
| Basalt | $6.8\times10^3$ | $3.7\times10^3$ | $3.3\times10^{-4}$ | $0.7\times10^{-4}$ | $3.4\times10^{-4}$ | $0.5\times10^{-4}$ |
| Granite | $6.4\times10^3$ | $3.5\times10^3$ | $2.2\times10^{-4}$ | $0.9\times10^{-4}$ | $3.0\times10^{-4}$ | $0.6\times10^{-4}$ |

**TABLE 5.1** – Parameters derived from *Kern and Schenk* (1985) to compute seismic velocities in granites and basalts as a function of temperature and pressure. $\partial v_{p/s}/\partial T$ and $\partial v_{p/s}/\partial P$ are the seismic velocity gradients as a function of temperature and pressure, respectively ($v_s$ for S-waves, $v_p$ for P-waves). $v_{p_0}$ and $v_{s_0}$ correspond to the seismic velocities at reference pressure $P_r = 600$ MPa and temperature $T_r = 270$ K.

The experiments of *Kern and Schenk* (1985) are used to estimate velocity gradients as a function of temperature and pressure. At a given depth $z$, the compressional velocity $v_p$ is computed with :

$$v_p^{N/S}(z,P,T) = v_{p_0} + \frac{\partial v_p}{\partial T}(T(z)^{N/S} - T_r) + \frac{\partial v_p}{\partial P}(P(z)^{N/S} - P_r) \tag{5.2}$$

and the shear velocity $v_s$ given :

$$v_s^{N/S}(z,P,T) = v_{s_0} + \frac{\partial v_s}{\partial T}(T(z)^{N/S} - T_r) + \frac{\partial v_s}{\partial P}(P(z)^{N/S} - P_r) \tag{5.3}$$

where $T_r = 270$ K is the reference temperature at which *Kern and Schenk* (1985) have realized their variable-pressure experiments, and $P_r = 600$ MPa (depth of $\sim 50$ km) the reference pressure at which they have conducted their variable-temperature measurements. $v_{p_0}$ and $v_{s_0}$ correspond respectively to the compressional and shear velocities at the reference pressure and temperature. The superscript $N/S$ indicates that a parameter differs between the northern and southern hemispheres, $T(z)^{N/S}$ and $P(z)^{N/S}$ are the temperature and pressure profiles of the *UCMref1* and *NUCMref2* reference models. All the parameters used to compute crustal seismic velocities are summarized in Table 5.1.

In the *UCMref1* case seismic velocities are computed assuming a basaltic composition both in the southern and in the northern crusts (see chapter 4 and Table 4.5 for details). However, in the *NUCMref2* case the lower part of the southern crust has a lower density (2830 kg m$^{-3}$) than the northern crust and the upper part of the southern one (3100 kg m$^{-3}$) for which we assume a purely basaltic composition. For the lower southern crust we consider a mixture of basaltic and felsic rocks and assume seismic velocity values intermediate to the characteristics values for granites and basalts. Considering a mixed composition in the lower southern crust implies the presence of a low-velocity zone in the crust since higher seismic velocities are assumed in the basaltic upper southern layer (see southern structural model on Figure 5.5b).

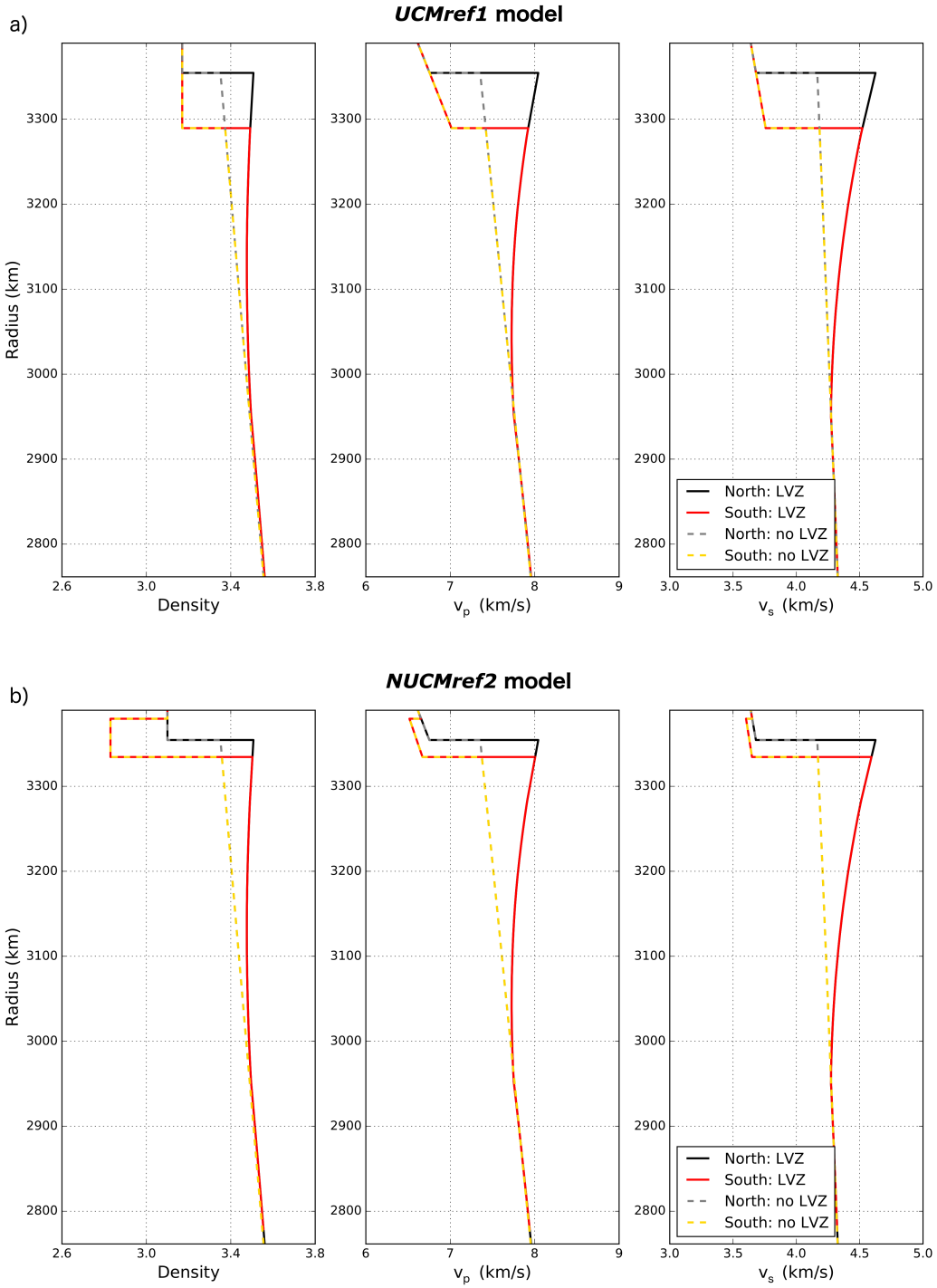


**FIGURE 5.5** – From left to right : vertical profiles of density, P and S-wave velocities for our reference crustal models, *UCMref1* in (a) and *NUCMref2* in (b), if accounting only for north/south differences in crustal structure. Given the north/south crustal properties of those models (thicknesses and densities, see chapter 4 and Table 4.5 for details) their associated velocity profiles are derived from initial seismological models : DW (black and red lines for the northern and southern hemispheres, respectively) and DWnoLVZ (gray and yellow dashed lines for the northern and southern hemispheres, respectively).

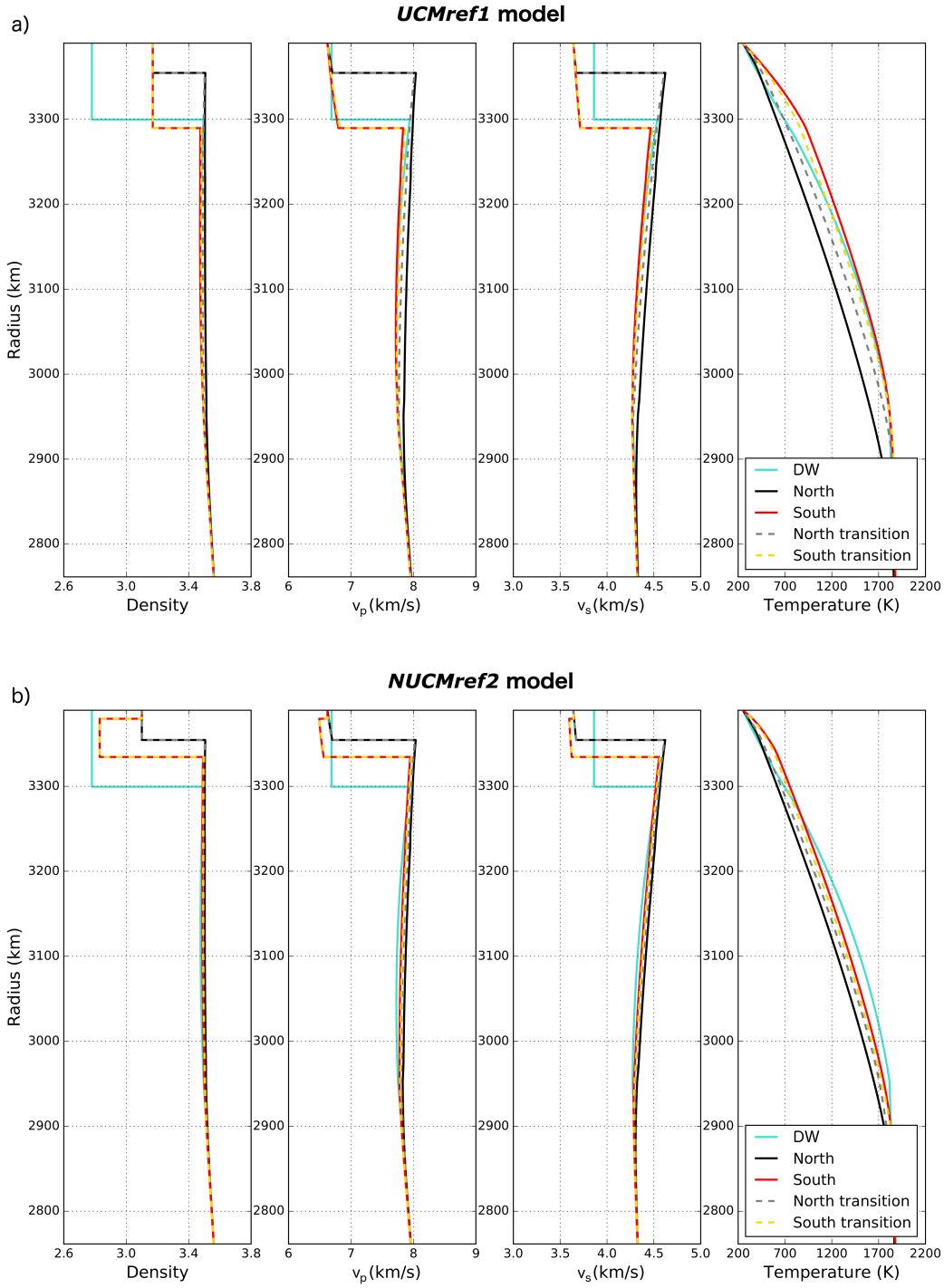


**FIGURE 5.6** – From left to right : vertical profiles of density, P and S-wave velocities, present-day temperature for our reference crustal models, *UCMref1* in (a) and *NUCMref2* in (b), if accounting for north/south differences in crustal structure and lithospheric temperature profiles. Given the crustal and thermal properties of those models (see chapter 4 and Table 4.5 for details) their associated north/south velocity profiles (black and red lines, respectively) are derived from the initial seismological DW model (blue line). The profiles are also shown for the northern and southern sides of the transition zone (grey and yellow dashed lines, respectively, see chapter 4 section 4.3.a for delimitation).

#### 4.2.b Seismological models for representative UCM and NUCM simulations

In a first step, we only adjust the DW and DWnoLVZ initial seismological models given the northern and southern crustal properties (composition, density and thickness) and neglect thermal effects (see Figure 5.5). This allows to distinguish the thermal and structural effects of our reference crustal models on the Rayleigh wave group velocities. Moreover, accounting for the thermal effects when adjusting the DWnoLVZ initial seismological model would lead to the presence of a LVZ in the northern hemisphere, which has no sense for this model. Northern and southern mantle seismic velocities and densities are thus similar to those of the initial seismological model. In the northern and southern crusts we compute the velocities as a function of pressure given the crustal composition, which is assumed to be entirely basaltic except for the lower southern crust of the *NUCMref2* model for which we consider an intermediate composition (see section 4.2.a). If the crust is thinner than that of the initial seismological models (90 km) we interpolate mantle density and velocity vertical profiles up to the base of the crust.

In a second step, in addition to the adjustment of the DW initial seismological model according to north/south crustal properties, we also account for the present-day temperature profiles predicted by the *UCMref1* and *NUCMref2* models. Such adjustments can be realized if knowing the temperature profile assumed in the DW model (blue lines on Figure 5.6) and the values of $dln(v_p)/dT$, $dln(v_s)/dT$ and $dln(\rho_m)/dT$ within the mantle that provide the sensitivity of the DW model to temperature variations at a given depth. Such values have been provided by the InSight team and used to compute the density and seismic velocities corresponding to the north/south temperature profiles of the *UCMref1* and *NUCMref2* models. In the crust we compute the seismic velocities as a function of pressure and temperature. We apply the same method to construct vertical profiles of velocity for the northern and southern sides of the transition zone (gray and yellow lines on Figure 5.6, respectively), which have the same crustal structure than the northern and southern hemispheres but slightly different temperature profiles.

# 5 Results

## 5.1 North/south Rayleigh wave group velocities

Surface wave group velocities are sensitive to different internal structures depending on their frequency : the higher their period, the deeper they sample. The effect of the crust is thus maximal for short period ($\sim 10-100$ s, depending on the crustal thickness) (e.g. *Lognonné and Johnson*, 2007). Of particular interest is the presence in the dispersion curve of local maxima and minima, called Airy phases. The surface wave energy for those phases and periods travels with nearly the same velocity and arrives at about the same time at the seismic station. Since it implies that more energy arrives at once, such Airy phases are, therefore, dominant on a seismogram. For instance, a pronounced Airy phase for Rayleigh waves traveling through the continental crust is observed with period around 20 s (brown curve on Figure 5.2) and is used

to estimate the surface wave magnitude because of its stability. Here we present the dispersion curves obtained given the *a priori* structural models described in section 4.2. In particular, we investigate the effects of different parameters (crustal properties, thermal structure and presence of a lithospheric LVZ) on the Airy phases that will be recorded by the InSight mission.

### 5.1.a Effect of a lithospheric LVZ on group velocities

In this section we consider the northern and southern structural models derived from the DW and DWnoLVZ initial seismological models if those latters are only adjusted given the crustal properties (thickness, density and composition) of the *UCMref1* and *NUCMref2* models (see Figure 5.5 and sections 4.1 and 4.2 for structural models).

Let us first consider the dispersion curves derived from the DWnoLVZ initial model and the *UCMref1* crustal case (black and red dotted lines on Figure 5.7a, respectively). In the north, after a crustal Airy phase at $\sim 20$ s, Rayleigh wave group velocities fastly increase due to the jump in P and S wave velocities at the crust-mantle boundary and then increase monotically for periods $\gtrsim 60$ s. In the thicker southern crust (98 km versus 35 km in the north) the Airy phase is observed at lower frequencies and covers a wider range of periods around 55 s : it might thus be associated to higher amplitudes compared to the northern Airy phase. As previously reported (e.g. *Lognonné and Johnson*, 2007; *Bormann et al.*, 2009), group velocities are especially sensitive to the crustal structure : the north/south dispersion curves present the largest differences for period of $\sim 20-100$ s and then converge to similar values for higher periods that are less sensitive to crustal properties. Interestingly, those north/south differences in group velocities are very similar to those observed between the typical dispersion curves of Earth's continental and oceanic crusts (see Figure 5.2). Indeed, although they are in this latter case shifted to lower period values, they also reflect differences in crustal properties (and, especially, in crustal thickness) between two distinct types of crust.

If a lithospheric low-Velocity Zone is assumed (models derived from the DW initial structural model, dashed lines on Figure 5.7a), a first observation is the larger amplitude of the differences between the northern and southern dispersion curves for periods sensitive to crustal properties ($< 100-120$ s). Such large differences are linked to the higher jump in seismic velocities assumed at the crust-mantle boundary in the DW initial model compared to the DWnoLVZ one. On the other hand, accounting for a lithospheric LVZ does not change at all the periods at which the crustal Airy phases are observed. This implies that the period of a crustal Airy phase is strongly linked to the crustal thickness and not to the jump in seismic velocity assumed at the crust-mantle interface. However, as previously reported by *Zheng et al.* (2015), the existence of a LVZ below the crust induces the presence of another Airy phase at periods sensitive to lithospheric mantle properties. For the *UCMref1* crustal case, this lithospheric Airy phase covers wide ranges of periods around 100 s or 210 s for waves traveling through the northern or southern hemisphere, respectively. Since the lithospheric vertical profiles of density and seismic velocities assumed in the northern and southern hemispheres are strictly identical

(see Figure 5.5), this difference in Airy phase period for surface waves traveling through the two hemispheres is linked to the slow group velocities observed in the southern crust. Indeed, this latter is almost three times thicker than the northern crust in the *UCMref1* case : the effect of such slow group velocities in the southern crust is still visible for periods $> 100$ s, which leads to different dispersion curves for the northern and southern hemisphere structures at high periods. The differences between the northern and the southern group velocities are also visible on the vertical components that will be recorded by the station for surface wave travels purely located in the north or in the south (Figure 5.8a). The surface waves traveling in the north with large period $> 100$ s are first recorded, whereas those traveling in the south at similar periods arrive with a slight delay and are more difficult to identify on the seismogram. In the *UCMref1* case, such surface wave periods might be smoothed by the large southern crustal thickness (98 km) that influences a large range of periods. Conversely, the southern crustal Airy phase is recorded before the northern one and has an higher amplitude.

Similar results are retrieved if considering the *NUCMref2* crustal model (see Figure 5.5b for structural models and Figure 5.7b for associated dispersion curves). This is especially true for the dispersion curves of rayleigh waves traveling through the northern hemisphere since this latter is characterized by almost identical crustal properties (composition and thickness) in the *UCMref1* and *NUCMref2* models (see chapter 4 and Table 4.5 for details). Consequently, the seismogram recorded for a purely northern travel is also similar to that observed for the *UCMref1* case (Figure 5.8b). However, the southern crust is thinner in the *NUCMref2* model (55 km versus 98 km in the *UCMref1* model), which shifts the crustal Airy phase to lower periods around 30 s (55 s in the *UCMref1* case) on the southern dispersion curve. On the other hand, because of the lower density and mixed composition that are assumed for the southern crust in the *NUCMref2* model, the crustal Airy phase has a higher velocity in the north than in the south, though it is not clear in the respective seismograms (Figures 5.8b). The opposite is observed for the *UCMref1* model for which a larger compressional effect in the thick southern crust leads to a higher velocity of the crustal Airy phase in this hemisphere. Another consequence of the lower contrast in crustal thickness between the two hemispheres in the model *NUCMref2* is the decrease of the differences between the northern and southern dispersion curves that fastly converge for period $> 100$ s for both the models with or without a lithospheric LVZ. Such a convergence is identifiable on the velocity seismograms predicted for travels located in the northern or in the southern hemispheres, as the large period surface waves, i.e. the first arrivals, are detected with only a slight delay in the south. As previously reported for the *UCMref1* case, no lithospheric Airy phases are present for the models without a LVZ below the crust (dotted lines on Figure 5.7b), whereas they are observed in models accounting for such a LVZ at periods around 100 s and 125 s on the northern and southern dispersion curves, respectively (dashed lines on Figure 5.7b).

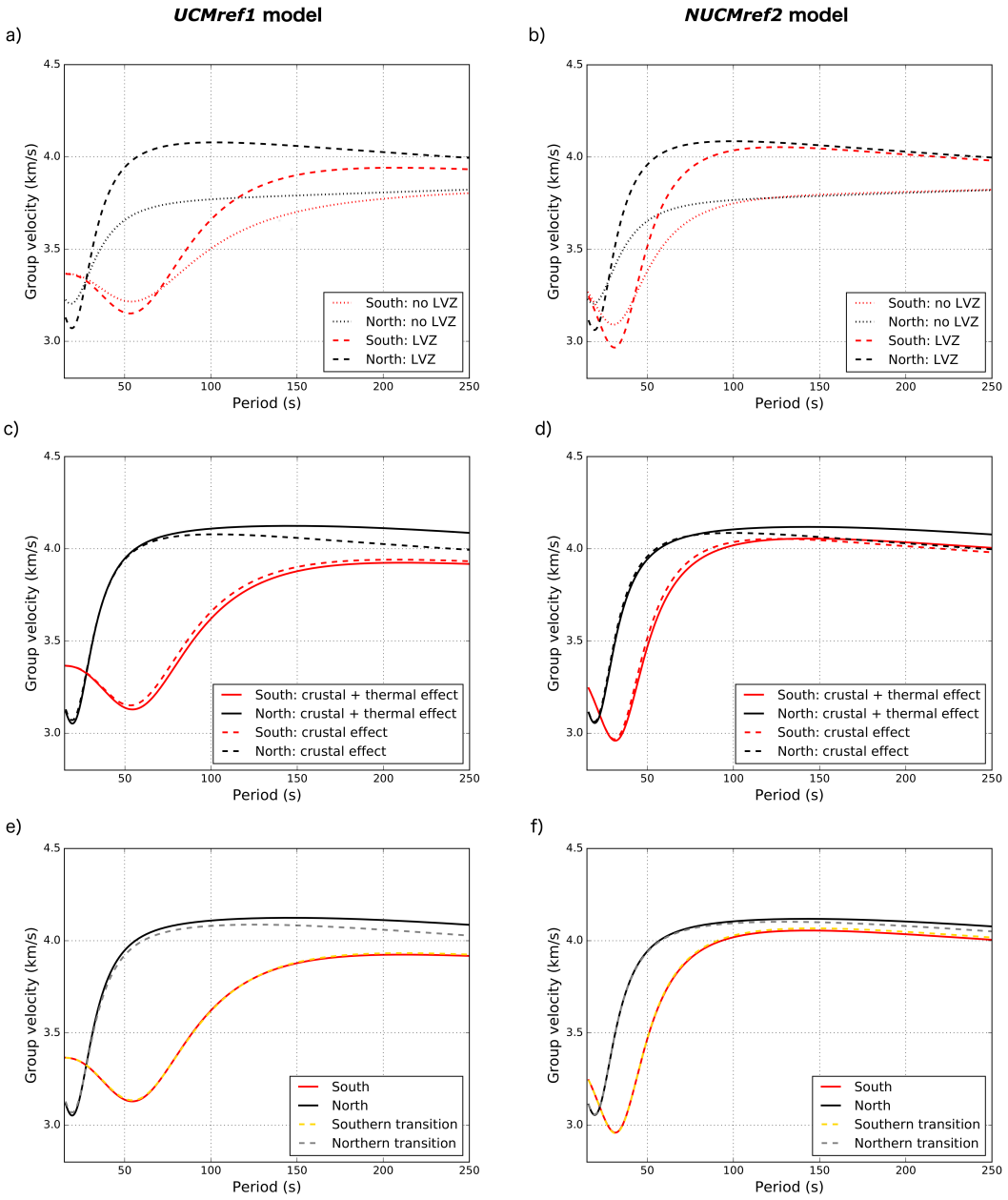


**FIGURE 5.7** – Dispersion curves of Rayleigh wave group velocities for the fundamental mode. Average group velocities for the northern (in black) and southern (in red) models are shown if the DW (dashed lines) and DWnoLVZ (dotted lines) initial structural models are adjusted given the crustal properties (thickness and composition) of the *UCMref1* and *NUCMref2* in (a) and (b), respectively (see Figure 5.5 for north/south structural models). In addition to crustal properties (dashed lines), the DW initial structural model is also adjusted given the present-day temperature profiles in (c) and (d) for the *UCMref1* and *NUCMref2* cases, respectively (solid lines, see Figure 5.6 for north/south structural models). Those typical Rayleigh wave dispersion curves for the north/south hemispheres are compared with those observed for the northern (gray dashed lines) and southern (yellow dashed lines) sides of the transition zone (see chapter 4, section 4.3.a for details) in (e) and (f) for the *UCMref1* and *NUCMref2* crustal models, respectively.

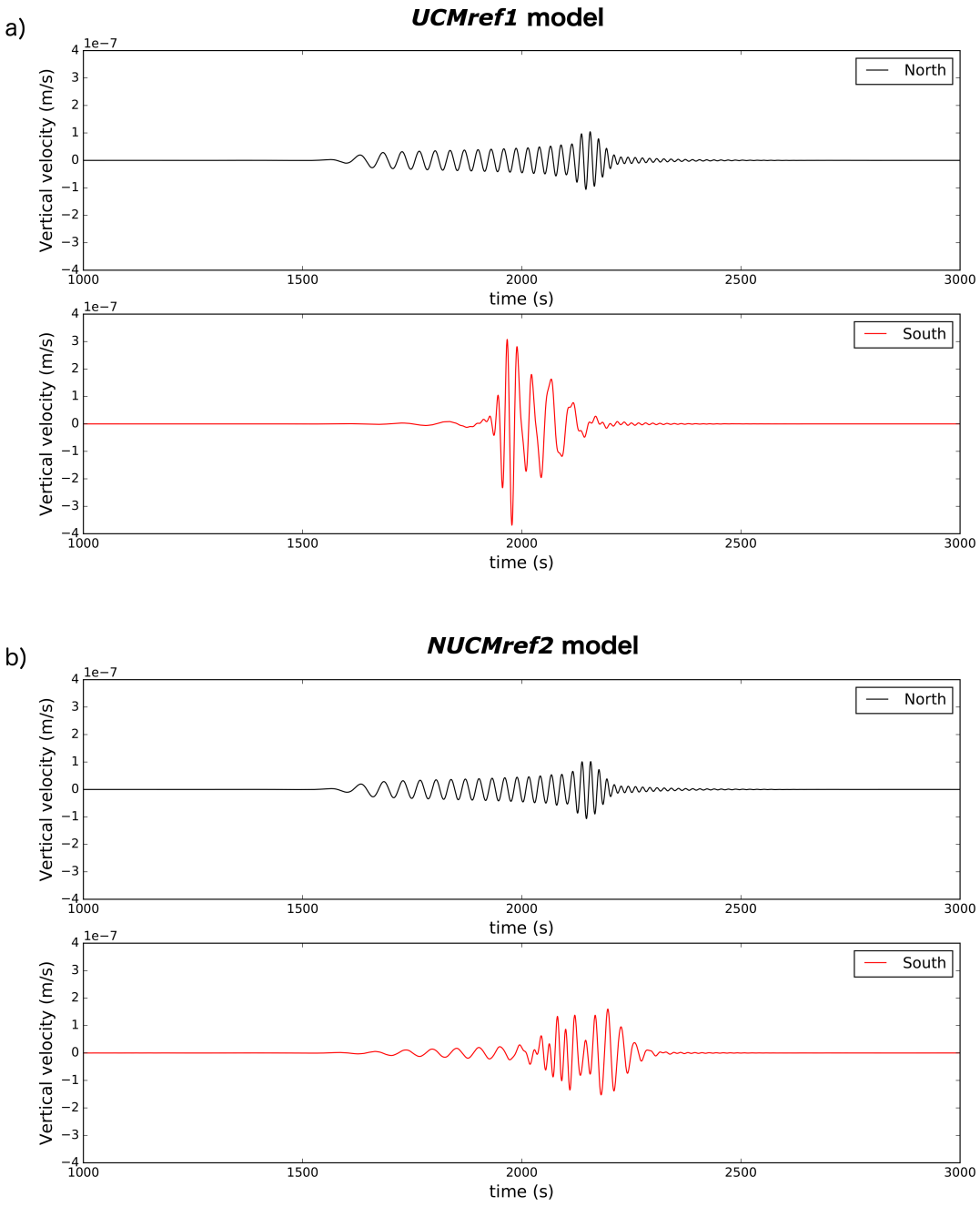


FIGURE 5.8 – Vertical components of velocity seismograms for the fundamental mode at epicentral distance of 30°. Results are shown for surface wave paths located in the northern and southern hemispheres when adapting the DW model with the crustal properties and lithospheric temperatures of the *UCMref1* case in (a) and of the *NUCMref2* ones in (b). We assume that the InSight station is located at (0°N, 136°E). The seismic moment of the event is $10^{17}$ Nm with an isotropic source at a depth of 60 km. The bandpass is filtered between 10 and 250 s.

### 5.1.b Effect of the thermal structure on group velocities

In this section, we consider the structural models that have been derived from the DW initial model when adding the thermal effect on group velocities of the present-day temperature profiles predicted by the *UCMref1* and *NUCMref2* crustal models (solid lines on Figure 5.7c and d). The dispersion curves obtained for such models are compared with those previously described in section 5.1.a when the DW model is only adjusted given the crustal structure of the *UCMref1* and *NUCMref2* models (dashed lines on Figure 5.7c and d).

For the *UCMref1* model, adding the thermal effect on surface wave group velocities leads to insignifiant differences at short periods sampling the crustal structure since the seismic velocities not differ much in the crust from those previously assumed in section 5.1.a (Figure 5.7c). However, at periods $> 50$ s the group velocities for surface wave traveling along the southern hemisphere are slower. This is due to the higher temperatures predicted by the *UCMref1* crustal model in the southern lithosphere compared to those assumed in the DW initial model (hot temperature profile from *Plesa et al.* (2015), blue line on the right plot of Figure 5.6). Such differences are, however, minor and the thermal effect does not increase at higher periods. Though it remains slight, the thermal effect on group velocities is larger for surface waves traveling in the north since the temperatures of the *UCMref1* model are significantly lower in this hemisphere than those assumed to construct the DW model. The higher the period, the more significant the difference between models adjusted with temperature or not is (black solid and dashed lines on Figure 5.7c, respectively). The thermal effect leads thus to a maximal added difference in group velocities of $\sim 0.2$ km/s (equivalent to 5 % of the velocity) between the northern and southern hemispheres for the highest period values considered here (i.e. 250 s).

For the *NUCMref2* crustal model, the northern and southern temperature profiles differ less and are both colder than the temperature profile assumed to build the DW model, except for the crust. Accounting for the thermal effect implies thus faster group velocities (solid lines on Figure 5.7d) in the two lithospheres in comparison with those obtained without thermal adjustment (dashed lines on Figure 5.7d). Again, the greatest effect is observed at high periods and slightly increases the differences in group velocity between the two hemispheres.

Accounting for the thermal effect does not change at all the periods at which the crustal Airy phases are observed. Those periods are indeed only sensitive to the guided effect of the crust. For the *UCMref1* crustal model, since the southern temperature profile is close to that assumed for the DW model, the lithospheric Airy phase observed in the southern dispersion curve is similar to that obtained if neglecting the thermal effect (around 210 s). However, the lithospheric Airy phases are shifted to higher periods around 140 s on all the other dispersion curves (northern group velocities of the *UCMref1* case, northern and southern ones of the *NUCMref2* case), reflecting the colder temperatures assumed for those structural models. This shift in period is accompanied by a flattening of the curve around the Airy phase, which implies a widening of the range of periods traveling with nearly the same velocity. *Zheng et al.* (2015)

have argued that this shift in period is linked to the stagnant lid thickness : the thicker the lid, the higher the period of the lithospheric Airy phase is. This is consistent with our results, which show a shift to higher period values when considering a colder temperature profile and thus a thicker stagnant lid. However, we note that the highest period of the lithospheric Airy phases is retrieved for the southern group velocities of the *UCMref1* crustal model (solid lines on Figure 5.7c), which presents the thinnest stagnant lid at the present day among all the structural models investigated here (see Table 4.5 in chapter 4). In this case, the period of the lithospheric Airy phase might be also sensitive to the very thick southern crust (98 km) that decreases the surface wave group velocities up to high periods.

### 5.1.c Group velocities in the north/south transition zone

Here we investigate the effect of the seismological models derived for the northern and southern sides of the transition zone on Rayleigh wave group velocities (see gray and yellow dashed lines, respectively, on Figure 5.6 for the structural models, and Figure 5.7e and f for the associated dispersion curves).

For a given side of the transition zone (northern or southern) we assume the same crustal thickness and composition as for the corresponding hemisphere. At periods $< 50$ s, the group velocities for paths along the northern/southern sides of the transition zone (gray/yellow dashed lines on Figure 5.6) are thus respectively nearly indistinguishable from the group velocities of surface waves traveling in the northern/southern hemisphere (black/red lines on Figure 5.6). At higher periods, the dispersion curve observed for the southern side of the transition zone is almost identical to that retrieved for the purely southern hemisphere since the temperature and seismic velocity profiles are very similar in those two areas for both the *UCMref1* and *NUCMref2* cases (red solid and yellow dashed lines on Figure 5.6). In the north, group velocities are slightly slowler at periods $\gtrsim 50-70$ s in the transition zone, which is hotter than the purely northern hemisphere (black solid and gray dashed lines on Figure 5.6, respectively). However, although those differences are higher than those observed in the south, they are still slight, especially for the *NUCMref2* case.

## 5.2 Dispersion of group velocities along potential great circles

In section 5.1 we consider paths that are strictly confined to a given north/south hemisphere or transition zone side. However, realistic Martian great circle paths go through those different propagation zones with variable proportions depending on the source and seismic station locations. To account for lateral variations in phase velocity, we investigate here the dispersion curves expected for Rayleigh waves traveling along distinct great circles.

The global group slowness $1/v_g$ along a given path is the integral of the local group slowness $1/v_{g_{local}}$ in the different segments of length $S$ constituting the great circle (*Woodhouse*, 1974; *Debayle and Sambridge*, 2004) :

$$\frac{1}{v_g} = \frac{1}{2\pi R_p} \int_{path} \frac{1}{v_{glocal}} \mathrm{d}S \tag{5.4}$$

which directly provides the average group velocity $v_g$ along the great circle considered. However, it is important to mention that this is a first order estimate, since we assume with this method that the velocity gradients are not strong along the path, which is probably not the case at the dichotomy boundary, though the north/south transition zone might smooth the amplitude of lateral variations in this area.

To investigate the effect of the path taken by the surface waves on the dispersion curves that will be recorded by the InSight mission, we consider two great circles with extreme ratios of travel in the northern and southern hemispheres. There is, however, a limited panel of distinct combinations between travels in the two hemispheres since the highlands cover 60 % of the surface. Moreover, the specific location of the InSight mission close to the dichotomy boundary (red square on Figure 5.9a) and the elliptical shape of this latter (*Andrews-Hanna et al.*, 2008) (black dotted line on Figure 5.9a) imply that most travels are preferentially located in the southern hemisphere.

An extremum case is represented by the path 1 (see Table 5.2 and blue dashed lines on Figure 5.9), which is located close to the equatorial line and goes predominantly along the southern areas (85 % in total if adding the southern hemisphere and transition zone side). This path does not go through the northern hemisphere and only crosses a small portion of the northern side of the transition zone ($\sim$ 15 % of the total path). Seismic events linked to stress generated by the large load of the Tharsis region (blue star on Figure 5.9) are potential seismic sources for such a great circle path (e.g. *Lognonné and Johnson*, 2007; *Panning et al.*, 2017). Since the path 1 is mainly located in the highlands, the associated dispersion curves (blue lines on Figure 5.9b-d) are mostly influenced by the group velocities observed for Rayleigh waves traveling in the southern hemisphere (red solid and yellow dashed lines on Figure 5.7 for the southern hemisphere and associated transition zone, respectively). For the *UCMref1* crustal model, though a slight Airy crustal phase is observed around 20 s due to the small incursion of the travel path in the northern transition zone, the dominant signal is linked to the crustal Airy phase observed for a travel in the south at a period around 50 s. As previously described

| | South | North | Southern transition zone | Northern transition zone |
|---|---|---|---|---|
| path 1 | 60 % | 0 % | 25 % | 15 % |
| path 2 | 45 % | 41 % | 7 % | 7 % |

**TABLE 5.2** – Distances in percentages of two potential paths for multiple orbit surface waves along the four propagation areas considered here : northern/southern hemispheres and a transition zone at the dichotomy boundary divided into northern and southern sides (see Figure 4.14). The paths 1 and 2 are represented by the blue and green dashed lines on Figure 5.9a, respectively.

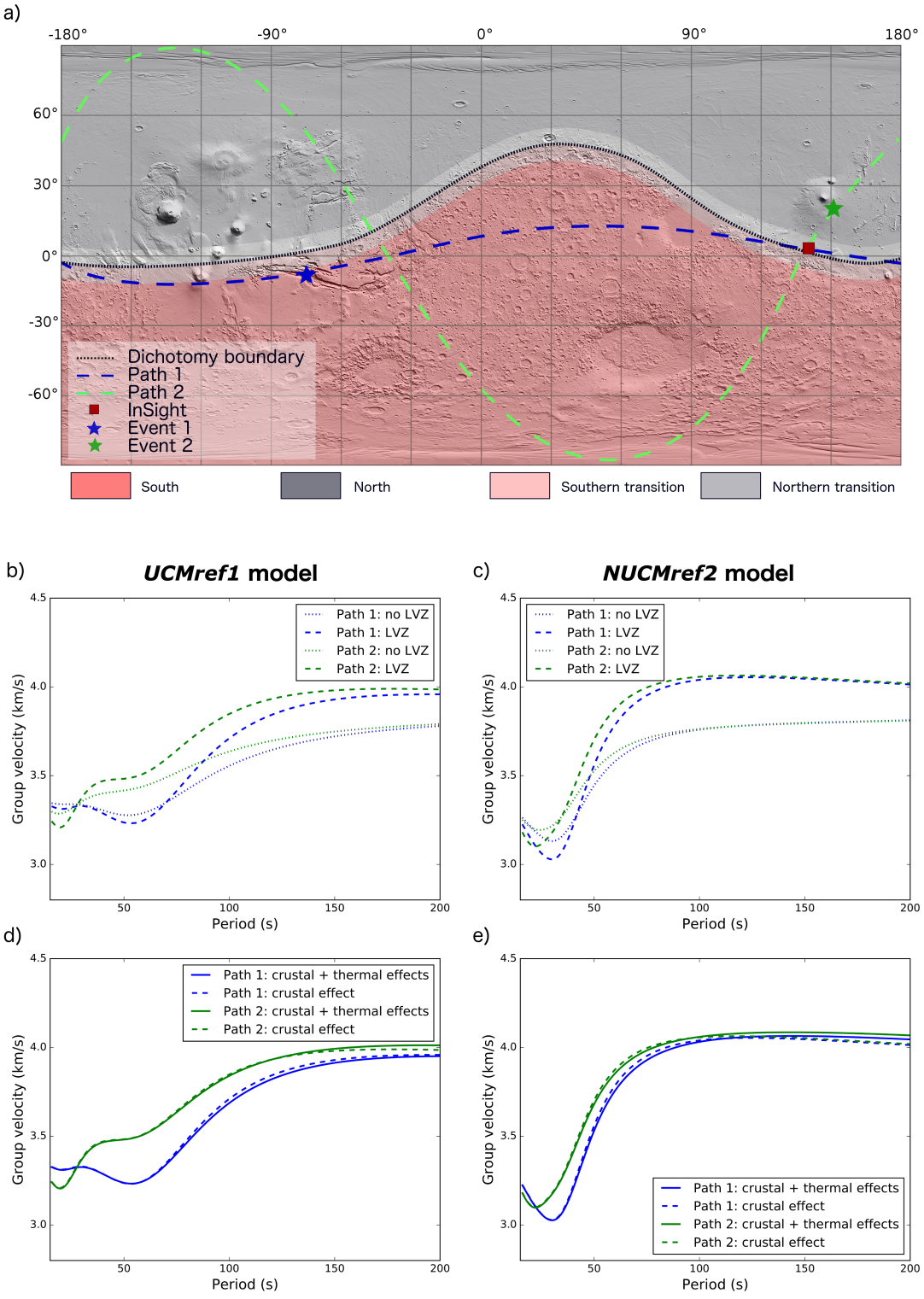
a)
-180°
-90°
0°
90°
180°
60°
30°
0°
-30°
-60°
Dichotomy boundary
Path 1
Path 2
InSight
Event 1
Event 2
South
North
Southern transition
Northern transition
b)
UCMref1 model
c)
NUCMref2 model
Path 1: no LVZ
Path 1: LVZ
Path 2: no LVZ
Path 2: LVZ
Group velocity (km/s)
Period (s)
d)
e)
Path 1: crustal + thermal effects
Path 1: crustal effect
Path 2: crustal + thermal effects
Path 2: crustal effect

FIGURE 5.9

**FIGURE 5.9** – Dispersion of Rayleigh-wave group velocities along potential great circles. Location of the potential events (stars) and of the expected InSight landing site (red square) are indicated over a MOLA-shaded relief topographic map in (a). To account for lateral variations in phase velocity the integral of the group slowness $1/v_g$ is computed along two distinct paths (blue and green dashed lines). We consider four propagation zones : southern (red) and northern (black) hemispheres and a transition zone divided into northern (gray) and southern (light red) areas on each side of the dichotomy boundary (black dashed line, delimitation of *Andrews-Hanna et al.*, 2008) (see Figure 4.14 for details). The average group velocities along the two paths are computed given the *DW* (dashed lines) and *DW-noLVZ* (dotted lines) seismological models when considering the crustal properties of the *UCMref1* and *NUCMref2* crustal models in (b) and (c), respectively (see Figure 5.5 for the corresponding seismological profiles). If considering the DW initial seismological model, the added effect of the characteristic temperature profiles of the four propagation zones is represented in (e) for the *UCMref1* crustal model and in (f) for the *NUCMref2* one (see Figure 5.6 for the corresponding seismological profiles).

for the structural models assuming a LVZ below the crust (dashed and solid blue lines on Figure 5.9b and d), a flat lithospheric Airy phase is observed at periods around 200 s and the increase in the group velocity in the lithosphere is larger due to a higher jump in P and S-wave velocities at the crust-mantle boundary. For the *NUCMref2* model a unique and pronounced crustal Airy phase is retrieved at a period of $\sim$ 30 s because the northern and southern crustal thicknesses - and thus their associated periods of crustal Airy phase - are more similar than those predicted by the *UCMref1* crustal model. In the presence of a lithospheric LVZ, a second flat Airy phase is observed at higher periods around 140 s or 120 s accounting or not for the thermal effect, respectively. As previously explained in section 5.1.b, this shift is due to the lower temperatures predicted by the *NUCMref1* model compared to those used to construct the DW reference structural model.

The pole to pole path 2 (see Table 5.2 and green dashed lines on Figure 5.9) presents one of the longest travel in the northern areas (almost 50% in total if adding the distances in the northern hemisphere and transition zone side). Such a great circle can be linked, for instance, to a marsquake epicenter located in the Elysium volcanic province (*Taylor et al.*, 2013; *Panning et al.*, 2017) (green star on Figure 5.9a). The group velocities that would be recorded for such a great circle are thus equally influenced by the properties of the two hemispheres. For the *UCMref1* model, a first crustal Airy phase linked to the travel in the northern hemisphere is present at a period of $\sim$ 20 s. A second minima in the dispersion curve is observed at periods around 50 s and coincides with the period of the crustal Airy phase observed for Rayleigh waves traveling in the south (see section 5.1). For the path 2 this second crustal Airy phase is, however, smoothed by the fast increase of the group velocities in the north for such periods. For the *NUCMref2* crustal model, a pronounced crustal Airy phase is observed at a period of $\sim$ 25 s that results from the combination of those observed for surface wave traveling in purely northern or southern hemispheres. If a LVZ is present in the lithospheric mantle (green dashed lines on Figure 5.9b-d), a second Airy phase is observed at periods of 120 s and 170 s for the *UCMref1* and *NUCMref2* crustal models, respectively, with a shift to higher periods of 140 s and 190 s if accounting for the thermal effect (green solid lines on Figure 5.9b-d).

# 6 Discussion

## 6.1 Estimates of north/south crustal properties with dispersion curves

The major differences between the group velocities of the fundamental mode for Rayleigh waves traveling in the north or in the south are observed at periods $< 100$ s, mainly sensitive to crustal properties. Though differences in thermal structure might exist in the crust between the two hemispheres of Mars, the period at which the crustal Airy phase is observed does not depend on the temperature and is entirely conditioned by the crustal thickness through a well-known guided effect (e.g. *Bormann et al.*, 2009). Along a path at the Martian surface that samples both the highlands and the lowlands (for instance the path 2, blue lines on Figure 5.9), the dispersion curve is thus influenced by the crustal Airy phases that are characterictic of each hemisphere taken separately. If the northern and southern crustal thicknesses do not strongly differ - as for instance in the *NUCMref2* crustal model (only 20 km difference) - a unique crustal Airy phase is visible on the dispersion curve, which results from the merging of the crustal Airy phases of each hemisphere at an intermediate period. Conversely, if the crustal thicknesses of the southern and northern crusts largely differ - as for instance in the *UCMref1* crustal model (see Table 4.5 in chapter 4 for details) - two distinct crustal Airy phases can be individualized on the dispersion curves. However, the recording of two identifiable crustal Airy phases depends on the travel path of surface waves. Indeed, if the dispersion curve is predominantly influenced by one hemisphere (most likely the southern one, see path 1, green lines on Figure 5.9), the Airy phase associated to this latter is the only one to be clearly recognizable on the group velocities, which might lead to the wrong conclusion that the northern and southern crustal thicknesses are fairly similar. To avoid such misinterpretations and obtain a good estimate of the dichotomy in crustal thickness, several quakes with R3 measurements from different source regions - or alternatively one that equally samples both hemispheres (i.e. the path 2) - are required. On the other hand, though the multiple-orbit surface waves preferentially sample the southern crust, the body waves produced by local seismic events such as impacts in the north are likely more sensitive to the northern crustal structure, since the InSight mission is located in this hemisphere. Complementary informations from body wave and multiple-orbit surface wave analysis could thus be combined to differentiate the northern and southern crustal structures.

The effect of the lithospheric thermal structure on group velocities is maximal for high periods ($\gtrsim 80$ s) (Figure 5.7c and d). For Rayleigh waves traveling along potential great circles the velocity at such periods depends on the percentage of the travel located in the northern hemisphere (Figure 5.9d and e). Although the differences are small between two paths, the dispersion curves that will be recorded by the InSight misssion will allow to constrain at first order the thermal stuctures of the two Martian hemispheres.

It is important to note that the phenomenological effect of the north/south crustal dichotomy mentioned so far may constitute an upper bound of what would in reality be observed on the Martian dispersion curves. Indeed, since the shorter path along the great circle is sampled

by both the R1 and R3 arrival times, group velocities would be more sensitive to its properties compared to those of the major arc path that is only sampled by the R3 arrival time (see section 3.3 for details on the multiple orbit surface wave approach). On the other hand, though we consider here a north/south transition zone at the dichotomy boundary, this latter does nearly not influence our results since we assume the same crustal thickness in each transition zone and its corresponding hemisphere. As previously mentioned, the north/south transition zone might rather correspond to a long-wavelength topography change over several hundred kilometers (e.g. *Watters*, 2003a; *Watters et al.*, 2007), which might thus smooth the crustal Airy phases along a given path. Moreover, lateral variations in thickness probably exist within each hemisphere. In particular, the crustal thickening of the Tharsis bulge or, on the contrary, the crustal thinning in the Hellas Basin, concern sufficiently large regions to influence the dispersion curves of group velocities (*Larmat et al.*, 2008). To account for such lateral variations, 3-D models of Mars's crustal thickness (e.g. *Wieczorek*, 2007) can be used to divide the travel path into narrower and more realistic segments.

## 6.2 Uncertainties on the R3 arrival time

Although the R1 first arrival time is expected to be easily pickable for a great marsquake, this is not the case for R3 due to the attenuation and dispersion of the Rayleigh surface waves during their propagation. *Panning et al.* (2015) have investigated the degree of reliability of the group velocity value estimated for each period, which directly depends on the quality of the R1 and R3 arrival time picking (see equation 5.1). When considering synthetic data for Mars (Figure 5.10a), only slight uncertainties of $\sim 0.1$ km/s are expected for group velocities at short-period $\lesssim 60$ s, implying that the crustal Airy phases previously described (maximal period around 50 s for the *UCMref1* crustal model, see section 5.2) will likely be well identifiable. However, the smooth deflection observed for instance at $\sim 20$ s for Rayleigh waves traveling along path 1 if considering the *UCMref1* crustal model (blue curves on Figure 5.9b and d) will probably not be detected. This smooth deflection is due to the short travel percentage in the north of this path : in this case another marsquake associated to a larger travel in the lowlands is thus required to constrain the northern crustal thickness. After a period value of 60 s, the uncertainties on the group velocities are expected to increase with the period (Figure 5.10a). Though the VBB components of the SEIS instruments have been specifically designed to be efficient at low-frequencies, this is likely to prevent the detection of the effect of the northern and southern thermal structures that is the largest at the highest periods (see section 5.1.b). When inverting the dispersion diagram obtained for $120,000$ sampled models (Figure 5.10a), the $v_s$ profiles are well defined up to a depth of 200 km, where the probability density functions (pdf) are the highest (Figure 5.10c).

Far from the idealized case considered so far, the signals recorded by the InSight mission will be deteriorated by noise linked to the characteristics of the instrument itself and its installation on Mars's surface. Moreover, if the wind noise was the main reason for the lack of seismic activity detection by the Viking 2 mission (*Nakamura et al.*, 1979), other potential sources of

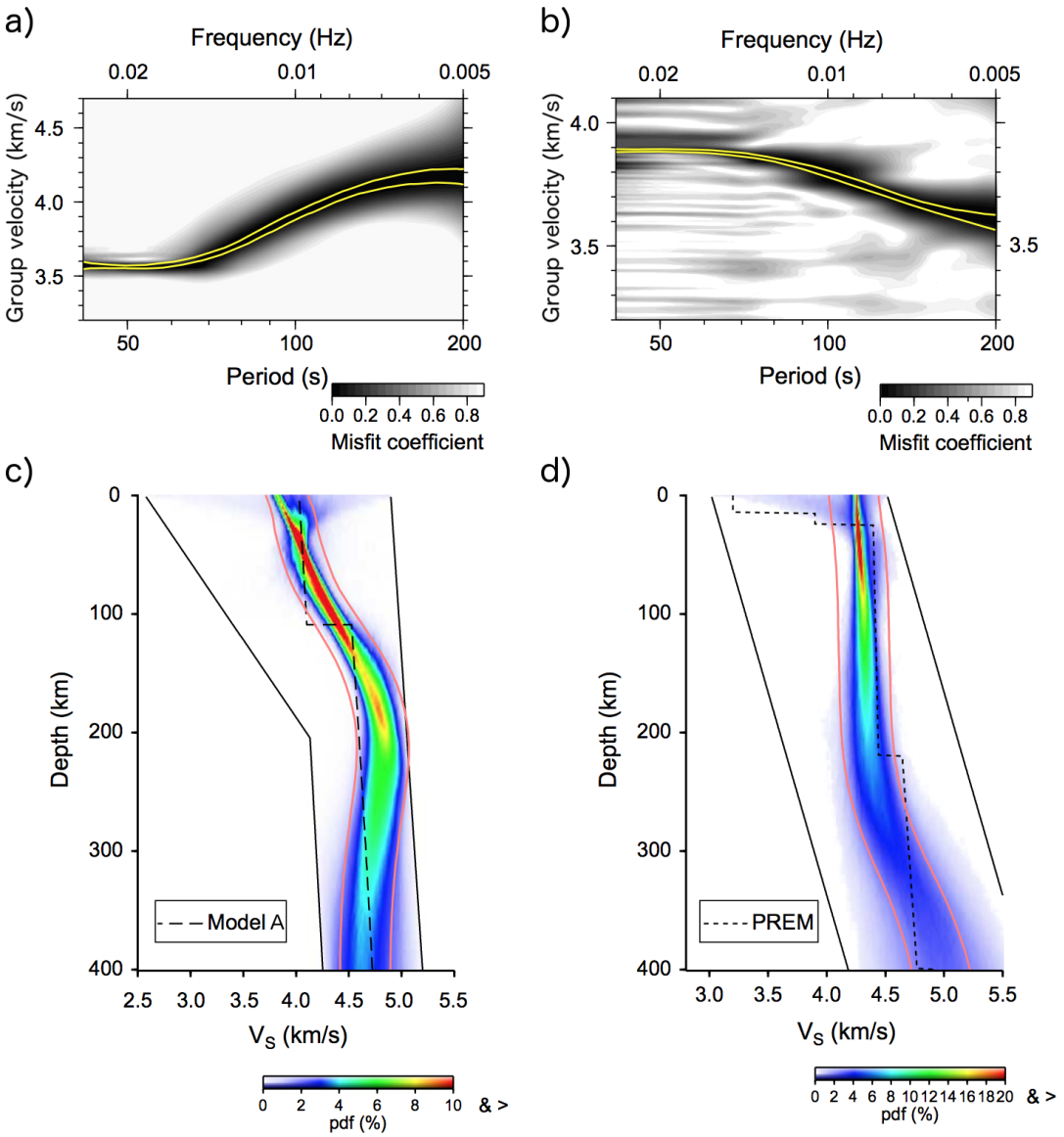


**FIGURE 5.10** – *A posteriori* probability density functions (pdf) of S-wave velocity and corresponding input dispersion diagrams (Figure from *Panning et al.*, 2015). The dispersion diagrams show the degree of reliability of the average group velocity value estimated for each period for 120,000 sampled models : in (a) for synthetic seismograms produced given the Martian velocity model A of *Sohl and Spohn* (1997) with a 110 km-thick crust, in (b) for terrestrial real data (event C200802210246A recorded at the BFO station, see *Panning et al.*, 2015). The gray scale shows the misfit coefficient to initial models that is due to the uncertainties for the R3 arrival time. Yellow curves delimit acceptable models, which have a low misfit coefficient. The S-profiles that are inverted given those dispersion diagrams are represented in (c) for the Martian synthetic data and in (d) for the real terrestrial data. Red and blue colors correspond to high and low probability, respectively. Solid black lines represent the minimum and maximum parameter values allowed and the black dashed lines show the model to retrieve. Pink curves delimite the interval between $\pm 5$ % of the median $v_s$ profile of the distribution.

seismic noise exist on Mars such as temperature fluctuations associated with the daily cycle, atmospheric pressure variations or internal heterogeneities leading to scattering of the signal. As observed on Earth (Figure 5.10b), the presence of noise would deterior the dispersion diagram, even at short periods, and consequently the probability density functions of the $v_s$ profiles that are inverted from it (Figure 5.10d).

## 6.3 Reliability of the *a priori* structural models

Several hypotheses are made when using *a priori* structural models such as DW, which are constructed by assuming a known and homogenous mantle composition (see section 8 for comparative results when using the composition model of *Sanloup et al.* (1999) rather than that of *Dreibus and Wanke*, 1985). Moreover, such models require assumptions on the present-day Martian average temperature profile that is poorly known and largely varies according to the conditions that are assumed in the thermal models (see for instance *Plesa et al.* (2016) for the ranges of potential internal temperatures). Finally, they assume a thermodynamical equilibrium for the mineral phase assemblages and that the elastic and anelastic properties of those phase assemblages are well represented by empirical relationships derived from laboratory experiments and observations specific to the Earth. Such assumption are not unrealistic in the hot mantle in which the temperatures are sufficiently high to lead to the permanent equilibrium renewal of mineral assemblages. However, temperatures $\lesssim$ 1000 K might prevent such equilibrium renewal and thus likely preserve some non-equilibrium phase assemblages in the upper part of the Martian conductive stagnant lid (up to $\sim 100-200$ km deep) (e.g. *Panning et al.*, 2017). Since the thermal lithosphere has thickened during Mars's evolution, a more rigorous approach would consist in assuming that the mineral assemblages located in the present-day shallow lithospheric layers acquired their stability at a temperature of $\sim$ 1000 K in the past and have not changed since then. Besides uncertainties in the stability of mineral phases at shallow depths, the crustal composition and layering is largely unknown. For instance, if the crustal composition and density of the southern crust are different from those assumed in our models, it would change the southern crustal thickness and thus shift both the crustal Airy phase's period and velocity observed for the southern hemisphere (see section 5.1.a). Moreover, making the difference between a linear compositional gradient or multi-layering in the crust, such as that proposed by the *NUCMref2* model, is probably impossible when inverting the group velocities (*Panning et al.*, 2015; *Panning et al.*, 2017).

Another example of the potential consequences of the uncertainties included in the *a priori* structural models is illustrated by the differences shown by the dispersion curves obtained with or without a lithospheric LVZ (DW and DWnoLVZ initial models, respectively). In the north/south structural models derived from the DW initial vertical profiles, there is a large jump in seismic velocity at the crust-mantle boundary (red and black lines on Figure 5.5), which leads to a strong increase of the group velocities in the lithosphere and to well-identifiable crustal Airy phases (dashed lines on the dispersion curves on Figures 5.7a-d and 5.9b-e). On the contrary, if assuming the DWnoLVZ initial seismological model (gray and yellow dashed

lines on Figure 5.5), the seismic velocity jump at the crust-mantle boundary is much more smooth, which results in a smaller increase in the group velocity in the lithosphere. In this case, though visible, the crustal Airy phases are less pronounced (dotted lines on Figure 5.9b and c) and might thus be hard to detect in the recorded noisy signal given the uncertainties in the R3 arrival time (Figure 5.10). This is especially true for the slight signal associated to the northern crust in the *UCMref1* crustal model (see section 6.1), which could lead to the wrong interpretation that the Martian crustal thickness is similar in the northern and southern hemispheres.

# 7 Conclusion

To investigate the effect of the dichotomy on the surface wave group velocities that will be recorded by the upcoming InSight mission, two initial structural models have been considered : the DW model of *Rivoldini et al.* (2011) and the DWnoLVZ model, similar to DW except there is no lithospheric LVZ. Those initial models were first adapted to the northern and southern crustal properties of the *UCMref1* and *NUCMref2* models, and then by accounting for the difference in thermal structure of each hemisphere. In a forward problem those northern and southern models have been used to compute the group velocities of the fundamental mode as a function of period (between 10 and 250 s) with the MINEOS package.

The largest differences in group velocity for Rayleigh waves traveling through the northern or the southern hemispheres are observed at periods sensitive to crustal properties ($\lesssim$ 100 s). A crustal Airy phase is observed on the dispersion curves at a larger period for a thicker crust. In models assuming a lithospheric LVZ, a second Airy phase is also observed at a period that increases for colder lithospheric temperatures or a larger amplitude of the LVZ. However, accounting for the northern and southern mantle temperature profiles predicted by our thermal models does not significantly change the group velocities at periods sensitive to crustal properties. Since the largest thermal effect is observed at periods sensitive to the lithospheric mantle properties ($\gtrsim$ 100 s), Mars's real data provided by the InSight mission might help to determine the northern and southern lithospheric mantle temperatures, though it will depend on the uncertainties for R3 arrival time that are predicted to be the highest at such high periods.

When considering the average group velocities along potential great circles on Mars's surface, we found that the dispersion curves are influenced by the properties of each hemisphere although surface velocities will likely be more sensitive to the properties of the southern hemisphere which covers a wider surface. However, only one crustal Airy phase is recognizable if the difference in crustal thickness between the north and the south is small ($\lesssim$ 20 km). Conversely, if the northern and southern crustal thicknesses largely differ, two crustal Airy phases are observed. However, if the northern hemisphere is not enough sampled along a given great circle the corresponding crustal Airy phase might be hard to identify given the uncertainties for the R3 arrival time picking. In this context, it will be challenging to determine the northern average crustal thickness with group velocity analysis only. Similarly, constraining the northern and

southern crustal thicknesses might be hard if only a small jump in seismic velocity is present at the crust-mantle boundary since the crustal Airy phases are in this case strongly smoothed. Several seismic events with distinct source locations are thus likely required to constrain the northern and southern crustal thicknesses with the multiple-orbit surface wave approach. The analysis of body waves produced by local events in the north should, however, provide complementary insights on the northern crustal structure.

# 8 Supplement : EH45 initial seismological model

Several *a priori* structural models have been developed for Mars by assuming different bulk mantle compositions (e.g. *Mocquet et al.*, 1996; *Sohl and Spohn*, 1997; *Zharkov and Gudkova*, 2005; *Rivoldini et al.*, 2011). The DW initial model considered as a reference model in sections 4 and 5 has been obtained given the compositional model of *Dreibus and Wanke* (1985). In this section, we investigate the effect on Rayleigh wave dispersion of using in the mantle the EH45 seismological model of *Rivoldini et al.* (2011) that is based on the compositional model of *Sanloup et al.* (1999). For a similar temperature profile as that assumed for the DWThot model (light blue lines on Figure 5.11), this model is mainly characterized by a higher core radius (1800 km versus 1750 km for the DW model) and lower P and S wave velocities in the mantle (Figure 5.11a).

The models derived from the EH45 initial model given the northern and southern crustal properties and present-day temperature profiles of the cases *UCMref1* and *NUCMref2* (gray and yellow dashed lines, respectively, on Figure 5.11b and c) are characterized by lower P and S-wave velocities in the mantle compared to the models derived from the DW model (black and red lines, respectively, on Figure 5.11b and c). Consequently, the Rayleigh wave group velocities predicted by the EH45 model are lower than those derived from the DW one in both the north and the south at periods $\gtrsim$ 80 s. Such differences will not likely be noticeable on the dispersion curves deduces from the signals recorded by SEIS due to the large uncertainties on the R3 arrival time (see Figure 5.10 and section 6.2). Finally, the periods of the crustal Airy phases, but also the lithospheric ones, are similar in both the models derived from the DW and EH45 ones, although the EH45 has lower mantle temperatures.

**FIGURE 5.11** – (a) From left to right : vertical profiles of density, P and S-wave velocities if considering the EH45 initial structural model of *Rivoldini et al.* (2011) constructed given the compositional model of *Sanloup et al.* (1999) (blue dashed lines). The EH45 initial model is adapted given the crustal properties (thickness, composition) and lithospheric temperature profiles of two representative exemples of our best crustal models : *UCMref1* in (b) and *NUCMref2* in (c) (gray and yellow dashed lines for the northern and southern hemispheres, respectively). To give a comparison, the DW initial model previously considered is represented by the light blue lines in (a) and by the black and red lines in (b) and (c) when it is adapted given the northern and southern properties of our reference crustal models, respectively.

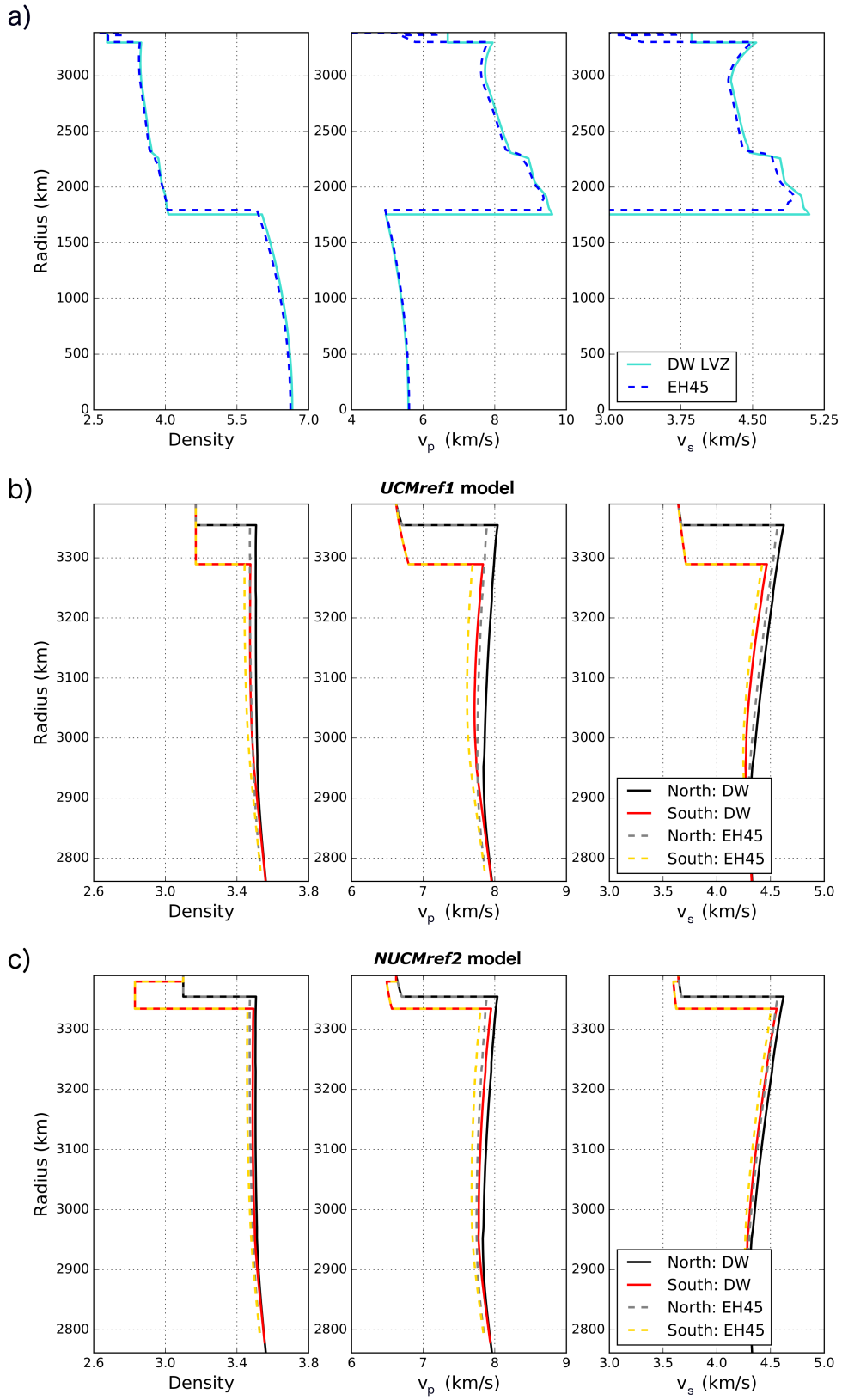
a)
Radius (km)
Density
$v_p$ (km/s)
$v_s$ (km/s)
DW LVZ
EH45
b)
UCMref1 model
North: DW
South: DW
North: EH45
South: EH45
c)
NUCMref2 model

FIGURE 5.11

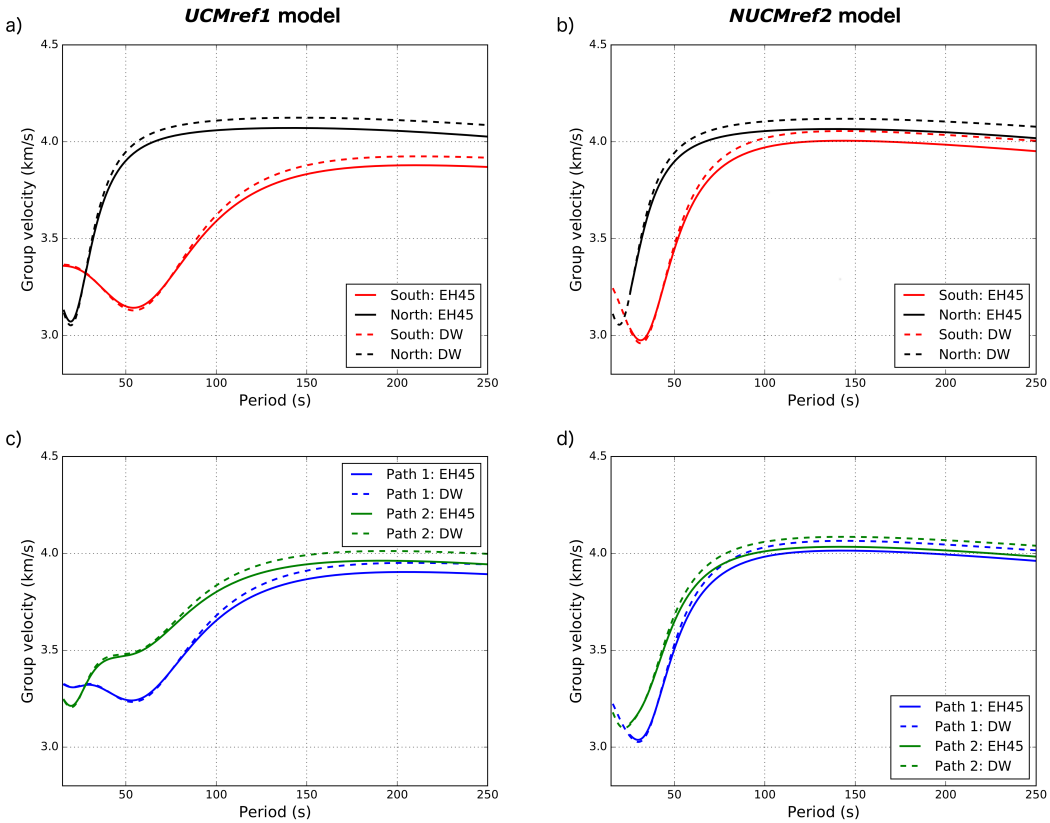


**FIGURE 5.12** – Rayleigh wave group velocities for the fundamental mode computed for the northern and southern structural models derived from the EH45 initial model given the crustal properties and temperature profiles of two reference crustal models : *UCMref1* on the left, *NUCMref2* on the right. Group velocities for surface waves traveling only in one hemisphere (in the north in black, in the south in red) are represented in (a) and (b). Average group velocities for surface waves traveling along the potential great circles path 1 (in blue) and path 2 (in green) are represented in (c) and (d) (see Figure 5.9a for the detailed paths).

# GENERAL CONCLUSION

To investigate the consequences of the Martian north/south prominent crustal dichotomy on its thermal evolution, we first searched for appropriate scaling parameters ($a_{rh}$ and $\beta^u$ here) to suitably describe the thermal evolution of a cooling planet in a stagnant lid regime with 1-D parametrized models. Although those scaling parameters are likely sensitive to the heating mode that evolves with time, we found that one set of $a_{rh}$ and $\beta^u$ can well retrieve the thermal evolution predicted by the 3-D dynamical models. Several combinations of $a_{rh}$ and $\beta^u$ can be used and represent a trade-off between the stagnant lid and the upper thermal boundary layer thicknesses. When considering the definition of the lid of *Reese et al.* (2005) in dynamical simulations, a best combination of $a_{rh} = 2.16$ and $\beta^u = 0.345$ is found for Mars, which remains valid when varying some critical parameters such as mantle aspect ratio, surface and internal temperatures, presence of a crust or pressure-dependence of the viscosity.

Using an appropriate scaling law for Mars, we searched for the north/south crustal parameters (thickness, density, thermal conductivity and enrichment factor) that could explain the evolution of the elastic lithosphere thickness and the observations of recent volcanic activity. We found that the elastic thickness estimates are fitted if $55-65$ % of the bulk radioelement content are in the crust, and mostly in the southern one ($43-51$ %). Our models also predict a dry mantle and a wet or dry crustal rheology today, which is consistent with an important mantle depletion in radioelements and volatiles. In most of our models, the southern crust is much thicker (up to three times) and equally or only slightly more enriched in radioelements than the northern one. Alternatively, some models predict a rather low density for the buried southern crust (up to 480 kg/m$^3$) and thus a smaller north/south contrast in crustal thickness. These models imply that a significant volume of felsic rocks are buried in the southern hemisphere. In this case the southern crust can be up to two times more enriched than the northern one. 3-D models accounting for the crustal properties of our best thermal models likely show a north/south asymmetric convection pattern : mantle downwellings are preferentially located in the south, whereas hot mantle plumes concentrate over time in the north. However, since mantle plumes are not well defined in our models, it has to be further investigated. At the present-day, all models predict large differences in the north /south thermal structures both in surface heat flux ($17.1-19.5$ mW/m$^2$ and $24.8-26.5$ mW/m$^2$, respectively) and lithospheric temperature profiles (difference of $170-304$ K in the shallow mantle).

We investigated the effect of the differences in crustal properties of our best models on surface wave velocities that will be recorded by the InSight mission. The largest differences in group velocity for Rayleigh waves traveling through the northern or the southern hemispheres are observed at periods sensitive to crustal properties ($\lesssim 100$ s). Velocities mainly depend on

north/south crustal thicknesses and, to a lesser extent, on their composition. The slight effect of the lithospheric temperatures is mainly observable at periods $> 50$ s and won't likely be detectable. Along a potential great circle path, although group velocities are influenced by the properties of the two hemispheres, they are more sensitive to those of the southern highlands that cover a higher area. If the northern hemisphere is not sampled enough, or if the contrast in crustal thickness between the two hemisphere is small ($\lesssim 20$ km), the northern crustal structure will be hard to define using surface-wave analysis only. However, complementary informations arising from the analysis of body-waves produced by local events in the north might help to constrain the northern crustal structure.

# OUTLOOK

## Further improvements for our models

— **Scaling law for core thermal evolution**

The scaling laws defined in chapter 3 well retrieved the thermal evolution of 3-D dynamical models (average temperature profile, stagnant lid thickness, CMB and surface heat flux). However, in some models (such as the case *Adiab* in section 4.1.a), a phase of core heating by the overlying hotter mantle is observed during the evolution. In this scenario, our models overestimate the CMB temperature and heat flux towards the core (see Figure 3.16b) since the equation 3.19 used for the lower TBL thickness computation is not appropriate anymore. A better parameterization needs thus to be found for the thermal evolution of the core when the CMB heat flux becomes negative.

— **Future constraints from InSight**

During this thesis, we developed a method that allows to determine suitable north/south crustal parameters given the available constraints that we have on Mars's thermal evolution, i.e. the evolution of the elastic lithosphere thickness estimates and the volcanic history. The InSight mission should soon provide additional information on both Mars's thermal state with the heat flux measurements of the $HP^3$ instrument and on the internal structure with the recording of seismic signals by SEIS. A further work could thus consist in accounting for such additional constraints (surface heat flux at the landing site in the north, northern or/and southern crustal thickness) in our Monte Carlo simulations.

— **Models coupling thermal and crustal evolution**

In our models we do not account for crustal formation by mantle partial melting and assume that the bulk of the crust is set up at the beginning of the simulations, and instantaneously formed in the north after the dichotomy-forming impact for the NUCM simulations. Using models coupling thermal and crustal evolution (e.g. *Hauck and Phillips*, 2002; *Breuer and Spohn*, 2006; *Morschhauser et al.*, 2011) would selfconsistently test the feasibility of our best NUCM and UCM cases in terms of crustal thickness and enrichment in radioelements. It would also provide an estimate of the mantle water depletion evolution, and thus on that of the mantle rheology.

— **3-D models accounting for lateral variations in crustal thickness**

To investigate the effect of our best crustal and thermal models on the Rayleigh wave group velocities that will be recorded by the mission InSight, we assume a phenomenological approach for which the dichotomy is modeled by two hemispheres with uniform properties

(lithospheric temperature, crustal thickness, density and composition). At the dichotomy boundary we, nonetheless, consider a transition zone divided into northern and southern sides to mimic the long-wavelength lateral variations in stagnant lid thickness between the two hemispheres. However, accounting for this north/south transition zone has almost no effect on the dispersion curves that we predict, since we assume the same crustal thickness and composition to that of the corresponding hemisphere.

A significant improvement would consist in accounting for the lateral variations in crustal thickness that are present at the dichotomy boundary and within each hemisphere due to, for instance, the presence of the large impact basins and huge volcanic provinces. This could be realized by computing a 3-D crustal thickness model for Mars given MOLA topography data and the predictions of our best UCM and NUCM models on the north/south average crustal densities and thicknesses. This model should, moreover, account for the lateral variations in temperature that are predicted by our thermal models (see the last part of the Outlooks' section). Such a 3-D crustal thickness model could be used in 3-D dynamical thermal models to provide estimates for the lateral variations in temperature (see for instance the models of *Plesa et al.*, 2016). By decomposing the surface wave path into more numerous surface elements $dS$ (see equation 5.4 in chapter 5), for which we have both the temperature profile and the crustal thickness, we might obtain more precise dispersion curve predictions. In particular, it would indicate if the crustal Airy phases that are well recognizable in our simplified approach -, at least for the southern hemisphere - would still be detectable by the SEIS instrument.

A 3-D thermal model accounting for lateral variations in crustal properties (thickness and enrichment factor) would also provide more reliable estimations of the convection patterns predicted by the best UCM and NUCM cases compared to those obtained when assuming uniform properties in a given hemisphere (Figures 4.12 and 4.13). In particular, it would allow to test the presence of stable mantle plumes at the dichotomy boundary below the Tharsis and Elysium regions.

## Stress at the dichotomy boundary

The present-day dichotomy boundary is characterized by a long wavelength change in topography marked by the presence of tectonic features that formed during the late Noachian or the Early Hesperian (e.g. *McGill and Dimitriou*, 1990; *Watters*, 2003a,b). This present-day north/south boundary results from the complex evolution of a poorly-known old boundary modified by subsequent tectonic, volcanic and erosion processes (e.g. *Watters et al.*, 2007). The distinct thermal structures of the northern and southern lithospheres predicted by our thermal models might also have played a role in the evolution of the dichotomy boundary. Indeed, the difference in temperature between the Martian hemispheres might lead to differential stresses at the dichotomy boundary that are due to potential different rates of contraction and expansion for the two hemispheres.

We have estimated the northern and southern planetary radius variations predicted by the *UCMref1* and *NUCMref2* cases. Such temporal radius variations can be computed given the volume changes associated with thermal expansion/contraction of the core and mantle (*Solomon*, 1977; *Tosi et al.*, 2013) :

$$\Delta T = \alpha_c (T_c(t) - T_{c_0}) \frac{R_c^3}{3R_p^2} + \frac{1}{R_p^2} \int_{R_c}^{R_p} \alpha_m (T_m(r,t) - T_{m_0}(r)) r^2 dr \tag{5.5}$$

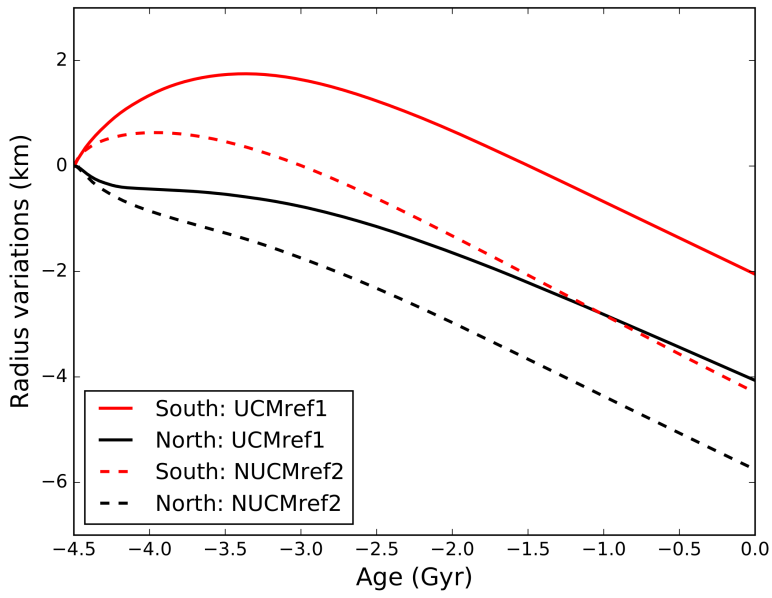


**FIGURE 5.13** – Time evolution of the planetary radius variations due to thermal expansion and contraction of the mantle and core in the northern (in black) and southern (in red) hemispheres of the *UCMref1* (solid lines) and *NUCMref2* (dashed lines) crustal models.

where $\alpha_c = 5.8 \times 10^{-5}$ K$^{-1}$ and $\alpha_m = 2 \times 10^{-5}$ K$^{-1}$ are the coefficients of thermal expansion of the core and the mantle, respectively.

For both the *UCMref1* and *NUCMref2* cases, the radius of the northern hemisphere decreases from the beginning of the evolution while an initial expansion is, in contrast, observed in the south. For the *UCMref1* case, an initial southern radius expansion of $\sim 2$ km is observed and takes place between 4.5 and 3.5 Gyr. For the colder southern hemisphere of the *NUCMref2* case, the radius increase is smaller ($\sim 0.7$ km) and ceases earlier at $\sim 4$ Gyr. After the initial phase of southern radius increase, a steady planetary contraction is observed in both hemispheres and the initial north/south difference in altitude due to thermal effects remains stable over time around values of $\sim 2$ km and $\sim 1.5$ km for the *UCMref1* and *NUCMref2* cases, respectively. However, those estimates of the north/south variations in planetary radius might be an upper bound since this effect is likely resisted by internal stresses within the lithosphere and, in particular, at the dichotomy boundary.

In our crustal models, the northern and southern crustal thicknesses are computed by assuming an isostatic equilibrium and a constant difference in altitude of $dh = 6$ km between the two hemispheres. This value of 6 km might represent an upper bound for the initial contrast in topography, since it does not account for the north/south differential expansion or contraction predicted by our thermal models. However, the present-day north/south difference in topography also depends on when the isostatic assumption becomes valid, since an equilibrium could take place late in the warm southern lithosphere. If the initial difference in altitude is smaller than that assumed in this study, it will likely have no impact on our predictions on the radioelement partition between the mantle and the northern and southern crusts. However, it would change the crustal thicknesses predicted by our best models, though they also depend on the crustal density.

The sustainability of the north/south difference in topography at the boundary represents another challenge for our crustal models. Indeed, lateral variations in crustal thickness lead to pressure gradients that can drive lateral flow in the lower crust of the highlands towards the colder lowlands. Such a process would decrease the difference in topography between the two hemispheres (*Nimmo and Stevenson*, 2001; *Nimmo*, 2005). *Nimmo and Stevenson* (2001) predicted that a value of 100 km might represent an upper bound for the maximal crustal thickness to explain the absence of viscous relaxation of the topography at the dichotomy boundary. However, since our models predict significantly hotter temperatures in the southern crust, lateral crustal flow are perhaps present for a lower value of the southern crustal thickness. A further work will thus consist in checking if our best crustal models are compatible with the absence of topographic relaxation at the dichotomy boundary.

## Gravity anomalies due to the north/south difference in temperature

Up to now, the crustal thickness models established for Mars from gravity and topography data (e.g. *Neumann et al.*, 2004; *Wieczorek*, 2007; *Goossens et al.*, 2017) do not account for lateral variations in temperature, though the thermal state directly conditions the density of the materials constituting a layer and, thus, the gravity signal. In our models, we predict large north/south variations in lithospheric temperatures, up to $\sim 170-300$ K, which might have a non negligible influence on the gravity signal. We estimate here the gravity anomaly induced by the north/south differences in temperature predicted by two of our best thermal models (*UCMref1* and *NUCMref2*, see Table 4.5 in chapter 4). For this purpose we assume that the southern lithosphere can be represented by an infinitely large plateau that shows a density anomaly $\Delta\rho = \alpha\rho(r)(T^S(r) - T^N(r))$ compared to the northern lithosphere. The gravity anomaly $\Delta\gamma$ of such a structure is given by :

$$\Delta\gamma \sim 2\pi G \int_{D_l^S}^{0} \alpha\rho(z)(T^S(z) - T^N(z))dz \tag{5.6}$$

where $G = 6.67 \times 10^{-11}$ m$^3$ kg$^{-1}$ s$^{-2}$ is the gravitational constant, $T^N$ and $T^S$ the northern and southern temperature profiles, respectively. For a thermal expansion value of $\alpha = 2 \times 10^{-5}$ K$^{-1}$, we found that the *UCMref1* and *NUCMref2* cases predict average gravity anomalies of $\sim -330$ mGal and $\sim -230$ mGal, respectively, linked to the north/south differences in temperature. Since those values represent $\sim 1/4$ of the total range of gravity anomaly values that are observed on Mars's gravity field (see Figure 1.6b), lateral variations in thermal structure have to be considered to compute a suitable crustal thickness model from gravity and topography data. Conversely, a further improvement for our models would consist in accounting for such a thermal effect on the density when constraining the crustal properties (density and thickness) that are required to fit the constraints on elastic thickness estimates and recent melt formation.

# LIST OF NOTATIONS

**Acronyms**

| | |
|---|---|
| *CMB* | Core-Mantle Boundary |
| *CRISM* | Compact Reconnaissance Imaging Spectrometer for Mars |
| *DLR* | Deutsches Zentrum für Luft und Raumfahrt |
| *ESA* | European Space Agency |
| *FU* | Freie Universitaet |
| *GRS* | Gamma-Ray Spectrometer |
| *HiRISE* | High Resolution Imaging Science Experiment |
| $HP^3$ | Heat flow and Physical Properties Package |
| *HRSC* | High Resolution Stereo Camera |
| *InSight* | Interior Exploration Using Seismic Investigations, Geodesy and Heat Transport |
| *JPL* | Jet Propulsion Laboratory |
| *KREEP* | Potassium - Rare Earth Elements - Phosphor |
| *LVZ* | Low Velocity Zone |
| *MARSIS* | Mars Advanced Radar for Subsurface and Ionospheric Sounding |
| *MGS* | Mars Global Surveyor |
| *MOLA* | Mars Orbiter Laser Altimeter |
| *MRO* | Mars Reconnaissance Orbiter |
| *NASA* | National Aeronautics and Space Administration |
| *NUCM* | Non-Uniform Crustal Model |
| *NUCM*2 | Non-Uniform Crustal Model for which the enrichment factor of the northern crust is allowed to vary |
| *PBR* | Fraction of the bulk radioelement content contained in the crust |
| *pdf* | Probability density function |
| *PREM* | Preleminary Reference Earth Model |
| *R*1 | First surface wave group arrival |
| *R*2 | Second surface wave group arrival |
| *R*3 | Third surface wave group arrival |
| *RISE* | Rotation and Interior Structure Experiment |
| *SEIS* | Seismic Experiment for Interior Structures |
| *SHF* | Surface heat flux |

| | |
|---|---|
| $SLT$ | Stagnant lid thickness |
| $SNC$ | Shergottite - Nakhlite - Chassignite |
| $SP$ | Short Period (InSight seismometer) |
| $TBL$ | Thermal Boundary Layer |
| $THEMIS$ | Thermal Emission Imaging System |
| $UCM$ | Uniform Crustal Model |
| $USGS$ | United States Geological Survey |
| $VBB$ | Very Broad Band (InSight seismometer) |

**Parameters**

| | |
|---|---|
| $\alpha$ | Thermal expansion coefficient [$K^{-1}$] |
| $\alpha_c$ | Thermal expansion coefficient of the core [$K^{-1}$] |
| $\alpha_m$ | Thermal expansion coefficient of the mantle [$K^{-1}$] |
| $\beta$ | Exponant for scaling laws of mantle convection |
| $\beta^c$ | Exponant for the lower thermal boundary layer thickness computation |
| $\beta^u$ | Exponant for the upper thermal boundary layer thickness computation |
| $\beta_m$ | Exponant for the approach below the lid |
| $\beta_t$ | Exponant for the whole layer approach |
| $\Delta\gamma$ | Gravity anomaly [Gal] |
| $\Delta T$ | Temperature difference across the shell [K] |
| $\Delta T^c$ | Temperature difference used to compute the lower boundary layer thickness [K] |
| $\Delta T^u$ | Temperature difference used to compute the upper boundary layer thickness [K] |
| $\Delta T_i$ | Impact temperature increase [K] |
| $\Delta T_{conv}$ | Temperature difference across the convecting mantle [K] |
| $\Delta T_{rh}$ | Rheological temperature difference across the upper thermal boundary layer [K] |
| $\Delta T_v$ | Viscous temperature scale [K] |
| $\delta$ | Geometric exposant |
| $\delta^c$ | Lower thermal boundary layer thickness [m] |
| $\delta^u$ | Upper thermal boundary layer thickness [m] |
| $\dot{\varepsilon}$ | Strain rate due to mantle convection [$s^{-1}$] |
| $\dot{\varepsilon}_{cap}$ | Strain rate due to glacial loading [$s^{-1}$] |
| $\varepsilon_c$ | Ratio between the average core temperature and core-mantle boundary temperature |
| $\varepsilon_m$ | Ratio between the average temperature of the convecting mantle and the temperature at the top of the convecting mantle |
| $\eta$ | Viscosity [Pa s] |
| $\eta'$ | Dimensionless viscosity |
| $\eta_0$ | Reference viscosity [Pa s] |

| | |
|---|---|
| $\gamma$ | Exponent generally equals to $1+\beta$ |
| $\kappa$ | Mantle thermal diffusivity [$m^2$ $s^{-1}$] |
| $\Lambda^N$ | Enrichment factor of the northern crust |
| $\Lambda_1^S$ | Enrichment factor of the upper southern crust |
| $\Lambda_2^S$ | Enrichment factor of the lower southern crust |
| $\lambda_i$ | Decay constant for the radiogenic species [s] |
| $\rho^N$ | Density of the northern crust [kg $m^{-3}$] |
| $\rho_1^S$ | Density of the upper southern crust [kg $m^{-3}$] |
| $\rho_2^S$ | Density of the lower southern crust [kg $m^{-3}$] |
| $\rho_c$ | Density of the core [kg $m^{-3}$] |
| $\rho_m$ | Density of the mantle [kg $m^{-3}$] |
| $\sigma_B$ | Brittle deformation [Pa] |
| $\sigma_D$ | Intracrystalline ductile creep [Pa] |
| $\sigma_V$ | Effective vertical stress [Pa] |
| $\sigma_y$ | Bounding stress [Pa] |
| $\theta$ | Frank-Kamenetskii parameter |
| $\vec{e_r}$ | Radial unit vector |
| $\vec{v}$ | Velocity vector |
| $A$ | Activation energy [J $mol^{-1}$] |
| $a$ | Constant for scaling laws of mantle convection |
| $a_m$ | Constant for scaling laws of mantle convection |
| $A_n$ | Activation energy for a non-linear rheology [J $mol^{-1}$] |
| $A_c$ | Surface of the core [$m^2$] |
| $A_m$ | Surface of the mantle [$m^2$] |
| $a_{rh}$ | Proportionality coefficient for scaling laws of mantle convection |
| $B$ | Rheological prefactor [$Pa^{-n}s-1$] |
| $C$ | Proportionality coefficient for scaling laws of mantle convection |
| $C_c$ | Heat capacity of the core [J $kg^{-1}$ $K^{-1}$] |
| $C_m$ | Heat capacity of the mantle [J $kg^{-1}$ $K^{-1}$] |
| $D$ | Thickness of the shell [m] |
| $d^N$ | Thickness of the northern crust [m] |
| $d^S$ | Thickness of the southern crust [m] |
| $d_1^S$ | Thickness of the upper southern crust [m] |
| $d_2^S$ | Thickness of the lower southern crust [m] |
| $D_l$ | Stagnant lid thickness [m] |
| $d_r$ | Regolith thickness [m] |
| $D_{conv}$ | Thickness of the convecting mantle [m] |
| $dh$ | North-south mean altitude difference [m] |

| | |
|---|---|
| $F^n$ | Surface fraction of the northern hemisphere |
| $G$ | Gravitational constant [$m^3\ kg^{-1}\ s^{-2}$] |
| $g$ | Gravity [$m\ s^{-2}$] |
| $g^c$ | Gravity at the core-mantle boundary [$m\ s^{-2}$] |
| $g^u$ | Surface gravity [$m\ s^{-2}$] |
| $H$ | Total thickness of the stagnant lid and the upper TBL [m] |
| $j$ | Layers of the stagnant lid, i.e. the regolith, the upper crust, the lower crust and the lithospheric mantle |
| $k$ | Thermal conductivity [$W\ m^{-1}\ K^{-1}$] |
| $k^N$ | Thermal conductivity of the northern crust [$W\ m^{-1}\ K^{-1}$] |
| $k_1^S$ | Thermal conductivity of the upper southern crust [$W\ m^{-1}\ K^{-1}$] |
| $k_2^S$ | Thermal conductivity of the lower southern crust [$W\ m^{-1}\ K^{-1}$] |
| $k_2$ | Love number |
| $k_m$ | Mantle thermal conductivity [$W\ m^{-1}\ K^{-1}$] |
| $k_r$ | Regolith thermal conductivity [$W\ m^{-1}\ K^{-1}$] |
| $M_0$ | Seismic moment [N m] |
| $M_{silicate}$ | Mass of the silicate bulk [kg] |
| $M_w$ | Moment magnitude |
| $N$ | Total number of time steps in thermal simulations |
| $n$ | Stress exponent [K] |
| $N/S$ | Northern (N) and southern (S) hemispheres |
| $N_s$ | Number of seismic events per Earth year |
| $Nu_m$ | Nusselt number below the lid |
| $Nu_{surf}$ | Nusselt number at the surface |
| $P$ | Hydrostatic pressure [Pa] |
| $p$ | Dynamical pressure [Pa] |
| $P_r$ | Reference pressure (seismological models) [Pa] |
| $P_{ref}$ | Reference pressure (thermal models) [Pa] |
| $Q$ | Internal heating rate [$W\ kg^{-1}$] |
| $Q_0$ | Initial heating rate [$W\ kg^{-1}$] |
| $Q_{4.5}$ | Present-day heating rate [$W\ kg^{-1}$] |
| $Q_{cr}$ | Heat production in the crust [$W\ kg^{-1}$] |
| $q_c$ | Heat flux at the core-mantle boundary [$W\ m^{-2}$)] |
| $q_l$ | Heat flux in the stagnant lid [$W\ m^{-2}$)] |
| $q_m$ | Heat flux at the base of the stagnant lid [$W\ m^{-2}$)] |
| $q_s$ | Heat flux at the surface [$W\ m^{-2}$)] |
| $R$ | Gas constant [$J\ K^{-1}\ mol^{-1}$] |
| $r$ | Radial distance [m] |

| | |
|---|---|
| $R_c$ | Radius of the core [m] |
| $R_l$ | Radius at the lid base [m] |
| $R_p$ | Planetary radius [m] |
| $Ra^c_{crit}$ | Critical Rayleigh number for the lower thermal boundary layer |
| $Ra^c_{rh}$ | Rheological Rayleigh number for the lower thermal boundary layer |
| $Ra^u_{crit}$ | Critical Rayleigh number for the upper thermal boundary layer |
| $Ra^u_{rh}$ | Rheological Rayleigh number for the upper thermal boundary layer |
| $Ra_i$ | Internal Rayleigh number |
| $Ra_Q$ | Rayleigh-Roberts number |
| $S$ | Length of a northern or southern portion along a great circle [m] |
| $T$ | Non-dimensional temperature |
| $t$ | Time [s] |
| $T_e$ | Elastic thickness [m] |
| $T_b$ | Temperature at the base of the convecting mantle [K] |
| $T_{c_0}$ | Initial temperature at the core-mantle boundary [K] |
| $t_{char}$ | Characteristic time for radioelement decay [s] |
| $T_c$ | Temperature at the core-mantle boundary [K] |
| $T_{e,c}$ | Elastic thickness of the crust [m] |
| $T_{e,m}$ | Elastic thickness of the lithospheric mantle [m] |
| $T_l$ | Temperature at the base of the stagnant lid [K] |
| $T_{m_0}$ | Initial temperature of the mantle [K] |
| $T_m$ | Temperature at the top of the convecting mantle [K] |
| $T_{plume}$ | Plume temperature [K] |
| $T_{ref}$ | Reference temperature (thermal models) [K] |
| $T_r$ | Reference temperature (seismological models) [K] |
| $T_{solidus}$ | Solidus temperature [K] |
| $T_s$ | Temperature at the surface [K] |
| $V$ | Activation volume [$m^3$ $mol^{-1}$] |
| $v_g$ | Surface wave group velocity [m $s^{-1}$] |
| $v_p$ | Compressional velocity [m $s^{-1}$] |
| $v_s$ | Shear velocity [m $s^{-1}$] |
| $V_c$ | Volume of the core [$m^3$] |
| $v_{g_{local}}$ | Local surface wave group velocity [m $s^{-1}$] |
| $V_m$ | Volume of the mantle [$m^3$] |
| $v_{p_0}$ | Compressional velocity at the reference pressure $P_r$ and temperature $T_r$ [m $s^{-1}$] |
| $v_{s_0}$ | Shear velocity at the reference pressure $P_r$ and temperature $T_r$ [m $s^{-1}$] |
| $V_{silicate}$ | Volume of the silicate bulk [$m^3$] |
| $W_{error}$ | Weighted error [%] |

| | |
|---|---|
| $W_{scale}$ | Weighted scale |
| $z$ | Depth [m] |

# BIBLIOGRAPHY


Abe, Y. (1997), Thermal and chemical evolution of the terrestrial magma ocean, *Physics of the Earth and Planetary Interiors*, *100*, 27–39, doi :10.1016/S0031-9201(96)03229-3. 24

Abe, Y., and T. Matsui (1985), The formation of an impact-generated h2o atmosphere and its implications for the early thermal history of the earth, *Journal of Geophysical Research : Solid Earth*, (S02), doi :10.1029/JB090iS02p0C545. 24

Acuna, M., J. Connerney, R. Lin, D. Mitchell, C. Carlson, J. McFadden, K. Anderson, H. Rème, C. Mazelle, D. Vignes, et al. (1999), Global distribution of crustal magnetization discovered by the mars global surveyor mag/er experiment, *Science*, *284*, 790–793, doi : 10.1126/science.284.5415.790. 44, 45

Agee, C., N. Wilson, F. McCubbin, K. Ziegler, V. Polyak, Z. Sharp, Y. Asmerom, M. Nunn, R. Shaheen, M. Thiemens, A. Steele, M. Fogel, R. Bowden, M. Glamoclija, Z. Zhang, and S. Elardo (2013), Unique Meteorite from Early Amazonian Mars : Water-Rich Basaltic Breccia Northwest Africa 7034, *Science*, *339*, 780–785, doi :10.1126/science.1228858. 34, 112

Anderson, D. L. (1989), *Theory of the Earth*. 164

Anderson, D. L., W. Miller, G. Latham, Y. Nakamura, M. Toksöz, A. Dainty, F. Duennebier, A. R. Lazarewicz, R. Kovach, and T. Knight (1977), Seismology on mars, *Journal of Geophysical Research*, *82*, 4524–4546, doi :10.1029/JS082i028p04524. 156, 157

Andrews-Hanna, J., M. Zuber, and W. Banerdt (2008), The Borealis basin and the origin of the martian crustal dichotomy, *Nature*, *453*, 1212–1215, doi :10.1038/nature07011. 15, 18, 21, 22, 23, 24, 25, 26, 27, 31, 33, 111, 112, 114, 115, 119, 175, 177

Aoudjehane, H., G. Avice, J.-A. Barrat, O. Boudouma, G. Chen, M. Duke, I. Franchi, J. Gattacceca, M. Grady, R. Greenwood, C. Herd, R. Hewins, A. Jambon, B. Marty, P. Rochette, C. Smith, V. Sautter, A. Verchovsky, P. Weber, and B. Zanda (2012), Tissint Martian Meteorite : A Fresh Look at the Interior, Surface, and Atmosphere of Mars, *Science*, *338*, 785–788, doi :10.1126/science.1224514. 34, 112

Arkani-Hamed, J., and P. Olson (2010), Giant impacts, core stratification, and failure of the Martian dynamo, *Journal of Geophysical Research Planets*, *115*, E07,012, doi :10.1029/2010JE003579. 21, 124

Ashwal, L. D. (2010), The temporality of anorthosites, *The Canadian Mineralogist*, *48*, 711–728, doi :10.3749/canmin.48.4.711. 34

Bandfield, J., C. Edwards, D. Montgomery, and B. Brand (2013), The dual nature of the martian crust : Young lavas and old clastic materials, *Icarus*, *222*, 188–199, doi :10.1016/j.icarus.2012.10.023. 14, 33, 34, 43, 54, 113, 124, 125

Baratoux, D., M. Toplis, M. Monnereau, and O. Gasnault (2011), Thermal history of Mars inferred from orbital geochemistry of volcanic provinces, *Nature*, *472*, 338–341, doi :10.1038/nature09903. 34, 44, 112

Baratoux, D., H. Samuel, C. Michaut, M. Toplis, M. Monnereau, M. Wieczorek, R. Garcia, and K. Kurita (2014), Petrological constraints on the density of the Martian crust, *Journal of Geophysical Research Planets*, *119*, 1707–1727, doi :10.1002/2014JE004642. 14, 30, 31, 36, 43, 45, 54, 113, 125, 136, 142

Barnett, D., and F. Nimmo (2002), Strength of Faults on Mars from MOLA Topography, *Icarus*, *157*, 34–42, doi :10.1006/icar.2002.6817. 50, 110

Belleguic, V., P. Lognonné, and M. Wieczorek (2005), Constraints on the Martian lithosphere from gravity and topography data, *Journal of Geophysical Research*, *110*, E11,005, doi :10.1029/2005JE002437. 49, 54, 110

Bibring, J.-P., Y. Langevin, F. Poulet, A. Gendrin, B. Gondet, M. Berthé, A. Soufflot, P. Drossart, M. Combes, G. Bellucci, et al. (2004), Perennial water ice identified in the south polar cap of mars, *Nature*, *428*, 627, doi :10.1038/nature02461. 10

Bills, B. G., G. A. Neumann, D. E. Smith, and M. T. Zuber (2005), Improved estimate of tidal dissipation within mars from mola observations of the shadow of phobos, *Journal of Geophysical Research : Planets*, *110*(E7), doi :10.1029/2004JE002376. 45, 162

Blichert-Toft, J., J. D. Gleason, P. Télouk, and F. Albarède (1999), The lu–hf isotope geochemistry of shergottites and the evolution of the martian mantle–crust system, *Earth and Planetary Science Letters*, *173*, 25–39, doi :10.1016/S0012-821X(99)00222-8. 24

Booker, J., and K. Stengel (1978), Further thoughts on convective heat transport in a variable-viscosity fluid, *Journal of Fluids Mechanics*, *86*, 289–291, doi :10.1017/S0022112078001135. 59

Borg, L. E., L. E. Nyquist, L. A. Taylor, H. Wiesmann, and C.-Y. Shih (1997), Constraints on martian differentiation processes from rb-sr and sm-nd isotopic analyses of the basaltic shergottite que 94201, *Geochimica et Cosmochimica Acta*, *61*, 4915–4931, doi :10.1016/S0016-7037(97)00276-7. 31

Borg, L. E., L. E. Nyquist, H. Wiesmann, C.-Y. Shih, and Y. Reese (2003), The age of dar al gani 476 and the differentiation history of the martian meteorites inferred from their radiogenic isotopic systematics, *Geochimica et Cosmochimica Acta*, *67*, 3519–3536, doi :10.1016/S0016-7037(03)00094-2. 31

Bormann, P., E. Engdahl, and R. Kind (2009), *Seismic Wave Propagation and Earth models*, 1–70 pp., doi :10.2312/GFZ.NMSOP_r1_ch2. 158, 159, 169, 178

Bottke, W., and J. Andrews-Hanna (2017), A post-accretionary lull in large impacts on early Mars, *Nature Geoscience*, *10*, 344–348, doi :10.1038/ngeo2937. 112

Bouley, S., D. Baratoux, J. Vaubaillon, A. Mocquet, M. Le Feuvre, F. Colas, Z. Benkhaldoun, A. Daassou, M. Sabil, and P. Lognonné (2012), Power and duration of impact flashes on the moon : Implication for the cause of radiation, *Icarus*, *218*, 115–124, doi :10.1016/j.icarus.2011.11.028. 158

Boynton, W., W. Feldman, S. Squyres, T. Prettyman, J. Brückner, L. Evans, R. Reedy, R. Starr, J. Arnold, D. Drake, et al. (2002), Distribution of hydrogen in the near surface of mars : Evidence for subsurface ice deposits, *science*, *297*, 81–85, doi :10.1126/science.1073722. 10

Boynton, W., G. Taylor, L. G. Evans, R. Reedy, R. Starr, D. Janes, K. Kerry, D. Drake, K. Kim, R. Williams, et al. (2007), Concentration of h, si, cl, k, fe, and th in the low- and mid-latitude regions of mars, *Journal of Geophysical Research : Planets*, *112*, doi :10.1029/2007JE002887. 36

Brandon, A., R. Walker, J. Morgan, and G. Goles (2000), Re-os isotopic evidence for early differentiation of the martian mantle, *Geochimica et Cosmochimica Acta*, *64*, 4083–4095, doi :10.1016/S0016-7037(00)00482-8. 53

Brasser, R., and S. Mojzsis (2017), A colossal impact enriched Mars' mantle with noble metals, *Geophysical Research Letters*, *44*, 5978—-5985, doi :10.1002/2017GL074002. 112

Breuer, D., and W. Moore (2015), Dynamics and thermal history of the terrestrial planets, the moon, and io, *Physics of Terrestrial Planets and Moons*, *10*, 255–305, doi :10.1016/B978-0-444-53802-4.00166-4. 96

Breuer, D., and T. Spohn (2003), Early plate tectonics versus single-plate tectonics on Mars : Evidence from magnetic field history and crust evolution, *Journal of Geophysical Research*, *108*, 5072, doi :10.1029/2002JE001999. 35, 45

Breuer, D., and T. Spohn (2006), Viscosity of the Martian mantle and its initial temperature : Constraints from crust formation history and the evolution of the magnetic field, *Planetary and Space Science*, *54*, 153–169, doi :10.1016/j.pss.2005.08.008. 36, 46, 127, 189

Breuer, D., D. A. Yuen, and T. Spohn (1997), Phase transitions in the martian mantle : Implications for partially layered convection, *Earth and Planetary Science Letters*, *148*, 457–469, doi :10.1016/S0012-821X(97)00049-6. 23, 48

Breuer, D., A.-C. Plesa, N. Tosi, and M. Grott (2016), Water in the Martian interior-The geodynamical perspective, *Meteoritics and Planetary Science*, *51*, 1959–1992, doi :10.1111/maps.12727. 73, 85, 96, 142

Brown, C. D., and R. J. Phillips (2000), Crust-mantle decoupling by flexure of continental lithosphere, *Journal of Geophysical Research : Solid Earth*, *105*, 13,221–13,237, doi :10.1029/2000JB900069. 50

Brückner, J., G. Dreibus, R. Rieder, and H. Wänke (2003), Refined data of alpha proton x-ray spectrometer analyses of soils and rocks at the mars pathfinder site : Implications for surface chemistry, *Journal of Geophysical Research : Planets*, *108*, doi :10.1029/2003JE002060. 35

Bullen, K. E., K. E. Bullen, and B. A. Bolt (1985), *An introduction to the theory of seismology*, doi :doi.org/10.1111/j.1365-246X.1986.tb01083.x. 159

Bunge, H.-P., M. A. Richards, and J. R. Baumgardner (1996), Effect of depth-dependent viscosity on the planform of mantle convection, *Nature*, *379*, 436, doi :10.1038/379436a0. 23

Burov, E., and M. Diament (1995), The effective elastic thickness ($t_e$) of continental lithosphere : What does it really mean ?, *Journal of Geophysical Research*, *100*, 3905–3927, doi :10.1029/94JB02770. 49, 122

Byerlee, J. (1978), Friction of Rocks, *J. PAGEOPH*, *116*, 615–626, doi :10.1007/BF00876528. 121

Byrne, P. K., L. R. Ostrach, C. I. Fassett, C. R. Chapman, B. W. Denevi, A. J. Evans, C. Klimczak, M. E. Banks, J. W. Head, and S. C. Solomon (2016), Widespread effusive volcanism on mercury likely ended by about 3.5 ga, *Geophysical Research Letters*, *43*, 7408–7416, doi :10.1002/2016GL069412. 95

Caldwell, J., and D. Turcotte (1979), Dependence of the thickness of the elastic oceanic lithosphere on age, *Journal of Geophysical Research : Solid Earth*, *84*, 7572–7576, doi :10.1029/JB084iB13p07572. 49

Canup, R. M. (2004), Simulations of a late lunar-forming impact, *Icarus*, *168*, 433–456, doi :10.1016/j.icarus.2003.09.028. 45

Canup, R. M. (2008), Accretion of the earth, *Philosophical Transactions of the Royal Society of London A : Mathematical, Physical and Engineering Sciences*, *366*, 4061–4075, doi :10.1098/rsta.2008.0101. 24

Caristan, Y. (1982), The transition from high temperature creep to fracture in Maryland diabase, *Journal of Geophysical Research*, *87*, 6781–6790, doi :10.1029/JB087iB08p06781. 122, 123

Carr, M. (1996), Water on mars, 229 pp. 43

Carr, M. H. (1995), The martian drainage system and the origin of valley networks and fretted channels, *Journal of Geophysical Research : Planets*, *100*, 7479–7507, doi :10.1029/95JE00260. 10

Carr, M. H., and J. W. Head (2003), Oceans on mars : An assessment of the observational evidence and possible fate, *Journal of Geophysical Research : Planets*, *108*(E5), doi :10.1029/2002JE001963. 10

Carter, J., and F. Poulet (2013), Ancient plutonic processes on Mars inferred from the detection of possible anorthositic terrains, *Nature Geosci*, *6*, 1008–1012, doi :10.1038/NGEO1995. 14, 31, 33, 35, 36, 43, 54, 112, 113, 125

Chen, J., and G. Wasserburg (1986), Formation ages and evolution of shergotty and its parent planet from u-th-pb systematics, *Geochimica et Cosmochimica Acta*, *50*, 955–968, doi :10.1016/0016-7037(86)90376-5. 31

Choblet, G. (2012), On the scaling of heat transfer for mixed heating convection in a spherical shell, *Physics of the Earth and Planetary Interiors*, *206*, 31–42, doi :10.1016/j.pepi.2012.06.007. 95

Choblet, G., and E. Parmentier (2009), Thermal Convection Heated both Volumetrically and from Below : Implications for Predictions of Planetary Evolution., *Physics of the Earth and Planetary Interiors*, *173*, pp.290, doi :10.1016/j.pepi.2009.01.005. 95

Choblet, G., and C. Sotin (2000), 3d thermal convection with variable viscosity : can transient cooling be described by a quasi-static scaling law ?, *Physics of the Earth and Planetary Interiors*, *119*(3-4), 321–336, doi :10.1016/S0031-9201(00)00136-9. 72, 96

Choblet, G., and C. Sotin (2001), Early transient cooling of mars, *Geophysical research letters*, *28*(15), 3035–3038, doi :10.1029/2001GL012896. 72

Christensen, P. (1983), Convection in a variable-viscosity fluid : Newtonian versus power-law rheology, *Earth and Planetary Science Letters*, *64*, 153–162, doi :10.1016/0012-821X(83)90060-2. 63, 118

Christensen, P., J. Bandfield, R. Clark, K. Edgett, V. Hamilton, T. Hoefen, H. Kieffer, R. Kuzmin, M. Lane, M. Malin, et al. (2000), Detection of crystalline hematite mineralization on mars by the thermal emission spectrometer : Evidence for near-surface water, *Journal of Geophysical Research : Planets*, *105*, 9623–9642, doi :10.1029/1999JE001093. 10

Christensen, P., H. McSween, Jr, J. Bandfield, S. Ruff, A. Rogers, V. Hamilton, N. Gorelick, M. Wyatt, B. Jakosky, H. Kieffer, M. Malin, and J. Moersch (2005), Evidence for magmatic evolution and diversity on Mars from infrared observations, *Nature*, *436*, 504–509, doi :10.1038/nature03639. 34, 112

Christensen, U. (1984), Heat transport by variable viscosity convection and implications for the Earth's thermal evolution, *Physics of the Earth and Planetary Interiors*, *35*, 264–282, doi :10.1016/0031-9201(84)90021-9. 59, 61

Christensen, U., and D. Yuen (1985), Layered Convection induced by Phase Transitions, *Journale of Geophysical Research Atmospheres*, *90*, 10,291–10,300, doi :10.1029/JB090iB12p10291. 63, 99

Citron, R. I., M. Manga, and E. Tan (2018), A hybrid origin of the martian crustal dichotomy : Degree-1 convection antipodal to a giant impact, *Earth and Planetary Science Letters*, *491*, 58–66, doi :10.1016/j.epsl.2018.03.031. 14, 27, 48, 53, 149

Clauser, C., and E. Huenges (1995), Thermal conductivity of rocks and minerals, *In : Ahrens, T. J. (Ed.), Rock Physics & Phase Relations : A Handbook of Physical Constants, American Geophysical Union*, pp. 105–126, doi :10.1029/RF003p0105. 125

Clifford, S. M., and T. J. Parker (2001), The evolution of the martian hydrosphere : Implications for the fate of a primordial ocean and the current state of the northern plains, *Icarus*, *154*, 40–79, doi :10.1006/icar.2001.6671. 10

Clinton, J. F., D. Giardini, P. Lognonné, B. Banerdt, M. van Driel, M. Drilleau, N. Murdoch, M. Panning, R. Garcia, D. Mimoun, et al. (2017), Preparing for insight : An invitation to participate in a blind test for martian seismicity, *Seismological Research Letters*, *88*, 1290–1302, doi :10.1785/0220170094. 162

Connerney, J., M. Acuna, P. J. Wasilewski, N. F. Ness, H. Reme, C. Mazelle, D. Vignes, R. Lin, D. Mitchell, and P. Cloutier (1999), Magnetic lineations in the ancient crust of mars, *Science*, *284*, 794–798, doi :10.1126/science.284.5415.794. 26

Connerney, J., M. Acuña, N. Ness, G. Kletetschka, D. Mitchell, R. Lin, and H. Reme (2005), Tectonic implications of Mars crustal magnetism, *Proc. Natl. Acad. Sci. USA*, *102*, 14,970–14,975, doi :10.1073/pnas.0507469102. 44

Darwin, G. (1882), *A numerical estimate of the rigidity of the Earth*. 155

Davaille, A., and C. Jaupart (1993), Transient high-Rayleigh-number thermal convection with large viscosity variations, *J. Fluid Mech*, *253*, 141–166, doi :10.1017/S0022112093001740. 59, 60, 61, 66, 68, 70, 88, 94, 119

Davaille, A., and C. Jaupart (1994), Onset of thermal convection in fluids with temperature-dependent viscosity : Application to the oceanic mantle, *Journal of Geophysical Research*, *99*, 19,853–19,866, doi :10.1029/94JB01405. 60, 69, 88

Davies, G. (1980), Thermal Histories of Convective Earth Models and Constraints on Radiogenic Heat Production in the Earth, *Journal of Geophysical Research*, *85*, 2517–2530, doi : 10.1029/JB085iB05p02517. 59

Debaille, V., A. Brandon, C. O'Neill, Q.-Z. Yin, and B. Jacobsen (2009), Early martian mantle overturn inferred from isotopic composition of nakhlite meteorites, *Nature Geoscience*, *2*, 548–552, doi :10.1038/ngeo579. 20, 25

Debayle, E., and M. Sambridge (2004), Inversion of massive surface wave data sets : model construction and resolution assessment, *Journal of Geophysical Research : Solid Earth*, *109*, doi :10.1029/2003JB002652. 174

Deit, L. L., E. Hauber, F. Fueten, M. Pondrelli, A. P. Rossi, and R. Jaumann (2013), Sequence of infilling events in gale crater, mars : Results from morphology, stratigraphy, and mineralogy, *Journal of Geophysical Research : Planets*, *118*, 2439–2473, doi :10.1002/2012JE004322. 35

Deschamps, F., and C. Sotin (2000), Inversion of two-dimensional numerical convection experiments for a fluid with a strongly temperature-dependent viscosity, *Geophysical Journal International*, *143*, 204–218, doi :10.1046/j.1365-246x.2000.00228.x. 61, 68, 70, 73, 76, 77, 78, 88, 90, 94, 118

Deschamps, F., C. Yao, P. Tackley, and C. Sanchez-Valle (2012), High Rayleigh number thermal convection in volumetrically heated spherical shells, *Journal of Geophysical Research*, *117*, E09,006, doi :10.1029/2012JE004090. 57, 59

Doin, M.-P., L. Fleitout, and U. Christensen (1997), Mantle convection and stability of depleted and undepleted continental lithosphere, *Journal of Geophysical Research, Solid Earth*, *102*, 2771—-2787, doi :10.1029/96JB03271. 61, 69, 94

Dreibus, G., and H. Wanke (1985), Mars, a volatile-rich planet, *Meteoritics*, *20*, 367–381. 162, 163, 181, 184

Dumoulin, C., M.-P. Doin, and L. Fleitout (1999), Heat transport in stagnant lid convection with temperature- and pressure-dependent Newtonian or non-Newtonian rheology, *Journal of Geophysical Research*, *104*, 12,759–12,778, doi :10.1029/1999JB900110. 61, 69

Durham, W., and C. Goetze (1977a), Plastic flow of oriented single crystals of olivine : 1. Mechanical data, *Journal of Geophysical Research*, *82*, 5737–5753, doi :10.1029/JB082i036p05737. 122

Durham, W., and C. Goetze (1977b), A comparison of the creep properties of pure forsterite and iron-bearing olivine, *Tectonophysics*, *40*, 15–18, doi :10.1016/0040-1951(77)90063-4. 122

Dziewonski, A. M., and D. L. Anderson (1981), Preliminary reference earth model, *Physics of the earth and planetary interiors*, *25*, 297–356, doi :10.1016/0031-9201(81)90046-7. 162

Elkins-Tanton, L., E. Parmentier, and P. Hess (2003), Magma ocean fractional crystallization and cumulate overturn in terrestrial planets : Implications for Mars, *Meteoritics and Planetary Science*, *38*, 1753–1771, doi :10.1111/j.1945-5100.2003.tb00013.x. 14, 20, 24, 25, 45, 46, 123, 136

Elkins-Tanton, L., P. Hess, and E. Parmentier (2005), Possible formation of ancient crust on Mars through magma ocean processes, *Journal of Geophysical Research*, *110*, E12S01, doi :10.1029/2005JE002480. 25, 35, 45, 46, 111, 123

Elkins-Tanton, L. T. (2008), Linked magma ocean solidification and atmospheric growth for earth and mars, *Earth and Planetary Science Letters*, *271*, 181–191, doi :10.1016/j.epsl.2008.03.062. 20

Elkins-Tanton, L. T. (2012), Magma oceans in the inner solar system, *Annual Review of Earth and Planetary Sciences*, pp. 113–139, doi :10.1146/annurev-earth-042711-105503. 24

Elkins-Tanton, L. T., S. E. Zaranek, E. Parmentier, and P. Hess (2005), Early magnetic field and magmatic activity on mars from magma ocean cumulate overturn, *Earth and Planetary Science Letters*, *236*, 1–12, doi :10.1016/j.epsl.2005.04.044. 20, 25, 38

Farley, K., C. Malespin, P. Mahaffy, J. Grotzinger, P. Vasconcelos, R. Milliken, M. Malin, K. Edgett, A. Pavlov, J. Hurowitz, et al. (2014), In situ radiometric and exposure age dating of the martian surface, *science*, *343*, 1247,166, doi :10.1126/science.1247166. 36

Feldman, W., W. Boynton, R. Tokar, T. Prettyman, O. Gasnault, S. Squyres, R. Elphic, D. Lawrence, S. Lawson, S. Maurice, et al. (2002), Global distribution of neutrons from mars : Results from mars odyssey, *Science*, *297*, 75–78, doi :0.1126/science.1073541. 10

Foley, C. N., M. Wadhwa, L. Borg, P. Janney, R. Hines, and T. Grove (2005), The early differentiation history of mars from 182w-142nd isotope systematics in the snc meteorites, *Geochimica et Cosmochimica Acta*, *69*, 4557–4571, doi :10.1016/S0016-7037(03)00094-2. 31, 53

Folkner, W., C. Yoder, D. Yuan, E. Standish, and R. Preston (1997), Interior structure and seasonal mass redistribution of mars from radio tracking of mars pathfinder, *Science*, *278*, 1749–1752, doi :10.1126/science.278.5344.1749. 45

Fowler, A. (1985), Fast Thermoviscous Convection, *Studies in Applied Mathematics*, *72*, 189–219. 59, 61

Fraeman, A. A., and J. Korenaga (2010), The influence of mantle melting on the evolution of mars, *Icarus*, *210*, 43–57, doi :10.1016/j.icarus.2010.06.030. 95

Frey, H. (2006a), Impact constraints on, and a chronology for, major events in early mars history, *Journal of Geophysical Research : Planets*, *111*, doi :10.1029/2005JE002449. 19, 20

Frey, H. (2006b), Impact constraints on the age and origin of the lowlands of mars, *Geophysical research letters*, *33*, doi :10.1029/2005GL024484. 20

Frey, H. (2008), Ages of very large impact basins on Mars : Implications for the late heavy bombardment in the inner solar system, *Geophysical Research Letters*, *35*, L13,203, doi : 10.1029/2008GL033515. 112

Frey, H., and R. A. Schultz (1988), Large impact basins and the mega-impact origin for the crustal dichotomy on mars, *Geophysical Research Letters*, *15*, 229–232, doi :10.1029/GL015i003p00229. 20, 21

Frey, H., S. E. Sakimoto, and J. Roark (1998), The mola topographic signature at the crustal dichotomy boundary zone on mars, *Geophysical research letters*, *25*, 4409–4412, doi :10.1029/1998GL900095. 16

Frey, H. V., J. H. Roark, K. M. Shockey, E. L. Frey, and S. E. Sakimoto (2002), Ancient lowlands on mars, *Geophysical Research Letters*, *29*, doi :10.1029/2001GL013832. 18, 19, 20

Fuller, E. R., and J. W. Head (2002), Amazonis planitia : The role of geologically recent volcanism and sedimentation in the formation of the smoothest plains on mars, *Journal of Geophysical Research : Planets*, *107*, doi :10.1029/2002JE001842. 16

Gagnepain-Beyneix, J., P. Lognonné, H. Chenet, D. Lombardi, and T. Spohn (2006), A seismic model of the lunar mantle and constraints on temperature and mineralogy, *Physics of the Earth and Planetary Interiors*, *159*, 140–166, doi :10.1016/j.pepi.2006.05.009. 126

Gault, D., and J. Wedekind (1978), Experimental impact" craters" formed in water : gravity scaling realized, *EOS Transactions*, *59*. 21

Gilbert, F., and A. M. Dziewonski (1975), An application of normal mode theory to the retrieval of structural parameters and source mechanisms from seismic spectra, *Phil. Trans. R. Soc. Lond. A*, *278*, 187–269, doi :10.1098/rsta.1975.0025. 161

Goetze, C., and B. Evans (1979), Stress and temperature in the bending lithosphere as constrained by experimental rock mechanics, *Geophysical Journal International*, *59*, 463–478, doi : 10.1111/j.1365-246X.1979.tb02567.x. 48

Goins, N. R., and A. R. Lazarewicz (1979), Martian seismicity, *Geophysical Research Letters*, *6*, 368–370, doi :10.1029/GL006i005p00368. 157

Golabek, G., T. Keller, T. Gerya, G. Zhu, P. Tackley, and J. Connolly (2011), Origin of the martian dichotomy and Tharsis from a giant impact causing massive magmatism, *Icarus*, *215*, 346–357, doi :10.1016/j.icarus.2011.06.012. 21, 22, 25, 112

Golombek, M. (2002), A revision of mars seismicity from surface faulting, in *Lunar and Planetary Science Conference*, vol. 33. 157, 158

Golombek, M., and N. Bridges (2000), Erosion rates on mars and implications for climate change : Constraints from the pathfinder landing site, *Journal of Geophysical Research : Planets*, *105*, 1841–1853, doi :10.1029/1999JE001043. 10

Golombek, M. P., W. B. Banerdt, K. L. Tanaka, and D. M. Tralli (1992), A prediction of mars seismicity from surface faulting, *Science*, *258*, 979–981, doi :10.1126/science.258.5084.979. 157, 158

Goossens, S., T. Sabaka, A. Genova, E. Mazarico, J. Nicholas, and G. Neumann (2017), Evidence for a low bulk crustal density for Mars from gravity and topography, *Geophysical Research Letters*, *44*, doi :10.1002/2017GL074172. 30, 43, 113, 136, 193

Grasset, O., and E. Parmentier (1998), Thermal convection in a volumetrically heated, infinite Prandtl number fluid with strongly temperature-dependent viscosity : Implications for planetary thermal evolution, *Journal of Geophysical Research*, *103*, 18,171–18,181, doi : 10.1029/98JB01492. 60, 61, 66, 116

Greeley, R., and J. Guest (1987), Geologic map of the eastern equatorial region of mars. 17

Greeley, R., and B. D. Schneid (1991), Magma generation on mars : Amounts, rates, and comparisons with earth, moon, and venus, *Science*, *254*, 996–998, doi :10.1126/science.254.5034.996. 33, 95

Greeley, R., and P. D. Spudis (1981), Volcanism on mars, *Reviews of Geophysics*, *19*, 13–41, doi :10.1029/RG019i001p00013. 33

Grott, M. (2005), Late crustal growth on Mars : Evidence from lithospheric extension, *Geophysical Research Letters*, *32*, L23,201, doi :10.1029/2005GL024492. 124

Grott, M., and D. Breuer (2008a), Constraints on the radiogenic heat production rate in the Martian interior from viscous relaxation of crustal thickness variations, *Geophysical Research Letters*, *35*, L05,201, doi :10.1029/2007GL033021. 36, 49, 54

Grott, M., and D. Breuer (2008b), The evolution of the martian elastic lithosphere and implications for crustal and mantle rheology, *Icarus*, *193*, 503–515, doi :10.1016/j.icarus.2007.08.015. 42, 44, 50, 52, 53, 57, 59, 65, 110, 113, 116, 120, 135, 142

Grott, M., and D. Breuer (2009), Implications of large elastic thicknesses for the composition and current thermal state of Mars, *Icarus*, *201*, 540–548, doi :10.1016/j.icarus.2009.01.020. 27, 33, 36, 42, 52, 53, 54, 101, 110, 111, 126, 127, 135, 137

Grott, M., and D. Breuer (2010), On the spatial variability of the Martian elastic lithosphere thickness : Evidence for mantle plumes ?, *Journal of Geophysical Research*, *115*, E03,005, doi :10.1029/2009JE003456. 42, 46, 47, 52, 111

Grott, M., E. Hauber, S. Werner, P. Kronberg, and G. Neukum (2005), High heat flux on ancient Mars : Evidence from rift flank uplift at Coracis Fossae, *Geophysical Research Letters*, *32*, L21,201, doi :10.1029/2005GL023894. 50, 110

Grott, M., E. Hauber, S. Werner, P. Kronberg, and G. Neukum (2007), Mechanical modeling of thrust faults in the Thaumasia region, mars, and implications for the Noachian heat flux, *Icarus*, *186*, 517–526, doi :10.1016/j.icarus.2006.10.001. 50, 110

Grott, M., A. Morschhauser, D. breuer, and E. Hauber (2011), Volcanic outgassing of CO2 and H2O on Mars, *Earth and Planetary Science Letters*, *308*, 391–400, doi :10.1016/j.epsl.2011.06.014. 49, 110

Grott, M., D. Baratoux, E. Hauber, V. Sautter, J. Mustard, O. Gasnault, S. Ruff, S.-I. Karato, V. Debaille, M. Knapmeyer, F. Sohl, T. Van Hoolst, D. Breuer, A. Morschhauser, and M. Toplis (2013), Long-Term Evolution of the Martian Crust-Mantle System, *Space Sci Rev*, *174*, 49–111, doi :10.1007/s11214-012-9948-3. 27, 51, 110, 113, 115, 163

Gudkova, T., and V. Zharkov (2004), Mars : interior structure and excitation of free oscillations, *Physics of the Earth and Planetary Interiors*, *142*, 1–22, doi :10.1016/j.pepi.2003.10.004. 156

Guerrero, J., J. P. Lowman, F. Deschamps, and P. Tackley (2018), The influence of curvature on convection in a temperature-dependent viscosity fluid : Implications for the 2-d and 3-d modeling of moons, *Journal of Geophysical Research : Planets*, *123*, 1863–1880, doi : 10.1029/2017JE005497. 65, 83, 92

Guest, A., and S. E. Smrekar (2007), New constraints on the thermal and volatile evolution of mars, *Physics of the Earth and Planetary Interiors*, *164*, 161–176, doi :10.1016/j.pepi.2007.06.010. 52

Gunnarsson, B., B. D. Marsh, and H. P. Taylor (1998), Generation of icelandic rhyolites : silicic lavas from the torfajökull central volcano, *Journal of Volcanology and Geothermal Research*, *83*, 1–45, doi :10.1016/S0377-0273(98)00017-1. 35

Gutenberg, B. (1948), On the layer of relatively low wave velocity at a depth of about 80 kilometers, *Bulletin of the Seismological Society of America*, *38*, 121–148. 164

Gutenberg, B. (1959), *Physics of the Earth's Interior*. 164

Halliday, A., H. Wänke, J.-L. Birck, and R. Clayton (2001), The accretion, composition and early differentiation of mars, *Space Science Reviews*, *96*, 197–230, doi :10.1023/A:1011997206080. 24

Hansen, U., and D. Yuen (1993), High rayleigh number regime of temperature-dependent viscosity convection and the earth's early thermal history, *Geophysical research letters*, *20*, 2191–2194, doi :10.1029/93GL02416. 61

Harder, H. (2000), Mantle convection and the dynamic geoid of mars, *Geophysical Research Letters*, *27*, 301–304, doi :10.1029/1999GL008418. 23

Harder, H., and U. R. Christensen (1996), A one-plume model of martian mantle convection, *Nature*, *380*, 507, doi :10.1038/380507a0. 23, 48

Hart, S., F. Nimmo, D. Korycansky, and C. Agnor (2007), Probing the giant impact hypothesis of the martian crustal dichotomy, in *Seventh International Conference on Mars*, vol. 1353, p. 3332. 21

Hartmann, W., and D. Malin (2000), Elysium Planitia lava flows : Crater count chronology and geological implications, *Journal of Geophysical Research*, *105*, 15,011–15,025, doi : 10.1029/1999JE001189. 111, 124

Hartmann, W., M. Malin, A. McEwen, M. Carr, L. Soderblom, P. Thomas, E. Danielson, P. James, and J. Veverka (1999), Evidence for recent volcanism on Mars from crater counts, *Nature*, *397*, 586–589, doi :10.1038/17545. 25, 33, 50, 111, 114, 124, 132

Hartmann, W. K., and G. Neukum (2001), Cratering chronology and the evolution of mars, in *Chronology and evolution of Mars*, pp. 165–194, doi :10.1007/978-94-017-1035-0_6. 16, 17

Hauber, E., J. Bleacher, K. Gwinner, D. Williams, and R. Greeley (2009), The topography and morphology of low shields and associated landforms of plains volcanism in the Tharsis region of Mars, *Journal of Volcanology and Geothermal Research*, *185*, 69–95, doi :10.1016/j.jvolgeores.2009.04.015. 124

Hauber, E., P. Brož, F. Jabert, P. Jodlowski, and T. Platz (2011), Very recent and widespread basaltic volcanism on Mars, *Geophysical Research Letters*, *38*, L10,201, doi : 10.1029/2011GL047310. 17, 25, 50, 114, 132

Hauck, S., and R. Phillips (2002), Thermal and crustal evolution of Mars, *Journal of Geophysical Research*, *107*, E75,052, doi :10.1029/2001JE001801. 36, 43, 46, 59, 127, 138, 189

Head, J., R. Greeley, M. Golombek, W. Hartmann, E. Hauber, R. Jaumann, P. Masson, G. Neukum, L. Nyquist, and M. Carr (2001), Geological processes and evolution, *Space Science Reviews*, *96*, 263–292, doi :10.1023/A:1011953424736. 31

Head, J. W., M. A. Kreslavsky, and S. Pratt (2002), Northern lowlands of mars : Evidence for widespread volcanic flooding and tectonic deformation in the hesperian period, *Journal of Geophysical Research : Planets*, *107*, doi :10.1029/2000JE001445. 16, 33

Head, J. W., J. F. Mustard, M. A. Kreslavsky, R. E. Milliken, and D. R. Marchant (2003), Recent ice ages on mars, *Nature*, *426*, 797, doi :10.1038/nature02114. 18

Head, J. W., A. L. Nahm, D. R. Marchant, and G. Neukum (2006), Modification of the dichotomy boundary on mars by amazonian mid-latitude regional glaciation, *Geophysical Research Letters*, *33*, doi :10.1029/2005GL024360. 18

Hernlund, J. W., and P. J. Tackley (2008), Modeling mantle convection in the spherical annulus, *Physics of the Earth and Planetary Interiors*, *171*, 48–54, doi :10.1016/j.pepi.2008.07.037Get. 81

Herzberg, C., K. Condie, and J. Korenaga (2010), Thermal history of the earth and its petrological expression, *Earth and Planetary Science Letters*, *292*, 79–88, doi :10.1016/j.epsl.2010.01.022. 44

Hiesinger, H., J. Head III, U. Wolf, R. Jaumann, and G. Neukum (2003), Ages and stratigraphy of mare basalts in oceanus procellarum, mare nubium, mare cognitum, and mare insularum, *Journal of Geophysical Research : Planets*, *108*, doi :10.1029/2002JE001985. 95, 96

Hood, L., N. Richmond, E. Pierazzo, and P. Rochette (2003), Distribution of crustal magnetic fields on mars : Shock effects of basin-forming impacts, *Geophysical Research Letters*, *30*, doi :10.1029/2002GL016657. 44

Hoogenboom, T., and S. Smrekar (2006), Elastic thickness estimates for the northern lowlands of Mars, *Earth and Planetary Science Letters*, *248*, 830–839, doi :10.1002/2014GL061779. 49, 110, 113, 129

Howard, L. (1966), Convection at high Rayleigh number, *Applied Mechanics*, pp. 1109–1115. 60

Huang, J., and L. Xiao (2014), Knobby terrain on ancient volcanoes as an indication of dominant early explosive volcanism on Mars, *Geophysical Research Letters*, *41*, 7019–7024, doi :10.1002/2014GL061779. 112, 113, 126

Humayun, M., A. Nemchin, B. Zanda, R. H. Hewins, M. Grange, A. Kennedy, J.-P. Lorand, C. Göpel, C. Fieni, S. Pont, and D. Deldicque (2013), Origin and age of the earliest Martian crust from meteorite NWA 7533, *Nature*, *503*, 513–517, doi :10.1038/nature12764. 34, 112

Hüttig, C., and K. Stemmer (2008), The spiral grid : A new approach to discretize the sphere and its application to mantle convection, *9*, Q02,018, doi :10.1029/2007GC001581. 62, 145

Hüttig, C., N. Tosi, and W. B. Moore (2013), An improved formulation of the incompressible Navier-Stokes equations with variable viscosity, *40*, 113–129, doi :10.1016/j.pepi.2013.04.002. 62, 145

Hynek, B. M., and R. J. Phillips (2003), New data reveal mature, integrated drainage systems on mars indicative of past precipitation, *Geology*, *31*, 757–760, doi :10.1130/G19607.1. 10

Irwin, R. P., T. R. Watters, A. D. Howard, and J. R. Zimbelman (2004), Sedimentary resurfacing and fretted terrain development along the crustal dichotomy boundary, aeolis mensae, mars, *Journal of Geophysical Research : Planets*, *109*, doi :10.1029/2004JE002248. 18

Iwase, Y., and S. Honda (1998), Effects of geometry on the convection with core-cooling, *Earth Planets Space*, *50*, 387–395, doi :10.1186/BF03352125. 61, 95

Jaeger, W., L. Keszthelyi, A. McEwen, C. Dundas, and P. S. Russell (2007), Athabasca valles, mars : A lava-draped channel system, *Science*, *317*, 1709–1711, doi :10.1126/science.1143315. 17

Jagoutz, E. (1991), Chronology of SNC meteorites, *Space Science Reviews*, *56*, 13–22, doi :10.1007/BF00178386. 33, 53, 125

Jarvis, G., G. Glatzmaier, and V. Vangelov (1995), Effect of curvature, aspect ratio, and plan form in two- and three-dimensional spherical models of thermal convection, *Geophysical and Astrophysical Fluid Dynamics*, *79*, 147–171, doi :10.1080/03091929508228995. 61

Jaupart, C., and J.-C. Mareschal (2003), Constraints on crustal heat production from heat flow data, *3*, 65–84, doi :10.1016/B0-08-043751-6/03017-6. 38

Karato, S.-I., and P. Wu (1993), Rheology of the Upper Mantle : A Synthesis, *Science*, *260*, 771–778, doi :10.1126/science.260.5109.771. 43, 63, 102, 116, 118, 122, 123, 138

Ke, Y., and V. Solomatov (2006), Early transient superplumes and the origin of the martian crustal dichotomy, *Journal of Geophysical Research : Planets*, *111*, doi :10.1029/2005JE002631. 45

Ke, Y., and V. Solomatov (2009), Coupled core-mantle thermal evolution of early Mars, *Journal of Geophysical Research*, *114*, E07,004, doi :10.1029/2008JE003291. 45, 65, 118

Kedar, S., J. Andrade, B. Banerdt, P. Delage, M. Golombek, M. Grott, T. Hudson, A. Kiely, M. Knapmeyer, B. Knapmeyer-Endrun, et al. (2017), Analysis of regolith properties using seismic signals generated by insight's hp 3 penetrator, *Space Science Reviews*, *211*, 315–337, doi :10.1007/s11214-017-0391-3. 158

Kern, H., and V. Schenk (1985), Elastic wave velocities in rocks from a lower crustal section in southern calabria (italy), *Physics of the Earth and Planetary Interiors*, *40*, 147–160, doi : 10.1016/0031-9201(85)90126-8. 165

Khan, A., and J. Connolly (2008), Constraining the composition and thermal state of mars from inversion of geophysical data, *Journal of Geophysical Research : Planets*, *113*(E7), doi :10.1029/2007JE002996. 45, 156, 161

Khan, A., M. van Driel, M. Böse, D. Giardini, S. Ceylan, J. Yan, J. Clinton, F. Euchner, P. Lognonné, N. Murdoch, et al. (2016), Single-station and single-event marsquake location and inversion for structure using synthetic martian waveforms, *Physics of the Earth and Planetary Interiors*, *258*, 28–42, doi :10.1016/j.pepi.2016.05.017. 161

Kiefer, W. (2004), Gravity evidence for an extinct magma chamber beneath Syrtis Major, Mars : a look at the magmatic plumbing system, *Earth and Planetary Science Letters*, *222*, 349–361, doi :10.1016/j.epsl.2006.06.035. 49, 110

Kiefer, W., and Q. Li (2009), Mantle convection controls the observed lateral variations in lithospheric thickness on present-day Mars, *Geophysical Research Letters*, *36*, L18,203, doi : 10.1029/2009GL039827. 52, 111

Kiefer, W., J. Filiberto, C. Sandu, and Q. Li (2015), The effects of mantle composition on the peridotite solidus : Implications for the magmatic history of Mars, *Geochimica et Cosmochimica Acta*, *162*, 247–258, doi :10.1016/j.gca.2015.02.010. 133

Kleine, T., C. Münker, K. Mezger, and H. Palme (2002), Rapid accretion and early core formation on asteroids and the terrestrial planets from hf–w chronometry, *Nature*, *418*, 952, doi :10.1038/nature00982. 24

Knapmeyer, M., J. Oberst, E. Hauber, M. Wählisch, C. Deuchler, and R. Wagner (2006), Working models for spatial distribution and level of mars' seismicity, *Journal of Geophysical Research : Planets*, *111*, doi :10.1029/2006JE002708. 157, 158

Konopliv, A., C. Yoder, E. Standish, D.-N. Yuan, and W. Sjogren (2006), A global solution for the Mars static and seasonal gravity, Mars orientation, Phobos and Deimos masses, and Mars ephemeris, *Icarus*, *182*, 23–50, doi :10.1016/j.icarus.2005.12.025. 125

Korenaga, J. (2009), Scaling of stagnant-lid convection with arrhenius rheology and the effects of mantle melting, *Geophysical Journal International*, *179*, 154–170, doi :10.1111/j.1365-246X.2009.04272.x. 95

Kronberg, P., E. Hauber, M. Grott, S. Werner, T. Schäfer, K. Gwinner, B. Giese, P. Masson, and G. Neukum (2007), Acheron Fossae, Mars : Tectonic rifting, volcanism, and implications for lithospheric thickness, *Journal of Geophysical Research*, *112*, E04,005, doi :10.1029/2006JE002780. 50, 110

Labrosse, S. (2002), Hotspots, mantle plumes and core heat loss, *Earth and Planetary Sciences Letters*, *199*, 147–156, doi :10.1016/S0012-821X(02)00537-X. 57, 70

Laneuville, M., M. Wieczorek, D. Breuer, and N. Tosi (2013), Asymmetric thermal evolution of the moon, *Journal of Geophysical Research : Planets*, *118*, 1435–1452, doi :10.1002/jgre.20103. 27, 96

Larmat, C., J.-P. Montagner, Y. Capdeville, W. Banerdt, P. Lognonné, and J.-P. Vilotte (2008), Numerical assessment of the effects of topography and crustal thickness on martian seismograms using a coupled modal solution–spectral element method, *Icarus*, *196*, 78–89, doi : 10.1016/j.icarus.2007.12.030. 179

Laskar, J., P. Robutel, F. Joutel, M. Gastineau, A. Correia, and B. Levrard (2004), A long-term numerical solution for the insolation quantities of the Earth, *Astronomy and Astrophysics*, *428*, 261–285, doi :10.1051/0004-6361:20041335. 122

Latham, G., M. Ewing, and G. Sutton (1969), The apollo passive seismic experiment, *Science*, *165*, 241–250, doi :10.1126/science.165.3890.241. 156

Lay, T., and T. C. Wallace (1995), *Modern global seismology*, vol. 58, doi :10.1785/gssrl.66.6.92. 162

Lee, D.-C., and A. N. Halliday (1995), Hafnium–tungsten chronometry and the timing of terrestrial core formation, *Nature*, *378*, 771, doi :10.1038/378771a0. 24

Lee, D.-C., and A. N. Halliday (1997), Core formation on mars and differentiated asteroids, *Nature*, *388*, 854, doi :10.1038/42206. 53

Lenardic, A., F. Nimmo, and L. Moresi (2004), Growth of the hemispheric dichotomy and the cessation of plate tectonics on mars, *Journal of Geophysical Research : Planets*, *109*, doi :10.1029/2003JE002172. 14, 20, 25

Leonard, G. J., and K. L. Tanaka (2001), *Geologic map of the Hellas region of Mars*. 35

Leone, G., P. Tackley, T. Gerya, D. May, and G. Zhu (2014), Three-dimensional simulations of the southern polar giant impact hypothesis for the origin of the Martian dichotomy, *Geophysical Research Letters*, *41*, 8736–8743, doi :10.1002/2014GL062261. 112

Li, Q., and W. Kiefer (2007), Mantle convection and magma production on present-day Mars : Effects of temperature-dependent rheology, *Geophysical Research Letters*, *34*, L16,203, doi : 10.1029/2007GL030544. 33, 46, 47, 132

Lillis, R. J., S. Robbins, M. Manga, J. S. Halekas, and H. V. Frey (2013), Time history of the martian dynamo from crater magnetic field analysis, *Journal of geophysical research : planets*, *118*, 1488–1511, doi :10.1002/jgre.20105. 45

Lodders, K., and B. J. Fegley (1997), An Oxygen Isotope Model for the Composition of Mars, *Icarus*, *126*, 373–394, doi :10.1006/icar.1996.5653. 36

Lognonné, P., and C. Johnson (2007), Planetary seismology, *Treatise on Geophysics*, *10*, 69–122, doi :10.1016/B978-044452748-6.00154-1. 155, 159, 162, 168, 169, 175

Lognonné, P., and C. Johnson (2015), Planetary seismology, *Treatise on Geophysics*, *10*, 65–120, doi :10.1016/B978-0-444-53802-4.00167-6. 158

Lognonné, P., and B. Mosser (1993), Planetary seismology, *Surveys in Geophysics*, *14*, 239–302, doi :10.1007/BF00690946. 157, 160

Lognonné, P., J. G. Beyneix, W. B. Banerdt, S. Cacho, J. F. Karczewski, and M. Morand (1996), Ultra broad band seismology on intermarsnet, *Planetary and space science*, *44*, 1237–1250, doi :10.1016/S0032-0633(96)00083-9. 158

Lognonné, P., D. Giardini, B. Banerdt, J. Gagnepain-Beyneix, A. Mocquet, T. Spohn, J. Karczewski, P. Schibler, S. Cacho, W. Pike, et al. (2000), The netlander very broad band seismometer, *Planetary and Space Science*, *48*, 1289–1302, doi :10.1016/S0032-0633(00)00110-0. 156

Lourenço, D. L., A. B. Rozel, T. Gerya, and P. J. Tackley (2018), Efficient cooling of rocky planets by intrusive magmatism, *Nature Geoscience*, *11*, 322, doi :10.1038/s41561-018-0094-8. 95

Mackwell, S., M. Zimmerman, and D. Kohlstedt (1998), High-temperature deformation of dry diabase with application to tectonics on Venus, *Journal of Geophysical Research*, *103*, 975–984, doi :10.1029/97JB02671. 122, 123

Marinova, M., O. Aharonson, and E. Asphaug (2008), Mega-impact formation of the Mars hemispheric dichotomy, *nature*, *453*, 1216–1219, doi :10.1038/nature07070. 14, 20, 21, 22, 25, 111, 123

Masters, G., W. J. H, and G. Freeman (2011), Mineos v1.0.2 [software], *Computational Infrastructures for Geodynamics*. 161

McEwen, A. S., M. C. Malin, M. H. Carr, and W. K. Hartmann (1999), Voluminous volcanism on early mars revealed in valles marineris, *Nature*, *397*, 584, doi :10.1038/17539. 31, 33

McGill, G. E. (2000), Crustal history of north central arabia terra, mars, *Journal of Geophysical Research : Planets*, *105*, 6945–6959, doi :10.1029/1999JE001175. 26, 35

McGill, G. E., and A. M. Dimitriou (1990), Origin of the martian global dichotomy by crustal thinning in the late noachian or early hesperian, *Journal of Geophysical Research : Solid Earth*, *95*, 12,595–12,605, doi :10.1029/JB095iB08p12595. 14, 20, 23, 191

McGill, G. E., and S. W. Squyres (1991), Origin of the martian crustal dichotomy : Evaluating hypotheses, *Icarus*, *93*, 386–393, doi :10.1016/0019-1035(91)90221-E. 20, 21

McGovern, P., S. Solomon, D. Smith, M. Zuber, M. Simons, M. Wieczorek, R. Phillips, G. Neumann, O. Aharonson, and J. Head (2004), Correction to 'localized gravity/topography admittance and correlation spectra on Mars : Implications for regional and global evolution', *Journal of Geophysical Research*, *109*, E07,007, doi :10.1029/2004JE002286. 30, 49, 110, 113, 122

McNamara, A., and S. Zhong (2005), Degree-one mantle convection : Dependence on internal heating and temperature-dependent rheology, *Geophysical Research Letters*, *32*, L01,301, doi :10.1029/2004GL021082. 57

McNutt, M. (1984), Lithospheric flexure and thermal anomalies, *Journal of Geophysical Research*, *89*, 180–194. 48

McNutt, M., M. Diament, and M. Kogan (1988), Variations of elastic plate thickness at continental thrust belts, *Journal of Geophysical Research*, *93*, 8825–8838, doi :10.1029/JB093iB08p08825. 49, 121

McNutt, M. K., and H. Menard (1982), Constraints on yield strength in the oceanic lithosphere derived from observations of flexure, *Geophysical Journal International*, *71*, 363–394, doi :10.1111/j.1365-246X.1982.tb05994.x. 49

McSween, H., M. Wyatt, R. Gellert, J. Bell III, R. Morris, K. Herkenhoff, L. Crumpler, K. Milam, K. Stockstill, L. Tornabene, R. Arvidson, P. Barlett, D. Blaney, N. Cabrol, P. Christensen, B. Clark, J. Crisp, D. Des Marais, T. Economou, J. Farmer, W. Farrand, A. Ghosh, M. Golombek, S. Gorevan, R. Greeley, V. Hamilton, J. Johnson, B. Joliff, G. Klingelhöfer, A. Knudson, S. McLennan, D. Ming, J. Moersch, R. Rieder, S. Ruff, C. Schröder, P. de Souza Jr., S. Squyres, H. Wänke, A. Wang, A. Yen, and J. Zipfel (2006), Characterization and petrologic interpretation of olivine-rich basalts at Gusev Crater, Mars, *Journal of Geophysical Research*, *111*, E02S10, doi :10.1029/2005JE002477. 34, 112

McSween, H. Y., T. L. Grove, and M. B. Wyatt (2003), Constraints on the composition and petrogenesis of the martian crust, *Journal of Geophysical Research : Planets*, *108*, doi :10.1029/2003JE002175. 34

McSween, Jr, H., T. Grove, R. Lentz, J. Dann, A. Holzheid, L. Riciputi, and J. Ryan (2001), Geochemical evidence for magmatic water within Mars from pyroxenes in the Shergotty meteorite, *Nature*, *409*, 487–490, doi :10.1038/35054011. 116

Médard, E., and T. Grove (2006), Early hydrous melting and degassing of the Martian interior, *Journal of Geophysical Research*, *111*, E11,003, doi :10.1029/2006JE002742. 116

Mei, S., and D. Kohlstedt (2000a), Influence of water on plastic deformation of olivine aggregates : 1. Diffusion creep regime, *Journal of Geophysical Research*, *105*, 21,457–21,469, doi :10.1029/2000JB900179. 43, 116

Mei, S., and D. Kohlstedt (2000b), Influence of water on plastic deformation of olivine aggregates : 2. Dislocation creep regime, *Journal of Geophysical Research*, *105*, 21,471–21,481, doi :10.1029/2000JB900180. 43, 116

Mellon, M., W. Feldman, and T. Prettyman (2004), The presence and stability of ground ice in the southern hemisphere of Mars, *Icarus*, *169 (2)*, 324–340, doi :10.1016/j.icarus.2003.10.022. 125

Meyer, C. J. (2003), Mars meteorite compendium, *NASA Johnson Space Cent., Houston, Tex.*, *Rep.27672, rev. B*, (Available at http ://curator. jsc.nasa.gov/antmet/mmc/mmc.htm). 36

Michalski, J. R., and J. E. Bleacher (2013), Supervolcanoes within an ancient volcanic province in arabia terra, mars, *Nature*, *502*, 47, doi :10.1038/nature12482. 33, 34

Michaut, C., and C. Jaupart (2004), Nonequilibrium temperatures and cooling rates in thick continental lithosphere, *Geophysical research letters*, *31*, L24,602, doi :10.1029/2004GL021092. 67, 121, 137

Milbury, C., G. Schubert, C. Raymond, S. Smrekar, and B. Langlais (2012), The history of mars' dynamo as revealed by modeling magnetic anomalies near tyrrhenus mons and syrtis major, *Journal of Geophysical Research : Planets*, *117*, doi :10.1029/2012JE004099. 45

Mocquet, A., and M. Menvielle (2000), Complementarity of seismological and electromagnetic sounding methods for constraining the structure of the martian mantle, *Planetary and Space Science*, *48*, 1249–1260, doi :10.1016/S0032-0633(00)00107-0. 164

Mocquet, A., P. Vacher, O. Grasset, and C. Sotin (1996), Theoretical seismic models of mars : the importance of the iron content of the mantle, *Planetary and space science*, *44*, 1251–1268, doi :10.1016/S0032-0633(96)00086-4. 156, 161, 162, 164, 184

Mocquet, A., P. Rosenblatt, V. Dehant, and O. Verhoeven (2011), The deep interior of venus, mars, and the earth : A brief review and the need for planetary surface-based measurements, *Planetary and Space Science*, *59*, 1048–1061, doi :10.1016/j.pss.2010.02.002. 162

Montési, L. G., and M. T. Zuber (2003), Clues to the lithospheric structure of mars from wrinkle ridge sets and localization instability, *Journal of Geophysical Research : Planets*, *108*, doi :10.1029/2002JE001974. 46

Montgomery, D. R., S. M. Som, M. P. Jackson, B. C. Schreiber, A. R. Gillespie, and J. B. Adams (2009), Continental-scale salt tectonics on mars and the origin of valles marineris and associated outflow channels, *Geological Society of America Bulletin*, *121*, 117–133, doi :10.1130/B26307.1. 9

Moore, W. (2008), Heat transport in a convecting layer heated from within and below, *Journal of Geophysical Research*, *113*, B11,407, doi :10.1029/2006JB004778. 70

Moore, W. B., and A. A. G. Webb (2013), Heat-pipe earth, *Nature*, *501*, 501, doi :10.1038/nature12473. 95

Moresi, L.-N., and S. Solomatov (1995), Numerical investigation of 2D convection with extremely large viscosity variation, *Physics of Fluids*, *7*, 2154–2162, doi :10.1063/1.868465. 59, 60

Morgan, J. W., and E. Anders (1979), Chemical composition of mars, *Geochimica et Cosmochimica Acta*, *43*, 1601–1610, doi :10.1016/0016-7037(79)90180-7. 36

Morris, S., and D. Canright (1984), A boundary-layer analysis of Benard convection in a fluid of strongly temperature-dependent viscosity, *Physics of the Earth and PLanetary Interiors*, *36*, 355–373, doi :10.1016/0031-9201(84)90057-8. 59, 61

Morschhauser, A., M. Grott, and D. breuer (2011), Crustal recycling, mantle dehydration, and the thermal evolution of Mars, *Icarus*, *212*, 541–558, doi :10.1016/j.icarus.2010.12.028. 43, 46, 52, 57, 59, 95, 135, 137, 138, 189

Mueller, S., and R. Phillips (1995), On the reliability of lithospheric constraints derived from models of outer-rise flexure, *Journal of Geophysical Research*, *123*, 887–902, doi :10.1111/j.1365-246X.1995.tb06896.x. 121

Mustard, J., F. Poulet, A. Gendrin, J.-P. Bibring, Y. Langevin, B. Gondet, N. Mangold, G. Bellucci, and F. Altieri (2005), Olivine and Pyroxene Diversity in the Crust of Mars, *Science*, *307*, 1594–1597, doi :10.1126/science.1109098. 34, 35, 112

Mustard, J. F., S. L. Murchie, S. Pelkey, B. Ehlmann, R. Milliken, J. A. Grant, J.-P. Bibring, F. Poulet, J. Bishop, E. N. Dobrea, et al. (2008), Hydrated silicate minerals on mars observed by the mars reconnaissance orbiter crism instrument, *Nature*, *454*, 305–309, doi :10.1038/nature07097. 10

Mutch, T. A., R. E. Arvidson, J. Head III, K. L. Jones, and R. S. Saunders (1976), The geology of mars, *Princeton, NJ, Princeton University Press, 1976. 409 p.* 15

Nakagawa, T., and P. J. Tackley (2010), Influence of initial cmb temperature and other parameters on the thermal evolution of earth's core resulting from thermochemical spherical mantle convection, *Geochemistry, Geophysics, Geosystems*, *11*, doi :10.1029/2010GC003031. 81

Nakamura, Y. (1983), Seismic velocity structure of the lunar mantle, *Journal of Geophysical Research : Solid Earth*, *88*, 677–686, doi :10.1029/JB088iB01p00677. 164

Nakamura, Y., and D. L. Anderson (1979), Martian wind activity detected by a seismometer at viking lander 2 site, *Geophysical Research Letters*, *6*, 499–502, doi :10.1029/GL006i006p00499. 157

Nakamura, Y., G. V. Latham, H. J. Dorman, A.-B. Ibrahim, J. Koyama, and P. Horvath (1979), Shallow moonquakes-depth, distribution and implications as to the present state of the lunar interior, in *Lunar and Planetary Science Conference Proceedings*, vol. 10, pp. 2299–2309. 157, 179

Nataf, H., and F. Richter (1982), Convection experiments in fluids with highly temperature-dependent viscosity and the thermal evolution of the planets, *Physics of the Earth and Planetary Interiors*, *29*, 320–329, doi :10.1016/0031-9201(82)90020-6. 59

Neukum, G., R. Jaumann, H. Hoffmann, E. Hauber, J. Head, A. Basilevsky, B. Ivanov, S. Werner, S. van Gasselt, J. B. Murray, T. McCord, and The HRSC Co-Investigator Team (2004), Recent and episodic volcanic and glacial activity on Mars revealed by the High Resolution Stereo Camera, *Nature*, *432*, 971–979, doi :10.1038/nature03231. 17, 25, 50, 111, 114, 132

Neumann, G., M. Zuber, M. Wieczorek, P. McGovern, F. Lemoine, and D. Smith (2004), Crustal structure of Mars from gravity and topography, *Journal of Geophysical Research*, *109*, E08,002, doi :10.1029/2004JE002262. 15, 17, 18, 26, 28, 30, 31, 33, 114, 125, 136, 140, 193

Nimmo, F. (2005), Tectonic consequences of martian dichotomy modification by lower-crustal flow and erosion, *Geology*, *33*, 533–536, doi :10.1130/G21342.1. 28, 192

Nimmo, F., and U. Faul (2013), Dissipation at tidal and seismic frequencies in a melt-free, anhydrous mars, *Journal of Geophysical Research : Planets*, *118*, 2558–2569, doi :10.1002/2013JE004499. 44, 160, 164

Nimmo, F., and D. Stevenson (2000), Influence of early plate tectonics on the thermal evolution and magnetic field of Mars, *Journal of Geophysical Research*, *105*, 11,969–11,979, doi :10.1029/1999JE001216. 44, 45

Nimmo, F., and D. Stevenson (2001), Estimates of Martian crustal thickness from viscous relaxation of topography, *Journal of Geophysical Research*, *106*, 5085–5098, doi :10.1029/2000JE001331. 25, 28, 30, 36, 125, 126, 135, 192

Nimmo, F., and K. Tanaka (2005), Early crustal evolution of Mars, *Annual Reviews Earth and Planetary Sciences*, *33*, 133–161, doi :10.1146/annurev.earth.33.092203.122637. 20, 21, 33, 112

Nimmo, F., S. Hart, D. Korycansky, and C. Agnor (2008), Implications of an impact origin for the martian hemispheric dichotomy, *Nature*, *453*, 1220, doi :10.1038/nature07025. 22, 25

Norman, M. (2002), Thickness and composition of the martian crust revisited : Implications of an ultradepleted mantle with a nd isotopic composition like that of que94201, in *Lunar and Planetary Science Conference*, vol. 33. 31

Nyquist, L., D. Bogart, C.-Y. Shih, A. Greshake, D. St'offler, and O. Eugster (2001), Ages and Geologic Histories of Martian Meteorites, *Space Science Reviews*, *96*, 105–164, doi :10.1023/A:1011993105172. 35, 112

Ogawa, M., and T. Yanagisawa (2011), Numerical models of martian mantle evolution induced by magmatism and solid-state convection beneath stagnant lithosphere, *Journal of Geophysical Research : Planets*, *116*(E8), doi :10.1029/2010JE003777. 25

Ogawa, M., G. Schubert, and A. Zebib (1991), Numerical simulations of three-dimensional thermal convection in a fluid with strongly temperature-dependent viscosity, *Journal of Fluids Mechanics*, *233*, 299–328, doi :10.1017/S0022112091000496. 59

Ohtake, M., T. Matsunaga, J. Haruyama, Y. Yokota, T. Morota, C. Honda, Y. Ogawa, M. Torii, H. Miyamoto, T. Arai, et al. (2009), The global distribution of pure anorthosite on the moon, *Nature*, *461*, 236, doi :10.1038/nature08317. 35

Oldham, R. D. (1906), The constitution of the interior of the earth, as revealed by earthquakes, *Quarterly Journal of the Geological Society*, *62*, 456–475, doi :10.1144/GSL.JGS.1906.062.01-04.21. 155

O'Neill, C., A. Lenardic, A. M. Jellinek, and W. S. Kiefer (2007), Melt propagation and volcanism in mantle convection simulations, with applications for Martian volcanic and atmospheric evolution, *Journal of Geophysical Research*, *112*, E07,003, doi :10.1029/2006JE002799. 132

Panning, M., E. Beucler, M. Drilleau, A. Mocquet, P. Lognonné, and W. Banerdt (2015), Verifying single-station seismic approaches using Earth-based data : Preparation for data return from the InSight mission to Mars, *Icarus*, *248*, 230–242, doi :10.1016/j.icarus.2014.10.035. 140, 154, 157, 158, 160, 179, 180, 181

Panning, M. P., P. Lognonné, W. B. Banerdt, R. Garcia, M. Golombek, S. Kedar, B. Knapmeyer-Endrun, A. Mocquet, N. A. Teanby, J. Tromp, et al. (2017), Planned products of the mars structure service for the insight mission to mars, *Space Science Reviews*, *211*, 611–650, doi :10.1007/s11214-016-0317-5. 157, 158, 160, 162, 175, 177, 181

Papike, J., J. Karner, C. Shearer, and P. Burger (2009), Silicate mineralogy of martian meteorites, *Geochimica et Cosmochimica Acta*, *73*, 7443–7485, doi :10.1016/j.gca.2009.09.008. 33, 53, 96, 125

Parmentier, E., and M. Zuber (2007), Early evolution of Mars with mantle compositional stratification or hydrothermal crustal cooling, *Journal of Geophysical Research*, *112*, E02,007, doi :10.1029/2005JE002626. 28, 125, 127

Pauer, M., and D. Breuer (2008), Constraints on the maximum crustal density from gravity topography modeling : Applications to the southern highlands of Mars, *Earth and Planetary Science Letters*, *276*, 253–261. 54, 113, 142

Phillips, R. (1991), Expected rate of marsquakes, *Scientifc Rationale and Requirements for a Global Seismic Network on Mars*, pp. 35–38. 157, 158

Phillips, R., M. Zuber, S. Smrekar, M. Mellon, J. Head, K. Tanaka, N. Putzig, S. Milkovich, B. Campbell, J. Plaut, A. Safaeinili, R. Seu, D. Biccari, L. Carter, G. Picardi, R. Orosei, P. Mohit, E. Heggy, R. Zurek, A. Egan, E. Giacomoni, F. Russo, M. Cutigni, E. Pettinelli, J. Holt, C. Leuschen, and L. Marinangeli (2008), Mars North Polar Deposits : Stratigraphy, Age, and Geodynamical Response, *Science*, *320*, 1182–1185, doi :10.1126/science.1157546. 42, 50, 52, 53, 110, 111, 114, 122

Phillips, R. J., M. T. Zuber, S. C. Solomon, M. P. Golombek, B. M. Jakosky, W. B. Banerdt, D. E. Smith, R. M. Williams, B. M. Hynek, O. Aharonson, et al. (2001), Ancient geodynamics and global-scale hydrology on mars, *Science*, *291*, 2587–2591, doi : 10.1126/science.1058701. 16, 18

Phinney, R. A. (1964), Structure of the earth's crust from spectral behavior of long-period body waves, *Journal of Geophysical Research*, *69*, 2997–3017, doi :10.1029/JZ069i014p02997. 158

Picardi, G., J. J. Plaut, D. Biccari, O. Bombaci, D. Calabrese, M. Cartacci, A. Cicchetti, S. M. Clifford, P. Edenhofer, W. M. Farrell, et al. (2005), Radar soundings of the subsurface of mars, *science*, *310*, 1925–1928, doi :10.1126/science.1122165. 19

Pike, R. J. (1980), Control of crater morphology by gravity and target type-mars, earth, moon, in *Lunar and Planetary Science Conference Proceedings*, vol. 11, pp. 2159–2189. 34

Piqueux, S., and P. Christensen (2009a), A model of thermal conductivity for planetary soils : 1. theory for unconsolidated soils, *Journal of Geophysical Research*, *114*, E09,005, doi : 10.1029/2008JE003308. 113

Piqueux, S., and P. Christensen (2009b), A model of thermal conductivity for planetary soils : 2. theory for cemented soils, *Journal of Geophysical Research*, *114*, E09,006, doi :10.1029/2008JE003309. 113

Plesa, A.-C., N. Tosi, and D. Breuer (2014), Can a fractionally crystallized magma ocean explain the thermo-chemical evolution of Mars ?, *Earth and Planetary Science Letters*, *403*, 225–235, doi :10.1016/j.epsl.2014.06.034. 24, 25, 46, 95

Plesa, A.-C., N. Tosi, M. Grott, and D. Breuer (2015), Thermal evolution and urey ratio of mars, *Journal of Geophysical Research : Planets*, *120*, 995–1010, doi :10.1002/2014JE004748. 44, 57, 73, 81, 173

Plesa, A.-C., M. Grott, N. Tosi, D. Breuer, T. Spohn, and M. Wieczorek (2016), How large are present-day heat flux variations across the surface of Mars ?, *Geophysical Research Planets*, *121*, 2386–2403, doi :10.1002/2016JE005126. 42, 47, 52, 111, 114, 121, 125, 141, 142, 162, 181, 190

Plescia, J. (2004), Morphometric properties of martian volcanoes, *Journal of Geophysical Research : Planets*, *109*(E3), doi :10.1029/2002JE002031. 7

Poulet, F., N. Mangold, B. Platevoet, J.-M. Bardintzeff, V. Sautter, J. Mustard, J.-P. Bibring, P. Pinet, Y. Langevin, B. Gondet, et al. (2009), Quantitative compositional analysis of martian mafic regions using the mex/omega reflectance data : 2. petrological implications, *Icarus*, *201*, 84–101, doi :10.1016/j.icarus.2008.12.042. 34

Pruis, M., and K. Tanaka (1995), The martian northern plains did not result from plate tectonics, in *Lunar and Planetary Science Conference*, vol. 26. 26

Purucker, M., D. Ravat, H. Frey, C. Voorhies, T. Sabaka, and M. Acuna (2000), An altitude-normalized magnetic map of mars and its interpretation, *Geophysical Research Letters*, *27*, 2449–2452, doi :10.1029/2000GL000072. 26

Quantin, C., J. Flahaut, H. Clenet, P. Allemand, and P. Thomas (2012), Composition and structures of the subsurface in the vicinity of valles marineris as revealed by central uplifts of impact craters, *Icarus*, *221*, 436–452, doi :10.1016/j.icarus.2012.07.031. 36

Reese, C., and V. Solomatov (2006), Fluid dynamics of local martian magma oceans, *Icarus*, *184*, 102–120, doi :10.1016/j.icarus.2006.04.008. 25

Reese, C., V. Solomatov, and L.-N. Moresi (1998), Heat transport efficiency for stagnant lid convection with dislocation viscosity : Application to mars and venus, *Journal of Geophysical Research : Planets*, *103*, 13,643–13,657, doi :10.1029/98JE01047. 61

Reese, C., V. Solomatov, J. Baumgardner, and W.-S. Yangc (1999), Stagnant lid convection in a spherical shell, *Physics of the Earth and Planetary Interiors*, *116*, 1–16, doi :10.1016/S0031-9201(99)00115-6. 60, 61, 69, 95

Reese, C., V. Solomatov, and J. Baumgardner (2005), Scaling laws for time-dependent stagnant lid convection in a spherical shell, *Physics of the Earth and Planetary Interiors*, *149*, 361–370, doi :10.1016/j.pepi.2004.11.004. 61, 69, 70, 78, 79, 81, 83, 87, 88, 89, 90, 91, 93, 95, 105, 187

Reese, C., C. Orth, and V. Solomatov (2010), Impact origin for the Martian crustal dichotomy : Half emptied or half filled ?, *Journal of Geophysical Research*, *115*, E05,004, doi :10.1029/2009JE003506. 14, 21, 22, 111

Richter, F. (1978), Mantle convection models, *Ann. Rev. Earth Planet. Sci.*, *6*, 9–19, doi : 10.1146/annurev.ea.06.050178.000301. 118

Richter, F., H.-C. Nataf, and S. Daly (1983), Heat transfer and horizontally averaged temperature of convection with large viscosity variations, *Journal of Fluids Mechanics*, *129*, 173–192, doi :10.1017/S0022112083000713. 59

Ritzer, J., and S. Hauck (2009), Lithospheric structure and tectonics at Isidis Planitia, Mars, *Icarus*, *201*, 528–539, doi :10.1016/j.icarus.2009.01.025. 49, 110, 114

Rivoldini, A., T. Van Hoolst, O. Verhoeven, A. Mocquet, and V. Dehant (2011), Geodesy constraints on the interior structure and composition of mars, *Icarus*, *213*, 451–472, doi : 10.1016/j.icarus.2011.03.024. 154, 156, 161, 162, 163, 164, 182, 184

Robbins, S. J., G. Di Achille, and B. M. Hynek (2011), The volcanic history of mars : High-resolution crater-based studies of the calderas of 20 volcanoes, *Icarus*, *211*, 1179–1203, doi : 10.1016/j.icarus.2010.11.012. 34

Roberts, J., and J. Arkani-Hamed (2014), Impact heating and coupled core cooling and mantle dynamics on Mars, *Journal of Geophysical Research Planets*, *119*, 729–744, doi :10.1002/ 2013JE004603. 21, 124

Roberts, J., and S. Zhong (2006), Degree-1 convection in the Martian mantle and the origin of the hemispheric dichotomy, *Journal of Geophysical Research*, *111*, E06,013, doi :10.1029/ 2005JE002668. 14, 20, 23, 25, 35, 46, 47, 48, 111

Rodriguez, J., K. L. Tanaka, H. Miyamoto, and S. Sasaki (2006), Nature and characteristics of the flows that carved the simud and tiu outflow channels, mars, *Geophysical research letters*, *33*, doi :10.1029/2005GL024320. 18

Roman, A., and C. Jaupart (2017), Postemplacement dynamics of basaltic intrusions in the continental crust, *Journal of Geophysical Research : Solid Earth*, *122*, 966–987, doi :10. 1002/2016JB013912. 38

Rosenblatt, P., S. Charnoz, K. M. Dunseath, M. Terao-Dunseath, A. Trinh, R. Hyodo, H. Genda, and S. Toupin (2016), Accretion of phobos and deimos in an extended debris disc stirred by transient moons, *Nature Geoscience*, *9*, 581–583, doi :10.1038/ngeo2742. 21

Ruiz, J., C. Fernández, D. Gomez-Ortiz, J. Dohm, V. López, and R. Tejero (2008), Ancient heat flow, crustal thickness, and lithospheric mantle rheology in the Amenthes region, Mars, *Earth and Planetary Science Letters*, *270*, 1–12, doi :10.1016/j.epsl.2008.02.015. 50, 110

Safronov, V. S. (1972), Evolution of the protoplanetary cloud and formation of the earth and planets., *Evolution of the protoplanetary cloud and formation of the earth and planets., by Safronov, VS. Translated from Russian. Jerusalem (Israel) : Israel Program for Scientific Translations, Keter Publishing House, 212 p.* 24

Sanloup, C., A. Jambon, and P. Gillet (1999), A simple chondritic model of mars, *Physics of the Earth and Planetary Interiors*, *112*, 43–54, doi :10.1016/S0031-9201(98)00175-7. 181, 184

Sautter, V., M. Toplis, R. Wiens, A. Cousin, C. Fabre, O. Gasnault, S. Maurice, O. Forni, J. Lasue, A. Ollila, J. Bridges, N. Mangold, S. Le Mouélic, M. Fisk, P.-Y. Meslin, P. Beck, P. Pinet, L. Le deit, W. Rapin, E. Stolper, H. Newsom, D. Dyar, N. Lanza, D. Vaniman, S. Clegg, and J. Wray (2015), In situ evidence for continental crust on early Mars, *Nature Geosci*, *8*, 605–611, doi :10.1038/NGEO2474. 14, 31, 33, 35, 43, 54, 112, 113

Sautter, V., M. J. Toplis, P. Beck, N. Mangold, R. Wiens, P. Pinet, A. Cousin, S. Maurice, L. LeDeit, R. Hewins, et al. (2016), Magmatic complexity on early mars as seen through a combination of orbital, in-situ and meteorite data, *Lithos*, *254*, 36–52, doi :10.1016/j.lithos.2016.02.023. 14, 35, 54

Schott, B., A. Van den Berg, and D. Yuen (2001), Focussed time-dependent martian volcanism from chemical differentiation coupled with variable thermal conductivity, *Geophysical research letters*, *28*, 4271–4274, doi :10.1029/2001GL013638. 25

Schubert, G., and T. Spohn (1990), Thermal history of Mars and the sulfur content of its core, *Journal of Geophysical Research*, *95*, 14,095–14,104, doi :10.1029/JB095iB09p14095. 59, 127

Schubert, G., P. Cassen, and R. Young (1979), Subsolidus convective cooling histories of terrestrial planets, *Icarus*, *38*, 192–211, doi :10.1016/0019-1035(79)90178-7. 57, 59

Schubert, G., D. L. Turcotte, and P. Olson (2001), *Mantle convection in the Earth and planets*. 47, 57

Schultz, R., and T. Watters (2001), Forward mechanical modeling of the Amenthes Rupes thrust fault on Mars, *Geophysical Research Letters*, *28*, 4659–4662, doi :0094-8276/01/2001GL013468505.00. 50, 110

Schultz, R. A. (2002), Stability of rock slopes in valles marineris, mars, *Geophysical Research Letters*, *29*, doi :10.1029/2002GL015728. 34

Schumacher, S., and D. Breuer (2006), Influence of a variable thermal conductivity on the thermochemical evolution of Mars, *Journal of Geophysical Research*, *111*, E02,006, doi :10.1029/2005JE002429. 46, 126, 135, 149, 152

Scott, D., and M. Carr (1978), Geologic map of mars, map 1-1083, *US Geol. Surv., Reston, Va*. 16

Scott, D. H., DH, and K. L. Tanaka (1986), Geologic map of the western equatorial region of mars. 16, 17

Seipold, U. (1998), Temperature dependence of thermal transport properties of crystalline rocks — a general law, *Tectonophysics*, *291*, 161–171, doi :10.1016/S0040-1951(98)00037-7. 125

Sekhar, P., and S. King (2014), 3D spherical models of Martian mantle convection constrained by melting history, *Earth and Planetary Science Letters*, *388*, 27–37, doi :10.1016/j.epsl.2013.11.047. 27, 36, 43, 47, 54, 101, 111, 136

Shahnas, M., J. Lowman, G. Jarvis, and H.-P. Bunge (2008), Convection in a spherical shell heated by an isothermal core and internal sources : Implications for the thermal state of planetary mantles, *Physics of the Earth and Planetary Interiors*, *168*, 6–15, doi :10.1016/j.pepi.2008.04.007. 61

Sharp, R. P. (1973), Mars : Fretted and chaotic terrains, *Journal of geophysical research*, *78*, 4073–4083, doi :10.1029/JB078i020p04073. 18

Sharpe, H. N., and W. R. Peltier (1978), Parameterized mantle convection and the Earth's thermal history, *Geophysical Research Letters*, *5*, 737–740, doi :10.1029/GL005i009p00737. 57, 59

Skinner Jr, J., K. Tanaka, T. Hare, J. Kargel, G. Neukum, S. Werner, and J. Rodriguez (2004), Mass-wasting of the circum-utopia highland/lowland boundary : processes and controls, in *Workshop on Hemispheres Apart : The Origin and Modification of the Martian Crustal Dichotomy*, vol. 1213, p. 58. 16

Sleep, N. H. (1994), Martian plate tectonics, *Journal of Geophysical Research : Planets*, *99*, 5639–5655, doi :10.1029/94JE00216. 14, 20, 25, 26

Smith, D. E., M. T. Zuber, H. V. Frey, J. B. Garvin, J. W. Head, D. O. Muhleman, G. H. Pettengill, R. J. Phillips, S. C. Solomon, H. J. Zwally, et al. (2001), Mars orbiter laser altimeter : Experiment summary after the first year of global mapping of mars, *Journal of Geophysical Research : Planets*, *106*, 23,689–23,722, doi :10.1029/2000JE001364. 29

Sohl, F., and T. Spohn (1997), The interior structure of mars : Implications from snc meteorites, *Journal of Geophysical Research : Planets*, *102*, 1613–1635, doi :10.1029/96JE03419. 156, 161, 180, 184

Solomatov, V. (1995), Scaling of temperature- and stress-dependent viscosity convection, *Physics of fluids*, *7*, 266–274, doi :10.1063/1.868624. 59, 60

Solomatov, V. (2000), Fluid dynamics of a terrestrial magma ocean, *Origin of the Earth and Moon*, pp. 323–338. 24

Solomatov, V., and L.-N. Moresi (2000), Scaling of time-dependent stagnant lid convection : Application to small-scale convection on earth and other terrestrial planets, *Journal of Geophysical Research : Solid Earth*, *105*, 21,795–21,817, doi :10.1029/2000JB900197. 60, 69

Solomon, S., O. Aharonson, J. Aurnou, W. Banerdt, M. Carr, A. Dombard, H. Frey, M. Golombek, S. Hauck, II, J. Head, III, B. Jakosky, C. Johnson, P. McGovern, G. Neumann, R. Phillips, D. Smith, and M. Zuber (2005), New Perspectives on Ancient Mars, *Science*, *307*, 1214–1220, doi :10.1126/science.1101812. 20, 22, 23, 25, 27, 33, 35, 111

Solomon, S. C. (1977), The relationship between crustal tectonics and internal evolution in the moon and mercury, *Physics of the Earth and Planetary Interiors*, *15*, 135–145, doi : 10.1016/0031-9201(77)90026-7. 191

Solomon, S. C., D. L. Anderson, W. B. Banerdt, R. G. Butler, P. M. Davis, F. K. Duennebier, Y. Nakamura, E. A. Okal, and R. J. Phillips (1991), Scientific rationale and requirements for a global seismic network on mars. 158

Sotin, C., and S. Labrosse (1999), Three-dimensional thermal convection in an iso-viscous, infinite Prandtl number fluid heated from within and from below : applications to the transfer of heat through planetary mantles, *Physics of the Earth and Planetary Interiors*, *112*, 171–190, doi :10.1016/S0031-9201(99)00004-7. 57, 61

Squyres, S., J. Grotzinger, R. Arvidson, J. Bell, W. Calvin, P. Christensen, B. Clark, J. Crisp, W. Farrand, K. E. Herkenhoff, et al. (2004), In situ evidence for an ancient aqueous environment at meridiani planum, mars, *science*, *306*, 1709–1714, doi :10.1126/science.1104559. 10

Šrámek, O., and S. Zhong (2010), Long-wavelength stagnant lid convection with hemispheric variation in lithospheric thickness : Link between martian crustal dichotomy and tharsis ?, *Journal of Geophysical Research : Planets*, *115*, doi :10.1029/2010JE003597. 46, 47, 48, 53, 148

Stein, C., J. Lowman, and U. Hansen (2013), The influence of mantle internal heating on lithospheric mobility : Implications for super-earths, *Earth and Planetary Science Letters*, pp. 448–459, doi :10.1016/j.epsl.2012.11.011. 65

Stevenson, D. (1988), Fluid dynamics of core formation, in *Topical Conference Origin of the Earth*, vol. 681, p. 87. 24

Stevenson, D., T. Spohn, and G. Schubert (1983), Magnetism and thermal evolution of the terrestrial planets, *Icarus*, *54*, 466–489, doi :10.1016/0019-1035(83)90241-5. 57, 59, 96, 119

Stevenson, D. J. (2001), Mars' core and magnetism, *Nature*, *412*, 214, doi :10.1038/35084155. 45

Susko, D., S. Karunatillake, G. Kodikara, J. Skok, J. Wray, J. Heldmann, A. Cousin, and T. Judice (2017), A record of igneous evolution in Elysium, a major martian volcanic province, *Scientific reports*, *7*, 43,177, doi :10.1038/srep43177. 50, 114, 132

Tackley, P. J. (2000), Self-consistent generation of tectonic plates in time-dependent, three-dimensional mantle convection simulations, *Geochemistry, Geophysics, Geosystems*, *1*, doi : 10.1029/2000GC000036. 65

Tackley, P. J., D. J. Stevenson, G. A. Glatzmaier, and G. Schubert (1993), Effects of an endothermic phase transition at 670 km depth in a spherical model of convection in the earth's mantle, *Nature*, *361*, 699, doi :10.1038/361699a0. 23

Takahashi, E. (1990), Speculations on the Archean Mantle : Missing link between komatiite and depleted garnet peridotite, *Journal of Geophysical Research*, *95*, 15,941–15,954, doi : 10.1029/JB095iB10p15941. 127, 132, 133

Tanaka, K., J. Skinner, T. Hare, T. Joyal, and A. Wenker (2003), Resurfacing history of the northern plains of mars based on geologic mapping of mars global surveyor data, *Journal of Geophysical Research : Planets*, *108*, doi :10.1029/2002JE001908. 16, 18, 50

Tanaka, K., S. Robbins, C. Fortezzo, J. Skinner Jr., and T. Hare (2014), The digital global geologic map of Mars : Chronostratigraphic ages, topographic and crater morphologic characteristics, and updated resurfacing history, *Planetary and Space Science*, *95*, 11–24, doi : 10.1016/j.pss.2013.03.006. 17, 51, 115

Tanaka, K. L., and D. H. Scott (1987), *Geologic map of the polar regions of Mars*. 17

Tanaka, K. L., N. K. Isbell, D. H. Scott, R. Greeley, and J. E. Guest (1988), The resurfacing history of mars-a synthesis of digitized, viking-based geology, in *Lunar and Planetary Science Conference Proceedings*, vol. 18, pp. 665–678. 17

Tanaka, K. L., J. A. Skinner, and T. M. Hare (2005), Geologic map of the northern plains of mars. 16, 18

Taylor, G., W. Boynton, J. Brückner, H. Wänke, G. Dreibus, K. Kerry, J. Keller, R. Reedy, L. Evans, R. Starr, S. Squyres, S. Karunatillake, O. Gasnault, S. Maurice, C. d'Uston, P. Englert, J. Dohm, V. Baker, D. Hamara, D. Janes, A. Sprague, K. Kim, and D. Drake (2006), Bulk composition and early differentiation of Mars, *Journal of Geophysical Research Planets*, *111*, E03S10, doi :10.1029/2005JE002645. 36, 37, 38, 112, 126, 134, 135

Taylor, J., N. Teanby, and J. Wookey (2013), Estimates of seismic activity in the cerberus fossae region of mars, *Journal of Geophysical Research : Planets*, *118*, 2570–2581, doi : 10.1002/2013JE004469. 157, 158, 161, 177

Taylor, S. (1982), Lunar and terrestrial crusts : a constrast in origin and evolution, *Physics of the Earth and Planetary Interiors*, *29*, 233–241, doi :10.1016/0031-9201(82)90014-0. 62, 65

Teanby, N. (2015), Predicted detection rates of regional-scale meteorite impacts on mars with the insight short-period seismometer, *Icarus*, *256*, 49–62, doi :10.1016/j.icarus.2015.04.012. 157, 158

Teanby, N., and J. Wookey (2011), Seismic detection of meteorite impacts on mars, *Physics of the Earth and Planetary Interiors*, *186*, 70–80, doi :10.1016/j.pepi.2011.03.004. 158

Thiriet, M., C. Michaut, D. Breuer, and A.-C. Plesa (2018), Hemispheric dichotomy in lithosphere thickness on mars caused by differences in crustal structure and composition, *Journal of Geophysical Research : Planets*, *123*, 823–848, doi :10.1002/2017JE005431. 110

Thiriet, M., D. Breuer, C. Michaut, and A.-C. Plesa (2018b), Scaling laws of convection for cooling planets in a stagnant lid regime, *Physics of the Earth and Planetary Interiors*, doi : 10.1016/j.pepi.2018.11.003. 59

Thomson, W. (1862), On the rigidity of the earth., *Proceedings of the Royal Society of London Series I*, *12*, 103–104. 155

Titus, T. N., H. H. Kieffer, and P. R. Christensen (2003), Exposed water ice discovered near the south pole of mars, *Science*, *299*, 1048–1051, doi :10.1126/science.1080497. 10

Tonks, W. B., and H. J. Melosh (1993), Magma ocean formation due to giant impacts, *Journal of Geophysical Research : Planets*, *98*, 5319–5333, doi :10.1029/92JE02726. 21, 24

Tosi, N., M. Grott, A.-C. Plesa, and D. Breuer (2013), Thermochemical evolution of Mercury's interior, *Journal of Geophysical Research*, *118*, 1–14, doi :10.1002/jgre.20168. 62, 65, 96, 191

Townsend, A. (1964), Natural convection in water over an ice surface, *Quarterly Journal of the Royal Meteorological Society*, *90*, 248–259, doi :10.1002/qj.49709038503. 57

Tozer, D. (1970), Factors determining the temperature evolution of thermally convecting earth models, *Physics of the Earth and Planetary Interiors*, *2*, 393–398, doi :10.1016/0031-9201(69)90036-3. 85

Travis, B., and P. Olson (1994), Convection with internal heat sources and thermal turbulence in the Earth's mantle, *Geophysical Journal*, *118*, 1–19, doi :10.1111/j.1365-246X.1994.tb04671.x. 57

Treiman, A., J. Jones, and M. Drake (1987), Core formation in the shergottite parent body and comparison with the Earth, *Journal of Geophysical Research*, *92*, E627–E632, doi :10.1029/JB092iB04p0E627. 36

Trompert, R., and U. Hansen (1998), On the Rayleigh number dependence of convection with a strongly temperature-dependent viscosity, *Physics of Fluids*, *10*, 351–360, doi :10.1063/1.869527. 61, 62

Turcotte, D., and G. Schubert (1982), Geodynamics : Application of Continuum Physics to Geological Problems, *Cambridge Univ. Press, New York*, p. 450 pp, doi :10.1017/S0022112083223439. 59, 72, 95

Turcotte, D., and G. Schubert (2002), Geodynamics, second ed, *Cambridge Univ. Press, New York*, p. 456 pp. 68, 118

van Keken, P. (2001), Cylindrical scaling for dynamical cooling models of the Earth, *Physics of the Earth and Planetary Interiors*, *124*, 119–130, doi :10.1016/S0031-9201(01)00195-9. 58, 81

Vangelov, V., and G. Jarvis (1994), Geometrical effects of curvature in axisymmetric spherical models of mantle convection, *Journal of Geophysical Research*, *99*, 9345–9358, doi :10.1029/93JB03133. 61

Vaucher, J., D. Baratoux, N. Mangold, P. Pinet, K. Kurita, and M. Gregoire (2009), The volcanic history of central Elysium Planitia : Implications for martian magmatism, *Icarus*, *204*, 418–442, doi :10.1016/j.icarus.2009.06.032. 17, 132

Verhoeven, O., A. Rivoldini, P. Vacher, A. Mocquet, G. Choblet, M. Menvielle, V. Dehant, T. Van Hoolst, J. Sleewaegen, J.-P. Barriot, et al. (2005), Interior structure of terrestrial planets : Modeling mars' mantle and its electromagnetic, geodetic, and seismic properties, *Journal of Geophysical Research : Planets*, *110*(E4), doi :10.1029/2004JE002271. 161

Vilella, K., and F. Deschamps (2018), Temperature and heat flux scaling laws for isoviscous, infinite prandtl number mixed heating convection, *Geophysical Journal International*, *214*, 265–281, doi :10.1093/gji/ggy138. 70

Vinnik, L., H. Chenet, J. Gagnepain-Beyneix, and P. Lognonne (2001), First seismic receiver functions on the moon, *Geophysical Research Letters*, *28*, 3031–3034, doi :10.1029/2001GL012859. 158

Wänke, H., and G. Dreibus (1994), Chemistry and Accretion History of Mars, *Philosophical Transactions : Physical Sciences and Engineering*, *349*, 285–293, doi :10.1098/rsta.1994.0132. 36, 38, 62, 65, 126, 134

Warner, N., M. P. Golombek, J. Sweeney, R. Fergason, R. Kirk, and C. Schwartz (2017), Near Surface Stratigraphy and Regolith Production in Southwestern Elysium Planitia, Mars : Implications for Hesperian-Amazonian Terrains and the InSight Lander Mission, *Space Science Reviews*, pp. 1–44, doi :10.1007/s11214-017-0352-x. 125

Warren, P. (1985), The magma ocean concept and lunar evolution., *Annual Review Earth and Planetary Sciences*, *13*, 201–40, doi :10.1146/annurev.ea.13.050185.001221. 35

Watters, T. R. (2003a), Lithospheric flexure and the origin of the dichotomy boundary on mars, *Geology*, *31*, 271–274, doi :10.1130/0091-7613(2003)031<0271:LFATOO>2.0.CO;2. 16, 148, 179, 191

Watters, T. R. (2003b), Thrust faults along the dichotomy boundary in the eastern hemisphere of mars, *Journal of Geophysical Research : Planets*, *108*(E6), doi :10.1029/2002JE001934. 16, 191

Watters, T. R., and P. J. McGovern (2006), Lithospheric flexure and the evolution of the dichotomy boundary on mars, *Geophysical research letters*, *33*, doi :10.1029/2005GL024325. 18, 148

Watters, T. R., C. J. Leuschen, J. J. Plaut, G. Picardi, A. Safaeinili, S. M. Clifford, W. M. Farrell, A. B. Ivanov, R. J. Phillips, and E. R. Stofan (2006), Marsis radar sounder evidence of buried basins in the northern lowlands of mars, *Nature*, *444*, 905, doi :10.1038/nature05356. 19

Watters, T. R., P. J. McGovern, and R. P. Irwin Iii (2007), Hemispheres apart : The crustal dichotomy on mars, *Annu. Rev. Earth Planet. Sci.*, *35*, 621–652, doi :10.1146/annurev.earth.35.031306.140220. 15, 16, 19, 22, 26, 31, 148, 179, 191

Watts, A. (1978), An analysis of isostasy in the world's oceans 1. hawaiian-emperor seamount chain, *Journal of Geophysical Research : Solid Earth*, *83*, 5989–6004, doi :10.1029/JB083iB12p05989. 49

Watts, A. (1992), The effective elastic thickness of the lithosphere and the evolution of foreland basins, *Basin Research*, *4*, 169–178, doi :10.1111/j.1365-2117.1992.tb00043.x. 49

Weber, R. C., P.-Y. Lin, E. J. Garnero, Q. Williams, and P. Lognonne (2011), Seismic detection of the lunar core, *science*, *331*, 309–312, doi :10.1126/science.1199375. 156

Weider, S. Z., L. R. Nittler, R. D. Starr, E. J. Crapster-Pregont, P. N. Peplowski, B. W. Denevi, J. W. Head, P. K. Byrne, S. A. Hauck II, D. S. Ebel, et al. (2015), Evidence for geochemical terranes on mercury : Global mapping of major elements with messenger's x-ray spectrometer, *Earth and Planetary Science Letters*, pp. 109–120, doi :10.1016/j.epsl.2015.01.023. 96

Werner, S. (2009), The global martian volcanic evolutionary history, *Icarus*, *201*, 44–68, doi : 10.1016/j.icarus.2008.12.019. 17, 25, 33, 46, 50, 111, 114, 124, 132

Wetherill, G. W. (1980), Formation of the terrestrial planets, *Annual review of astronomy and astrophysics*, *18*, 77–113, doi :10.1146/annurev.aa.18.090180.000453. 24

Wieczorek, M. (2007), The gravity and topography of the terrestrial planets, *Treatise on Geophysics*, *10*, 165–206, doi :10.1016/B978-044452748-6/00156-5. 28, 29, 30, 42, 54, 179, 193

Wieczorek, M. (2008), Constraints on the composition of the martian South polar cap from gravity and topography, *Icarus*, *196*, 506–517, doi :10.1016/j.icarus.2007.10.026. 49, 50, 52, 110, 111, 114, 122, 129

Wieczorek, M., and M. Zuber (2004), Thickness of the Martian crust : improved constraints from geoid-to-topography ratios, *Journal of Geophysical Research*, *109*, E01,009, doi :10. 1029/2003JE002153. 28, 31, 43, 125, 136

Wilhelms, D. E., and S. W. Squyres (1984), The martian hemispheric dichotomy may be due to a giant impact, *Nature*, *309*, 138, doi :10.1038/309138a0. 17, 20, 21

Williams, J.-P., and F. Nimmo (2004), Thermal evolution of the martian core : Implications for an early dynamo, *Geology*, *32*, 97–100, doi :10.1130/G19975.1. 45

Wise, D. U., M. P. Golombek, and G. E. McGill (1979), Tharsis province of mars : Geologic sequence, geometry, and a deformation mechanism, *Icarus*, *38*, 456–472, doi :10.1016/ 0019-1035(79)90200-8. 14, 20, 23

Wolstencroft, M., J. Davies, and D. Davies (2009), Nusselt-Rayleigh number scaling for spherical shell Earth mantle simulation up to a Rayleigh number of $10^9$, *Physics of the Earth and Planetary Interiors*, *176*, 132–141, doi :10.1016/j.pepi.2009.05.002. 61

Wood, J., J. Dickey Jr, and B. Powell (1870), Lunar anorthosites and a geophysical model of the moon, *Proceedings of the Apollo 11 Lunar Science Conference*, pp. 965–988. 35

Woodhouse, J. (1974), Surface waves in a laterally varying layered structure, *Geophysical Journal International*, *37*, 461–490, doi :10.1111/j.1365-246X.1974.tb04098.x. 174

Woodhouse, J. (1988), The calculation of the eigenfrequencies and eigenfunctions of the free oscillations of the earth and sun, *Seismological algorithms : computational methods and computer programs*, pp. 321–370. 161

Wray, J., S. Hansen, J. Dufek, G. Swayze, S. Murchie, F. Seelos, J. Skok, R. Irwin III, and M. Ghiorso (2013), Prolonged magmatic activity on Mars inferred from the detection of felsic rocks, *Nature Geosci*, *6*, 1013–1017, doi :10.1038/NGEO1994. 14, 31, 33, 35, 36, 43, 54, 112, 113

Xiao, L., J. Huang, P. Christensen, R. Greeley, D. Williams, J. Zhao, and Q. He (2012), Ancient volcanism and its implication for thermal evolution of Mars, *Earth and Planetary Science Letters*, *323-324*, 9–18, doi :10.1016/j.epsl.2012.01.027. 31, 33, 112, 113, 125

Yao, C., F. Deschamps, J. Lowman, C. Sanchez-Valle, and P. Tackley (2014), Stagnant lid convection in bottom-heated thin 3-d spherical shells : Influence of curvature and implications for dwarf planets and icy moons, *Journal of Geophysical Research : Planets*, *119*, 1895–1913, doi :10.1002/2014JE004653. 70, 83, 92

Yoder, C., A. Konopliv, D. Yuan, E. Standish, and W. Folkner (2003), Fluid core size of mars from detection of the solar tide, *Science*, *300*, 299–303, doi :10.1126/science.1079645. 162

Yoshida, M., and A. Kageyama (2006), Low-degree mantle convection with strongly temperature- and depth-dependent viscosity in a three-dimensional spherical shell, *Journal of Geophysical Research*, *111*, B03,412, doi :10.1029/2005JB003905. 111

Zhang, S., and C. O'Neill (2016), The early geodynamic evolution of mars-type planets, *Icarus*, *265*, 187–208, doi :10.1016/j.icarus.2015.10.019. 45

Zhang, S., and D. A. Yuen (1995), The influences of lower mantle viscosity stratification on 3d spherical-shell mantle convection, *Earth and Planetary Science Letters*, *132*, 157–166, doi :10.1016/0012-821X(95)00038-E. 23

Zharkov, V., and T. Gudkova (2005), Construction of martian interior model, *Solar System Research*, *39*, 343–373, doi :10.1007/s11208-005-0049-7. 161, 184

Zheng, Y., F. Nimmo, and T. Lay (2015), Seismological implications of a lithospheric low seismic velocity zone in mars, *Physics of the Earth and Planetary Interiors*, *240*, 132–141, doi :10.1016/j.pepi.2014.10.004. 164, 169, 173

Zhong, S. (2009), Migration of tharsis volcanism on mars caused by differential rotation of the lithosphere, *Nature Geoscience*, *2*, 19, doi :10.1038/ngeo392. 46, 47, 48, 53, 148

Zhong, S., and M. Zuber (2001), Degree-1 mantle convection and the crustal dichotomy on Mars, *Earth and Planetary Science Letters*, *189*, 75–84, doi :10.1016/S0012-821X(01)00345-4. 20, 23, 47

Zhong, S., E. Parmentier, and M. T. Zuber (2000), A dynamic origin for the global asymmetry of lunar mare basalts, *Earth and Planetary Science Letters*, *177*, 131–140, doi :10.1016/S0012-821X(00)00041-8. 38

Zuber, M., S. Solomon, R. Phillips, D. Smith, G. Tyler, O. Aharonson, G. Balmino, W. Banerdt, J. Head, C. Johnson, F. Lemoine, P. McGovern, D. R. G.A. Neumann and, and S. Zhong (2000), Internal Structure and Early Thermal Evolution of Mars from Mars Global Surveyor Topography and Gravity, *Science*, *287*, 1788–1793, doi :10.1126/science.287.5459.1788. 17, 20, 28, 30, 125

Zuber, M. T. (2001), The crust and mantle of mars, *Nature*, *412*, 220, doi :10.1038/35084163. 18, 19, 30, 31, 46, 47